MICROCOPY RESOLUTION TEST CHART
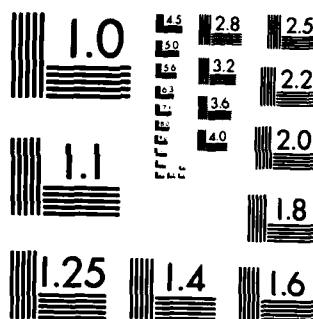
NATIONAL BUREAU OF STANDARDS-1963-A

AD-A152 805

GEOPHYSICAL PLASMAS

AND ATMOSPHERIC MODELING

FINAL REPORT

SAIC 85/1621

March 1985

DTIC FILE COPY

Science Applications International Corporation

GEOPHYSICAL PLASMAS

AND ATMOSPHERIC MODELING

FINAL REPORT

SAIC 85/1621

March 1985

SAIC™

Science Applications International Corporation

Post Office Box 1303, 1710 Goodridge Drive, McLean, Virginia 22102, (703) 821-4300

GEOPHYSICAL PLASMAS

AND ATMOSPHERIC MODELING

FINAL REPORT

SAIC 85/1621

March 1985

Submitted to

Dr. Joseph Huba
Geophysical and Plasma Dynamics Branch
Plasma Physics Division
Naval Research Laboratory
Washington, D.C. 20375

Prepared by:

Ellis Hyman with
Pradeep Chaturvedi, James Chen, Jim Drake, Gurudas Ganguli,
Supriya Ganguli, Charles Goodrich, Adil Hassam, Y.C. Lee,
Horace Mitchell, Dennis Papadopoulos, Harvey Rowland, Keith
Sashegyi, Punyamurthula Satyanarayana, Robert A. Smith and
Darrell Strobel

Prepared Under:

Contract No. N00014-84-C-2032

SCIENCE APPLICATIONS INTERNATIONAL CORPORATION

1710 GOODRIDGE DRIVE, MCLEAN, VA. 22102 (703) 734-5840

TABLE OF CONTENTS

Section I

TECHNICAL DISCUSSION

The work performed by Science Applications International Corporation (SAIC) on this contract, "Geophysical Plasmas and Atmospheric Modeling," Contract Number N00014-84-C-2032, SAIC Project Number 1-157-17-518, encompasses a wide range of topics in space plasma physics and atmospheric modeling in support of the programs of the Geophysical and Plasma Dynamics Branch of the Naval Research Laboratory (NRL). This report covers the period 1 December 1983 to 1 February 1985. In this section we will summarize the various subjects studied and the results obtained. Details will be included in Appendices which will document reports and publications resulting from our work.

In the following subsections we will describe the major accomplishments in each of the following research efforts: (A) the collisionless tearing instability in a non-Maxwellian neutral sheet, (B) the role of nonlocalities in magnetosphere-ionosphere coupling, (C) auroral plasma transport and magnetosphere-ionosphere coupling, (D) a steady state model of the auroral ionosphere, (E) high latitude ionospheric irregularities [I], (F) high latitude ionospheric irregularities [II], (G) ionospheric turbulence, (H) hybrid code simulations for HANE, (I) spectral indices

1

from power spectral densities due to spatial irregularities in HANE plasma clouds, (J) the effects of finite parallel resistivity on the structuring of barium clouds, (K) finite temperature effects on structuring barium clouds, (L) collective particle accelerator studies, (M) models for the earth's middle atmosphere, (N) the dynamics of the Indian summer monsoon and (O) energy partitioning in the I_0 plasma torus.

(A)   The Collisionless Tearing Instability in a Non-Maxwellian Neutral Sheet

As part of our program to investigate magnetospheric processes, we have completed the integro-differential formulation and full solution of the collisionless tearing instability in a non-Maxwellian neutral sheet. The new formalism provides a theoretical and mathematical method to treat the orbit integrals which are necessary for complete evaluation of the linear properties. All the complicated orbits occurring in the neutral sheet geometry are included analytically and exactly so that the numerics required are minimal. More important, the limitations due to various approximations such as weak anisotropy and constant-ψ approximations, which were used by essentially all previous theoretical works, are removed. Another standard

2

approximation, the low-frequency approximation, has been retained since the scalar potential is neglected for the purpose of developing the method. This, however, is not an inherent limitation of the formalism.

The specific equilibrium chosen for demonstrating the application of the formalism is of the sharp-boundary type. This configuration is intrinsically non-Maxwellian, with no globally isotropic limit. It also gives rise to a number of singularities (albeit integrable) which would be smoothed out in a diffuse profile. Thus, the method developed here is expected to be more than adequate for treating diffuse profiles.

As discussed above, the analysis is carried out for low-frequency electromagnetic perturbations ($|\omega| \ll \omega_{ci}$) with $\underline{k} \parallel \underline{B}_0$, where $\underline{B}_0$ is the field-reversed equilibrium magnetic field. The treatment is linear, self-consistent and kinetic for both ions and electrons. The integro-differential equation utilizing all the exact orbits is solved using the Galerkin method to obtain the dispersion relation and the eigenmode structure. We find that the eigenmode is strongly localized to a region of the order of $(\rho_e Z_p)^{\frac{1}{2}} \ll Z_p$ at the null-plane, where ρ_e is a measure of the electron gyroradius in the asymptotic magnetic field and Z_p is the thickness of the sheet. We find that the eigenfunction is indeed highly structured in this narrow region so that the constant-ψ

3

approximation used in the "conventional" techniques is invalid for the present non-Maxwellian system.

The dispersion relation is forced to have the general form $\gamma/kv_{e\parallel} \sim$ constant, where $v_{e\parallel}$ is the electron thermal velocity along $\underline{B}_0$. Consistent with the previous analyses of Chen and Palmadesso [Phys. Fluids $\underline{27}$, 1198 (1984)] and Chen et al., [Geophys. Res. Lett. $\underline{11}$, 12 (1984)], the growth rate of the collisionless tearing mode is significantly enhanced in the presence of non-Maxwellian features in the distribution function. In the present system, it is the electrons that are chiefly responsible for the enhancement. Specifically, in comparison with the isotropic case, the growth rate can be enhanced by several orders of magnitude. In addition, the small wavelength modes are strongly favored. This latter point may be important for the nonlinear behavior of the neutral sheet.

In addition to the full solution, a method to determine the sufficient condition for instability is given on the basis of a quadratic form and the eigenvalues of a self-adjoint integro-differential operator. This method allows one to determine gross instability properties without extensive numerical computation, especially for complicated systems.

The detailed documentation has been submitted to the Physics of Fluids for publication and has been accepted

4

conditionally. It appears in this report as Appendix A, entitled "Collisionless Tearing Instability in a Non-Maxwellian Neutral Sheet: An Integro-Differential Formulation."

B. The Role of Nonlocalities in Magnetosphere-Ionosphere Coupling

We have previously developed a nonlocal formalism for electrostatic waves and have applied it to study the important and essential inhomogeneities such as magnetic shear, produced by field aligned currents and the finite width of the current channels on the current driven ion cyclotron instability (CDICI) [Ganguli and Bakshi, Phys. Fluids 25, 1830 (1982); Baskshi, Ganguli and Palmadesso, Phys. Fluids 26, 1808 (1983)]. The magnetospheric applications were also discussed [Ganguli et al., J. Geophys. Res. 89, 945 (1984)]. Experimental verification of filamental quenching due to the finite width current channels has been reported [Cartier et al., Phys. Fluids (to appear) Jan. 1985].

The studies up to now, however, focussed primarily on the normal mode properties; whereas the CDICI is a convective instability. Consequently, a very relevant question remains, that is what, if any, is the modification

5

introduced by nonlocalities on the convective properties of the CDICI? Recently we have examined this problem [Ganguli et al. Phys. Fluids 27, 2039 (1984)]. The following are the important results:

(a) L_C/L_S is the parameter of importance, L_C and L_S being the characteristic length scales associated with the current channels and magnetic shear.

(b) $L_C \geq 0.1 \, L_S$: The temporal growth rate is much reduced from its local value. However, the instability becomes absolute in the direction along the magnetic field, the z direction. There is no energy flow in the x direction, the direction of the inhomogeneity perpendicular to the magnetospheric field, and the energy flow in the y direction is ignorable if $\partial/\partial y = 0$.

(c) $L_C < 0.01 \, L_S$: The nonlocal theory reproduces the local result.

(d) $L_C \sim \rho_i \ll L_S$: The finite width of the current channel becomes important leading to filamental quenching. But when further reduced so that $L_C < \rho_i$, both V_{gz} and V_{gy} become reduced and

eventually negative. Here ρ_i is the ion gyro radius and V_{gz} and V_{gy} are the group velocities in the z and the y directions respectively. These results are described in more detail in Appendix B entitled "Nonlocal Effects on the Convective Properties of the Electrostatic Current-Driven Ion-Cyclotron Instability."

By changing the propagation characteristics from convective to absolute the nonlocal effect on one hand reduces the temporal growth rate offering stability, but on the other hand makes the instability absolute thereby inducing destability. Thus, depending on the strength of the field aligned current one can expect nonlocal effects either to totally damp the ion cyclotron waves or to make them more explosive.

In trying to make the ambient field configuration more realistic of magnetospheric conditions we have included a mild inhomogeneity in the magnetic field along the z-direction. This is to simulate the dipolar nature of the earth's magnetic field on top of the stronger inhomogeneities (discussed earlier) in the x-direction. Using a perturbation technique we develop a two dimensional analytic model (Ganguli et al, In Proc. of International Conf. on Plasma Physics, Lusanne, Switzerland 1984 and

7

appearing in this report as Appendix C entitled "Two Dimensional Nonlocal Formalism for Electrostatic Waves in the Magnetosphere") to study electrostatic ion cyclotron waves. The model needs further improvements. Ultimately a two dimensional integral equation will become necessary to study the problems concerning the wave properties in the real magnetosphere. A review and application of our work so far to the magnetosphere-ionosphere coupling problem has been presented at the COSPAR meeting in Graz, Austria, 1984 and will appear in Advances in Space Physics. It is included in this report as Appendix D, entitled "The Role of Nonlocalities in Magnetosphere-Ionosphere Coupling Processes," by Ganguli and Palmadesso.

(C) Auroral Plasma Transport and Magnetosphere-Ionosphere Coupling

An existing numerical simulation of the transport of plasma along an auroral field line has been used to investigate the effect of enhanced parallel resistivity in the auroral plasma. This multi-moment multi-fluid model was used to simulate the effects of momentum transfer due to such resistivity when more than one ion species is present and the results were published in a paper entitled "O^+ Acceleration Due to Resistive Momentum Transfer in the

8

Auroral Field Line Plasma" (H.G. Mitchell, Jr., and P.J. Palmadesso, J. Geophys. Res. 89, 7573-7576, 1984). This paper has been included in this report in Appendix E.

In order to enhance our understanding of high-latitude magnetosphere-ionosphere coupling and to provide a theoretical and observational background for our one-dimensional auroral field line model, we have performed research on the polar cap plasma outside of our direct modelling efforts. The results of this research and our proposals for new directions in this effort were reported on at the Chapman Conference on the Magnetospheric Polar Cap (August 1984). An abstract of this presentation is included here.

Nonideal Processes on Polar Cap Field Lines*

P.J. Palmadesso (Naval Research Laboratory, Washington, D.C. 20375) H.G. Mitchell, Jr. (Science Applications, Inc., McLean, VA 22102)

The importance of nonideal processes in the auroral region is well established and it is known that the mapping of electric fields between the ionosphere and the magnetosphere is often profoundly influenced by electrodynamic processes occurring on auroral field lines. The situation at higher latitudes is less clear. On the one hand, the reduced levels of field aligned currents typical of the polar cap rule out a number of mechanisms invoked to account for parallel electric fields in the auroral regions; on the other hand, the existence of polar cap aurora and the apparently wave associated acceleration of injected barium ions observed in the CAMEO[1] releases suggest significant electrodynamic activity on polar cap field lines. While it is possible that transient local enhancements of field aligned current levels occur as a result of transient distortions of magnetic field

geometries or some other mechanism, nonideal electrodynamic processes not associated with large currents must also be considered. Current efforts to develop global dynamic simulation models which include interactions between the magnetosphere and the polar ionosphere, and attempts to understand the dynamics of high latitude ionospheric irregularities, provide additional motivation for the study of I-M coupling processes at polar cap latitudes.

We review relevant observational data and summarize major theoretical concepts for the generation and maintenance of parallel electric fields, with emphasis on the polar cap application. Some less familiar approaches to this problem will also be discussed.

[1]Heppner et al., J.G.R., 86,3519 (1981).

We have also been participating in efforts to simulate microscopic plasma turbulence effects associated with parallel electric fields. It is our goal to include the results of these computer simulations in our macroscopic auroral transport model in order to better understand the large scale effects resulting from this turbulence. These results have been presented at the Fall, 1984 meeting of the American Geophysical Union, and the abstract of this presentation follows.

The Role of Plasma Turbulence in Auroral Electrodynamic Processes

P.Palmadesso (Naval Research Laboratory, Washington,D.C. 20375) H. Mitchell (Science Applications, Inc., McLean, VA 22102) H. Rowland, (University of Maryland, College Park, MD 20742)

A number of physical mechanisms have been proposed to account for the formation of parallel electric fields on auroral field lines, including mirror force

processes, double layers or electrostatic shocks, anomalous resistivity, kinetic Alfven waves, etc. These are not mutually exclusive; in fact it is likely that many or all of these processes operate and interact during active auroral conditions. Plasma turbulence is predicted theoretically and observed in the unstable field aligned currents associated with active auroral events, and is believed to play an important role in several of these electrodynamic processes. Turbulent wave-particle interactions can modify the spatial distribution of parallel electric fields associated with mirror force processes. Anomalous resistivity due to strong turbulence leads to parallel E fields in large amplitude kinetic Alfven waves or larger scale current systems, when the electron-ion drift velocity lies above a threshold value but below the value required to excite strong double layers. At the upper end of this range there is an "intermediate regime" where anomalous resistivity and weak double layer effects coexist and interact. We discuss the results of computer simulations conducted to clarify the physics of the intermediate regime in a magnetized plasma, and comparison of these results with observational data.

The fact that electric fields perpendicular to the magnetic field in the high-latitude ionosphere map upward along the magnetic field for thousands of kilometers into the magnetosphere implies that structuring instabilities in the ionosphere are dynamically coupled to a large amount of magnetospheric plasma. In order to study this coupling, we have adapted a numerical simulation for low-latitude ionospheric structuring to the high latitude ionosphere. In this model, the magnetospheric plasma effectively increases the inertia of the unstable ions, and the growth of the unstable structures in the ionospheric plasma is slowed.

11

Our model of this phenomenon and our initial simulations of linear growth were presented at the Spring, 1984 meeting of the American Geophysical Union. An abstract of this talk follows.

Numerical Simulation of the Effect of Magnetosphere-Ionosphere Coupling on High Latitude Ionospheric Plasma Structure*

H. Mitchell (Science Applications, Inc., McLean, VA 22102), J. Fedder and S. Zalesak (both at Naval Research Laboratory, Washington, D.C. 20375)

Large-scale plasma density enhancements are a confirmed feature of the high latitude F-region ionosphere, and both theoretical and experimental studies indicate that the existence of such enhancements in a region of convection can lead to density irregularities and structuring due to plasma instabilities. The fact that the F-region plasma is on flux tubes which thread the magnetosphere implies that the development of high-latitude F-region structure is affected by the inertia of the large height-integrated magnetospheric plasma density on these flux tubes. In this paper we present initial simulations of the effects of magnetosphere-ionosphere coupling on such structure. The magnetospheric and ionospheric plasmas are modeled as separate two-dimensional convecting layers whose dynamics are coupled by the mapping of the perpendicular electric fields along the magnetic field lines threading the two layers.

We have continued our simulations of this region and investigated the nonlinear development of high-latitude structures. We have found that the inclusion of magnetospheric ion inertia tends to spread the ionospheric density striations perpendicular to their normal direction of growth, thus inhibiting the breakup of unstable density

enhancements and leading to structures of quite a different nature than those at low latitudes. Our results were presented at the Chapman Conference on the Magnetospheric Polar Cap (August, 1984), an abstract of which is included here:

Role of Magnetospheric Coupling in Polar Cap Ionospheric Instabilities and Structure*

M.J. Keskinen (Naval Research Laboratory, Washington, D.C. 20375) H. Mitchell (Science Applications, Inc., McLean, VA 22102) J.A. Fedder and S.T. Zalesak (Naval Research Laboratory, Washington, D.C. 20375)

Recently, large scale plasma density enhancements and associated small scale kilometer-sized plasma density fluctuations have been observed both in the auroral and polar cap F-region ionosphere. Theoretical studies indicate that convective plasma instabilities might be responsible, in part, for the small scale fluctuations. For example, the ExB instability has been invoked to explain small scale plasma density irregularities near convecting large scale polar cap ionospheric F-region plasma enhancements or patches. The fact that the polar cap ionospheric plasma resides on flux tubes which thread the magnetosphere and the very high Alfven velocity to transmit signals along field lines implies that the development of polar cap ionospheric plasma structure is affected by the inertia of the magnetospheric plasma on these flux tubes. In this paper we present a theoretical analysis and numerical simulations of the effects of magnetospheric coupling on polar cap ionospheric plasma instabilities and structure. The magnetospheric and ionospheric plasma are modeled as separate two dimensional convecting layers whose dynamics are coupled by the mapping of electric fields along the magnetic field lines threading the two layers. Specific applications to the dynamics and stability of enhanced polar cap ionospheric plasma density patches will be made.

13

These results have also been submitted in more complete form
and accepted for publication in Geophysical Research
Letters.

Finally, the recent work of H.L. Rowland, H. Mitchell,
and P. Palmadesso on magnetospheric-ionospheric coupling was
presented at the 25th COSPAR meeting. Results from recent
particle simulations on anomalous resistivity showed good
agreement with the parallel electric fields observed in the
auroral acceleration region. Also reported were simulations
of plasma transport, heating and electric field generation
based on a one dimensional multimoment, multifluid model of
an auroral field line. These showed the interactions
involving potentials generated by anomalous resistivity,
magnetic mirror processes and thermoelectric effects. An
abstract of this paper follows.

Interaction of Electrodynamic Ionosphere-Magnetosphere Coupling Processes on Auroral Field Lines

P.Palmadesso (Plasma Physics Division, Naval Research
Laboratory, Washington, D.C. 20375, U.S.A.)
H. Mitchell, and H. Rowland* (Both at Science
Applications, Inc., McLean, VA 22102, U.S.A.)

A number of different physical mechanisms, such as
double layers, anomalous resistivity, kinetic Alfven
waves, and mirror related processes, have been studied
in connection with the generation of field aligned
potential drops on current carrying auroral field
lines. We have conducted simulation studies of the
dynamic interaction of some of these processes in an
attempt to gain insight into the nature of the role

14

played by each. Simulations of plasma transport, heating, and electric field generation based on a one dimensional multimoment, multifluid model[1] of an auroral field line exhibit interactions involving potentials generated by anomalous resistivity, magnetic mirror processes, and thermoelectric effects. Preferentially accelerated beam-like oxygen flows are also observed. New particle simulations intended to clarify the relationship between the anomalous resistivity mechanism proposed by Rowland et al.[2] and the "multiple weak double layer" phenomenon have also been conducted, and suggest that anomalous resistivity is likely to dominate at low and moderate current levels with a transition to double layer dominance when the current becomes very large. Comparisons of theoretically predicted potential structure shapes with observational data have also been made. This work was supported by the National Aeronautics and Space Administration and the Office of Naval Research.

D.   A Steady State Model of the Auroral Ionosphere

We have developed a numerical model to study the steady state behavior of a fully ionized plasma (H^+, O^+ and electrons) in a geomagnetic field. For theoretical formulation we have used the 16-moment system of transport equations of A.R. Barakat and R.W. Schunk, "Transport Equations for MultiComponent Anisotropic Space Plasmas," Plasma Physics 24, 389-418, 1982. The 13-moment system of equations has already been used to study the polar wind by

15

Schunk and Watkins (1981, 1982) and Mitchell and Palmadesso (1982). The 13-moment system of transport equations allow for different species temperature parallel and perpendicular to the field lines. In addition to this, the 16 moment equations allow transverse and parallel thermal energy to be transported separately, which simulates the behavior of a large temperature anisotropy for a collisionless plasma better than the 13-moment equations.

The results or these simulations will be published as a NRL Memorandum Report entitled "Behavior of Ionized Plasma in the High Latitude Topside Ionosphere." It appears in this report as Appendix F. Our results are in good agreement with previous theoretical studies of the polar wind and recent experimental observations. This is the first successful steady state solution to the 16-moment set of transport equations.

At present, work is in progress to study the properties of equilibria of the field aligned return currents. The return currents flow from the magnetosphere to the ionosphere and are carried by cold electrons of ionospheric origin. The importance of field aligned currents in magnetosphere-ionosphere coupling is well known.

(E) High Latitude Ionospheric Irregularities [I]

The high latitude ionosphere is known to be a highly
disturbed medium. An understanding of the various physical
processes occurring in this region is important from the
viewpoint of transionospheric communications since the
presence of irregularities in the medium results in
scintillations in a RF signal. We are investigating the
various causes of these irregularities (e.g. plasma
instabilities, structured particle precipitation, etc.) and
the effect on them of realistic conditions. Thus:

(i) We have carried out a nonlocal study on the effect
of magnetic-field shear on the intermediate scale size (-
few kms) causing plasma instabilities, such as the
interchange mode, and have found that magnetic field shear
induced stabilization occurs predominantly at long
wavelengths. [Manuscript under preparation.]

(ii) The effects of finite current channel width on
the current-driven collisional ion-cyclotron instability
were studied, since this instability may have relevance at
lower altitudes in the auroral ionosphere. It was found
that the instability is quenched for widths of a few
ion-Larmour radius size. [Manuscript in preparation.]

17

(iii) A nonlinear saturation mechanism was considered for the case of the collisional current-drive ion-cyclotron instability, based upon resonance broadening theory. Estimates of saturation amplitudes were calculated for the high-latitude ionosphere situation. This paper, entitled "Stabilization of the Collisional Current-Driven Ion Cyclotron Instability" appears in this report as Appendix G.

(iv) A possibility of artificial (parametric) excitation (or suppression) of the collisional ion-cyclotron instability was considered using powerful HF electromagnetic waves. Threshold field-intensities required for such an experiment were computed for the high latitude ionosphere. This paper appears in this report as Appendix H, entitled "Production and Control of Ion Cyclotron Instabilities in the High Latitude Ionosphere by High Power Radio Waves."

(F) High Latitude Ionospheric Irregularities [II]

To understand the physical mechanisms that generate high latitude ionospheric irregularities and in our continuing efforts to focus on realistic geometry and parameters of interest to HILAT and auroral observations, we have studied (1) the effects of finite current channel on the current convective instability, (2) the collisional

18

(electron) current driven ion cyclotron instability, and (3) stability boundaries in stratified flows in a gravitationally driven partially ionized plasma.

(1) Current Convective Instability

It has been conjectured by researchers at NRL that the current convective instability (CCI) operating at high latitudes could possibly generate km scale irregularities in the ionospheric F region. Several papers from NRL have addressed questions regarding the effects of magnetic shear, velocity shear, nonlinear stabilization, etc. Recent observations have indicated that the currents generating the instability are constrained to narrow channels with channel widths (d) comparable to or smaller than the gradient scale length (L). These observations motivated us to study the effects of finite current channel widths on CCI. A paper on this research has been accepted for publication in the Journal of Geophysical Research. Details are given in Appendix I. The paper is entitled "Effects of Finite Current Channel Width on the Current Convective Instability" and also has been published as NRL Memorandum Report 5494, March 1985.

In essence we have analyzed the effects of finite current channel width on the current convective instability which results from the coupling of a magnetic field aligned current and a density gradient perpendicular to the magnetic

19

field. For a current with perpendicular scale size 2d and a plasma density gradient scale length L, our analytical results indicate a monotonic decrease in the growth rate γ of the current convective instability for $d/L < 1$ both in the collisional ($\nu_{in} >> \omega$) and inertial limits ($\nu_{in} << \omega$). For $d/L << 1$, we find $\gamma \propto V_d d/L^2$ in the collisional limit while $\gamma \propto (V_d d/L^2)^\alpha$, $\alpha < 1$ in the inertial limit. In general, the growth rate of the current convective instability is reduced by the finite width of the current channel from that of the local case in which the current distribution is infinite in extent.

Recent data by Bythrow et al (1984) shows that $d \sim 1.9$ km, $L \sim 6$ km, and $V_d \doteq 30$ km/sec. In the case of the ionospheric F region, $\nu_{ei}/\Omega_e \sim 10^{-4}$ and $\nu_n/\Omega_i \sim 10^{-3}$. The growth rate for different values of λ are as follows. For $\lambda = 1, 2,$ and 10 km $\gamma \sim 0.0028 \ \Omega_i$, $0.00264\Omega_i$, and $0.00146 \ \Omega_i$, respectively. On the other hand, for $d/L >> 1$, the local growth rate is $\sim 0.0031 \ \Omega_i$. For narrower current channel and large density gradients or longer wavelength modes the growth rate could be substantially lower.

(2) Collisional Ion Cyclotron Instability

Recent observations have indicated large magnetic field aligned currents in the collisional bottomside and

20

quasi-collisional topside of the high latitude ionosphere. Kindel and Kennel (1971) proposed that the ion cyclotron instability based on the inverse ion Landau damping mechanism could be active in the quasi-collisional topside of the ionosphere. Chaturvedi (1976) using a fluid model proposed that collisional instability based on the collisional destabilization of the negative energy wave could be a source of small and intermediate scale irregularities in the collisional bottomside of the F region. No theory exists that addresses the transition between the collisionless and collisional excitation, the approximate altitude of transition and the dependence of the growth rate on ambient high latitude ionospheric plasma parameters. We investigate these problems using a kinetic theory based on the BGK collision model.

A manuscript is under preparation summarizing our results. Our research shows that the growth rate of the instability is maximum at an altitude of about 300 km and the growth rate of the lighter ion instability is larger than that of the heavier ion instability. For example, the hydrogen ion cyclotron instability is much greater than the instabilities at O^+ or NO^+ cyclotron frequencies. The growth rate scales as (m/M), where m is the electron mass and M is the ion mass. Furthermore, the critical drift velocity for the onset of the instability at the NO^+ or O^+

21

cyclotron frequency is much smaller than for the excitation of the instability at the H$^+$ cyclotron frequency. In view of this result, we propose that the NO$^+$ ion cyclotron instability is most likely to be excited in the collisional bottomside auroral F region. Detailed parameter studies based on realistic collision models are presented.

(3) Stability Boundaries in Stratified Flows in a Gravitationally Driven Partially Ionized Plasma.

In our continuing effort to understand the effects of velocity shear on interchange type instabilities, we examined the effects of collisions on the stability boundary for Rayleigh-Taylor instability. We investigate these stability boundaries in stratified shear flows in a partially ionized gravitationally unstable plasma. A continuous velocity distribution with a velocity reversal point, $V = V_o \tanh (x/L)$ was used to represent the shear layer. An exponential density profile, $\exp(-x/d)$, varying along the direction of gravity was used. By including all the inhomogeneous terms we show that the stability boundary represents oscillations of finite real frequency as opposed to the neutrally stable boundary obtained by Drazin (J. Fluid Mech. 4, 214 (1958)]. The theory is further extended to partially ionized plasmas and the effects of ion-neutral collisions on the stability boundary are studied. We show that the wavelength domain is more restrictive when ion

neutral collisions are included. We also investigate the stability boundary for a highly collisional plasma.

(G)   Ionospheric Turbulence

Ionospheric irregularities arc believed to result from interchange instabilities. These instabilities include the Rayleigh-Taylor instability (driven by the gravitational field) and the $E \times B$ instability (driven by a neutral wind). In each case, these instabilities may be collision-dominated or collisionless depending on the level of ion-neutral collisions. In the past year we have sharpened our understanding of the nonlinear behavior of these instabilities from a unified viewpoint. We have developed a set of mode coupling equations describing both instabilities and we have shown the following:

(1) both instabilities are described by equations that are structurally identical to each other and, further, are structurally similar to the equations describing the Rayleigh-Benard instability of ordinary fluids; (2) at the lowest level of description, the nonlinear equations may be reduced to a three mode system that is identical to the 3 mode equations obtained by Lorenz to describe Rayleigh-Benard turbulence.

The Lorenz equations have been extensively studied by workers in nonlinear dynamics because of the richness in behavior that is predicted: for low growth rate, the equations predict steady state nonlinear convecting equilibria. However, past a threshold in the growth rate, chaotic behavior in convection patterns is obtained (a "strange attractor" is present as nonlinear dynamicists would have it). Applying this to the ionosphere we conclude as follows: the growth rate threshold corresponds precisely to the transition from collision-dominated to collisionless regimes (which occurs at an altitude of about 500 km). Thus below 500 km, we would expect steady state convection while above this altitude chaotic convection patterns would be present.

The foregoing conclusions were reported in Geophysical Research Letters. This paper is included here as Appendix J, entitled "Ionospheric Turbulence: Interchange Instabilities and Chaotic Fluid Behavior." It must be emphasized that these results were drawn from a three mode analysis. In order to more realistically assess the 3 mode predictions, we have modified the pseudo-spectral code of Fyfe, et al. [D. Fyfe, G. Joyce, and D. Montgomery, J. Plasma Phys. 17, 317 (1977)] to study collisional/ collisionless interchange turbulence from the many mode context. We have shown that the steady states are not as

24

robust as the 3 mode equations would predict. We have also made preliminary measurements of the power spectral density resulting from fully developed turbulence in both collisional and collisionless regimes.

(H)   Hybrid Code Simulations for HANE

During the last year, we have investigated the coupling process between the debris plasma created in a HANE and the ambient air plasma.   The debris-air interaction can be divided into three characteristic stages: (1) magnetic field compression, (2) piston formation, and (3) shock formation and evolution.   Our work in this year has focused primarily on piston formation, i.e., the process of momentum coupling between the debris and air, and high mach number shock formation and structure.   Our studies to date have assumed the debris flow is perpendicular to the magnetic field.   We are presently extending our results to more general oblique geometry.

To elucidate the key momentum coupling processes, we have performed extensive numerical simulations with a 1-D hybrid code which includes ion kinetic effects.   The detailed results of this study can be found in Goodrich, Huba and Papadopoulos, ["Early Time Coupling Studies", NRL Memorandum, (in press) 1985].   The primary results are that

25

some debris ions are accelerated at the interface and subsequently propagate into the air. At the same time, the air ions are reflected at the interface. Electrostatic turbulence develops on a longer time scale which partially couples the accelerated debris, reflected air, and ambient air ions; the coupling is weak for the most energetic debris ions, which propagate farthest upstream into the ambient plasma.

The implications of these results for shock formation are detailed in Papadopoulos, Goodrich, Mitchell, and Huba, ["Time Scale for Shock Formation Following a HANE," NRL Memorandum, (in press) 1985]. We have found that the presence of the accelerated debris ions inhibits the formation of a shock in the air plasma. Since these ions are not effectively scattered by the electrostatic turbulence near the interface, they are coupled to the air by Larmor effects. We find the shock formation time to be approximately $(4-6)M_A/\Omega_i$, where M_A is the Alfven mach number of the debris, and Ω_i is the air cyclotron frequency.

We also began a study of the implications of the structure of very high mach number shocks for the structuring of debris patches observed in HANE's. Moderately high mach number shocks are known to have a complex spatial structure with a characterisic length of approximately an ion (streaming) gyroradius. Our

26

preliminary simulations of the very high mach number shocks characteristic of a HANE indicate an even stronger spatial structure as well as large temporal fluctuations. We are currently investigating this problem.

(I) Spectral Indices from Power Spectral Densities Due to Spatial Irregularities in HANE Plasma Clouds

Spatial structuring of the ionosphere following HANE events is likely to persist for hours. Since defense detectors typically operate in the ir and are sensitive to the nature of the structuring it is important to estimate the spatial characteristics of ir emissions. We have investigated several aspects of this problem which have been summarized in 3 papers.

In the first paper we consider idealized "scan" functions, namely functions of one variable that can arise from three-dimensional optical scources observed by remote sensors. We established the relationship between continuity properties of these functions or their derviatives and the spectral index of their transforms. We showed how inadequate resolution, whether in measured data or numerical simulations, introduces errors in estimates of spectral indices. Specifically, we discussed the errors that arise from "aliasing" and the number of data samples required to

27

obtain an adequate separation of scales. These effects were illustrated with numerical examples. This work was published as NRL Memorandum Report 5298, March 1984, entitled "Estimating Spectral Indices from Transforms of Discrete Representations of Density Functions" and appears in this report as Appendix K.

In a second paper, we related spectral properties of multidimensional emitting sources to spectral properties of the scan functions. For sources (i.e. plasma clouds) of constant emitting intensity the spectral index of the power spectral density (PSD) of the scan profile is determined by the curvature of the cloud's boundary curve at points where projection rays are tangent to the boundary curve. Where the cloud has a gradient in emitting intensity at its boundary, the spectral index will be dependent, in addition, on the nature of the fall off. This work is described in more detail in Appendix L, entitled "Projections of Plasma Cloud Structures and Their Spectra," which has been published as NRL Memorandum Report 5561, March 1985.

In a third paper, we describe an asymmetrical 6-parameter analytical model of an isolated late-time high altitude striation from a high altitude nuclear explosion (HANE). We use parameters suggested by recent computer simulations at NRL. The model is consistent with available HANE and barium cloud data. It is used to study the

28

sensitivity of the spectral index to edge parameters and the direction of observation. It has also been used to compare with optical Checkmate data. This paper has been submitted as a NRL Memorandum Report entitled, "A Striation Model and Spectral Characteristics of Optical-IR Emission from HANE."

(J) The Effects of Finite Parallel Resistivity on the Structuring of Barium Clouds

The development of mathematical models to describe the structuring of barium clouds has been an important topic of record for many years. In the past most of this work has been based on two-dimensional models in which the dynamics of the cloud along the ambient magnetic field B (third dimension) is unimportant. In the limit in which the parallel conductivity of the plasma is infinite this 2-D model is reasonable. The magnetic field lines in this case are equipotental surfaces so that all the plasma on a given magnetic field moves as a whole. On the other hand, the parallel conductivity of any real plasma is finite and therefore the potentials which develop within the cloud do not map perfectly along the magnetic field. Of particular interest is the role of finite parallel conductivity on the gradient drift instability, which is responsible for the observed structuring of barium clouds, and the phenomenon of

freeezing, in which the continued bifurcation of the cloud ceases once a critical minimum scale size is reached.

A detailed investigation of the effect of finite parallel resistivity on the linear stability of barium clouds of finite length along B has been completed. In the cold plasma limit we have shown that while long wavelength modes map long disances along the ambient magnetic field, short wavelength modes become increasingly localized in the vicinity of the cloud. As a consequence, the effective integrated Pedersen conductivity (the integrated conductivity over the extent of the mode) is much larger for long wavelength than for short wavelength modes and the growth rates of long wavelength modes are significantly reduced compared with those of the short wavelength modes. The growth rate of the gradient drift instability peaks at short wavelength. These results have been published in the Journal of Geophysical Research and appear here as Appendix M, entitled "The Role of Finite Parallel Length on the Stability of Barium Clouds."

When finite temperature is included in the calculation, the modes are no longer purely growing but begin to propagate at the diamagnetic frequency, ω_k. For long wavelength modes $\omega_k \propto k$, where k is the mode wavenumber, is small compared with the growth rate so that the modes are unaffected by finite temperaure. For short wavelength

30

modes, however, ω_k is much larger than the growth rate and the gradient drift instability is stabilized. Simple expressions for the critical wavelength for stability have been derived.

The importance of this stabilization mechanism of short wavelength in understanding the freezing of striations in barium clouds is currently under investigation. These results will appear in the Journal of Geophysical Research under the title "Finite Temperature Stabilization of the Gradient Drift Instability in Barium Clouds" and is contained in this report as Appendix N.

(K) Finite Temperature Effects on Structuring Barium Clouds

In an attempt to explain the 'freezing' phenomenon in artificially released barium clouds in the ionosphere, a simulation study was carried out using the two-level cloud-background incompressible ionosphere model and finite temperature effects were introduced. The resulting stabilizing influence of the presence of a finite pressure background ionosphere was discussed in the light of observations. It is shown that striations can be long-lived, quasi-stable, nonbifurcating structures hundreds of meters in diameter. They have a 'tadpole' shape with a dense head, steep density gradients at the front, and a

long, less dense tail. Further details are contained in NRL Memorandum Report 5346, 1984, entitled "Finite Temperature Effects on the Evolution of Ionospheric Barium Clouds in the Presence of a Conducting Background Ionosphere. I. A High Altitude Incompressible Background Ionosphere." This report appears here as Appendix O.

(L) Collective Particle Accelerator Studies

We have previously investigated the stability of a charged beam propagating through a relativistic annular electron beam in connection with the NRL Collective Particle Accelerator (CPA) [Ganguli and Palmadesso, J. Appl. Phys., 55,2715 (1984)].

We have extended our study to the single particle orbits under the force fields prevailing in the CPA. Extensive numerical studies to obtain the surface of section plots for typical CPA parameters have been completed. Interesting results emerge. We have also completed the study of the particle lag time inside the device as a function of the injection phase. If the lag time is large it results in a charge cloud build-up inside the device which in turn disables the normal operation of the CPA. We have identified the initial phase and the initial energy of injection which are detrimental to the operation of the

device. A manuscript will soon be completed which will summarize all the results that we have obtained.

(M) Models for the Earth's Middle Atmosphere

The chemistry, dynamics, heat balance, and physics of the earth's middle atmosphere were reviewed to identify key observations that NRL's experimental program could make and would be important in testing theoretical models. In addition, important theoretical problems were identified which could form the basis for building a theoretical group and program at NRL.

Ozone plays a fundamental role in the chemistry and heat balance of the middle atmosphere. Above 50km most theoretical models underpredict ozone concentrations when the most recent and best available laboratory data are used in the photochemical calculations. Because ozone is the principal absorber of solar uv radiation which heats the middle atmosphere, it is extremely important that ozone densities be accurately measured and known. Above 75km ozone densities are generally inferred from measurements of 1.27μ radiation from $O_2(^1\Delta)$, of which the Solar Mesosphere Explorer (SME) measurements are representative. The accuracy of this type of measurement is questionable and some independent measurement technique is highly desirable.

33

The heat balance of the mesosphere is very important as it may yield constraints on gravity wave induced eddy diffusion of constituents and heat. Breaking gravity waves generate and maintain a background level of turbulence which is capable of producing substantial cooling and/or heating in the upper mesosphere and lower thermosphere. The net thermodynamic effect of breaking gravity waves is critically dependent on the eddy Prandtl number (P_t) applicable. When $P_t \sim 1$, our calculations of the heat budget for the mesopause region with SME ozone densities for solar uv heating imply that the globally averaged eddy or turbulent diffusion coefficient cannot exceed $10^6 cm^2 s^{-1}$. A full discussion of this research is contained in a paper entitled "Energy Balance Constraints on Gravity Wave Induced Eddy Diffusion in the Mesosphere and Lower Thermosphere" which is being prepared for publication in J. Geophys. Res. with John P. Apruzese (NRL) and Mark R. Schoeberl (Goddard Space Flight Center) as co-authors.

(N) The Dynamics of the Indian Summer Monsoon

The summer monsoon circulation is dominated at low levels by a cross equatorial jet, which runs along the East African topography and across the Arabian Sea to India. Models of the jet have not satisfactorily explained the wind

maximum off the Somali coast or the curvature of the flow in the region. In order to separate the various influences of topography and the convective and sensible heating on the jet structure, the three dimensional, five layer, primitive equations model in sigma coordinates of Chang and Madala (1980) has been adapted to study the Indian summer monsoon. The study, described in a report (see Appendix P) is in collaboration with Dr. Simon Chang of the Naval Research Laboratory. The regional model with topography is integrated for six days from an initial zonal average wind field for cases with and without a prescribed convective heat source. The resolution is one degree in longitude and two degrees in latitude. The planetary boundary layer is modelled by a single layer. The horizontal structure of the heat source is the same as the distribution of observed average July rainfall, but with a rainfall rate of five times, due to the shorter integration period. The initial zonal average flow field is initialized and maintained with nudging of the wind.

Without the prescribed convective heat source, the response is largely confined to the lower troposphere. The SE trades are deflected across the equator by the East African topography, as a low level jet. The jet doesn't penetrate farther north than 8 N, curving southward on its eastward path over the Arabian Sea to cross the extreme

35

southern tip of India. With the monsoon heat source included, the low level cross equatorial flow is stronger and broader. The low level jet penetrates farther north to 16 N in a broad stream of southwesterly flow across the Arabian Sea, before turning into a SW flow over the Bay of Bengal.

The study demonstrates that the summer monsoon circulation is primarily driven by the large scale convective heating in the presence of topography. In particular, the low level wind maximum off the coast of Somalia is dynamically related to the lower tropospheric Northern Hemisphere cyclonic gyre forced by the convective heating. The sensitivity of flow to the vertical heating structure is also tested. The effect of the large surface sensible heat fluxes caused by the high surface temperatures over Somalia and Saudi Arabia during the summer are currently being investigated. A multi-layer planetary boundary layer formulation has been developed which will be added to the model. The sensitivity of the low level flow to increased vertical resolution in the boundary layer will be assessed. The study is expected to be completed and the results submitted for publication in April 1985. The results are being presented at the Canadian Meteorological Society's Annual Meeting in Montreal in June 1985. More details are presented in Appendix P, entitled "A Three

Dimensional Model of the Summer Monsoon."

(O) Energy Partitioning in the I_O Plasma Torus

We have studied the plasma state of the hot torus with a local, homogeneous, steady-state model described by a set of coupled quasilinear equations for the distribution functions of S^+, S^{++}, S^{+++}, O^+, and O^{++}. The equations contain model Fokker-Planck operators for ion-ion and ion-electron collisions, a species- and energy-independent loss rate τ^{-1}, impact ionization of S, S^+, S^{++}, O, and O^+, recombination of S^{+++}, and eleven charge-exchange reactions.

The only free parameters, which are not governed by physical processes contained in the model, are the ion confinement or residence lifetime τ and the neutral densities of sulfur, n_S, and oxygen, n_O. Equivalently, if n_S, n_O, and the electron density n_e are adopted as parameters, then τ is determined by imposing charge neutrality.

Under the constraints that the pickup mechanism for newly created ions is the dominant energy source and that the torus is in equilibrium between collisional energy loss from ions to electrons and radiative UV loss from ions excited by ion-electron collisions, the densities, average energies, and distribution functions of all ion species and

37

the temperature of the electrons, which are assumed to be Maxwellian, are calculated as a function of the input parameters. Among the results are:

(i) The ion velocity distributions are significantly non-Maxwellian for the major species, with high energy tails extending to the pickup energy. A quasi-thermal core exists for the O^+ and/or S^+ ion velocity distribution functions only if the EUV lumirosity of the torus is less than 0.2 eV cm^{-3} s^{-1}. The core "temperature" is at most T_i ~ 100 eV; the average energy of the total distribution is generally less than 0.5 of the pickup energy. The ion velocity distributions do not drive the ion loss-cone instability for parameters generally typical of the torus.

(ii) The EUV luminosity of the torus during the Voyager 1 encounter was ~ 0.15 eV cm^{-3} s^{-1}, a factor of ~ 1.8 less than reported by Shemansky and Smith (1981). This downward revision in the EUV intensities is in agreement with calibration adjustments adopted by Holberg et al. (1982) at longer wavelengths (912-1050 A).

38

(iii) During the Voyager 1 encounter the approximate average torus ion densities were $S^+:\angle$ 350, $S^{++}:420$, $S^{+++}:10$; $O^+:660$, $O^{++}:40$ cm^{-3} with T_e - 4.8 eV, τ - 60 days, and n_e - 2000 cm^{-3}. The average neutral torus densities were n_S - 6 and n_O - 30 cm^{-3} and consistent with an SO_2 source.

(iv) The upper limit obtained by Brown et al. (1983b) on O^{++} concentrations is only applicable to short duration periods when transient, large eruptions of sulfur driven volcanoes occur on the surface of Io (McEwen and Soderblom, 1983) and mass loading of the neutral torus is preferentially by sulfur. The resultant plasma torus contains S^+ and S^{++} densities of - 600, O^+ - 120, $O^{++} \angle$ 10, and S^{+++} - 25 cm^{-3}. The increased mass loading reduces τ to - 1 week.

A paper on this work has been submitted for publication to the Journal of Geophysical Research.

APPENDIX A

Collisionless Tearing Instability in a Non-Maxwellian
Neutral Sheet: An Integro-Differential Formulation

COLLISIONLESS TEARING INSTABILITY IN A NON-MAXWELLIAN

NEUTRAL SHEET: AN INTEGRO-DIFFERENTIAL FORMULATION

J. Chen and Y.C. Lee*

Science Applications International Corporation
1710 Goodridge Drive
McLean, VA 22102

July 10, 1984

---

* Permanent address: Laboratory of Plasma and Fusion
Energy Studies, University of Maryland, College Park,
Maryland 20742

ABSTRACT

An integro-differential formalism is developed to study the collisionless tearing instability in a non-Maxwellian neutral sheet. The exact unperturbed particle orbits are used analytically in the orbit integrals. The treatment is linear, self-consistent and kinetic for both ions and electrons. The analysis is carried out for low-frequency, purely growing electromagnetic perturbations ($|\omega| \ll \omega_{ci}$). Using the Galerkin method, the integro-differential equation is solved to obtain the dispersion relation and the eigenmode structure. A sufficient condition for instability is given on the basis of a quadratic form and the eigenvalues of a self-adjoint integro-differential operator. The formalism is applied to a specific model distribution. For the case where the electrons and ions are both non-Maxwellian, it is shown that the instability is dominated by the axis-crossing electrons and that the eigenmode is strongly localized to a region of the order of $\rho_e^{1/2}$ at the null-plane, where ρ_e is a measure of the electron gyroradius in the asymptotic magnetic field. Furthermore, the dispersion relation has the general form $\gamma/kv_{e\parallel}=$constant where $\underline{k} \parallel \underline{B}_0$ and $v_{e\parallel}$ is the electron thermal velocity along $\underline{B}_0$, the equilibrium magnetic field.

I. INTRODUCTION

The properties of the collisionless tearing instability in the neutral sheet geometry have attracted considerable attention in the last two decades.[1-13] A physical system in which the instability may be particularly relevant is the earth's magnetotail.[7,10,13] In its classic form,[1,2] the inertia of the current carriers leads to the collisionless tearing instability because of inverse Landau damping. The previous studies of the instability have mainly used isotropic Maxwellian distributions. However, in a collisionless plasma, the particle motion parallel to the magnetic field is decoupled from the perpendicular motion. Laval and Pellat[14] showed that collisionless tearing-mode properties can sensitively depend on weak electron temperature anisotropy. They showed that the $\underline{k} \parallel \underline{B}_0$ mode can be stabilized by a very small degree of electron temperature anisotropy, $(T_{e\perp}/T_{e\parallel} - 1) < \rho_e/\delta \ll 1$, where $\underline{k}$ is the wavevector, $\underline{B}_0$ is the equilibrium magnetic field, ρ_e is the electron Larmor radius, and δ is the characteristic half-thickness of the neutral sheet. The quantities $T_{e\perp}$ and $T_{e\parallel}$ are temperatures associated with the particle motion perpendicular and parallel to the magnetic field $\underline{B}_0$, respectively. Forslund[10] obtained an approximate dispersion relation for the case where the electrons are weakly anisotropic with $(T_{e\perp}/T_{e\parallel} - 1) < \rho_e/\delta \ll 1$. This work showed

a substantial enhancement of the tearing mode growth rate for $T_{e\perp}/T_{e\parallel} > 1$. In this work the effects of axis-crossing ion orbits extending beyond the electron inner region of the order of $(\rho_e \delta)^{1/2}$ are taken to be negligibly small (the conventional "two-region" approximation). However, Chen and Palmadesso[12] have recently identified the existence of an ion intermediate region of the order of $(\rho_i \delta)^{1/2} \gg (\rho_e \delta)^{1/2}$ where the axis-crossing ion orbits make a major contribution. This work shows that a more adequate treatment of the anisotropic collisionless tearing mode must include the ion intermediate region. More specifically, Ref. 12 shows that, when the ion intermediate region is included, a given degree of ion anisotropy ($T_{i\perp}/T_{i\parallel} > 1$) can increase the growth rate by nearly one order of magnitude over the result obtained on the basis of the two-region approximation.[10] In comparison with the isotropic result, the enhancement of the growth rate using the three-region approximation can significantly exceed one order of magnitude. This implies that only a small to modest degree of ion anisotropy is needed to effect a large modifcation to the tearing-mode properties. The underlying physical process for the enhancement of the growth is identified as the Lorentz force acting on the particles in the directions parallel to the equilibrium magnetic field. Moreover, a recent numerical simulation study[15] shows that the linear growth rate is indeed greatly enhanced when a small degree

of ion temperature anisotropy ($T_{i\perp}/T_{i\parallel} > 1$) exists. In this study, the electrons are assumed to be cold, providing charge neutrality.

In addition to the obvious influence of temperature anisotropy, the work of Ref. 12 demonstrates that a proper treatment of particle orbits is important for a more complete understanding of the instability. In Ref. 12, the large axis-crossing ion orbits were modelled using the "straight-line" approximation[7], with the eigenfunction assumed to be nearly constant in the electron inner region and the ion intermediate region (the "constant-ψ" approximation). While these simplifications appeared to be adequate for small to modest degrees of anisotropy, they nevertheless constitute a serious limitation if greater degrees of anisotropy are to be considered. Indeed, it will be shown that the constant-ψ approximation is invalid in general for non-Maxwellian distributions. Moreover, an exact treatment has not been given before so that the effects of the exact orbits versus the approximate orbits cannot be assessed. The difficulty of treating the orbits is due to the complicated particle motion in the region where the magnetic field reverses its direction. Numerically, Holdren[16] demonstrated the feasibility of an integro-differential treatment of the exact orbits in a relativistic neutral sheet. However, in this noteworthy by

rarely referenced work, the orbits were calculated numerically and the numerics required were substantial. It is thus desirable to formulate a theory which treats all the orbits exactly with minimal numerical computation.

In this paper, we develop a formalism to calculate the tearing-mode properties of non-Maxwellian neutral sheets using all the exact particle orbits analytically. We also provide a general prescription based on quadrature to determine the sufficient condition for instability in a given system without resorting to extensive numerical computation. The formalism is then illustrated by using a highly non-Maxwellian distribution function. The technique developed here can be generalized to other distribution functions.

II. GENERAL INTEGRO-DIFFERENTIAL FORMULATION

In this paper, we study the collisionless tearing mode properties of a neutral sheet in which the particle distribution is highly non-Maxwellian. We develop a formalism whereby the exact single-particle orbits are used analytically in the solution of the first order Vlasov-Maxwell equations. Figure 1 shows a schematic drawing of the geometry and the coordinate system. The equilibrium magnetic field $\underline{B}_0(z) = B_x^0(z)\underline{x}$, indicated by the solid lines, is generated self-consistently by the current $\underline{J}_0(z) = J_0(z)\underline{y}$. The magnetic field reverses its direction in the plasma at $z=0$, and $J_0(z)$ is even in z. Both electrons and ions are collisionless and assumed to contribute to the current. We assume that there is no equilibrium electrostatic field and no $\underline{E}x\underline{B}$ motion of the plasma (i.e. the rest frame of the sheet).

We consider a class of equilibria described by $F_j = F_j$ $(H_{\perp j} - v_j P_{yj}, H_{\parallel j})$, where $j=e,i$ and $(H_{\perp j}, P_{yj}, H_{\parallel j})$ are the single-particle constants of the motion. Here, $H_{\perp j} = (m_j/2)(v_y^2 + v_z^2)$, $P_{yj} = m_j v_j + (q_j/c)A_y^0(z)$ is the canonical momentum, $H_{\parallel j} = (m_j/2)v_x^2$, and $A_y^0(z)$ is the equilibrium vector potential. For the species j, q_j is the electric charge, m_j is the mass and $V_j = $ constant is the mean drift velocity in the y direction.

A. BASIC EQUATIONS

The tearing instability can be described by perturbations of the form $\psi(x,z,t) = \psi(z)\exp(ikx - i\omega t)$, where the wave vector $\underline{k} = k\underline{x}$ is parallel to the equilibrium magnetic field. The perturbed magnetic field is schematically shown by dashed lines in Fig. 1. The characteristic perturbation frequency ω is small in comparison with the ion cyclotron frequency $\omega_{ci} \equiv eB_0/m_ic$ defined in the asymptotic magnetic field $B_0 \equiv B_x^0$ ($z=\infty$). Under these assumptions, it can be shown (see, for example, Ref. 12) that the perturbed scalar potential can be neglected. Using the standard method of characteristics, the first-order Vlasov distribution function for each species is

$$f_j = -q_j\beta_j \frac{\partial F_j}{\partial H_{\perp j}}\psi + i\omega q_j \frac{\partial F_j}{\partial H_{\perp j}} S_{yj}$$

$$- ikq_j\left[\frac{\partial F_j}{\partial H_{\perp j}} - \frac{\partial F_j}{\partial H_{\parallel j}} \right] v_x S_{yj}, \qquad (1)$$

where $\beta_j \equiv V_j/c$ and S_{yj} is the orbit integral along the unperturbed orbits given by

$$S_{yj} \equiv -\frac{1}{c} \int_{-\infty}^{t} dt' v_{y}' \psi \quad ,$$

where ψ is the perturbed vector potential $\underline{A}_1 \equiv \psi\,(x,z,t)\,\underline{y}$. Here, $(\underline{x}',\underline{v}')$ represents the particle orbits in the equilibrium field with the conditions $\underline{x}'(t'=t) = \underline{x}$ and $\underline{v}'(t'=t) = \underline{v}$. All perturbation quantities vanish as $t \to -\infty$. The perturbed vector potential $\underline{A}_1$ satisfies

$$\underline{B}_1 = \underline{\nabla} \times \underline{A}_1 \quad , \tag{2}$$

$$\underline{E}_1 = -\frac{1}{c} \frac{\partial \underline{A}_1}{\partial t} \quad , \tag{3}$$

and

$$\underline{\nabla} \times \underline{B}_1 = (4\pi/c)\underline{J}_1, \tag{4}$$

where the scalar potential has been neglected. In this paper, we choose the Coulomb gauge ($\underline{\nabla} \cdot \underline{A} = 0$). Because the perturbation frequency is low ($|\omega| \ll \omega_{ci}$), we assume charge neutrality to first order in this paper. Note that $B_{1y}(x,z,t) = 0$ for the tearing perturbation so that $\underline{J}_1 = J_{1y}(x,z,t)\,\underline{y}$ and $\underline{A}_1 = \psi(x,z,t)\underline{y}$. Ampere's law then gives

$$\frac{d^2\psi}{dz^2} - k^2\psi(z) + \frac{4\pi}{c} J_{1y}(z) = 0 \quad . \tag{5}$$

Here $J_{1y(z)}$ is the perturbed current density given by $J_{1y} = q_i \int d^3\underline{v}\; v_y\; f_j$. Thus, it depends on the global structure of ψ through the orbit integral S_{yj}. The purpose of this paper is to solve the integro-differential equation (5) for the mode structure including all equilibrium orbits exactly. In the remainder of this paper, the species index j will be suppressed where no confusion arises.

In equilibrium, the particle motion in the z direction is periodic with the period for each species given by $T = T(H_\perp, P_y)$. This means that the integrand of S_y, which is evaluated along equilibrium trajectories, is a periodic function of time t' and is uniquely determined for each orbit in terms of the coordinates $(\underline{x}, \underline{v})$ at the present time t. Thus, along each orbit we can write

$$\Phi(z'|z) \equiv v_y(z')\psi(z') \quad .$$

Moreover, for a given orbit corresponding to $H_\perp$ and P_y, we can expand $\Phi(z'|z)$ as

$$\Phi(z'|z) = \sum_{n=0}^{\infty} \Phi_n(z) \exp[in\Omega(t-t')] \qquad (6)$$

where the orbital frequency is

$$\Omega \equiv 2\pi/T(H_\perp, P_y)$$

and

$$\Phi_n(z) \equiv \frac{1}{T} \int_0^T d\tau \ \Phi(z'|z) \exp[in\Omega(t-\tau)] \qquad (7)$$

where $z'=z'(\tau)$. Note that, at $t'=t$, we have $z'=z$ and

$$\Phi(z) = \sum_{n=0}^{\infty} \Phi_n(z).$$

The advantage of expressing the integrand in this way is that the explicit dependence on t' is now in the exponent so that the expansion coefficient depends only on the present time t. Using Eq.(6) in the orbit integral S_y, we obtain

$$S_y(t) = -\frac{i}{c} \sum_n \frac{\exp[i(kx-\omega t - n\Omega t)]}{\omega + n\Omega - kv_x} \frac{1}{T}$$

$$x \oint dz' \frac{v_y'(z')\psi(z')}{|v_z'(z')|} \exp(in\Omega t') \quad , \qquad (8)$$

where the t'-integration has been changed to a z'-integration over one cycle and where the velocity component v_x is a constant of the motion. Thus, we have converted the orbit integral to an infinite sum of t'-integrations over one period.

Using the orbit integrals, the perturbed current density for each species is obtained by integrating f_j over the velocity space. Then, we obtain quite generally

$$J_{1y}(z) = -e^2 \beta \psi(z) \int d^3\underline{v} \ v_y \frac{\partial F_j}{\partial H_\perp} + \sum_j J_{an}(z) \qquad (9)$$

where

$$J_{an}(z) = ie^2 \left[\left[\frac{\omega}{kv_{j\parallel}} \right] I_1 - I_2 \right]$$

$$I_1 \equiv kv_{j\parallel} \int d^3\underline{v} \ v_y \frac{\partial F}{\partial H_\perp} S_y,$$

$$I_2 \equiv k \int d^3\underline{v}\, v_x\, v_y \left[\frac{\partial F}{\partial H_\perp} - \frac{\partial F}{\partial H_\parallel} \right] S_y$$

and

$$v_{j\parallel} \equiv \left[\frac{2T_{j\parallel}}{m_j} \right]^{1/2}$$

is the parallel thermal velocity. In the neutral sheet geometry, the perpendicular motion and the parallel motion are decoupled. We consider equilibrium distribution functions of the separable type $F_j = F_\perp(H_\perp - V_j P_y)\, F_\parallel(H_\parallel)$ with $\int_{-\infty}^{\infty} dv_x F_\parallel(H_\parallel) = 1$. In particular, we choose the parallel distribution to be Maxwellian for both species so that

$$F_\parallel(H_\parallel) = (2\pi T_{j\parallel}/m_j)^{-1/2} \exp\left[-\frac{H_\parallel}{T_{j\parallel}} \right] \qquad . \qquad (10)$$

Then, the thermal velocity $v_{j\parallel}$ in Eq.(9) can be identified in the Maxwellian sense. Note that the first term in Eq.(9) is the so-called adiabatic term. However, the term J_{an} includes contribution from both adiabatic and nonadiabatic motion of particles.

After performing the v_x-integration, we obtain

$$I_1 = \frac{i}{m_j^2 c} \sum_n \int dP_y dH_\perp \frac{\partial F_\perp}{\partial H_\perp} Z(b_n) \frac{1}{T}$$

$$\times \oint dz' \frac{v_y v'_y}{|v_z||v'_z|} \exp[-in\Omega(t-t')] \qquad (11)$$

and

$$I_2 = \frac{i}{m_j^2 c} \sum_n \int dP_y dH_\perp \left[\frac{\partial F_\perp}{\partial H_\perp} + \frac{1}{T_{j\parallel}} F_\perp \right] W(b_n) \frac{1}{T}$$

$$\times \oint dz' \frac{v_y v'_y}{|v_z||v'_z|} \exp[-in\Omega(t-t')] \, \psi(z'), \quad (12)$$

where $v_y = v_y(z)$, $v'_y = v'_y(z')$, $v_z = v_z(z)$, $v'_z = v'_z(z')$, $T = T(H_\perp, P_y)$ and $\Omega = 2\pi/T(H_\perp, P_y)$. Here the dispersion functions are given by

$$Z(\xi) = \pi^{-1/2} \int_{-\infty}^{\infty} dx \frac{\exp(-x^2)}{x-\xi}$$

and $W(\xi) = 1 + \xi Z(\xi)$, with

$$b_n \equiv \frac{\omega + n\Omega}{kv_{j\parallel}} . \qquad (13)$$

Combining the terms I_1 and I_2, we can write

$$J_{an}(z) = \frac{e^2}{m_j^2 c \, T_{j\parallel}} \sum_n \oint dz' \psi(z') \int \frac{dP_y dH_\perp}{T} W(b_n) F_\perp \frac{v_y v_y'}{|v_z||v_z'|}$$

$$+ \frac{e^2}{m_j^2 c} \sum_n \oint dz' \psi(z') \int \frac{dP_y dH_\perp}{T} \left[1 + \frac{n\Omega}{kv_{j\parallel}} Z(b_n) \right] \frac{\partial F_\perp}{\partial H_\perp} \frac{v_y v_y'}{|v_z||v_z'|}.$$

$$(14)$$

Note that the first term in Eq.(14) comes from the $\partial F/\partial H_\parallel$ term in I_2 and describes how the system changes in response to infinitesinal changes in the parallel energy of particle motion.

In the neutral sheet geometry, the velocity components can be expressed in terms of an effective potential. Along each orbit, we have

$$v_z^2 = \frac{2}{m_j} [H_\perp - \Gamma_j(z)] \qquad (15)$$

and

$$v_y^2 = \frac{2}{m_j} \Gamma_j(z) \quad , \qquad (16)$$

where the effective potential $\Gamma_j(z)$ is such that $m_j d^2z/dt^2 = -\partial \Gamma_j/\partial z$. Note that $\Gamma_j(z)$ is uniquely determined for given $H_\perp$ and P_y. The orbital period $T = T(H_\perp, P_y)$ is given by

$$T(H_\perp, P_y) \equiv \oint \frac{dz}{|v_z(z)|} \quad , \qquad (17)$$

where the integration is carried out over one complete cycle. Equations (14) through (17) are valid for any $F_\perp$ where the separable form of the distribution function F is applicable. For a given neutral sheet equilibrium, Eqs. (15) and (17) and, hence, the perturbed current density $J_{1y}(z)$, are completely determined. Equation (5), in conjunction with Eq. (9) and Eqs. (14) through (17), is the fundamental integro-differential equation describing the instability. The boundary condition for ψ is that ψ must vanish as $|z| \to \infty$.

It is useful to express the left hand side of Eq. (5) as an integro-differential operator L, which can be written as

$$L\,\psi \equiv \frac{d^2\psi}{dz^2} - k^2\psi + \frac{4\pi e^2}{c} \sum_j \beta_j \psi(z) \int d^3\underline{v}\ v_y\ \frac{\partial F_j}{\partial H_\perp}$$

$$+ \frac{4\pi e^2}{c} \sum_j \frac{1}{m_j^2 c} \int dz' \left[\frac{1}{T_{j\parallel}} \kappa_1(z,z') + \kappa_2(z,z')\right] \psi(z') \quad .$$

$$(18)$$

A-20

Here, the kernels are given by

$$\kappa_1(z,z') = \sum \int \frac{dP_y \, dH_\perp}{T(H_\perp, P_y)} \, W(b_n) F_\perp \, \frac{v_y(z) v_y'(z)}{|v_z(z) \, v_z'(z')|} \, , \quad (19)$$

and

$$\kappa_2(z,z') = \sum_n \int \frac{dP_y \, dH_\perp}{T(H_\perp, P_y)} \left[1 + \frac{n\Omega}{kv_{j\parallel}} Z(b_n) \right] \frac{\partial F_\perp}{\partial H_\perp} \frac{v_y(z) v_y'(z')}{|v_z(z) v_z'(z')|}.$$

$$(20)$$

Equation (5) can then be written as

$$L \, \psi(z) = 0 \quad . \quad\quad\quad (21)$$

We can further define a quadratic form I by

$$I(\phi|\psi) \equiv \int dz \, \phi^*(z) \, L \, \psi(z) \quad , \quad\quad (22)$$

where z-integration is carried out over all space. Using the variational principle, Eq. (5), or equivalently, Eq. (21), can be recovered by requiring $\delta I(\phi|\phi) = 0$. This implies that $I(\psi|\psi) = 0$ is true simulataneously. It is instructive to note that by multiplying L by -1 and taking the $k^2\psi$ term to the right hand side, Eq. (21) can be cast in the form of a Shroedinger equation in which $-k^2$ plays the

role of the energy of a particle in a potential well, which corresponds to the perturbed current density. Thus, in effect, we seek bound-state solutions.

Consider an arbitrary set of basis functions, $\{u_\ell(z)\}$. If we let $\psi(z) = \sum_\ell Q_\ell u_\ell(z)$, then Eq. (21) can be converted into a matrix representation

$$\sum_{m=1} M_{\ell m} Q_m = 0 \tag{23}$$

for all ℓ. Here, the matrix elements are given by $M_{\ell m} = I(u_\ell | u_m)$. Note that κ_1 and κ_2 are symmetric in z and z' so that $M_{\ell m}$ is a symmetric matrix. A particularly useful method of solving the integro-differential equation (21) [or Eq. (5)] is the Galerkin method.[17] We use only a finite number of basis functions to construct the matrix M and solve Eq. (23). The dispersion relation is then given by the condition $\det |M| = 0$. Equivalently, in this paper, we choose to determine the dispersion relation by solving for zero eigenvalues.

Note that if we take the fundamental harmonic n=0 and take $F_\perp$ to be Maxwellian with a temperature of $T_{j\perp} = T_{j\parallel}$, then the "1" in the square brackets cancels the "1" in $W(b_0)$. The leading term is then proportional to $b_0 = \omega/kv_{j\parallel}$

<< 1, giving rise to the conventional collisionless tearing mode (see, for example, Refs. 9 and 12). This shows that the conventional tearing mode is in a sense a weak "residual" instability that occurs when the particle distribution is exactly Maxwellian so that the mirror force contribution represented by I_2 is zero. However, if the particle distribution deviates from the exact isotropic Maxwellian, then the cancellation of the two large "1's" does not occur even for n=0. This leads to a much stronger instability of the tearing type.[12,13]

In the remainder of this paper, we will consider the fundamental harmonic (n=0) for the purely growing mode ($\omega = i\gamma$). Before proceeding to specific model calculations, we will discuss a number of general features of Eq. (21).

B. A CRITERION FOR INSTABILITY

For the purely growing mode wtih n=0, we note that the operator L and, therefore, the matrix M are self-adjoint since L is real and symmetric in z and z'. The eigenvalues are real and the eigenfunctions can be chosen to be orthonormal. If we let $\phi_m(z) = \sum_s g_{ms} u_s(z)$ be an eigenfunction with the eigenvalue λ_m, then

$$I(\phi_m | \phi_m) = \lambda_m$$

$$= -\int dz \left[\frac{d\phi_m}{dz}\right]^2 - k^2 \int dz \, \phi_m^2 + \frac{4\pi e^2}{c} \sum_j \beta_j \int dz \, \phi_m^2(z) \int d^3\underline{v} \, v_y \frac{\partial F_j}{\partial H_\perp}$$

$$+ \frac{4\pi e^2}{c} \sum_j \frac{1}{m_j^2 c} \int dz dz' \phi_m(z) \left[\frac{1}{T_{j\parallel}} \kappa_1(z,z') + \kappa_2(z,z')\right] \phi_m(z'),$$

$$(24)$$

where use has been made of the fact that ϕ_m vanishes for $z \to \pm \infty$ and we have chosen ϕ_m to be real without loss of generality. If we take the limit $\gamma \to -\infty$, then $W(i\gamma) - -2\pi^{1/2} \gamma \exp(\gamma^2) \to +\infty$ so that the right hand side of Eq. (24) is dominated by the κ_1 term. From Eq. (19), we see that this integral is positive definite. We, therefore, conclude quite generally that all the eigenvalues are positive for sufficiently negative γ. In the other limit, $\gamma \to +\infty$, we see that, for any fixed k, the explicit dependence of λ_m on γ disappears since the Z function vanishes. In addition, for any fixed k and finite γ, it is easy to see that $\lambda_m = I(\phi_m | \phi_m)$ is bounded from above. Note, however, that λ_m need not be bounded from below since $d\phi_m/dz$ can be made large without bounds. As γ is increased from $-\infty$, some eigenvalues can cross zero and become negative. The eigenfunctions and the associated values of γ for which the

eigenvalues are zero are the eigenmodes satisfying the fundamental equation (21) and the eigenfrequencies corresponding to the respective modes. For any finite γ, it can be shown that there are only finitely many positive eigenvalues. Thus, there are infinitely many stable branches. The above properties suggest a general method to determine the sufficient condition for instability without the need for extensive computation. The Galerkin method approximates the solution by using a finite $N \times N$ matrix in Eq.(23). This yields a finite spectrum of eigenvalues. We compute the spectrum at $\gamma=0$ and a large positive $\gamma=\gamma_1$ for a given k. Let n_0 and n_1 be the number of positive eigenvalues at $\gamma=0$ and $\gamma=\gamma_1$, respectively. If $n_0 \neq n_1$, then the approximate system possesses at least $|n_0-n_1|$ unstable modes. This prescription can be particularly useful for cases where computation of the matrix elements $M_{\ell n}$ for each value of γ is time consuming. An example is a system in which the parallel motion and the perpendicular motion cannot be separated. A more rigorous discussion of this method will be given elsewhere. The above method of determining the sufficient condition for instability is analogous to the energy principle analysis[20] for ideal MHD plasmas.

Moreover, it is possible to infer the general form of the dispersion relation from Eq. (24) if the k^2 term is

A-25

small, which will prove to be the case for the problem analyzed here (see Sec. III). Then, the dependence on ω and k occurs only in the form $\omega/k v_{j\parallel}$. If an eigenmode is found (i.e. $\lambda_m = 0$ for some m), the dispersion relation is given generally by ω/k = constant. This point will be discussed further in connection with Eq. (45).

C. EQUILIBRIUM

In order to apply the formalism to a neutral sheet whose particle distribution is highly non-Maxwellian, we adopt the following model equilibrium distribution function. We assume that the perpendicular energy distribution function is of the form,[18]

$$P_{\perp} = \left[\frac{m_j n_o}{2\pi} \right] \delta(H_{\perp} - V_j P_y - T_{j\perp}) \tag{25}$$

where V_j and $T_{j\perp}$ are constants. The particle density profile for each species is given by

$$n_o(z) = \begin{cases} n_o & \text{for } \Lambda_j(z) \geq 0 \\ 0 & \text{for } \Lambda_j(z) < 0 \end{cases} \tag{26}$$

where

$$\Lambda_j(z) \equiv \frac{q_j V_j}{c} A_{oy}(z) + \frac{1}{2} m_j V_j^2 + T_{j\perp}. \qquad (27)$$

Here, the equilibrium scalar potential has been set to zero. Then, the equilibrium current density is

$$J_{oj}(z) = q_j V_j n_o(z), \qquad (28)$$

and the vector potential is

$$A_{oy}(z) = \begin{cases} -\dfrac{2\pi e n_o}{c} (V_i - V_e) z^2, & \Lambda_j(z) \geqslant 0 \\[2mm] -B_o z, & \Lambda_j(z) < 0 \end{cases} \qquad (29)$$

Without loss of any generality, we can choose $(V_i - V_e) > 0$ so that $B_o > 0$. Inserting Eq.(29) into Eq.(27), we find that $\Lambda_j(z) \geqslant 0$ if and only if $|z| \leqslant z_p$ where

$$z_p^2 = \frac{m_j V_j^2 + 2T_{j\perp}}{4\pi e n_o (V_i - V_e)(q_i V_j)/c^2} . \qquad (30)$$

With the choice $(V_i - V_e) > 0$, we have $(q_j V_j) > 0$ for both species so that $V_i > 0$ and $V_e < 0$. The magnetic field can then be written as

$$B_{ox}(z) = \begin{cases} B_o \dfrac{z}{z_p} & |z| \leqslant z_p \\[2mm] B_o & |z| > z_p \end{cases} \qquad (31)$$

where the asymptotic field is given by

$$B_o = \frac{4\pi e n_o}{c} (V_i - V_e) z_p \quad .$$

Defining $\bar{V}_i \equiv |V_i|$ and $\bar{V}_e \equiv |V_e|$, we can write

$$z_p = (\omega_{ci}\bar{V}_i)^{-1} (\bar{V}_i^2 + v_{i\perp}^2) = (\omega_{ce}\bar{V}_e)^{-1} (\bar{V}_e^2 + v_{e\perp}^2) \quad (32)$$

where we have defined

$$v_{j\perp} \equiv \left[\frac{2T_{j\perp}}{m_j}\right]^{1/2} \quad .$$

It is clear that $z = \pm z_p$ correspond to the edges of the neutral sheet and we have used the fact that equilibrium charge neutrality requires that the electron and ion densities must be identical. It is also straightforward to show that the pressure tensor is diagonal with the elements $P_{\parallel j}(z) = T_{j\parallel} n_o(z)$ and $P_{\perp j}(z) = n_o(z)\Lambda_j(z)$, where $P_{\parallel} = P_{xx}$ and $P_{\perp} = P_{yy} = P_{zz}$. Because $F_{\parallel}$ is Maxwellian, the parallel temperature is constant inside the neutral sheet. In the

A-28

perpendicular direction, the quantity $\Lambda_j(z)$ plays the role of the local perpendicular temperature. Thus, the perpendicular temperature distribution is parabolic in z inside the neutral sheet:

$$\Lambda_j(z) = T_{j\perp}(1+V_j^2/v_{j\perp}^2)(1-z^2/z_p^2).$$

It will turn out that the term $V_j^2/v_{j\perp}^2$ is typically much smaller than unity for the case of interest so that $T_{j\perp}$ is essentially the perpendicular temperature near z=0 and $v_{j\perp}$ is essentially the perpendicular thermal velocity near z=0. Note that the temperature distribution is highly anisotropic throughout the neutral sheet with no isotropic limit. As a general remark, the equilibrium force balance is established by the Lorentz force balancing the pressure gradient in the z-direction.

It is convenient to define

$$\rho_j \equiv v_{j\perp}/\omega_{cj} \quad .$$

This quantity provides a measure of the size of typical orbits in the neutral sheet. Then, Eq.(22) yields two equilibrium solutions:

$$\frac{\overline{V}_j}{v_{j\perp}} = \frac{1}{2} \frac{z_p}{\rho_j} \left[1 \pm (1-4\rho_j^2/z_p^2) \right] .$$

Note that charge neutral equilibrium is possible only if $\rho_j/z_p \leqslant 1/2$. For all practical purposes, $\rho_j/z_p \ll 1/2$. The solution corresponding to the minus sign will be called the "slow" solution. This solution is such that the leading term is $V_i/v_{j\perp} \sim \rho_j/z_p$ which is typically much less than unity. This is similar to the Harris equilibrium where $V_j/v_{j\perp}$ is exactly equal to ρ_j/z_p. For the limiting case $\rho_j/z_p = 1/2$, we have $V_j/v_{j\perp} = 1$, which is the maximum value for the slow solution. The solution corresponding to the plus sign will be referred to as the "fast" solution. This gives $V_j/v_{j\perp} > 1$ with $\rho_j/z_p \ll 1/2$ yielding $V_j/v_{j\perp} \gg 2$. In physical systems, this means that the average drift is much greater than the typical thermal velocity. In this paper, we consider only the slow solution.

D. PARTICLE ORBITS

In the neutral sheet geometry with a magnetic field given by Eq.(31), the particles generally execute complicated orbits (see, for example, Ref. 19). It is the difficulty of treating such orbits that has forced all previous works to either use approximate analytic orbits

with severe restrictions on orbital size, frequency range, and eigenmode structure or extensive numerical calculation of orbits. In this paper, we include _all_ the equilibrium orbits analytically by using the first integrals of the motion (Sec. II.A).

For the particular model distribution functions, the effective potential [Eqs. (15) and (16)] is given by

$$\Gamma_j(z) = \alpha_j(z^2 - G_j P_y)^2 \quad , \tag{33}$$

where

$$\alpha_j \equiv \frac{e^2 B_o^2}{8 m_j c^2 z_p^2}$$

and

$$G_j \equiv -\frac{2 e z_p}{q_j B_o} \quad .$$

It is easy to see that the effective potential has two basic configurations. For $(G_j P_y) < 0$, $\Gamma_j(z)$ has only one minimum at $z=0$ and all orbits are of the axis-crossing type. For $(G_j P_y) > 0$, $\Gamma_j(z)$ has one local maximum at $z=0$ and two local minimums at $z=\pm z_*$ where $z_* = (G_j P_y)^{1/2}$ and $\Gamma_j(\pm z_*)=0$. In both cases, the outer turning points are at $z=\pm z_T$ where

A-31

$$z_T = \left[G_j P_y + (H_\perp/\alpha_j)^{1/2} \right]^{1/2} \qquad (34)$$

If, in addition, $H_\perp$ is less than $\Gamma_j(0)$, then the orbits are of the non-crossing type and have inner turning points at $z=\pm z_1$, where

$$z_1 = \left[G_j P_y - (H_\perp/\alpha_j)^{1/2} \right]^{1/2}.$$

If $H_\perp$ is greater than $\Gamma_j(0)$, then the orbits are of the axis-crossing type with the turning points given by Eq.(34).

The remaining quantity to be calculated in Eq.(14) is the orbital period $T(H_\perp, P_y)$ for each species. It is convenient to define a quantity ξ_j by

$$\xi_j \equiv \left\{ \frac{1}{2} [1 + (G_j P_y)(\alpha_j/H_\perp)^{1/2}] \right\}^{1/2} . \qquad (35)$$

It is then straightforward to show that an orbit is of the axis-crossing type if and only if $\xi_j < 1$ with the period of each species given by

$$T(H_\perp, P_y) = \frac{2}{z_T} \left[\frac{2m_j}{\alpha_j} \right]^{1/2} \xi_j K(\xi_j^2) \qquad (36)$$

where $K(\xi^2)$ is the complete elliptic integral of the first kind

$$K(\xi^2) = \int_0^{\pi/2} d\theta \ (1-\xi^2 \sin^2\theta)^{-1/2} .$$

Because these orbits cross the axis (z=0), we find

$$|G_j P_y| < (H_\perp/\alpha_j)^{1/2} .$$

Similarly, an orbit is of the non-crossing type if and only if $\xi_j > 1$ with the period given by

$$T(H_\perp, \ P_y) = \frac{1}{z_T} \left[\frac{2m_j}{\alpha_j}\right]^{1/2} K(\xi_j^{-2}) \quad , \tag{37}$$

and

$$G_j P_y > (H_\perp/\alpha_j)^{\frac{1}{2}} .$$

Note that $\xi_j = 1$ corresponds to the marginally crossing orbit with $T \to \infty$ as $T \propto -(1/2)\ln(1-\xi_j^2)$.

E. THE KERNELS

We now have all the information necessary to compute the perturbed current density [Eqs.(9) and (14)] for the

A-33

model distribution function, Eq. (25). Specifically, we calculate the kernels in Eq.(14). In this paper, we specialize to the fundamental harmonic, n=0.

By virtue of our choice of $F_\perp$, the $H_\perp$-integration can be performed trivially in Eq.(14). With a different choice of $F_\perp$, both P_y- and $H_\perp$-integrations may have to be done numerically. However, the velocity components can still be computed analytically so that the numerics required are minimal. Carrying out the $H_\perp$-integration, we obtain

$$J_{an}(z) = \frac{e^2 n_o z_p}{\pi m_j c} \left[\frac{z_p^2 \omega_{cj}}{G_j} \right] \left[\frac{W(b_o)}{T_{j\parallel}} \int dz' K_1(z,z') \ \psi(z') \right.$$

$$\left. + \int dz' K_2(z,z')\psi(z') \right] , \qquad (38)$$

where $b_o = \omega/k v_{j\parallel}$ and $s \equiv G_j P_y/z_p^2$. In the above equation and in the remainder of the paper, z, z' and other lengths will be scaled to z_p. The dimensionless kernel K_1 corresponds to κ_1 [Eq. (19)] and is given by

$$K_1(z,z') \equiv \int_a^b ds \ \frac{(z^2-s)(z'^2-s)}{T(s)[(s-a_j)(b_j-s)(s-a_j')(b_j'-s)]^{1/2}} , \qquad (39)$$

and K_2 corresponds to κ_2 [Eq. (20)] and is given by

$$K_2(z,z') \equiv - \frac{\partial}{\partial T_{j\perp}} K_1(z,z') \quad . \tag{40}$$

Here, the orbital period of each species has been normalized to ω_{cj} so that $T(s) = [T(H_\perp,P_y)/\omega_{cj}]$, evaluated at $H_\perp = V_j P_y + T_{j\perp}$. The quantities a_j and b_j correspond to the limits of s defined by the kinematic requirement that v_z be real:

$$a_j(z) = (z^2 - 2\eta_j) - 2\eta_j[\eta_j^{-1}(1 - z^2)]^{1/2} \tag{41}$$

$$b_j(z) = (z^2 - 2\eta_j) + 2\eta_j[\eta_j^{-1}(1 - z^2)]^{1/2} \quad , \tag{42}$$

$$\eta_j \equiv \frac{\bar{V}_j}{V_{j\perp}} \frac{\rho_j}{z_p} \quad .$$

Then, we can write

$$v_z = \frac{1}{2} (\omega_{cj} z_p) [(s-a_j)(b_j-s)]^{1/2}$$

so that at any given point z, an equilibrium orbit passing through that point has momentum P_y such that $s = G_j P_y/z_p^2$ is in the range $a_j(z) \leqslant s \leqslant b_j(z)$. For z', we have $a_j' \equiv a_j(z')$ and $b_j' \equiv b_j(z')$ so that the s-integration must be carried

out over the overlapped region of (a_j, b_j) and (a_j', b_j'). The integration limits a and b in Eq. (39) simply denote $a=a_j$ and b is the smaller of $b_j(z)$ or $b_j'(z')$. In Eq. (40), use has been made of the replacement $\partial/\partial H_\perp \rightarrow -\partial/\partial T_{j\perp}$, taking care to differentiate only those $T_{j\perp}$-dependent quantities that are affected by the $H_\perp$-integration. Note also that z'-integration in Eq.(38) has now been reduced to integration over one half of a cycle.

It is of interest to consider some properties of the functions $a_j(z)$, $b_j(z)$, and the kernels, $K_1(z,z')$ and $K_2(z,z')$. Figure 2 shows $a_j(z)$ and $b_j(z)$ for ions in which we have used, for convenience, $\rho_i/z_p = 0.2$. It is clear from Eqs. (41) and (42) that $a_j(z)$ is a monotonically increasing function for $0 \leqslant z \leqslant 1$, ranging from $-2(\eta_j^{1/2} + \eta_j)$ to $s_0 \equiv 1 - 2\eta_j$. The function $b_j(z)$ is positive for all $0 \leqslant z \leqslant 1$, ranging from $2(\eta_j^{1/2} - \eta_j)$ to s_0. It attains the maximum value $(1 - \eta_j)$ at $z = (1 - \eta_j)^{1/2}$. The value z_c is such that $a_j(z_c) = b_j(0)$. It can be shown that $\xi_j = 1$ at $s = b_j(0)$ for both species. In Fig. 3, we have plotted $K_1(z,z')$ for ions $(\rho_i/z_p = 0.2)$ at two values of z. Curve a corresponds to $z < z_c$ and Curve b corresponds to $z > z_c$. For $z \leqslant z_c$, the kernels $K_1(z,z')$ and $K_2(z,z')$ are non-zero for all $z' \leqslant z$. In this case, the contribution to the kernels includes both axis-crossing $(\xi_j < 1)$ and non-crossing $(\xi_j > 1)$ orbits. For $z > z_c$, let z_s be such

that $a_j(z) = b_j(z_s)$. Then, K_1 and K_2 are non-zero only if $z > z_s(z)$. In this case, the contribution to the kernels comes entirely from the non-crossing orbits. Straightforward calculation yields

$$z_c = 2 \, (\eta_j^{1/2} - \eta_j)^{1/2}$$

and

$$z_s(z) \equiv \left\{ a_j(z) - 2\eta_j \left[\left[\frac{v_{j\perp}}{\bar{v}_j} \right] - \frac{1}{\eta_j} a_j(z) \right]^{1/2} \right\}^{1/2}. \qquad (43)$$

For a given $z > z_c$, it can be shown that in the limit $z' \to z_s$ from above

$$K_1(z,z_s) = \frac{\pi(z^2 - a_j)(z_s^2 - a_j)}{T(a_j)[(a_j - a_j')(b_j - a_j)]^{1/2}} \qquad (44)$$

where $a_j' \equiv a_j(z_s)$. For $z' < z_s$, we have $K_1 = 0$. Thus, K_2 has a δ-function contribution at $z' = z_s(z)$.

For $z < 1$, we have $K_1(z,z') = 0$ for $z' < (1 - 4\eta_j)^{1/2}$. For $z' > (1 - 4\eta_j)^{1/2}$, it can be shown that

$$K_1(z=1,z') = \frac{\pi(1-s_o)(z'^2-s_o)}{T(s_o)[(s_o-a_j')(b_j'-s_o)]^{1/2}}$$

where $s_o = 1-2\eta_j$. As z' also approaches unity, K_1 diverges as

$$K_1(z=1, z' \to 1) \to \frac{\pi(1-s_o)^2}{T(s_o)} [b'(z')-s_o]^{-1}$$

As z' approaches $(1-4\eta_j)^{1/2}$, we find

$$K_1 \to \frac{\pi(1-s_o)(z'^2-s_o)}{T(s_o)(s_o-a_j')^{1/2}} [b'((1-4\eta j)^{1/2})-s_o]^{-1/2}$$

Finally, we note an important property of the orbital period. If $s = \bar{s} \equiv 2(\eta_j^{1/2}-\eta_j)$, then we have $\xi_j=1$, corresponding to the marginally crossing orbit. For $s \to \bar{s}$ from above (i.e. noncrossing orbits), then

$$T(s) \to \frac{-1}{2z_T} \left[\frac{2m_j}{\alpha_j} \right]^{1/2} \ln(\xi_j^2-1).$$

For $s \to \bar{s}$ from below (i.e. axis-crossing orbits), then

$$T(s) \to \frac{-1}{z_T} \left[\frac{2m_j}{\alpha_j} \right]^{1/2} \ln(1-\xi_j^2).$$

A-38

As a general remark, it is clear that the square-root singularities in the kernel [Eq. (39)] occur at the turning points where $v_z \approx 0$. This indicates that, at a given location z, a significant contribution to the perturbed current density comes from those orbits whose turning points occur at z.

III. SOLUTION

In order to solve the fundamental equation (5), we evaluate the kernels. By changing the integration variable to

$$t = \frac{-1}{b_j - a_j'} \; \ln \left[\frac{b_j - s}{s - a_j} \right] ,$$

we can write K_1 in the form

$$K_1 = \int_{t_a}^{t_{b'}} \frac{dt \; h(t)}{[(t - t_a)(t_{b'} - t)]^{1/2}}$$

where $h(t)$ is a well behaved function of t

$$h(t) = \frac{(z - s)(z'^2 - s)}{T(s)} \left[\frac{(s - a_j')(b_j - s)(t - t_a)(t_b' - t)}{(s - a_j)(b_j' - s)} \right]^{1/2}$$

with $s = s(t)$ and t_a, t_b' corresponding to t evaluated at $s = a_j$ and $s = b_j'$, respectively. We evalute K_1 to a typical relative accuracy of 10^{-7} or better. The kernel K_2 is simply obtained by numerically differentiating K_1 with respect to

$T_{j\perp}$ [Eq. (40)]. This operation gives a relative accuracy of roughly 10^{-4}.

The fundamental equation (21) is solved by the Galerkin method as discussed in Sec. II.A. That is to say that we solve the matrix equation (23) using a finite $N \times N$ matrix for the condition of γ and k such that an eigenvalue is zero. The corresponding Q_n are the components of the eigenvector describing the mode.

For our calculation, we have chosen the linearly independent basis functions

$$
u_\ell(z) = \begin{cases} \dfrac{z - z_{\ell-1}}{z_\ell - z_{\ell-1}} \,, & z_{\ell-1} \leqslant z < z_\ell \,, \\[2em] \dfrac{z_{\ell+1} - z}{z_{\ell+1} - z_\ell} \,, & z_\ell \leqslant z < z_{\ell+1} \,. \end{cases}
$$

Here, $z_1=0$ is the origin and the z_ℓ's are the nodes. In this work, we have divided the region $d_e = 2(2\rho_e/z_p)^{1/2}$ into $N_1=48$ intervals and the remainder of the sheet into $N_2=24$ intervals. Then, $z_N=1$ where $N=N_1+N_2+1=73$ and we have a

73x73 matrix. For z>1, Eq.(5) is exactly solvable and we choose

$$u_N(z) = e^{-\bar{k}(z-1)} \quad ,$$

where $\bar{k} \equiv k z_p$.

As Eq. (39) shows, for the fundamental harmonic (n = 0) in the equilibrium orbital period $T(H_\perp, P_y)$, the integrals do not depend on $(\omega/kv_{j\parallel})$ and the k dependence enters only through the boundary terms. This means all the nontrivial numerical computation needs to be done only once in order to obtain the dispersion relation for a given value of ρ_j/z_p. In addition, the integrals are also independent of $T_{j\perp}/T_{j\parallel}$.

In order to illustrate a specific application, we have computed the dispersion relation of even modes for the model distribution function given by Eq. (25). Figure 4 shows the plot of $\bar{\gamma} \equiv \gamma/\omega_{ci}$ versus $k \equiv kz_p$ for $\rho_i/z_p = 0.02$ and several values of $T_{e\perp}/T_{e\parallel}$. Since the instability and the non-Maxwellian effects are completely dominated by the electrons, we have set $T_{j\perp}/T_{i\parallel} = 1$ throughout. It is of interest to note the essentially linear dependence of γ/ω_{ci}

A-43

on kz_p. That is to say that the dispersion relation has the form

$$\frac{\bar{\gamma}}{\bar{k}} = \left[\frac{\rho_e}{z_p}\right] D\left[\frac{T_{e\perp}}{T_{e\parallel}}\right] , \qquad (45)$$

where D is a dimensionless function of $T_{e\perp}/T_{e\parallel}$ only. For large enough values of $T_{e\perp}/T_{e\parallel}$, D can be multi-valued. The behavior described by Eq. (45) is general for non-Maxwellian distriubitons in the low-frequency regime. As discussed in the preceeding paragraph, Eqs. (18) and (38) show that, for the fundamental harmonic (n = 0), the instability depends only on $\gamma/kv_{j\parallel}$ in the dispersion function except for very large k in which case the k^2 term can be important [Eq. (18)]. For $T_{e\parallel\perp}/T_{e\parallel} = 1$ (Curve a in Fig. 4), k must be of the order of 10^3 or larger in order for the k^2 term to be significant with correspondingly large growth rates. However, the present low-frequency analysis is clearly inapplicable for $\gamma/\omega_{ci} \gg 1$ so that the physical maximum γ and the corresponding k value cannot be determined. Consistent with the low-frequency approximation, we have shown results for $\bar{\gamma} < 0.5$. It is of interest to note that Curves e and f correspond to two distinct branches for $T_{e\perp}/T_{e\parallel} = 3$. In Fig. 5, we have plotted $\bar{\gamma}$ at k = 1 as a function of $T_{e\perp}/T_{e\parallel}$. The mode is completely stabilized for $T_{e\perp}/T_{e\parallel} < 0.98$.

In the previous analytical treatments, the eigenfunction ψ has been assumed to be constant inside the tearing region $|z| < (\rho_e z_p)^{1/2}$ (the "constant-ψ" approximation[7,9,12]). An objective of this paper is to remove this restrictive simplification. In Fig. 6 we have plotted the eigenmode structure for $|z| < 2(2\rho_e/z_p)^{1/2}$ for the most unstable branch corresponding to Curves a through e of Fig. 4. Because the eigenfunction ψ depends only on $W(\gamma/kv_{j\parallel})$ $(T_{j\perp}/T_{j\parallel})$ [Eq. (38)], the eigenfunctions are essentially identical for Curves a through e. It is clear that the constant-ψ approximation is not valid for this system. Note the oscillatory structure near $z = 0.036$, corresponding to $z = z_c$ for electrons. Axis-crossing electrons whose perpendicular energy $H_\perp$ is of the order $T_{e\perp}$ turn around in the neighborhood of this, contributing to the perturbed current density.

As the electron perpendicular temperature $T_{e\perp}$ is increased relative to $T_{e\parallel}$, another branch becomes unstable at $T_{e\perp}/T_{e\parallel} \cong 3$. Curve f of Fig. 3 gives the growth rate for $T_{e\perp}/T_{e\parallel} = 3$. In comparison with Curve e, we see that the new branch is more than two orders of magnitude slower. Figure 7 shows the eigenfunction corresponding to the second branch. Note, however, the second slower branch is still much faster than the conventional isotropic tearing mode[9] or anisotropic bi-Maxwellian tearing mode.[12] We add that Figs.

5 and 6 are both plotted by drawing smooth curves through approximately 50 points and the resolution is good. Note that, because the operator L is self-adjoint, an error of the order of ϵ in the eigenfunction leads to an error of the order of ϵ^2 so that the eigenvalues are expected to be accurate. The Galerkin method is well-suited for the present problem.

IV. SUMMARY

We have presented a general integro-differential formalism to study the collisionless tearing mode in a highly non-Maxwellian neutral sheet in which both electrons and ions are treated kinetically. The important feature of the theory is that all the exact unperturbed particle orbits are included analytically in calculating the perturbed distribution functions for both species. For the low frequency ($\gamma/\omega_{ci} \ll 1$) perturbation, an integro-differential equation [Eq. (21)] is obtained to calculate the eigenmode structure. This formalism removes the straight-line-orbit and constant-ψ approximations which are the two major limiting features of previous theoretical treatments.[7,9,12,13] In addition, it eliminates the need to match solutions obtained in different regions at artifically chosen locations. Using the Galerkin method, the fundamental integro-differential equation is converted into a matrix equation [Eq. (23)] which is then solved for the dispersion relation.

Note that, for the purely growing mode ($\omega = i\gamma$), the integro-differential operator L[Eq. (18)] is self-adjoint for the fundamental harmonic (n=0) in the orbital frequency $\Omega(H_\perp, P_y)$. A quadratic form [Eq. (24)] associated with the operator L is used to analyze the general properties of the

A-47

fundamental equation (21) in Sec. II.A. Based on these findings, we have presented (Sec. II.B) a general prescription to determine the sufficient condition for instability of a given system by computing the eigenvalue spectrum of the operator L for two values of γ; $\gamma = 0$ and $\gamma \to +\infty$ for a given value of k. This prescription may be a powerful tool in treating systems in which extensive numerical computation is necessary to obtain the matrix elements [Eq. (23)] for each value of γ.

The basic formalism is applied to a specific non-Maxwellian distribution [Eq. (25)]. The dispersion relation for this system is determined for the fundamental harmonic (n = 0) of the orbital frequency, Ω (Sec. II.A.). The dispersion relation is shown to be dominated by the electrons and to have the general form $\bar{\gamma}/k = (\rho_e/z_p)D(T_{e\perp}/T_{e\parallel})$ [Eq. (45)] where D is a function of $T_{e\perp}/T_{e\parallel}$ only. These results are shown in Figs. 4 through 7. It has been pointed out that the growth rate of non-Maxwellian distributions are generally much greater than that of the conventional isotropic tearing instability [see Sec. II.A following Eq. (23)]. The physical mechanism is the Lorentz force acting in the direction of $\underline{k}$ [I_2 following Eq. (9)] which is a large contribution to the perturbed current density. Thus, the mechanism of the instability is somewhat different from the classical collisionless tearing

mode. For the specific model distribution function corresponding to a sharp-boundary profile, the growth rate can be very large. However, this is a highly singular system and we expect a less singular system such as a bi-Maxwellian distribution to exhibit somewhat slower growth. An important point to note is that the eigenfunctions show (Figs. 6 and 7) that the constant-ψ approximation is in general not likely to be valid for non-Maxwellian systems. The eigenfunctions are found to be strongly localized to a small region of the order of $|z| <$ $(\rho_e z_p)^{1/2}$, which is comparable to the size of the thermal electron orbits near $z=0$. In addition, the strong localization implies that the boundary effects are negligibly small.

A physical system to which the present analysis may be particularly relevant is the earth's magnetotail. Since the magnetotail plasmas are highly collisionless, the particle distribution may be non-Maxwellian. The present analysis may also be relevant to experimental neutral sheets[21] in which the particle (electron) distribution is observed to be non-Maxwellian. The formalism can also be extended to cylindrical systems such as θ-pinches and field-reversed ion layers.[22,23]

In this paper, we have used a highly non-Maxwellian distribution [Eq. (25)]. The distribution exhibits a number of singularities (Sec. II.E) which would be smoothed out by less singular distribution functions such as a bi-Maxwellian distribution function, making the numerical computation less time-consuming. In addition, the scalar potential can be included in a straightforward manner. It is clear that the present formalism can be modified to treat such cases without any difficulty.

ACKNOWLEDGMENTS

REFERENCES

1. H.P. Furth, Nucl. Fusion Suppl. Pt. 1, 169 (1962).

2. D. Pfirsch, Z. Naturforsch. Teil A, $\underline{17}$, 861 (1962).

3. G. Laval and R. Pellat, C.R. Acad. Sci. Paris $\underline{259}$, 1706 (1964).

4. G. Laval, R. Pellat, and M. Vuillemin, in _Plasma Physics and Controlled Nuclear Fusion Research_ (IAEA, Vienna, 1966), Vol. 2, p. 259.

5. F.C. Hoh, Phys. Fluids $\underline{9}$, 277 (1966).

6. K. Schindler, in _Proceedings of the Seventh International Conference on Phenomena in Ionized Gases_ (Gradevinska Knjiga, Beograd, Yugoslavia, 1966), Vol. II, p. 736.

7. B. Coppi, G. Laval, and R. Pellat, Phys. Rev. Lett. $\underline{16}$, 1207 (1966).

8. K. Schindler and M. Soop, Phys. Fluids $\underline{11}$, 1192 (1968).

9. M. Dobrowolny, Nuovo Cimento B55, 427 (1968).

10. D.W. Forslund, Ph.D. thesis, Princeton University, 1968.

11. K. Quest and F.V. Coroniti, J. Geophysical Res. 86, 3299 (1981).

12. J. Chen and P. Palmadesso, Phys. Fluids 27, 1198 (1984).

13. J. Chen, P.J. Palmadesso, J.A. Fedder, and J.G. Lyon, Geophys. Res. Lett. 11, 12 (1984).

14. G. Laval and R. Pellat, in Proceedings of the ESRIN Study Group, Frascati, Italy, 1967, paper No. ESRO Sp-36, p. 5.

15. J. Ambrosiano, L.C. Lee, and Z.F. Fu, manuscript in preparation, to be submitted to J. Geophys. Res. (1984).

16. J.P. Holdren, Ph.D. thesis, Stanford University IPR Report No. 351, 1970.

17. L. Lapidus and G.F. Pinder, <u>Numerical Solution of Partial Differential Equations in Science and Engineering</u>, John Wiley & Sons, New ;York, 1982.

18. See, for example, R.C. Davidson, <u>Theory of Nonneutral Plasmas</u>, W.A. Benjamin, Inc., Reading, Massachusetts, 1974.

19. B.U.O. Sonnerup, J. Geophys. Res. <u>76</u>, 8211 (1971).

20. I.B. Bernstein, E.A. Frieman, M.D. Kruskal and R.M. Kulsrud, Proc. Roy. Soc. (London), <u>A244</u>, 17 (1958).

21. R.L. Stenzel, W. Gekelman, and N. Wild, Phys. Fluids <u>26</u>, 1949 (1983).

22. J. Chen and R.C. Davidson, Pnys. Fluids <u>24</u>, 2208 (1981).

23. H.S. Uhm and R.C. Davidson, Phys. Fluids <u>23</u>, 348 (1980).

FIGURE CAPTIONS

Fig. 1 Schematic drawing of a neutral sheet and the coordinate system. The magnetic field $\underline{B}_0(z) = 0$ at $z = 0$. The dashed lines describe the magnetic field including the perturbation.

Fig. 2 Plot of $a_i(z)$ and $b_i(z)$ [Eqs. (41) and (42)] for $\rho_i/z_p = 0.2$. The point z_c is such that $a_i(z_c) = b_i(0)$.

Fig. 3 Plot of $K_1(z,z')$ [Eq. (39)] versus z' for (a) $z/z_p = 0.5$ and (b) $z/z_p = 0.85$.

Fig. 4 The dispersion relation. The normalized growth rate $\bar{\gamma} = \gamma/\omega_{ci}$ is plotted versus $\bar{k} = kz_p$. The value of $T_{e\perp}/T_{e\parallel}$ is (a) 1.0, (b) 1.25, (c) 1.5, (d) 2.0, (e) 3.0, and (f) 3.0, the second branch to become unstable. $T_{i\perp}/T_{i\parallel} = 1$, $T_{e\perp}/T_{i\perp} = 0.5$, and $\rho_i/z_p = 0.02$.

Fig. 5 Plot of the normalized growth rate $\bar{\gamma}$ versus $T_{e\perp}/T_{e\parallel}$ with $T_{i\perp}/T_{i\parallel} = 1$ ($T_{e\perp}/T_{i\perp} = 0.5$ and $\rho_i/z_p = 0.02$).

Fig. 6   The eigenfunction corresponding to Curves a through e of Fig. 4.   ($T_{i\perp}/T_{i\parallel} = 1$, $T_{e\perp}/T_{i\perp} = 0.5$ and $\rho_i/z_p = 0.02$).

Fig. 7   The eigenfunction corresponding to Curve f of Fig. 4, the second unstable branch with $T_{e\perp}/T_{e\parallel} = 3.0$. ($T_{i\perp}/T_{i\parallel} = 1$, $T_{e\perp}/T_{i\perp} = 0.5$ and $\rho_i/z_p = 0.02$).
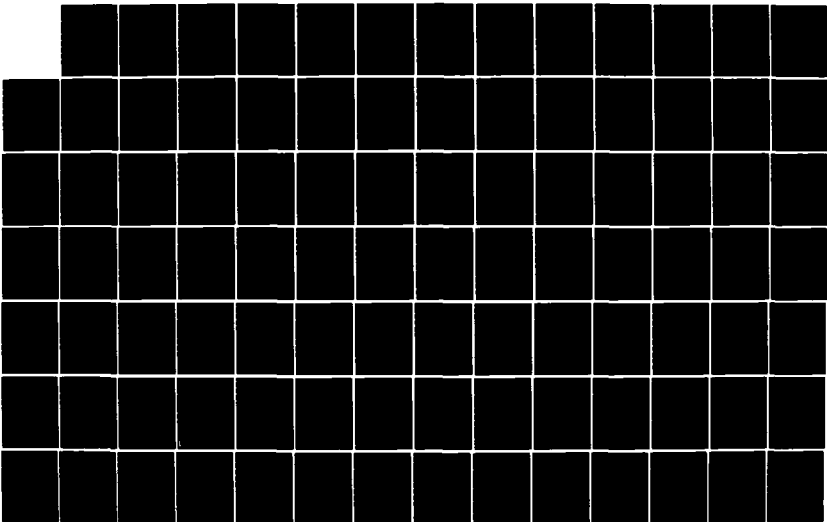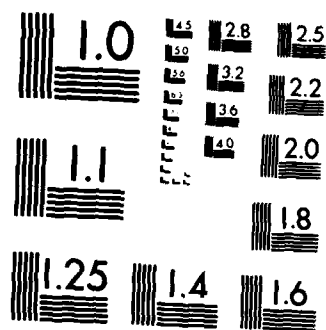
MICROCOPY RESOLUTION TEST CHART
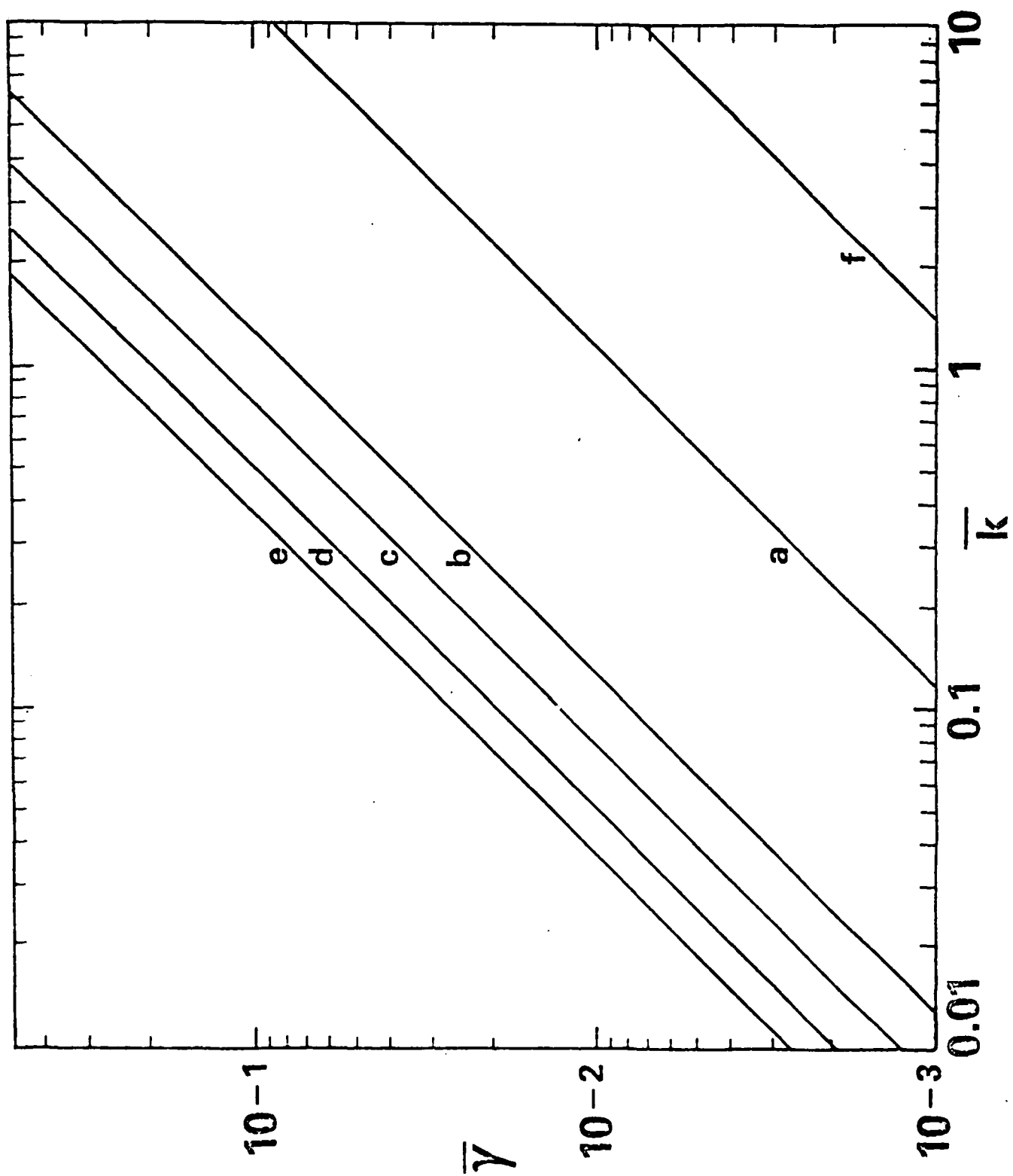NATIONAL BUREAU OF STANDARDS 1963-A
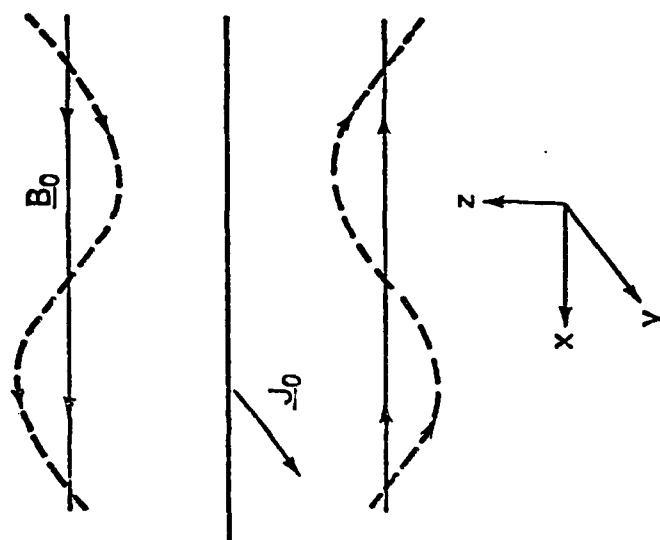
Figure 1
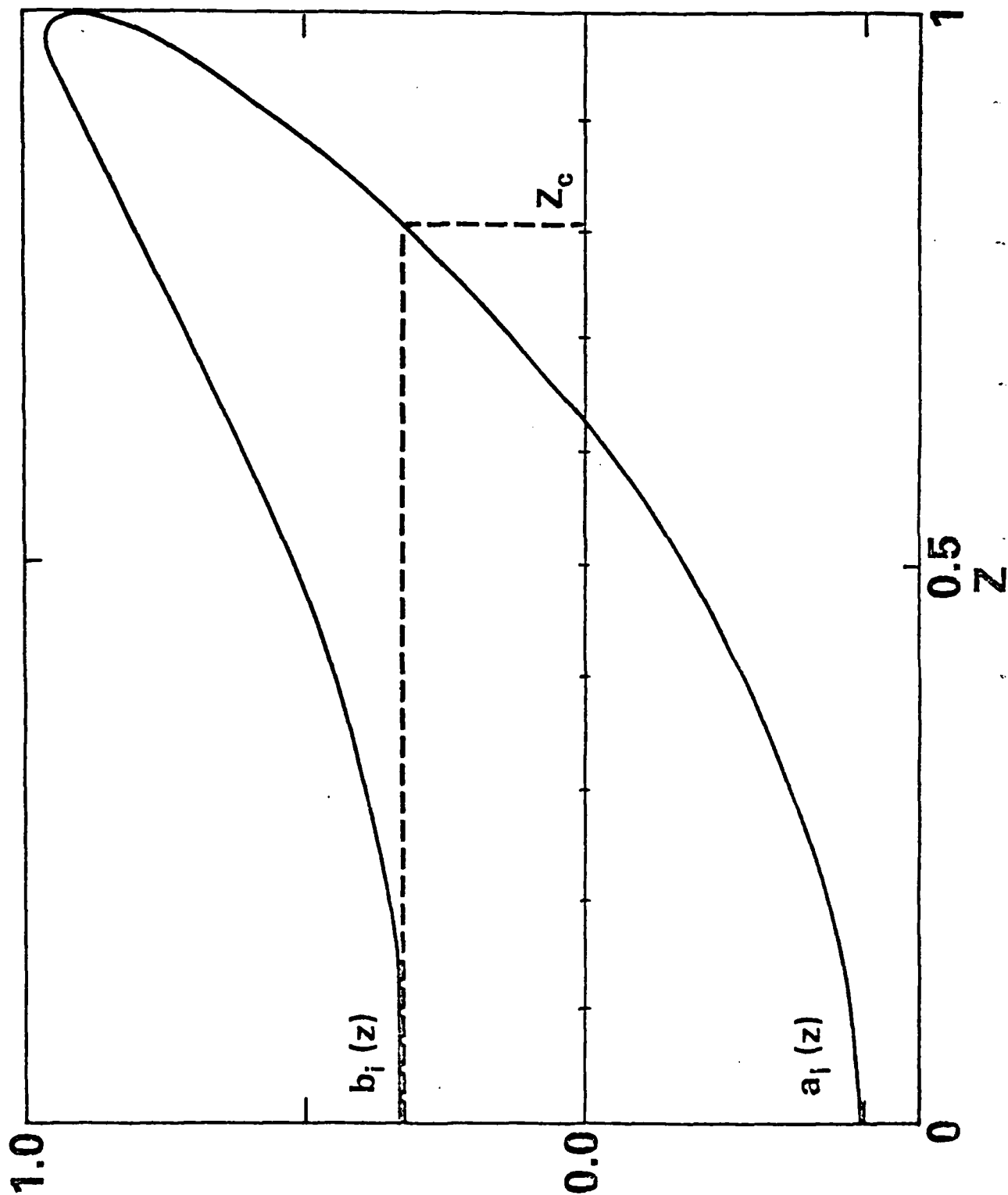
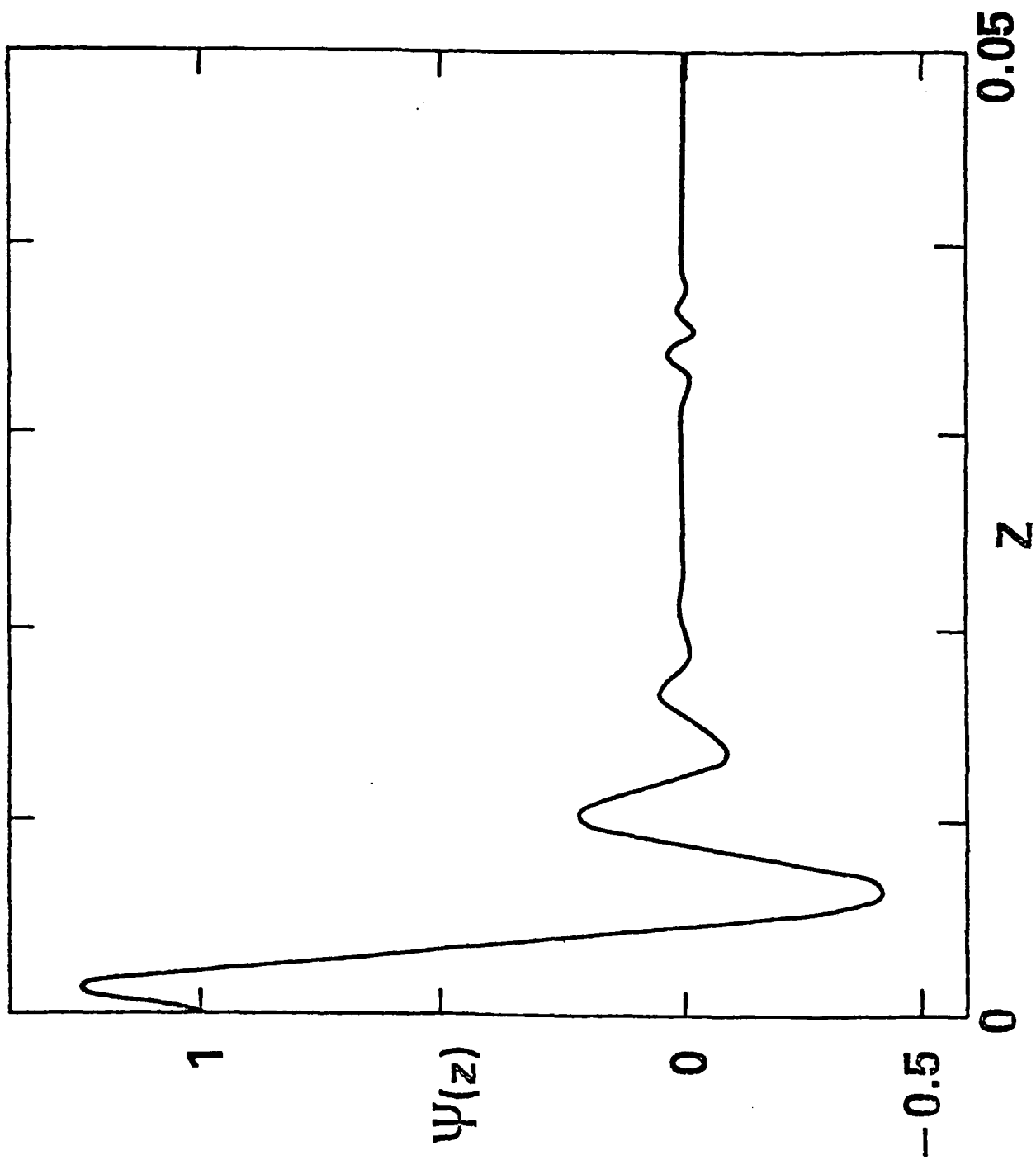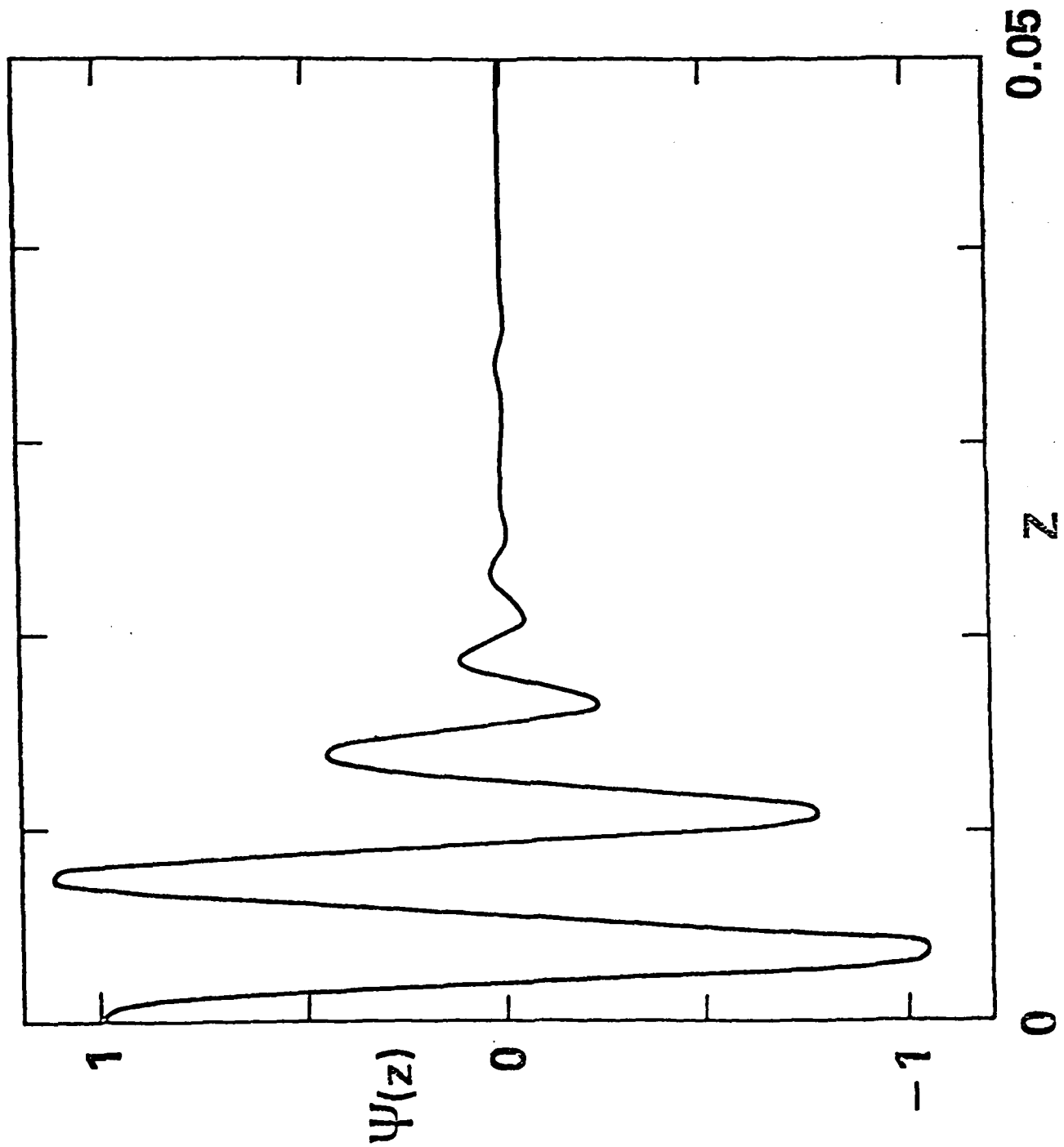Figure 2
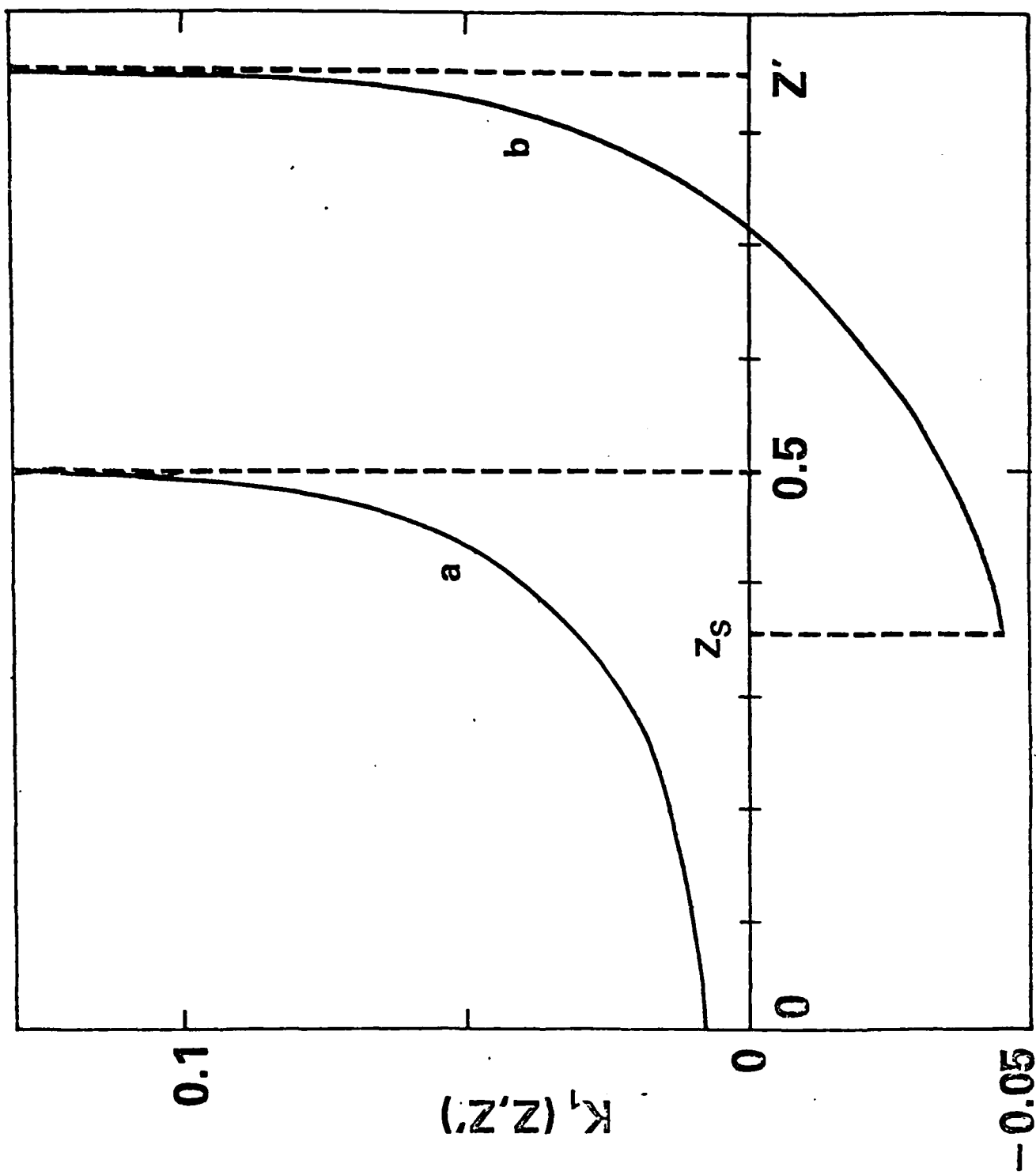
Figure 3

Figure 4
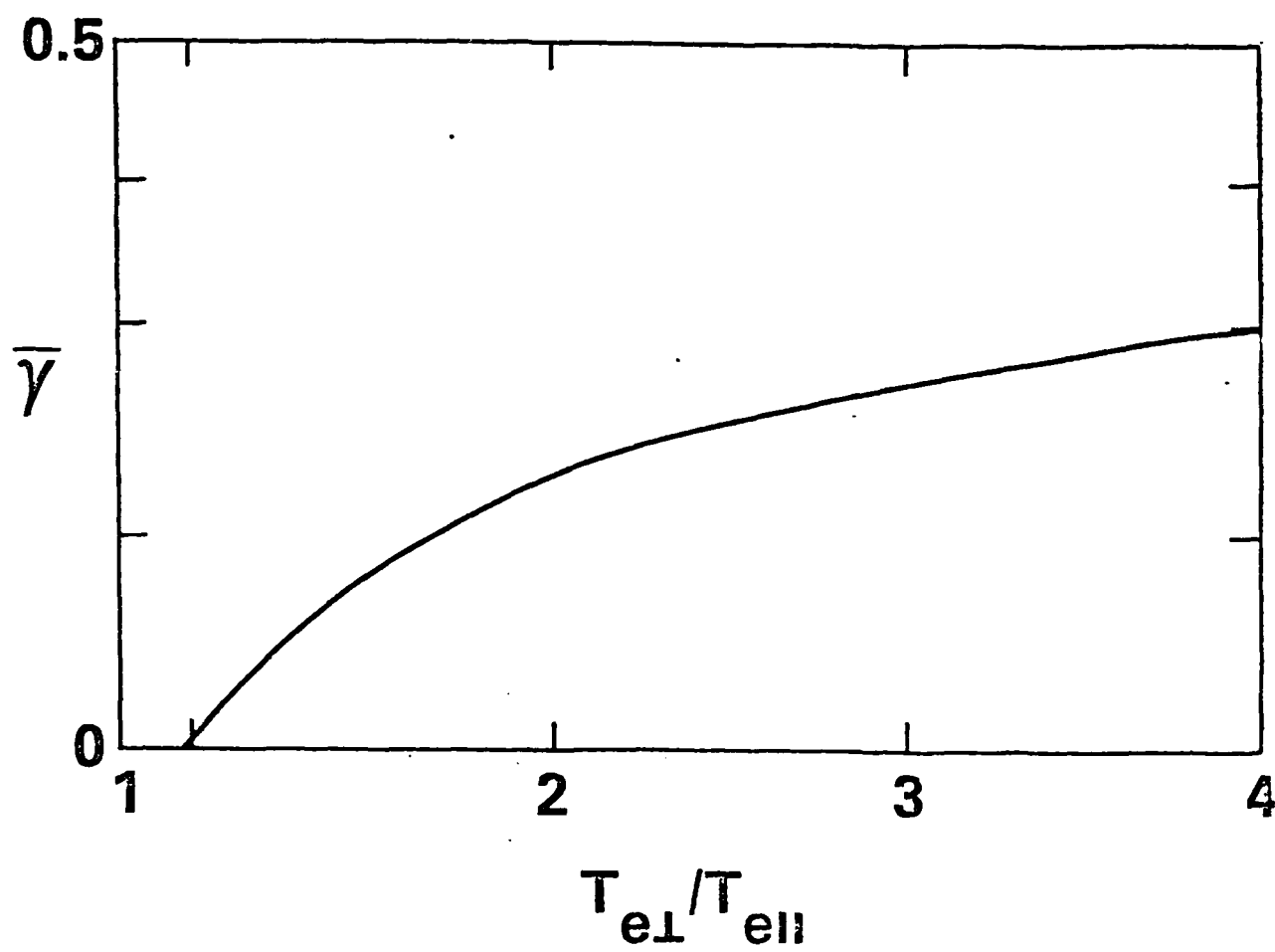
Figure 5

Figure 6

Figure 7

APPENDIX B

Nonlocal Effects on the Convective Properties of the

Electrostatic Current-Driven Ion-Cyclotron Instability

Nonlocal effects on the convective properties of the electrostatic current-driven ion-cyclotron instability

G. Ganguli and P. Bakshi[a]
Science Applications, Inc., McLean, Virginia 22102

P. Palmadesso
Geophysical and Plasma Dynamics Branch, Plasma Physics Division, Naval Research Laboratory, Washington, D.C. 20375

Nonlocal effects due to magnetic shear and finite current channel width on the convective characteristics of the current-driven ion-cyclotron instability have been investigated. When the magnetic shear length (L_s) is smaller than the current channel width (L_c), the group velocity parallel to the external magnetic field at the origin (V_{gz}) vanishes, and there is a reduction in the group velocity perpendicular to the external magnetic field (V_{gy}). For $L_c \sim 10^{-2} L_s$, the values of V_{gz} and V_{gy} as given by local theory are recovered. When $L_c \lesssim \rho_i$, where ρ_i is the mean ion Larmor radius, both V_{gz} and V_{gy} change sign, indicating a reversal of the direction of propagation.

I. INTRODUCTION

The current-driven ion-cyclotron instability[1] (CDICI) has been of considerable interest to both space and laboratory plasma physicists for more than two decades. Recently, we have demonstrated the importance of nonlocal effects due to magnetic shear[2,3] (produced by the field-aligned current) and the finite extent of the current channel.[4,5] Our past work dealing with these nonlocal aspects of the electrostatic CDICI was essentially based on a normal mode approach. The local treatment of the CDICI,[1,6,7] which assumes an infinite extent of the width of the current channel, predicts a finite group velocity of the CDICI in both the parallel and perpendicular directions relative to the external magnetic field. For a temporally growing mode, the presence or absence of a group velocity in a finite-sized region of space (as opposed to a point) makes an instability convective or absolute[8]; these are two vastly different physical scenarios. This fact has been elucidated by Ashour-Abdulla and Kennel,[7] in general, and more specifically for the CDICI by Ashour-Abdulla and Thorne.[9] In our earlier work[2–4] we noted a significant difference between the local and the nonlocal results as far as growth rates of normal modes are concerned. For instabilities like the CDICI which are convective, a normal mode analysis without regard to the convective growth cannot fully determine the stability of a bounded system, and hence is somewhat limited in its application. Thus, the main objective of this paper is to report the nonlocal effects due to magnetic shear and the finite current channel width on the convective aspects of the electrostatic CDICI.

II. THEORY

In our treatment we will follow the analytical approach as given in Bakshi *et al.*[4] We introduce a finite current chan-

nel width in the x direction. We take the electron distribution function to be Maxwellian with a drift velocity parallel to the magnetic field which is x dependent:

$$V_d(x) = V_d^0 g(x_g/L_c), \tag{1}$$

where $g(\xi) = \exp(-\xi^2)$ and $x_g = x + v_y/\Omega_e$. Assuming that $v_y/\Omega_e \sim O(\rho_e) \ll L_c$, where L_c is the characteristic length scale associated with the current channel, we approximate (1) by

$$V_d(x) \approx V_d^0 g(x/L_c). \tag{2}$$

Using (2) and following the methods illustrated in Ref. 4 we arrive at the nonlocal, differential equation for the CDICI:

$$\left[\left(\frac{\rho_i}{L_c}\right)^2 \frac{\partial^2}{\partial \xi^2} + Q(u, V_d) \right] \phi(\xi) = 0, \tag{3}$$

where Q is defined by

$$Q = -\rho_i^2(Q_1/A), \tag{4}$$

$$Q_1 = 1 + (k_y \lambda_i)^2 + \tau + \sum_n \Gamma_n(b)\zeta_i Z\left[(1 - np)\zeta_i\right] + \tau\{\zeta_e - [V_d(\xi)]/V_e]\}Z\{\zeta_e - [V_d(\xi)]/V_e]\}. \tag{5}$$

$$A = \frac{\rho_i^2}{2} \zeta_i \sum_n \Gamma_n'(b)Z\left[(1 - np)\zeta_i\right], \tag{6}$$

where $b = k_y^2 \rho_i^2/2$, $\Gamma_n' = \partial\Gamma_n/\partial b$, $\tau = T_i/T_e$, $p = \Omega_i/\omega$, $\zeta_i = \omega/|k_\parallel|v_i$, $\xi = x/L_c$, $\zeta_e = \omega/|k_\parallel|v_e$, $k_\parallel(x) = k_z + k_y(L_c/L_s)\int_0^\xi g(\xi)d\xi$, $u = k_\parallel(x)/k_y$, and L_s is the characteristic length associated with the shear in the magnetic field.

The dispersion relation is given by[4]

$$Q'(\omega, \xi_1) = 0, \tag{7a}$$

$$Q(\omega, \xi_1) = (2l + 1)(\rho_i/L_c)\{ -\tfrac{1}{2} Q''(\omega, \xi_1)\}^{1/2}, \tag{7b}$$

where Q' and Q'' are the first and second derivatives of Q with respect to ξ evaluated at ξ_1, which is defined by (7a). We solve Eqs. (7a) and (7b) numerically for the complex eigenfrequencies ω, given the perpendicular wave vector k_y, the par-

[a] Permanent address: Department of Physics, Boston College, Chestnut Hill, Massachusetts 02167.
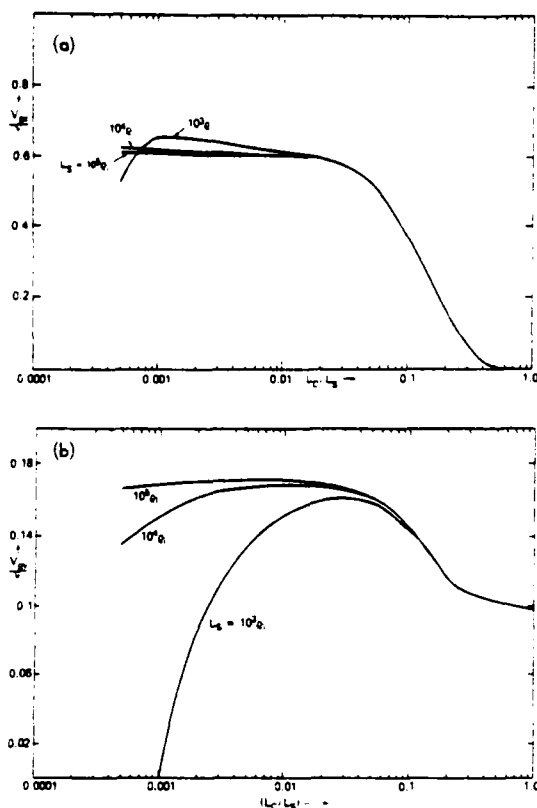
FIG. 1. A plot of the group velocity versus L_c/L_s for the first harmonic. Here $b = 0.6$, $\tau = 0.5$, $\mu = 1837$, and $V_d^0/v_e = 0.28$. (a) The group velocity in the z direction V_{gz}/v_i vs L_c/L_s; (b) the group velocity in the y direction V_{gy}/v_i vs L_c/L_i.
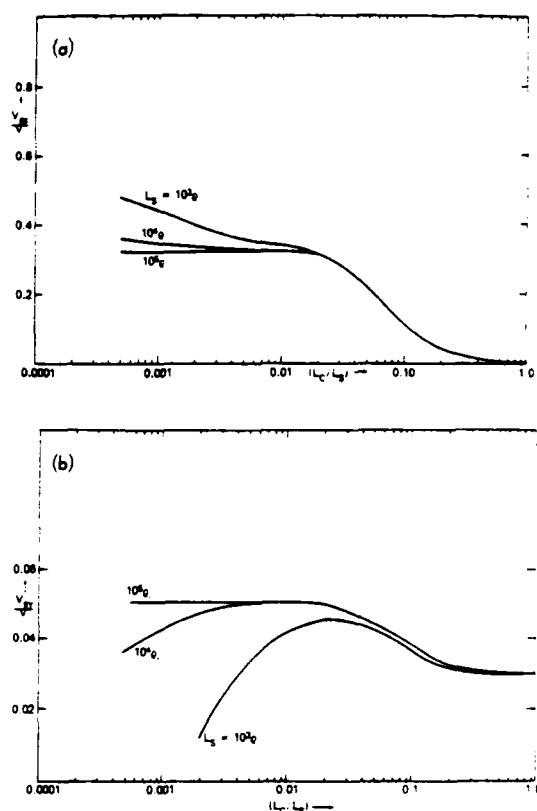
FIG. 2. A plot similar to Fig. 1 for the second harmonic. Here $b = 2.4$, $\tau = 1.0$, $\mu = 1837$ and $V_d^0/v_e = 0.55$. (a) V_{gz}/v_i vs L_c/L_s; (b) V_{gy}/v_i vs L_c/L_s.

allel wave vector at the origin k_z, and other parameters characterizing the system. For evaluating the group velocities V_{gz} and V_{gy} we take the derivatives of the real part of the eigenfrequency ω_r, with respect to k_z and k_y, respectively, i.e., $V_{gz} = \Delta\omega_r/\Delta k_z$ and $V_{gy} = \Delta\omega_r/\Delta k_y$. In the x direction the wave energy is confined to the vicinity of $\xi_1 = x_1/L_c$.

Figure 1(a) shows the parallel group velocity normalized by the ion thermal velocity v_i versus the ratio of the current channel size L_c and the magnetic shear length L_s for three different values of L_s. Here $b = 0.6$, $\tau = 0.5$, $\mu = 1837$ and $V_d^0/v_e = 0.28$. In order to evaluate the value of $(k_y\lambda_i)^2$ we have used the parameters of Ashour-Abdulla and Thorne,[9] i.e., $n_0 \sim 10 \text{ cm}^{-3}$, $B_0 \sim 0.06$ G, and $T_i \sim 2$ eV. For the first harmonic $(k_y\lambda_i)^2 \sim 0.01$, and that term in Eq. (5) contributes negligibly. The most interesting result of Fig. 1(a) is that in the limit $L_c \to \infty$, $V_{gz} \to 0$. One finds that as L_c is increased beyond L_s, V_{gz} approaches zero as $(L_s/L_c)^2$. Further, when L_c is made smaller than $10^{-2} L_s$ the value of V_{gz} attains its local value (i.e., the value predicted by local theories[1,6]) and stabilizes at that value. However, when L_c is further reduced such that $L_c < \rho_i$, V_{gz} once again decreases.

Figure 1(b) is a plot of V_{gy} vs L_c/L_s for the parameters of Fig. 1(a). Here too we find a reduction in V_{gy} in the shear dominated regime (i.e., $L_c \gtrsim L_s$) much in the same fashion as the temporal growth rate.[4] However, the difference between the local and the nonlocal values of V_{gy} is not as striking as

that of V_{gz}. As noted by Ashour-Abdulla and Thorne,[9] V_{gy} for the CDICI near the dominant normal mode [which occurs for $b \sim O(1)$] is extremely small; and combined with our results that $V_{gz} \to 0$ in the nonlocal regime the CDICI becomes, effectively, an absolute instability. For $L_c < \rho_i$, V_{gy} becomes negative. Figures 2(a) and 2(b) have plots similar to Figs. 1(a) and 1(b) for the second harmonic. Here we use $\tau = 1$, $V_d^0/v_e = 0.55$, and $b = 2.4$. The value of b for all the calculations corresponds to the maximum temporal growth
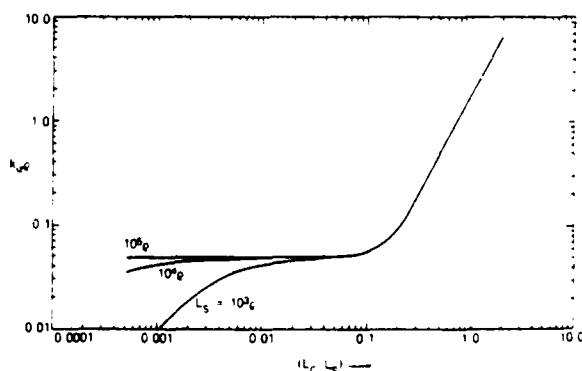

FIG. 3. A plot of the convective growth rate normalized by the ion Larmor radius k_{iz}/ρ, vs L_c/L_s, for the first harmonic. The other parameters are identical to Fig. 1(a).

B-4

rate. We see trends similar to Figs. 1(a) and 1(b) for the higher harmonic also.

In Fig. 3 we plot the convective growth rate $k_{iz} = \gamma / V_{gz}$ normalized by the mean ion Larmor radius versus L_c / L_s. We see two distinct regions joined smoothly. For very small L_c/L_s (i.e., $L_c/L_s \lesssim 10^{-3}$), $k_{iz} \rho_i < 0$ which indicates spatially damped waves. When L_c/L_s is increased the curves attain a plateau which corresponds to the local theory. Here we find a finite $k_{iz} \rho_i$ and, hence, a finite region in which the wave amplitude can be amplified by one e-fold. For $L_c \gtrsim L_s$, $k_{iz} \rho_i$ grows without bound, implying that the wave amplitude can e-fold in an insignificantly small region. (Recall that the system is assumed to be infinite and uniform in the y direction, hence, convection in this direction is ignorable.) Thus the character of CDICI is changed from *convective* to *absolute*.

We have so far considered only one species of ions characterized by a temperature T_i. In order to make the system more realistic, especially for space applications, we added a second ion species characterized by a hotter temperature but still with a Maxwellian distribution. The general features of the group velocity behavior is still the same as in a single ion species. A more detailed parametric study of the nonlocal convective aspects of CDICI with a loss cone distribution for the hotter ion species, along with the magnetospheric application will be presented elsewhere.

III. DISCUSSION

Thus, in contrast to local theory, nonlocal theory gives zero group velocity for the CDICI along the average exter-

nal magnetic field direction in the limit $L_c > L_s$. Clearly the ratio L_c/L_s is the important parameter and its magnitude must be well established before making definitive conclusions regarding the electrostatic CDICI. Depending on the value of L_c/L_s, the CDICI can be classified into three main regimes:

(i) $L_c \gtrsim 0.1\ L_s$. This regime is purely nonlocal with a temporal growth rate much reduced from its local value. Also the instability is absolute or only very weakly convective in the z direction which is the direction of the average external magnetic field and the current flow. There is no energy flow in the x direction, and energy flow in the y direction is ignorable if $\partial/\partial y \equiv 0$.

(ii) $L_c < 0.01\ L_s$. In this regime, nonlocal theory reproduces the results of local theory, and the instability becomes convective in the z direction with a convective, as well as a temporal growth rate, equal to the ones given by the local theory. There is a smooth transition between regimes (i) and (ii) as is evident in all the figures.

(iii) $L_c \sim \rho_i < L_s$. The finite channel width becomes important. There is once again a reduction in the temporal growth rate (filamental quenching[4]) but the instability remains convective, i.e., V_{gz} remains nonzero. However, when L_c is further reduced so that $L_c < \rho_i$, both V_{gz} and V_{gy} become reduced and eventually become negative.

Physically, the reason for vanishing parallel group velocity can be described as follows. Figure 4 shows the angle space where the imaginary part of the local dispersion relation $D_l < 0$, and the growth rate is positive for the CDICI. The extent of this unstable angular space Δu for the CDICI
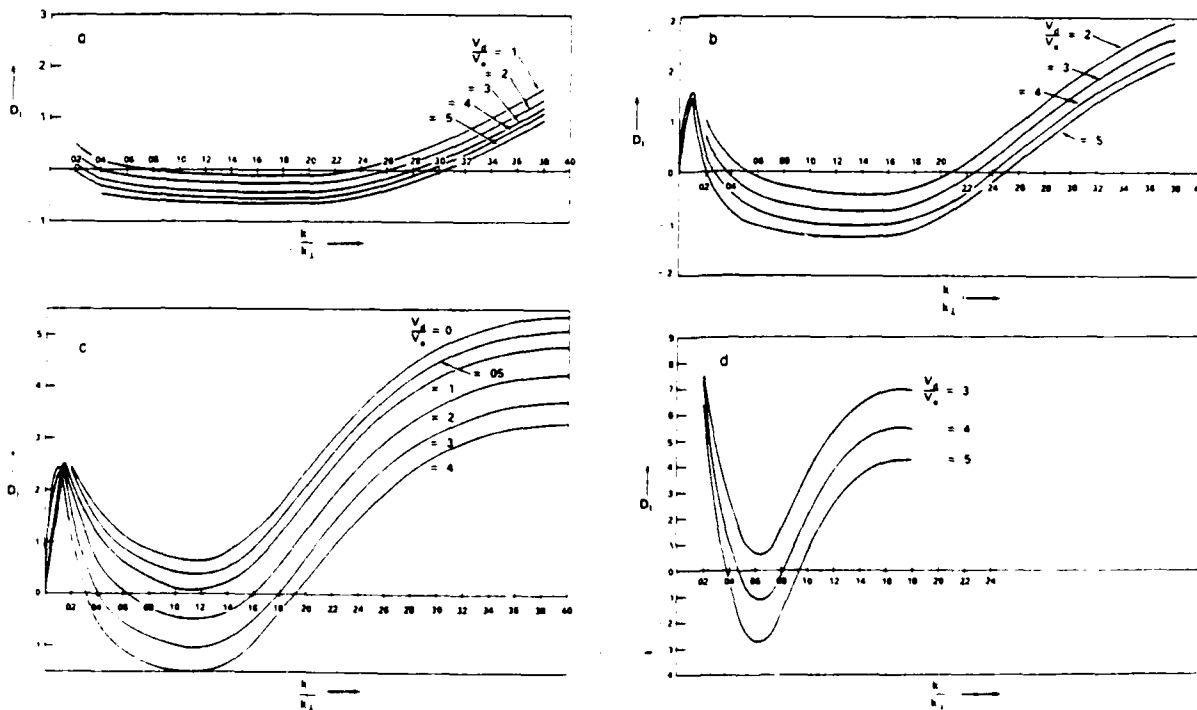

FIG 4 A plot of imaginary part of the local dispersion relation $D_l(\omega, k)$ vs $k_z/k_\perp$ (reproduced from Ref 2) for various V_d/V_e. Here $b = 0.5$, $u = 36^{-4}$ and four different values of the temperature ratio τ are (a) $\tau = 0.1$, (b) $\tau = 0.2$, (c) $\tau = 0.33$, and (d) $\tau = 1.0$.

in our parameter range is about 0.1. In the nonlocal theory, a wave packet is formed whose size is governed by the smaller of the two scale lengths L_c and $0.1 L_s$. When $L_c < 0.1 L_s$, the drift velocity $V_d(x)$ varies sufficiently fast as a function of x, or as a function of the angle u within the space Δu, so as to form an effective Q_1 curve which has the form of a steep well. The position of the bottom of this well is at $u_0 = k_z / k_y$; thus different choices of k_z center the well in different parts of the region Δu, and the corresponding wave packets (of size $\sqrt{\rho_i L_c}$) sample different regions of Δu which lead to different growth rates γ as well as different real frequencies ω_r. On the other hand, when $L_c > L_s$, the variation of $V_d(x)$ in the domain Δu is rather weak, and the effective Q_1 curve is governed by the variation of u rather than that of V_d in Eq. (3). Now, if we choose different k_z, an appropriate translation in x (i.e., moving away from the center of the slab) is sufficient to provide almost the same invariant Q_1 curve as a function of u. The resulting wave packet (of size $\sqrt{\rho_i L_s}$) forms at the same position in u space (even though we choose different k_z) and has the same growth rate γ and real frequency ω_r, independent of k_z. This makes the group velocity $\partial \omega_r / \partial k_z$ vanish in the limit $L_c \to \infty$.

IV. CONCLUSION

We have shown in this paper that the nonlocal effects due to the magnetic shear (produced by a field aligned current) and a finite channel current width can drastically alter the character of the electrostatic CDICI by making the instability effectively absolute in the z direction. The important parameter turns out to be the ratio of the two scale lengths involved in the problem L_c and L_s. Depending on the value of L_c / L_s, one can classify the CDICI in three regimes as described earlier, and a careful assessment of the value of L_c / L_s for a given physical situation becomes essential to draw any definitive conclusion regarding the growth and convective characteristics of the electrostatic CDICI. We would also like to note that the nonlocal effects due to magnetic shear can be expected to produce corresponding phenomena, including the vanishing of the parallel group velocity, in various other current-driven instabilities as well.

[1] W. E. Drummond and M. N. Rosenbluth, Phys. Fluids 5, 1507 (1962).
[2] G. Ganguli and P. Bakshi, Phys. Fluids 25, 1830 (1982).
[3] G. Ganguli, Ph.D thesis, Boston College, Chestnut Hill, MA, 1980.
[4] P. Bakshi, G. Ganguli, and P. Palmadesso, Phys. Fluids 26, 1808 (1983).
[5] G. Ganguli, P. Bakshi, and P. Palmadesso, J. Geophys. Res. 89, 945 (1984).
[6] J. M. Kindel and C. F. Kennel, J. Geophys. Res. 76, 3055 (1971).
[7] M. Ashour-Abdalla and C. F. Kennel, J. Geophys. Res. 83, 1531 (1978); C. F. Kennel and M. Ashour-Abdalla, Magnetospheric Plasma Physics (Reidel, Hingham, 1982), p. 245.
[8] R. N. Sudan, Phys. Fluids 8, 1899 (1965).
[9] M. Ashour-Abdalla and R. M. Thorne, J. Geophys. Res. 83, 4755 (1978).

2042   Phys. Fluids, Vol. 27, No. 8, August 1984   Ganguli, Bakshi, and Palmadesso   2042

B-6

APPENDIX C

Two Dimensional Nonlocal Formalism for
Electrostatic Waves in the Magnetosphere

TWO DIMENSIONAL NONLOCAL FORMALISM
FOR ELECTROSTATIC WAVES IN THE MAGNETOSPHERE

by

G. Ganguli, Y.C. Lee*, Science Applications, Inc., McLean, VA 22102 USA,

and P. Palmadesso, Naval Research Laboratory, Washington, D.C. 20375, USA

Abstract

We develop a two space scale nonlocal formalism which includes the strong inhomogeneities across and a weaker inhomogeneity along the external magnetic field. We apply this formalism to the current driven ion cyclotron instability.

Introduction

The current driven ion cyclotron instability (CDICI) has been of much importance to both space and laboratory plasmas. CDICI has been studied in connection with several phenomena relevant to the physics of ionosphere-magnetosphere coupling. In order to understand the influence of the CDICI in ionosphere-magnetosphere coupling one needs to understand its propagation and stability properties under conditions expected in the magnetospheric environment. Specifically, the effects of the ambient spatial inhomogeneities neglected in the widely used local theory should be considered. Significant departures from the local theory results in both the stability and the convective properties have been found by the use of a nonlocal theory taking into account the magnetic shear caused by the field aligned currents and the finiteness of the current channel.[1] Implications of these nonlocal effects on CDICI related observations in space have been discussed.[2]

In earlier works[1,2] only the stronger non-uniformities across the external magnetic field (assumed in the z direction) were considered. Both y and z directions were kept uniform. However, a true representation of the magnetospheric magnetic field in the auroral zone must include a weaker variation along the external magnetic field together with the stronger variations across. Thus we develop a more general two space scale nonlocal formalism for electrostatic waves taking into account a strong inhomogeneity across and a weak inhomogeneity along the external magnetic field.

Theory

The one dimensional nonlocal dispersion differential equation obtained earlier[1] is given by,

$$\left[\left(\frac{\rho_i}{L_c}\right)^2 \frac{\partial^2}{\partial \xi^2} + Q(\omega_o, u(\xi), V_d(\xi))\right]\phi(\xi) = 0 \qquad (1)$$

where,

$$G = -\frac{\omega_1}{\gamma^2}$$

and other standard symbols are defined in Ref. 1.

We now introduce a mild inhomogeneity in B_z along the z direction. As a result of this we can no longer Fourier transform in the z direction. Thus $u(\xi)$ becomes an operator ... and the electron drift acquires ... The "potential" G becomes ...

where $\bar{z} = z/L_z$, L_z is the scale length of the variation in the z direction and ... The exact nature of the z

dependence is constrained by the equilibrium conditions, and Maxwell's equations. For simplicity, we assume the pressure to be constant along the z direction. This simplification can be removed. The new differential equation for the system is:

... Consistent with this assumption and ... Maxwell's equation we ...

$$V_z(\xi,\bar{z}) = ...$$

Equation ... velocities ... to be of the form,

$$\phi(\xi,\bar{z}) = \frac{1}{2}\pi_k \bar{\phi} \, \phi_k(\xi) ...$$

Here k is the ... be ..., and the ... dropped. $\phi_k(\xi)$ is the ... parameter. Eliminating ... we get,

$$[\hat{G}(\omega_o, \bar{z}) - ...] ...$$

Since the variation in z is weak and ... $\phi = ...$ and a ... Also ... $Q = \omega_o u(\xi,\bar{z})$, etc., we rewrite ...

$$[\omega_1 Q_o - ...] ...$$

where the subscripts on ... fourth partial derivatives evaluated at ω_o and ... Now multiplying (5) by ... complex conjugate of ... and integrating over ... we obtain a differential equation for ...,

$$\frac{d^2}{d\bar{z}^2} + A \, \bar{z}(\bar{z}) \, a(\bar{z}) = 0 \qquad (6)$$

where,

$$\bar{z} = ...$$

and,

$$A = ...$$

$$B = ...$$

$$C(\bar{z}) = ...$$

$$C_1 = ...$$

$$C_2 = ...$$

Expanding ... around ..., we convert (6) into a wave equation which yields a dispersion relation for the complex frequency shift ...

Conclusions

Initially we considered a linear model for $E_y(z)$, $B_y(z)$ ... This will transform into ... in x and z ... stabilizing influence on the ... Details of the calculations and the plot of the growth rate ... parameters will be shown.

References

1. G. Ganguli, P. Palmadesso and Y.C. Lee, Geophys. Res. Lett. 1985 ... G. Ganguli and P. Palmadesso, Phys. Fluids 29, 1986 ...

2. E. Carlson, P. Palmadesso and P. Satyanarayana, Geophys. Res. Lett. 13, 945, 1986.

*Permanent address: University of Maryland, College Park, MD 20742.

APPENDIX D

The Role of Nonlocalities in Magnetosphere-Ionosphere

Coupling Processes

THE ROLE OF NONLOCALITIES IN MAGNETOSPHERE-IONOSPHERE COUPLING PROCESSES

G. Ganguli[*] and P. Palmadesso[**]

[*]Science Applications, Inc., McLean, Va. 22012 U.S.A., [**]Naval Research Laboratory, Code 4780, Washington, D.C. 20375, U.S.A.

ABSTRACT

Microinstabilities are believed to play a crucial role in the physics of Magnetosphere-Ionosphere coupling. The current driven ion cyclotron instability is a very important microinstability in this respect. We give a nonlocal formalism for studying the ion cyclotron instability in a more realistic magnetospheric environment than is available in the widely used local theory. This formalism includes the magnetic shear produced self-consistently by the field aligned currents and the finite extent of such currents. Significant departures from the local theory are noted.

INTRODUCTION

The current Driven Ion Cyclotron Instability (CDICI) has been of considerable interest to both space and laboratory plasmas. Drummond and Rosenbluth /1/ have shown that a uniform, low β, collisionless plasma immersed in a uniform magnetic field is unstable to the CDICI. This instability has been extensively studied in connection with several phenomena relevant to the physics of Magnetosphere-Ionosphere (M-I) coupling. For example, CDICI is believed to play a role in the evolution of the topside ionospheric ion temperature profiles /2/, transverse acceleration of O^+ ions (stochastic acceleration and ion conics) and anomalous resistivity on auroral field lines. In view of this importance, Kindel and Kennel /3/ undertook an indepth linear analysis of the CDICI pertinent to the magnetospheric plasmas. Ever since, this study of CDICI has been widely used in the context of the magnetospheric plasmas.

Most of the plasmas of interest (especially in the magnetosphere) are characterized by inhomogeneities; for example, non-uniform density, temperature and magnetic field, finiteness in the current channel width and the magnetic shear generated self-consistently by the field aligned currents. These inhomogeneities preclude the use of a local theory such as the one used in references 1 and 3. The local approach is only an approximation, which may be good for some types of inhomogeneities under proper restrictions, but is not valid in general. In order to understand the stability and the propagation characteristics of CDICI in a realistic magnetospheric environment we have developed a non-local formalism for the electrostatic waves. We study the influence of the magnetic shear generated by the field aligned currents /4/ and the finiteness of the current channel /5/ on the mode structure of the CDICI. The results from the nonlocal study show significant modifications to the conclusions of Kindel and Kennel and thereby affect the physics of the M-I coupling. In this paper we briefly describe the essential features of the nonlocal formalism and discuss the significant implications to the magnetospheric plasmas.

THEORY

(a) *Local*

Drummond and Rosenbluth /1/ considered a slab model with the magnetic field B_o in the z direction. Assuming plane wave nature for the electrostatic perturbation $\phi(r, \omega) \sim \exp[ik \cdot r - i\omega t]$, they solved the Vlasov-Poisson system of equations to arrive at a dispersion relation for the electrostatic CDICI. This dispersion relation can be cast in the following form:

$$D(\omega,k) = k^2 + \sum_{\alpha,n} \frac{\Gamma_n(b_\alpha)}{\lambda_\alpha^2}\left[1 + \zeta_\alpha \, Z(\zeta_\alpha)\right] = 0, \qquad (1)$$

where α denotes the species, k is the wave vector, v_α is the thermal velocity, Ω_α is the gyrofrequency, the relative drift is $V_{d\alpha}$ in the z direction, λ_α is the Debye length, $b_\alpha = k_\perp^2 \rho_\alpha^2/2$, $\Gamma_n(b) = I_n(b)e^{-b}$ and $I_n(b)$ is the modified Bessel's function. $Z(\zeta)$ is the plasma dispersion function and $\zeta_\alpha = (\omega - n\Omega_n - k_\parallel V_{d\alpha})^{1/2}/k_\parallel v_\alpha$. For a given wave vector k and other parameters, (1) can be solved for the allowed frequency ω.

(b) *Nonlocal (Magnetic Shear)*

Ganguli and Bakshi /4/ studied the effects of the magnetic shear produced by the field aligned currents neglected in /1/. They consider a uniform drift of electrons with respect to the ions in the z direction that produces a y component of the magnetic field $B_y(x) = B_o x/L_s$ ($L_s = cB_o/4\pi n_o eV_d$; the characteristic length associated with the magnetic shear) which is linear in x. Magnetic shear changes the mode structure in three main ways /5/; (1) *Local effect* $k_\parallel \rightarrow k_\parallel(x) = k_\parallel^o + k_y x/L_s$; i.e. the parallel wave vector is x dependent, (2) *Global effect* $ik \rightarrow \partial/\partial x$ giving localized wave packets in the x direction, and (3) *Orbital effect* $k_\parallel(x) \rightarrow k_\parallel(x_g)$, $x_g = x + v_y/\Omega$. Shear changes the particle orbits and introduces the Shear Kinematic Drift /5/. For small shears the orbital effects are weak /5/ and will be neglected. The new dispersion relation in general is given by,

$$D\left[\omega, k_y, -i\frac{\partial}{\partial x}, k_{||}(x)\right]\phi(x) = 0 \tag{2}$$

An exact solution of (2) is a formidable task. Further, for weak shears (2) can be well approximated by a second order differential equation given by,

$$\left[-\left(\frac{\rho_i}{L_s}\right)^2 Q_{1b}\frac{\partial^2}{\partial u^2} + Q_1(\omega, u)\right]\phi(u) = 0, \quad Q_{1b} = \frac{\partial}{\partial b}Q_1. \tag{3}$$

and $u(= x/L_s)$ is the angle of propagation $k_{||}/k_y$. In the limit $L_s \to \infty$ we recover the local theory [1]

(c) *Nonlocal* (Magnetic shear and finite current channel width)

So far the parallel current $J_{||}(= n_e e V_d)$ has been considered uniform in space. This, of course, is an idealization. Field aligned currents in the magnetosphere and in the laboratory experiments always have finite extents. Bakshi, et al. [6] introduced a finite current channel by choosing an x dependent drift i.e. $V_d = V_d(x) = V_d^0 \exp(-x/L_c)^2$, where L_c is the width of the current channel in the x direction while in the y and z directions the drift is still uniform. Note that $k_{||}(x)$ is no longer linear in x;

$$k_{||}(x) = k_{||}^0 + k_y\frac{L_c}{L_s}\int_o^\xi d\xi e^{-\xi^2}, \quad \xi = x/L_c^2.$$

Now there are two length scales L_c and L_s, and the new differential equation is [6],

$$\left[\left(\frac{\rho_i}{L_c}\right)^2\frac{d^2}{d\xi^2} + Q[u(\xi), V_d(\xi)]\right]\phi(\xi) = 0. \tag{4}$$

RESULTS AND DISCUSSIONS

Figure (1) is a plot of the nonlocal growth rates γ/Ω_i as obtained from equation (3) against b for various values of shear and $\tau = T_i/T_e = 0.5$, $\mu = m_i/m_e = 1837$ and $V_d/v_e = 0.25$. As compared to the local growth rate (the top curve) there is a large reduction in the growth rate even for extremely weak shear. This large reduction is due to the intrinsic difference in the boundary condition, giving rise to a localized wave pocket in the nonlocal theory. For stronger shears there is additional reduction in γ/Ω_i. Further, the range of unstable k_y is narrowed, enhancing the coherence of CDICI when observed from a moving frame such as a satellite.
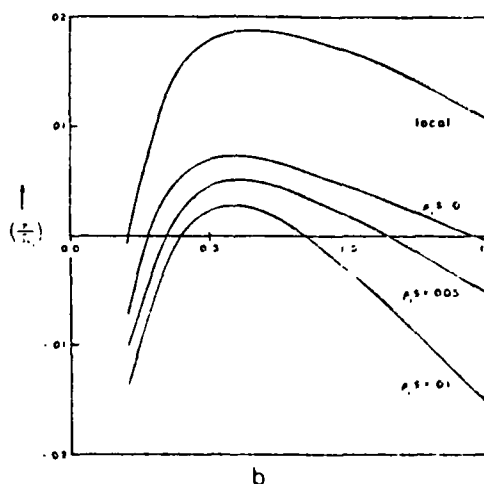
Fig 1. A plot of γ/Ω_i against b for various shear values. Here $\tau = 0.5$, $\mu = 1837$, $V_d/v_e = 0.25$. Equation (3) has been solved for this figure.

Figure (1) assumes a uniform V_d and therefore a uniform shear prevails over a large enough region of space. Figure (2) shows the important modifications to Figure (1) due to the introduction of a finite width of the current channel. Here $\tau = 0.5$, $\mu = 1837$ and $V_d^0/v_e = 0.28$. The dotted lines show the transition from local to nonlocal values as L_c approaches L_s. Figure (3) is a plot of γ/Ω_i against L_c/L_s. Here we see that for weak shears ($L_s \sim 10^5\rho_i$) when $L_c = 10^{-2}L_s$, our nonlocal theory given by equation (4) can reproduce the local theory values. For $L_c > 0.1 L_s$, it can reproduce the nonlocal results of the uniform drift approximation. However, for stronger shear ($L_s \sim 10^3\rho_i$) the local theory is not quite recovered. Irrespective of the shear strength, if L_c is made smaller ($L_c \leq 10\rho_i$) there is a new type of damping, filamental quenching [6], which can totally suppress the instability for sufficiently small L_c. This fact has been verified in a number of laboratory experiments [7]

Clearly the nonlocalities produced by the magnetic shear and the finite current channels can significantly modify the normal mode properties of the CDICI. However, CDICI is a convective instability and hence the convective growth rate
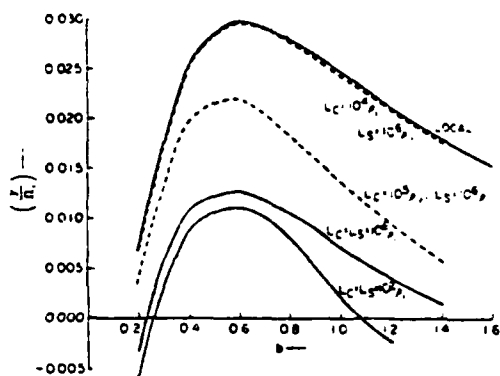
Fig. 2. A plot similar to Figure 1. Here $V_d/v_e = 0.28$ and equation (4) has been solved. This figure shows how finite current width L_c modifies the results of figure 1.
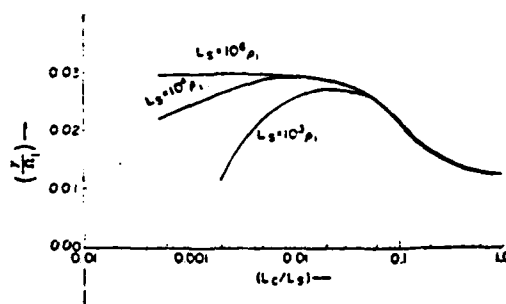
Fig. 3. Here γ/Ω is plotted against L_c/L_s. Parameters are same as Figure (2) and $b = 0.6$ is held constant.
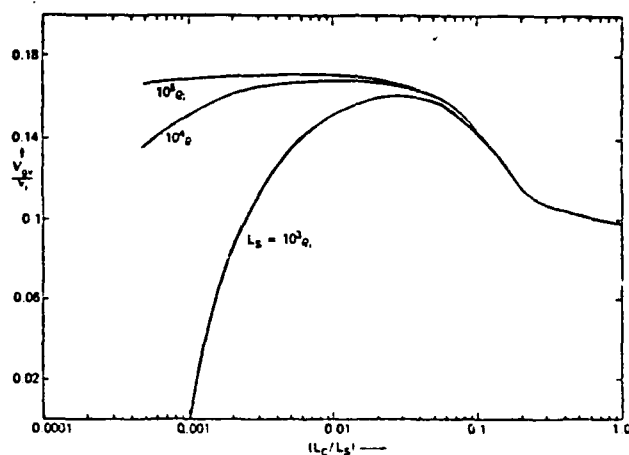
Fig. 4. Plot of V_g against L_c/L_s for the parameter range of figure 3
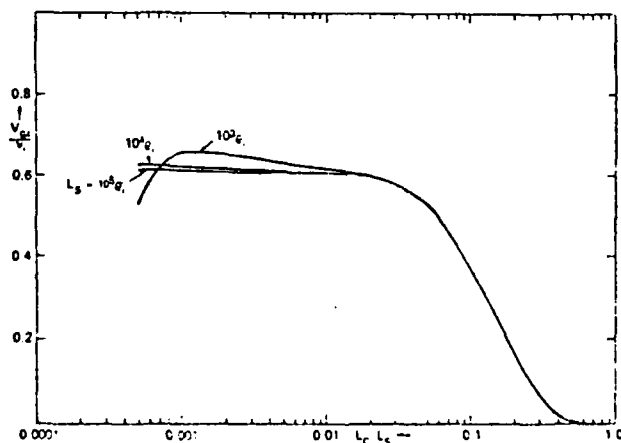
Fig. 5 A plot similar to figure 4 for V_g

$k_i = \gamma/V_g$, where V_g is the group velocity, is of much importance /5/. Thus it is important to investigate the effects, if any, of the nonlocalities described above on the convective properties of CDICI. Because k_i is dependent on the temporal growth rate γ, obviously there will be some modification since $\gamma_{NL} < \gamma_L$. However, the convective character of CDICI can change in a more subtle way if V_g is affected by the nolocalities. This aspect was recently investigated by Ganguli, et al. /9/ and the results are given in figures 4 and 5.

D-5

Figure 4 is a plot of the group velocity in the y direction V_{gy} as a function of L_c/L_s for $b \sim 0.6$, $\tau \sim 0.5$, $\mu \sim 1837$ and $V_d^2/v_e \sim 0.28$. For $L_s \sim 10^5 \rho$, we see that when $L_c/L_s \sim 10^{-2}$ our theory gives the same value of V_{gy} as expected from a local theory, but when $L_c/L_s \geq 0.1$ the value of V_{gy} is reduced. For smaller L_c, particularly when the shear is stronger ($L_s 10^3 \rho_i$), V_{gy} is reduced and becomes negative, implying a reversal in the direction of flow. Figure 5 is a plot of V_{gz} against L_c/L_s for the same parameters as figure 4. There is a significant change in the convective pattern in the z direction which is the direction of the average magnetic field and the current flow. For L_c/L_s, V_{gz} becomes negligibly small and approaches zero as $(L_s/L_c)^2$. Thus the convective growth rate $k_c \sim \gamma/V_{gz}$ becomes very large implying that the instability has become absolute in the z direction. This important modification in the basic nature of the instability is purely a nonlocal effect and is not obtainable by using a local theory.

CONCLUSIONS

Various implications of the nonlocal theory to the magnetospheric plasmas have been discussed by Ganguli, et al. /10/ In contrast to the local theory we can classify CDICI into three regions based on our nonlocal formalism: (1) $L_s < 0.1 \ L_s$: This is the shear dominated region /4/ characterized by a nonlocal growth rate much reduced from the local growth rate. The group velocity in the x direction is zero since we have a stationary wave packet, V_{gy} is reduced from its local value and $V_{gz} \approx 0$. Thus shear stabilizes CDICI by reducing the temporal growth but makes it more explosive by reducing V_{gy} and by making $V_{gz} = 0$. (2) $\rho_i \ll L_c \ll L_s$: In this limit the use of the local theory /1, 3/ is justified. (3) $L_c \sim \rho_i \ll L_s$: There is a new type of damping, *Filamental quenching*, implying that narrow arcs are stable. The instability remains convective but the values of the group velocities are different from the local values. For $L_s \sim \rho_i$ both V_{gy} and V_{gz} change sign. Thus, the local theory can not be applied without reservation. The important parameter is the ratio of the two scale lengths L_c and L_s. Depending on the value of L_c/L_s the instability falls into one of the three regions described above.

We would like to note that while our nonlocal formalism provides a more realistic representation of the magnetospheric environment than previously available, it is still far from reality. In particular the important variations along the external magnetic field can play a very important role. Recently Ganguli, et al. /11/ have developed a two dimensional nonlocal formalism for very weak inhomogeneities in the direction of the external magnetic field along with stronger inhomogeneities (described earlier) across the field. This theory needs to be improved by using integrodifferential equation methods to include more realistic variations. These are the current and future focus of our research.

ACKNOWLEDGMENT

REFERENCES

1.   W. E. Drummond and M. N. Rosenbluth, *Phys. Fluids* 5, 1507 (1962).

2.   P. J. Palmadesso, T. P. Coffey, S. L. Ossakow and K. Papadopoulos, *Geophys. Res. Lett.* 1, 105 (1974).

3.   J. M. Kindel and C. F. Kennel, *J. Geophys. Res.* 76, 3055 (1971).

4.   G. Ganguli and P. Bakshi, *Phys. Fluids* 25, 1830 (1982).

5   G. Ganguli, Ph. D. Thesis, Boston College, Chestnut Hill, Mass (1980).

6   P. Bakshi, G. Ganguli and P. Palmadesso, *Phys. Fluids*. 26, 1803 (1983).

7.   R. L. Merlino, Private Communication (1984): S. L. Cartier, N. D'Angelo, P. H. Krumm and R. L. Merlino, *Phys. Fluids*, (to appear), (1984).

8   M. Ashour-Abdalla and R. M. Thorne, *J. Geophys. Res* 83, 4755 (1978)

9   G. Ganguli, P. Bakshi and P. Palmadesso, *Phys. Fluids*, 27, 2039 (1934).

10   G. Ganguli, P. Bakshi and P. Palmadesso, *J. Geophys. Res* 89, 945 (1984).

11   G. Ganguli, Y. C. Lee and P. Palmadesso, in: International Conference in Plasma Physics, Lausanne (1984).

APPENDIX E

O$^+$ Acceleration Due to Resistive Momentum
Transfer in the Auroral Field Line Plasma

E-2

O⁺ Acceleration Due to Resistive Momentum Transfer in the Auroral Field Line Plasma

H. G. MITCHELL, JR.[1]

Science Applications. Inc.. McLean. Virginia

P. J. PALMADESSO

Geophysical and Plasma Dynamics Branch. Plasma Physics Division. Naval Research Laboratory. Washington. D C

Low-frequency electric fields maintained in a plasma by resistivity (either collisional or wave induced) imply a balance between the momentum transferred to the electrons by the electric field and that transferred by the resistivity from the electrons to other particle species. As a result, the electrons do not experience a net acceleration due to the electric field. If the plasma contains only one ion species, the momentum balance is the same for the ions, and the ion species is not accelerated either. If a second ion species is present which does not participate in the resistive momentum transfer, it may be accelerated by the electric field while the participating ions experience an acceleration opposite to the field This mechanism may be applied to the auroral field line plasma in the presence of a current along the magnetic field. Significant resistivity between the electrons and the hydrogen ions may accelerate the oxygen ions provided that the resistivity has the appropriate characteristics We have used an existing auroral field line plasma simulation to dynamically model this effect. This simulation is a one-dimensional multimoment dynamic model of a three-species plasma (e⁻, H⁺, and O⁺) along about 10 R_E of field line above an altitude of 800 km.

INTRODUCTION

The discovery of intense upward fluxes of energetic ions along high-latitude auroral field lines by the S3-3 satellite [Shelley et al., 1976] indicates that parallel acceleration mechanisms in this region allow the ionosphere to act as a source region for energetic magnetospheric ions. Horwitz [1982] has provided an extensive review of the work done on this concept in recent years A statistical survey of the upflowing ion fluxes performed by Gorney et al. [1981] revealed that these fluxes are of two types: ion conics and ion beams. Ion conics have a peak flux at an angle to the magnetic field direction and are most likely composed of ionospheric ions that have been heated transversely to the field at altitudes of 1000–2000 km and subsequently accelerated upward by the mirror force due to the magnetic field gradient [Klumpar, 1979]. An ion beam has a peak flux which is too field aligned to have resulted from a transversely heated ionospheric distribution and probably results from acceleration due to a quasi-static parallel electric field such as those associated with inverted V electron events. The extensive observations and theories concerning these electric fields have been reviewed by Shawhan et al. [1978] and Stern [1979], among others, and the occurrence frequencies for ion beams as a function of altitude, invariant latitude, and magnetic activity are consistent with the parallel electric field interpretation [Gorney et al., 1981]

Polar wind theory [Banks and Holzer, 1968] in the absence of a strong electric field predicts an upward flux of cold ionospheric H⁺ of around 10^8 cm⁻² s⁻¹ at 1000 km altitude on auroral field lines. This flux is sustained by the small plasma pressure at the magnetospheric end of the field line and the ambipolar electric field due to the small-scale height of the

[1] Permanent address. Naval Research Laboratory. Washington. D C

major ion (O⁺) at the ionospheric end of the field line. The O⁺ escape flux in this theory is strongly limited by gravity and has a magnitude of less than 10^{-3} that of H⁺. Recent observational evidence from the S3-3 satellite [Collin et al., 1981] and Dynamics Explorer 1 [Shelley et al., 1982] indicates, however, that not only are the upward ion fluxes much more energetic than predicted by polar wind theory but the major energetic ion flux is often O⁺ rather than H⁺ The presence of a strong parallel electric field along the field line could create the necessary energization of the upflowing ions. but it seems that such a field would energize all ion species equally. Some process is necessary, therefore. to preferentially accelerate O⁺ parallel to the magnetic field. Recent work by Moore [1980] suggests that the balance between the H⁺ and O⁺ fluxes can be altered by an acceleration mechanism in the low-altitude region where ion-neutral charge exchange reactions are important. In this paper we would like to suggest that there is a natural way in which the preferential parallel acceleration of an O⁺ beam might arise from a quasi-static parallel electric field if that electric field is sustained by some form of anomalous resistivity rather than by discontinuous structures such as electrostatic shocks or double layers We will also illustrate this mechanism by means of a numerical simulation we have developed of the auroral field line plasma

THEORY

Given a three-species plasma (e⁻, H⁺, and O⁺), suppose that there exists a mechanism for providing an anomalous friction between the electrons and the hydrogen ions By the application of an electric potential along one direction. say the x direction. the species' momentum equations for this direction. simplified in order to clarify the physics of interest here. may be written

$$\frac{\partial}{\partial t}(n_e m_e v_{ex}) = -e n_e E_x + n_e m_e v_{eH}^*(v_{Hx} - v_{ex}) \qquad (1)$$

$$\frac{\partial}{\partial t}(n_H m_H v_{Hx}) = e n_H E_x - n_H m_H v_{He}^*(v_{ex} - v_{Hx}) \qquad (2)$$

$$\frac{\partial}{\partial t}(n_O m_O v_{Ox}) = e n_O E_x \qquad (3)$$

where n_s, m_s, and v_{sx} are the number density, mass, and velocity in the x direction for species s. E_x is the electric field in the x direction; e is the electric charge; and v_{st}^* is the effective collision frequency for anomalous momentum transfer from species t to species s. These three equations may each be multiplied by the respective species' charge to mass ratio and then summed to yield an equation for the total current density J

$$\frac{\partial J}{\partial t} = \left(\frac{n_e}{m_e} - \frac{n_H}{m_H} - \frac{n_O}{m_O}\right)e^2 E_x + e(n_H v_{He}^* - n_e v_{eH}^*)(v_{ex} - v_{Hx}) \qquad (4)$$

If it is assumed that the electric field is quasi-static so that Alfvén fluctuations are ignored, the left-hand side of (4) can be neglected. Further, momentum is conserved in the anomalous momentum transfer process, so $n_e m_e v_{eH}^* = n_H m_H v_{He}^*$. Therefore the electric field is determined by the condition that the two terms on the right-hand side of (4) must balance. i.e.. that (neglecting terms of order m_e, m_H and m_e, m_O)

$$E_x = (m_e v_{eH}^*/e)(v_{Hx} - v_{ex}) \qquad (5)$$

This equation simply represents the fact that for a quasi-static electric field supported by a large-scale anomalous friction (rather than a small-scale charge separation), the electron momentum gained because of the electric field must balance, up to order m_e, m_s, the electron momentum lost to the other species because of the friction.

With the electric field determined by (5), the ion momentum equations may now be rewritten as

$$\frac{\partial}{\partial t}(n_H m_H v_{Hx}) = e n_H E_x - e n_e E_x = -e n_O E_x \qquad (6)$$

$$\frac{\partial}{\partial t}(n_O m_O v_{Ox}) = e n_O E_{Hx} - e n_H E_{Ox} \qquad (9)$$

where charge neutrality has been used in (6) to set $n_e = n_H + n_O$. The result is that momentum is gained by the oxygen ions from the electric field, while the hydrogen ions lose the same amount because of an imbalance between the momentum gained because of the electric field and the momentum lost because of friction. This effect can be seen to have a rather general application. If it is possible to view the hydrogen ions as consisting of two populations, one participating in the friction and one not, then the one not participating would also gain momentum from the electric field at the expense of the participating population. As a result, an observation of the ion fluxes would indicate the presence of both O^+ and H^+ fluxes which had been energized by the electric field, but the relative magnitude of the fluxes would have been altered from the preaccelerated value. Further, if the electrons experience a friction with both H^+ and O^+, then the ion momentum equations take the form

$$\frac{\partial}{\partial t}(n_H m_H v_{Hx}) = e n_H E_{Ox} - e n_O E_{Hx} \qquad (8)$$

$$\frac{\partial}{\partial t}(n_O m_O v_{Ox}) = e n_O E_{Hx} - e n_H E_{Ox} \qquad (9)$$

where E_{sx} is the electric field due to the friction between the electrons and ion species s, given by

$$E_{sx} = (m_e v_{es}^*/e)(v_{sx} - v_{ex}) \qquad (10)$$

and the total electric field is $E_x = E_{Hx} + E_{Ox}$. The net effect in this case depends strongly on the relative magnitudes of the two electron-ion resistivities and the ion densities.

SIMULATION

The model used to simulate this ion acceleration effect has been described previously [Mitchell and Palmadesso, 1983]. It is a dynamic one-dimensional, three-species (e^-, H^+, and O^+) model of the auroral field line plasma extending from an altitude of 800 km in the topside ionosphere out to $10\ R_E$ along the field line. Each species is characterized by five dynamic quantities: number density, velocity, and heat flow along the field line, and temperatures perpendicular and parallel to the field. The initial state of the simulation is a current-free polar wind, with the number densities shown in Figure 1 and a constant outward H^+ flux normalized to $10^8\ cm^{-2}\ s^{-1}$ at 1000 km. The oxygen ions have no velocity, and the electron flux is determined from the ion fluxes by the zero current condition. As the simulation begins, a current is applied along the field line. At each time step the electron density is determined by charge neutrality, the electron flux is calculated by assuming that the total field line current is constant, and the electric field is calculated from an Ohm's law equation similar to (5) but is constructed from the complete electron and ion momentum equations. The electron temperatures and heat flow and all of the dynamic ion quantities are calculated from the dynamic 13-moment transport equations of Schunk [1977].

In order to simulate ion acceleration it is necessary to add an anomalous friction to this model. For typical auroral field line currents, the critical drift velocity for electron-hydrogen ion cyclotron waves is exceeded along the field line, and theories of anomalous resistivity do exist which require the existence of such waves [e.g., Rowland and Palmadesso, 1983]. We will postulate a resistivity based on this critical drift, i.e.,

$$v_{eH}^* = 0.01\Omega_H\left(\frac{n_H}{n_e}\right)\left(\frac{v_d}{v_c} - 1\right)^2 \qquad v_d > v_c \qquad (11)$$

where Ω_H is the hydrogen ion cyclotron frequency, v_d is the magnitude of the electron-hydrogen ion drift velocity $v_e - v_H$, and v_c is the critical drift, approximated by
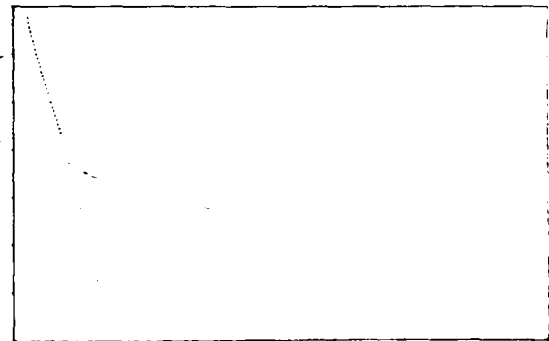

Fig. 1. Number densities for the steady state polar wind with no field-aligned current. n_e (solid curve), n_H (dashed curve), n_O (dotted curve).
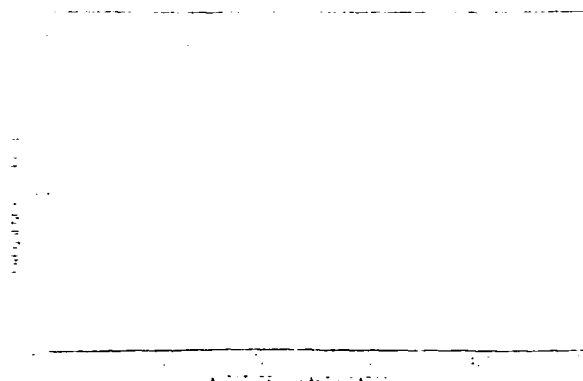
Fig. 2   Collision frequency $v_{eH}*$ for anomalous momentum transfer between e and H⁻ at 1 min after current onset.

Fig 3.   Electric field parallel to the field line at times of 0 (solid curve) and 1 (dashed curve) min after current onset.

$$V_c = \max\left(\frac{15T_H}{T_e}, 6\right)(2kT_H\ m_H)^{1/2} \qquad (12)$$

In (12), T_H and T_e are the total hydrogen ion and electron temperatures, respectively. For this simulation, no account is taken of the dependence of the critical drift on the hydrogen ion temperature anisotropy. As in the work by *Rowland and Palmadesso* [1983], the thermal energy generated by the resistivity is primarily given to the electrons, i.e.,

$$k\frac{\delta T_e}{\delta t} = v_{eH}*m_e V_d^2 \qquad (13)$$

As a result, the electrons heat rapidly because of the resistivity, reducing the critical drift in regions of roughly equal electron and hydrogen ion temperatures until $T_e \gtrsim 2.5T_H$ and the critical drift stabilizes.

At time $t = 0$, a constant current corresponding to 10^{-6} A m⁻² at an altitude of 800 km is applied to the field line. After 1 min the critical drift velocity has stabilized along the field line because of electron heating, and the anomalous collision frequency has the profile shown in Figure 2. The electric field profiles at 0 and 1 min after current onset are compared in Figure 3. Initially, the only significant electric field is the ambipolar field at the lower end of the field line, and the total field line potential is about 2 V. (Potentials in this model tend to be small, because only cold ionospheric electrons are included at present.) At 1 min the electric field due to the anomalous resistivity is evident above 4000 km altitude. At this point the field line potential drop has increased by an order of magnitude (to 23 V). The small increase in the electric field below 4000 km is the increased ambipolar field due to increased electron temperature. The change in the O⁻ velocity is shown in Figure 4. The oxygen ions are directly accelerated by the resistive electric field in the region above 4000 km and, to a lesser degee, by the ambipolar field below this altitude. The deceleration of the hydrogen ions is small (of order $n_o m_o$ $n_H m_H$) in this case and is overwhelmed by other effects such as acceleration by the ambipolar electric fields.

This simulation was continued until 5 min after current onset. During this time the oxygen ions continued to accelerate, but the distinction between the resistive and ambipolar electric fields became more difficult. As described in the work by *Mitchell and Palmadesso* [1983], the onset of current creates a precipitating electron population which heats in the converging magnetic field. As a result, the temperature at the lower end of the flux tube rises until the upward electron heat flux grows large enough to counteract this effect, and the ambipolar field exhibits large fluctuations during this time. In this case, with the anomalous resistivity forcing the electrons to heat even more rapidly, these fluctuations become the same order of magnitude as the resistive electric field and disrupt the clear picture of oxygen ions gaining momentum from the hydrogen ions through the resistive electric field. However, the anomalous friction continues to provide a species-dependent contribution to the total parallel electric field.
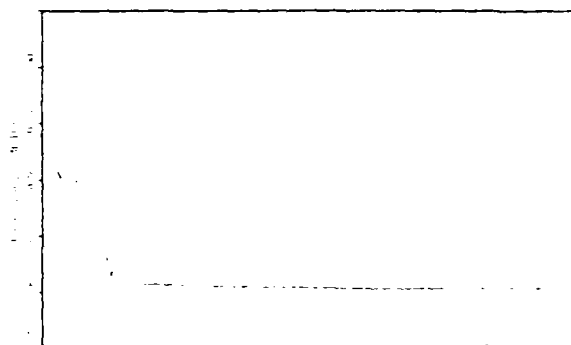
Our simulations indicate that the behavior of the field line plasma is very dynamic after the onset of field-aligned current. Thus it may not be accurate to propose the steady state energization of ion beams in a parallel electric field. The simulation described here produces an energetic flux of O⁻ even though it may not be sustained as the lower-altitude ion-neutral collision regions react to the increased outflow. A simulation which accurately models both high- and low-altitude regions is necessary to fully address these considerations. It should be noted that the magnitude of the effect discussed here may be quite large; the net energy gained by O⁻ will be of the order of the potential drop along the field line, which can be several kilovolts. The energy gain seen in the simulation was restricted to smaller values by the need to maintain numerical stability and stay within the limits of approximations implicit in the fluid equations.
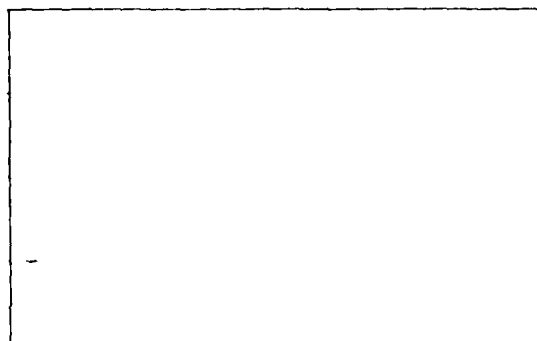
Fig. 4   O⁻ velocity parallel to the field line at times of 0 (solid curve) and 1 (dashed curve) min after current onset

SUMMARY

We have attempted to show here that the existence of anomalously energetic heavy ion fluxes on auroral field lines can be a result of the manner in which a parallel electric field is supported on the field lines. If the process is a form of resistive momentum transfer, then the ion species experiencing resistivity strongly lose momentum through the electric field to those ion species not participating. Thus the large relative magnitude of the O^+ to H^+ energetic fluxes may indicate that the parallel electric fields on these field lines are supported to some extent by some form of electron-hydrogen ion friction. The magnitude of this effect depends a great deal on the details of such a friction, a point we have not addressed in this report, but we feel that the general concept may have a broad applicability for the auroral field line plasma.

REFERENCES

Banks, P M., and T E Holzer. The polar wind. *J Geophys. Res.*, 73, 6846-6854. 1968

Collin, H L. R D Sharp, E G Shelley, and R G Johnson. Some general characteristics of upflowing ion beams over the auroral zone and their relationship to auroral electrons. *J Geophys. Res.*, 86, 6820-6826, 1981

Gorney, D J., A Clarke, D Croley, J Fennell, J Luhmann, and P Mizera. The distribution of ion beams and conics below 8000 km. *J Geophys Res.*, 86, 83-89, 1981

Horwitz, J L., The ionosphere as a source for magnetospheric ions *Rev Geophys Space Phys.*, 20, 929-952, 1982

Klumpar, D M. Transversely accelerated ions An ionospheric source of hot magnetospheric ions. *J Geophys Res.*, 84, 4229-4237, 1979

Mitchell, H G. Jr., and P J Palmadesso. A dynamic model for the auroral field line plasma in the presence of field-aligned current. *J Geophys Res.*, 88, 2131-2139. 1983

Moore, T E. Modulation of terrestrial ion escape flux composition (by low-altitude acceleration and charge exchange chemistry). *J Geophys Res.*, 85, 2011-2016, 1980

Rowland, H L. and P J Palmadesso Anomalous resistivity due to low-frequency turbulence. *J Geophys Res.*, 88, 7997-8002, 1983

Schunk, R W. Mathematical structure of transport equations for multispecies flows. *Rev Geophys Space Phys.*, 15, 429-445, 1977

Shawhan, S D. C-G Falthammar and L P Block. On the nature of large auroral zone electric fields at $1-R_E$ altitude. *J Geophys Res.*, 83, 1049-1054, 1978

Shelley, E G., R D Sharp, and R G Johnson. Satellite observations of an ionospheric acceleration mechanism. *Geophys Res Lett.*, 3, 654-656. 1976

Shelley, E G., W K Peterson, A J Ghielmetti, and J Geiss. The polar ionosphere as a source of energetic magnetospheric plasma. *Geophys. Res. Lett.*, 9, 941-944, 1982

Stern, D P. The electric field and global electrodynamics of the magnetosphere. *Rev Geophys Space Phys.*, 17, 626-640, 1979

H G Mitchell, Jr., Naval Research Laboratory, Code 4780, Washington, DC 20375

P J Palmadesso, Geophysical and Plasma Dynamics Branch, Plasma Physics Division, Naval Research Laboratory, Washington, DC 20375

APPENDIX F

Behavior of Ionized Plasma in the High

Latitude Topside Ionosphere

BEHAVIOR OF IONIZED PLASMA IN THE

HIGH LATITUDE TOPSIDE IONOSPHERE

Supriya Banerjee Ganguli and H. G. Mitchell, Jr.

Science Applications International Corporation
1710 Goodridge Drive
McLean, Virginia 22102

P. J. Palmadesso

Plasma Physics Division
Naval Research Laboratory
4555 Overlook Avenue, S. W.
Washington, D. C. 20375

January 1985

TABLE OF CONTENTS

F-6

INTRODUCTION

The behavior of plasma on the auroral magnetic field lines has been the subject of a number of studies in recent years. Theoretical models of the polar wind have been developed by Banks and Holzer [1968, 1969], Holzer *et al.*, [1971], and Lemaire and Scherer [1973]. Using the 13-moment system of transport equations of Schunk [1977], Schunk and Watkins [1981, 1982] have studied the steady state flow of a fully ionized H^+ - O^+ - electron plasma along geomagnetic field lines. In their first study of the polar wind [1981], they used the 13-moment equations for the electron gas and a simplified set of transport equations for the hydrogen and oxygen ions. Their results show that electron temperature anisotropy develops at altitudes above 2500 km. Below 2500 km the electron gas is essentially collision dominated. In their next study of the polar wind [1982], they have used the 13-moment system of equations for the hydrogen ions also. The results show that for supersonic flow at high altitudes, the hydrogen ion temperature parallel to the field line ($T_{p\parallel}$) is greater than the temperature perpendicular to the field line ($T_{p\perp}$). The reverse is true for subsonic flow.

Using the same 13-moment system of equations, Mitchell & Palmadesso [1983] developed a dynamic numerical model of the plasma along an auroral field line. This plasma consists of the electrons, hydrogen and oxygen ions. The electrons and the hydrogen ions are the dynamic species in the model. They have performed simulations for

the case of a current-free polar wind and the case in which a large
upward field aligned current was applied along the field line. The
results of the polar wind simulations have been compared to those of
Schunk and Watkins [1981, 1982]. It is seen that for low electron
temperatures and supersonic hydrogen ion outflow, both exhibit an
anisotropic hydrogen ion cooling and both have a region in which the
parallel temperature increases with altitude before adiabatic cooling
dominates. The electron temperature profiles, however, cannot be
directly compared. The lower boundary of Mitchell and Palmadesso
[1983] was held at a constant temperature and the simulation was run
until a steady-state was achieved. The outflow condition treats the
upper boundary as an electron heat sink and therefore the electron
temperature decreases with altitude. Schunk and Watkins [1981]
specified the electron temperature and a positive electron temperature
gradient at the lower end, as the initial condition to study the electron
temperature anisotropy. The upper boundary need not be specified in
this case.

We have developed a numerical model to study the steady state
behavior of the plasma encompassing geomagnetic field lines. For
theoretical formulation we have used the 16-moment system of transport
equations of Schunk et al. [1982]. The 13-moment system of transport
equations allow for different species temperature parallel and
perpendicular to the field line, but allows only a single heat flow per
species. The 16-moment equations allow transverse and parallel thermal

energy to be transported separately, which simulates the behavior of a large temperature anisotropy for a collisionless plasma better than the 13-moment equations. This is expected to be an important advantage in studies of auroral field aligned transport which include the effects of return currents and anomalous transport processes, such as anomalous resistivity and associated anisotropic heating. Such studies are now in procress, and will be the subject of a future report. We have used this model to perform polar wind simulations. This to our knowledge is the first successful steady state solution to the 16-moment set of transport equations for the polar wind problem.

THE MODEL

A numerical model has been developed to simulate the steady state behavior of a fully ionized plasma (H^+, O^+ and the electrons) along the geomagnetic field lines in the high-latitude topside ionosphere.

The electrons and the hydrogen ions are the dynamic species in the model and the oxygen ions form a static background population at a constant temperature. The H^+ and electron temperature anisotropies and heat flows are not sensitive to the oxygen temperature and heat flows, as noted by Schunk and Watkins [1981, 1982] Thus maintaining the O^+ ions at a constant temperature did not introduce appreciable errors as far as the H^+ ions and electrons are concerned [Schunk 1982].

The distribution function is considered to be gyrotropic about the field line direction, which reduces the 16-moments approximation to six moments: number density, velocity of the species parallel to the field line, temperatures parallel and perpendicular to the field line, and parallel and perpendicular heat flow along the field line. The resulting transport equations used for hydrogen and electrons are given as follows:

$$\frac{\partial n}{\partial t} + \frac{\partial nv}{\partial r} + \dot{A}nv = \frac{\delta n}{\delta t} \qquad (1)$$

$$\frac{\partial v}{\partial t} + v\frac{\partial v}{\partial r} + \frac{k}{mn}\frac{\partial nT_{\parallel}}{\partial r} + \frac{GM}{r^2} - \frac{eE}{m} + \frac{\dot{A}k}{m}(T_{\parallel} - T_{\perp}) = \frac{\delta v}{\delta t} \qquad (2)$$

$$k\frac{\partial T_{\parallel}}{\partial t} + kv\frac{\partial T_{\parallel}}{\partial r} + \frac{2}{n}\frac{\partial nh_{\parallel}}{\partial r} + 2\dot{A}(h_{\parallel} - h_{\perp}) + 2kT_{\parallel}\frac{\partial v}{\partial r} = \frac{\delta T_{\parallel}}{\delta t} \qquad (3)$$

$$k\frac{\partial T_{\perp}}{\partial t} + kv\frac{\partial T_{\perp}}{\partial r} + \frac{1}{n}\frac{\partial nh_{\perp}}{\partial r} + \dot{A}(2h_{\perp} + kT_{\perp}v) = k\frac{\delta T_{\perp}}{\delta t} \qquad (4)$$

$$\frac{\partial h_{\parallel}}{\partial t} + v\frac{\partial h_{\parallel}}{\partial r} + 3h_{\parallel}\frac{\partial v}{\partial r} + \frac{3}{2}\frac{k^2 T_{\parallel}}{m}\frac{\partial T_{\parallel}}{\partial r} = \frac{\delta h_{\parallel}}{\delta t} \qquad (5)$$

$$\frac{\partial h_\perp}{\partial t} + v\frac{\partial h_\perp}{\partial r} + h_\perp \frac{\partial v}{\partial r} + \frac{k^2 T_\perp}{m} \frac{\partial T_\perp}{\partial r}$$

$$(6)$$

$$+ \dot{A}(vh_\perp + \frac{T_\perp k^2}{m} (T_\| - T_\perp)) = \frac{\delta h_\|}{\delta t}$$

Charge neutrality

$$n_e = n_p + n_o \qquad (7)$$

where, n = number density

v = species velocity

A = cross-sectional area of a flux tube

(proportional to $1/B$)

B = magnetic field of the earth

E = Electric field parallel to the field line

G = gravitational constant

M = mass of the earth

m = mass of the particular species

$T_\|$ = temperature of the species parallel to the

field line

$T_\perp$ = temperature of the species perpendicular

to the field line

$h_\|$ = heat flow parallel to the field line

$h_\perp$ = heat flow perpendicular to the field line

k = Boltzmann constant

$$\dot{A} = \frac{1}{A} \frac{\partial A}{\partial r} = \frac{3}{r}$$

e = electrons

p = hydrogen ions

o = oxygen ions

For a given moment F of the distribution function, $\delta F / \delta t$ represents the change in F due to the effects of collision and we would include the effects of plasma turbulence such as anomalous resistivity when the model is further developed. The collision terms used in this model are those of Mitchell and Palmadesso [1983]. They have used Burger's [1979] collision terms for the case of Coulomb collisions with corrections for finite species velocity differences. The collision terms are given in Appendix A.

We have assumed that the total flux tube current I remains constant,

$$I = eA(n_p v_p - n_e v_e) \qquad (8)$$

which implies

$$v_e = \frac{1}{n_e} (n_p v_p - \frac{I}{eA}) \qquad (9)$$

In the following, the current I is assumed to be zero.

Using equations (2), (7) and (8) the electric field E parallel to the field line is calculated [Mitchell and Palmadesso, 1983].

$$E = \frac{m_s}{e n_e A} \frac{\partial}{\partial r} (n_p v_p^2 A - n_e v_e^2 A) - \frac{k}{e} \left[\frac{\partial T_{e\parallel}}{\partial r} + \frac{T_{e\parallel}}{n_e} \frac{\partial n_e}{\partial r} \right.$$

$$\tag{10}$$

$$\left. + \frac{(T_{e\parallel} - T_{e\perp})}{A} \frac{\partial A}{\partial r} \right] - \frac{n_o m_e GM}{n_e e r^2} + \frac{m_e}{e} \left[\frac{\delta v_e}{\delta t} - \frac{n_p}{n_e} \frac{\delta v_p}{\delta t} \right]$$

We will consider the steady state of the equations (1) – (6). This set of ordinary differential equations are solved by first eliminating all derivatives in a given equation except one and then integrating the resulting quantities numerically along the field line. The new set of equations are:

$$\frac{\partial n_p}{\partial r} = - \frac{n_p}{v_p} \frac{\partial v_p}{\partial r} - \frac{3}{r} n_p \tag{i}$$

$$\frac{\partial v_p}{\partial r} = \frac{1}{\left[v_p - \frac{k T_{p\parallel}}{v_p m_p} - \frac{T_{e\parallel} k n_p}{m_p v_p (n_o + n_p)} \right]}$$

$$\times \left[\frac{3k\, T_{p_\parallel}}{r\, m_p} + \frac{3\,k\,T_{e_\parallel}\,n_p}{r\,m_p\,(n_p + n_o)} - \frac{k}{m_p}\,\frac{\partial T_{p_\parallel}}{\partial r} \right.$$

$$- \frac{k}{m_p}\,\frac{\partial T_{e_\parallel}}{\partial r} - \frac{k\,T_{e_\parallel}}{m_p(n_o + n_p)}\,\frac{\partial n_o}{\partial r} - \frac{3k}{rm_p}\,(T_{e_\parallel} - T_{e_\perp})$$

$$- \frac{n_o m_e\, GM}{m_p r^2\,(n_o + n_p)} - \frac{GM}{r^2} + \frac{m_e}{m_p}\,\frac{\delta v_e}{\delta t}$$

$$\left. + \left[1 - \frac{m_e\,n_p}{m_p(n_o + n_p)} \right] \frac{\delta v_p}{\delta t} - \frac{3k\,(T_{p_\parallel} - T_{p_\perp})}{rm_p} \right]$$

$$\text{(ii)}$$

$$\frac{\partial T_\parallel}{\partial r} = \frac{1}{\left[kv - \dfrac{3k^2}{v}\,\dfrac{T_\parallel}{m} \right]} \times \left[-\frac{2}{n}\,h_\parallel\,\frac{\partial n}{\partial r} + \frac{6}{r}\,(h_\perp - h_\parallel) \right.$$

$$\text{(iii)}$$

$$\left. - \left[2T_\parallel k - \frac{6h_\parallel}{V} \right] \frac{\partial v}{\partial r} + k\,\frac{\delta T_\parallel}{\delta t} - \frac{2}{v}\,\frac{\delta h_\parallel}{\delta t} \right]$$

$$\frac{\partial T_\perp}{\partial r} = \frac{1}{\left[kv - \dfrac{k^2 T_\parallel}{m\,v}\right]} \left[\frac{h_\perp}{v}\frac{\partial v}{\partial r} - \frac{h_\perp}{n}\frac{\partial n}{\partial r} - \frac{3}{r}h_\perp - \frac{3k\,T_\perp\,v}{r}\right.$$

$$\text{(iv)}$$

$$\left. + \frac{3k^2 T_\perp}{mrv}(T_\parallel - T_\perp) + k\frac{\delta T_\perp}{\delta t} - \frac{1}{v}\frac{\delta h_\perp}{\delta t}\right]$$

$$\frac{\partial h_\parallel}{\partial r} = -\frac{3h_\parallel}{v}\frac{\partial v}{\partial r} - \frac{3}{2}\frac{k^2}{v}\frac{T_\parallel}{m}\frac{\partial T_\parallel}{\partial r} + \frac{1}{v}\frac{\delta h_\parallel}{\delta t} \qquad \text{(v)}$$

$$\frac{\partial h_\perp}{\partial r} = -\frac{h_\perp}{v}\frac{\partial v}{\partial r} - \frac{k^2 T_\parallel}{v\,m}\frac{\partial T_\perp}{\partial r}$$

$$\text{(vi)}$$

$$-\frac{3}{r}h_\perp - \frac{3k^2\,T_\perp}{v\,r\,m}(T_\parallel - T_\perp) + \frac{1}{v}\frac{\delta h_\perp}{\delta t}$$

The simulation is carried out on an unequally spaced grid. The cell size is selected small at the lower end of the flux tube. This enables us to determine the plasma dynamics properly in the presence of large density gradients due to the small scale height of oxygen.

The system of equations we have to solve is a system of stiff differential equations. A typical solution of a stiff system has a short initial interval in which it changes rapidly (called an initial transient) after which it settles down to a comparatively slowly varying state. Methods of solving stiff ordinary differential equations has been discussed by Gear *et al.*, [1979]. We will use the general procedure used by Watkins [1981].

SIMULATIONS AND RESULTS

Schunk and Watkins [1982] have performed polar wind simulations for both supersonic and subsonic hydrogen ion outflow. Until recently it was not clear if the polar wind is supersonic or subsonic. Nagai *et al.* [1984] first reported the supersonic nature of the polar wind along polar cap field lines. The data for this study were obtained from DE 1 satellite. This paper clearly shows that the hydrogen ion flow in the polar ionosphere is supersonic in nature. Subsonic polar wind has not yet been observed. We would consider hydrogen ion outflow as *supersonic.*

As noted above, solutions have been obtained for the current free case. The lower boundary is fixed at 1500 km. At this boundary we set the H^+ ion velocity at 16 km s^{-1}, H^+ ion density at 80 cm^{-3}, oxygen ion density at 5000 cm^{-3}. The hydrogen ion temperature at the lower boundary is 3500° K. The oxygen ion temperature was kept

constant at 1200° K. The results of this current free polar wind simulations are shown in figures 1a-1g. Figure 1a shows oxygen ion density. 1b shows H^+ ion density. 1c shows electron density. 1d shows hydrogen ion velocity. Oxygen ions are the dominant species only up to an altitude of 3500 km. Supersonic H^+ ions flow in divergent magnetic field lines. The hydrogen momentum balance equation shows that the ambipolar electric field value produces the sharp increase in H^+ ion velocity lower end of the tube. Electron velocity also increases as it is evident from equation (9) and is shown is Figure 1c. The total flux along the flux tube is conserved, i.e., nVA = constant. Therefore, as the velocity and the area increases, the density should decrease. The hydrogen ion density decreases as it flows through the diverging flux tube. The electron density also decreases, as it is evident from the charge neutrality equation (7).

A study of equation (11) reveals that at the upper end of the flux tube velocity variation results mainly from a balance between the terms containing hydrogen ion temperature difference $(T_{p_\parallel} - T_{p_\perp})$, electron temperature difference $(T_{e_\parallel} - T_{e_\perp})$, hydrogen ion temperature $(T_{p_\parallel})$ and electron temperature $(T_{e_\parallel})$ parallel to the field line, i.e. mirror forces and parallel pressure gradients.

Figure 1f shows the hydrogen ion temperature parallel and perpendicular to the geomagnetic field. H^+ temperature exhibits two basic characteristics:

(1)   Adiabatic cooling - Supersonic ion gas cools down as it expands
in a diverging magnetic field.

(2)   Temperature anisotropy.

These effects were also displayed by the previous studies of the
polar wind using the 13-moment system of equations by Schunk and
Watkins [1982] and Mitchell and Palmadesso [1982]. Like Schunk and
Watkins [1982], we obtained solutions for only positive H^+ heat flow at
the lower boundary. This implies that an upward flow of heat from the
lower ionosphere is required for a supersonic hydrogen ion outflow
[Schunk, 1982]. This upward flow of heat is associated with a negative
H^+ temperature gradient.

At the lower end of the flux tube, due to rapid expansion of the
supersonic ion gas, both $T_\perp$ and $T_\parallel$ decrease. This was also noted by
Schunk and Watkins [1982]. Hydrogen ion temperature perpendicular to
the field line decreases continuously. Appreciable temperature
anisotropy develops around 2500 km. The temperature anisotropy is
more prominent in the H^+ ions than in the electrons. This is because
of the fact that the hydrogen ions have supersonic velocities and in the
collisionless region heat transport is not efficient for H^+ ions, compared
to that for electrons. Also, as the particles move up in a decreasing
magnetic field, $v_\perp$ decreases in order to keep adiabatic invariant μ
constant. As the total energy of the particle is conserved, $\frac{1}{2} mv_\parallel^2$
increases at the expense of $\frac{1}{2}mv_\perp^2$. That is, the perpendicular energy
gets converted to the parallel energy. A study of equation (iii) and
(iv) show that the temperature variation is produced mainly as a balance

between the convection process and the mirror force effects. The collisions play an important role below 2500 km. In equations (v) and (vi) the temperature gradient terms are very important.

We compared our solutions of the equations based on the 16-moment system with that of Schunk and Watkins [1982] solution of the 13-moment equations. The general behavior of the H^+ ion temperature parallel and perpendicular to the field line remains the same, H^+ ion temperature perpendicular to the field line decreases continuously with altitude. Parallel temperature first decreases and then increases and finally tends to remain constant with altitude. We observe an anisotropy with $T_\perp > T_\parallel$ below 2500 km. Schunk and Watkins [1982] observed similar anisotropy for the low electron temperature case when they lowered the H^+ ion temperature and heat flow and when the oxygen ion density was increased at the lower end. They have pointed out that the results are sensitive to the boundary conditions used, in the sense that the qualitative picture remains the same only the quantitative picture differs.

We have also compared our results with those of Mitchell and Palmadesso [1983] and Holzer et al. [1971]. Mitchell and Palmadesso [1983] started their simulation at 800 km at the lower boundary. At this level the H^+ ion temperature increases with altitude due to Joule heating caused by H^+ ion collisions with oxygen ions. This effect rapidly decreases with altitude. The general qualitative picture here is in good agreement with our results.

Holzer *et al.* [1971] have compared the solutions of hydrodynamic and kinetic solutions for supersonic polar wind outflow in a collisionless regime. Both hydrodynamic and kinetic solutions show that $T_\perp$ decreases continuously. $T_\parallel$ for both cases decreases rapidly with altitude and then tends to become constant. For the hydrodynamic case at all altitudes the hydrogen ion temperature parallel to the field line was greater than that perpendicular to the field line. The kinetic solutions showed a region at the lower end where $T_\perp$ was greater that $T_\parallel$. The cross-over region was noticed at the lower end. In these cases also we notice that our solutions are in good agreement with Holzer *et al.* [1971].

Finally, we compared our results with Nagai *et al.* [1984]. Nagai *et al.* [1981] have used the data from Dynamics Explorer (DE) to demonstrate the supersonic nature of the polar wind. The obsevations were obtained from 65° to 81° invariant latitude and at an altitude near $2R_E$. The results show that for an estimated range of spacecraft potential of +3 to +5 V, the temperature range of 0.1 to 0.2 eV was obtained corresponding to flow velocities of 25 to 16 km s^{-1}. Calculated mach numbers ranged from 5.1 to 2.6. The Mach number calculated from our results corresponding to a flow velocity of 16 km per second is 2.2.

We have varied slightly the H^+ ion velocity, density and temperature at the lower end to study the sensitivity of the solutions. to these parameters. At the lower end the hydrogen ion density is

Increased to 100 cm^{-3}, velocity is decreased to 10km per second and the temperature is raised to 3800°K. The results of these changes are presented in Figures 2a - 2f. The qualitative picture and the relative importance of the contributing terms remain the same as before. The quantitative change is obvious as the initial conditions are changed. The mach number calculated in this case for a flow velocity of 16 km s^{-1} is 2.68. This is in good agreement with the value 2.6 calculated by Nagai et al. [1984].

Electron temperature parallel and perpendicular to the geomagnetic field lines are shown in Figure 1g. The most important effect exhibited by electron temperature is:

(1)   temperature anisotropy

(2)   Below 2500 km the electron gas is collision dominated, as noticed by Schunk et al. [1981].

"Collision dominated" implies that the collisional relaxation rate is greater than the rate associated with the driving term that produces the anisotropy. Appreciable temperature anisotropy develops above 2500 km. Both temperature parallel and perpendicular to the field line increases. Heat flow is considered downward here (that is, heat flows from the magnetosphere to the ionosphere) as considered by Schunk et al. [1981]. Also, as noticed by Schunk et al. [1981], the electron temperature ratio at the upper end is $T_\perp/T_\parallel$ - 2. The contributions from the collision terms are very important below 2500 km in equations (iii) and (iv). Since the collision terms are important in this region, the electron temperature anisotropy observed in this region is very

small. The anisotropy increases with altitude. Electron temperature variation is produced mainly as a balance between the convection process and the mirror force process. The heat flow is downward for the electrons and the perpendicular energy increases as the parallel energy decreases. The temperature gradient terms are important at all altitudes in equations (v) and (vi). The electron species velocity is less than the electron thermal velocity.

Our results here are in good agreement with Schunk and Watkin's [1981] low electron temperature case. Schunk and Watkins [1981] varied the boundary electron temperature gradients to see the extent to which their solutions are valid. Their results show that with the increase in boundary electron temperature gradient, the electron temperature increased but the direction of anisotropy remained the same. It is also clearly explained by Schunk and Watkins [1981] that this observed anisotropy is opposite to that predicted by the Chew-Goldberger-Low (double adiabatic) energy equations. The tendency of the adiabatic terms to produce an anisotropy with $T_\parallel > T_\perp$ is also present in our equations, but the heat flow effects dominate and act to produce the reverse anisotropy.

The electron temperature profiles cannot be directly compared to Mitchell and Palmadesso [1983]. They treated the upper boundary as an electron heat sink, which decreases the electron temperature with altitude.

DISCUSSIONS

We have studied the steady state behaviour of the plasma encompassing the geomagnetic field lines, using equations based on the 16-moment system of transport equations. The asymptotic behavior of the solutions of the transport equations at high altitudes is quite sensitive to the boundary conditions applied at the lower end of the flux tube. This, coupled with the absence of any standard set of assumptions for specifying those dynamic variables for which upper boundary conditions must be supplied, leads to considerable variation of results at high altitudes in the studies referenced above. Effectively, one finds similar ionospheres and widely different magnetospheres in this group of calculations. While this makes quantitative comparison of results somewhat difficult, it is clear that qualitative agreement among the various calculations is good.

Studies of auroral field line equilibria including the effects of return currents and anomalous transport processes, and using the 16 moment approach described here, are in progress.

APPENDIX 1

$$\frac{\delta n_s}{\delta t} = 0 \qquad (1)$$

$$\frac{\delta v_s}{\delta t} = \sum_a \nu_{sa}(v_a - v_s)(1 + \phi_{sa}) \qquad (2)$$

$$k\frac{\delta t_{s\parallel}}{\delta t} = \sum_a \frac{m_s \nu_{sa}}{(m_s + m_a)} \left\{ \frac{6}{5} kT_{a\parallel} - \left[2 + \frac{4 m_a}{5 m_s} \right] kT_{s\parallel} \right.$$

$$\left. + \frac{4}{5} kT_{a\perp} + \frac{4m_a}{5m_s} kT_{s\perp} + \left[2kT_a + \left[4+6 \frac{m_a}{m_s} \right] kT_s \right] \phi_{sa} \right\} \qquad (3)$$

$$k\frac{\delta T_{s\perp}}{\delta t} = \sum_a \frac{m_s \nu_{sa}}{(m_s + m_a)} \left[3kT_a - 3kT_s + m_a(v_a - v_s)^2 (1+\phi_{sa}) \right]$$

$$- \frac{k}{2} \frac{\delta T_{s\parallel}}{\delta t} \qquad (4)$$

$$\frac{\delta q_{\parallel s}}{\delta t} = - \nu_s q_{\parallel s} \qquad (5)$$

$$\frac{Sq_{\perp s}}{\delta t} = - \nu_s q_{\perp s} \tag{6}$$

Each sum includes all charged particles species in the simulation. The velocity – corrected coulomb collision frequency ν_{sa} is given by

$$\nu_{sa} = \frac{n_a (32\pi)^{1/2} e_s^2 e_a^2 (m_s + m_a) \ln \Lambda \exp (-x_{sa}^2)}{3 m_s^2 m_a \alpha_{sa}^3} \tag{7}$$

($\ln \Lambda$ is the Coulomb logarithm), and

$$T_s = \frac{1}{3} T_{s\|} + \frac{2}{3} T_{s\perp} \quad ,$$

$$\alpha_{sa}^2 = \frac{2kT_s}{m_s} + \frac{2kT_a}{m_a} \quad ,$$

$$x_{sa}^2 = \frac{(v_s - v_a)^2}{\alpha_{sa}^2} \quad ,$$

$$-\Phi_{sa} = \frac{2}{5} x_{sa}^2 + \frac{4}{35} x_{sa}^4 + \frac{8}{315} x_{sa}^6 \quad .$$

ACKNOWLEDGEMENTS

REFERENCES

Banks, P. M. and T. E. Holtzer, The Polar Wind, *J. Geophys. Res.*, 73, 6846-6854, 1968.

Banks, P. M. and T. E. Holtzer, High-Latitude Plasma Transport: The Polar Wind, *J. Geophys. Res.*, 74, 6317-6332, 1969.

Barakat, A. R., and R. W. Schunk, Transport Equations for Multi Component Anisotropic Space Plasmas, *Plasma Physics*, 24, 389-418, 1982.

Burgers, J. M., Flow Equations for Composite Gases, Academic Press, New York, 1969.

Holtzer, T. E., J. A. Fedder, and P. M. Banks, A Comparison of Kinetic and Hydrodynamic Models of an Expanding Ion-Exosphere, *J. Geophys. Res.*, 76, 2453-2468, 1971.

Lemaire, J., and M. Scherer, Kinetic Models of the Solar and Polar Winds, *Rev. Geophys. Space Phys.*, 11, 427-468, 1973.

Mitchell, H. G., and P. J. Palmadesso, A Dynamic Model for the Auroral Field Line Plasma in the Presence of Field-Aligned Current, *J. Geophys. Res.*, 88, 2131, 1983.

Nagai, T., J. H. Waite, Jr., J. L. Green, C. R. Chappell, R. C. Olsen, and R. H. Comfort, First Measurements of Supersonic Polar Wind in the Polar Magnetosphere, *J. Geophys. Res.*, 11, 669-672, 1984.

Schunk, R. W., Mathematical Structure of Transport Equations for Multispecies Flows, *Rev. Geophys. Space Phys.*, 15, 429-445, 1977.

Schunk, R.W. and D.S. Watkins, Electron Temperature Anisotropy in the Polar Wind, *J. Geophys. Res.*, 86, 91-102, 1981.

Schunk, R.W. and D.S. Watkins, Proton Temperature Anisotropy in the Polar Wind, *J. Geophys. Res.*, 87, 171-180, 1982.

Shampine, L.F. and C.W. Gear, A User's View of Solving Stiff Ordinary Differential Equations, *SIAM Rev.*, 21, 1-17, 1979.

Watkins, D.S. Efficient Initialization of Stiff Systems with One Unknown Initial Condition, *SIAM J. Numer. Anal.*, 1981.

FIGURE CAPTIONS

Figure 1   (a)   Oxygen ion density profile for steady state polar wind.

(b) H^+ ion density profile versus altitude.

(c) e^- density profile.

(d) H^+ velocity profile for steady state polar wind.

(e) e^- velocity profile versus altitude.

(f) H^+ ion temperature parallel and perpendicular to the geomagnetic field versus altitude.

(g) e^- temperature parallel and perpendicular to the geomagnetic field versus altitude.

Figure 2   (a) H^+ ion density profile for steady state polar wind versus altitude.

(b)   e density profile.

(c) H^+ ion velocity profile.

(d)   e velocity profile.

(e) H^+ ion temperature parallel and perpendiuclar to the geomagnetic field.

(f)   e temperature parallel and perpendicular to the geomagnetic field.
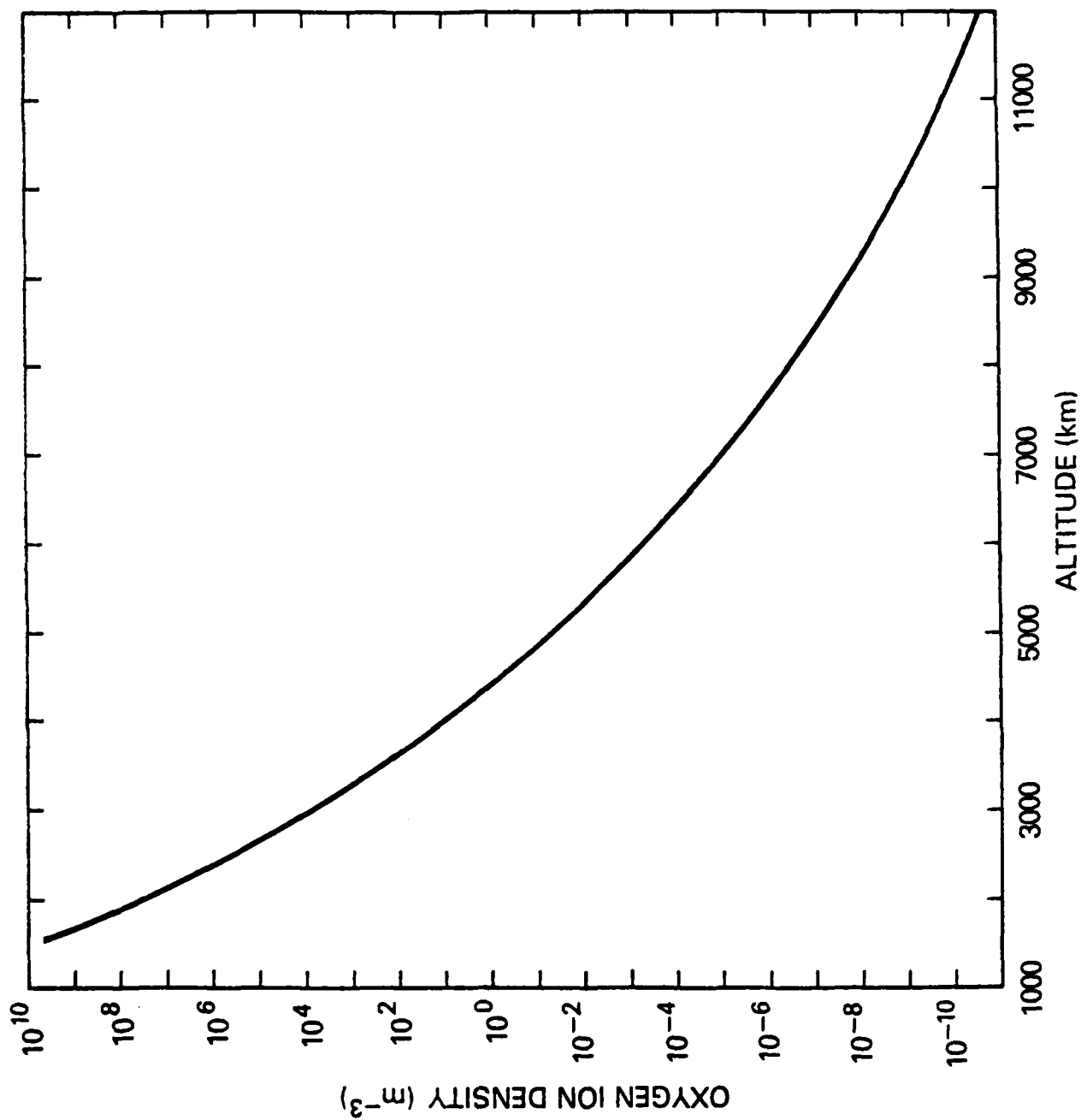
Figure 1 (a)
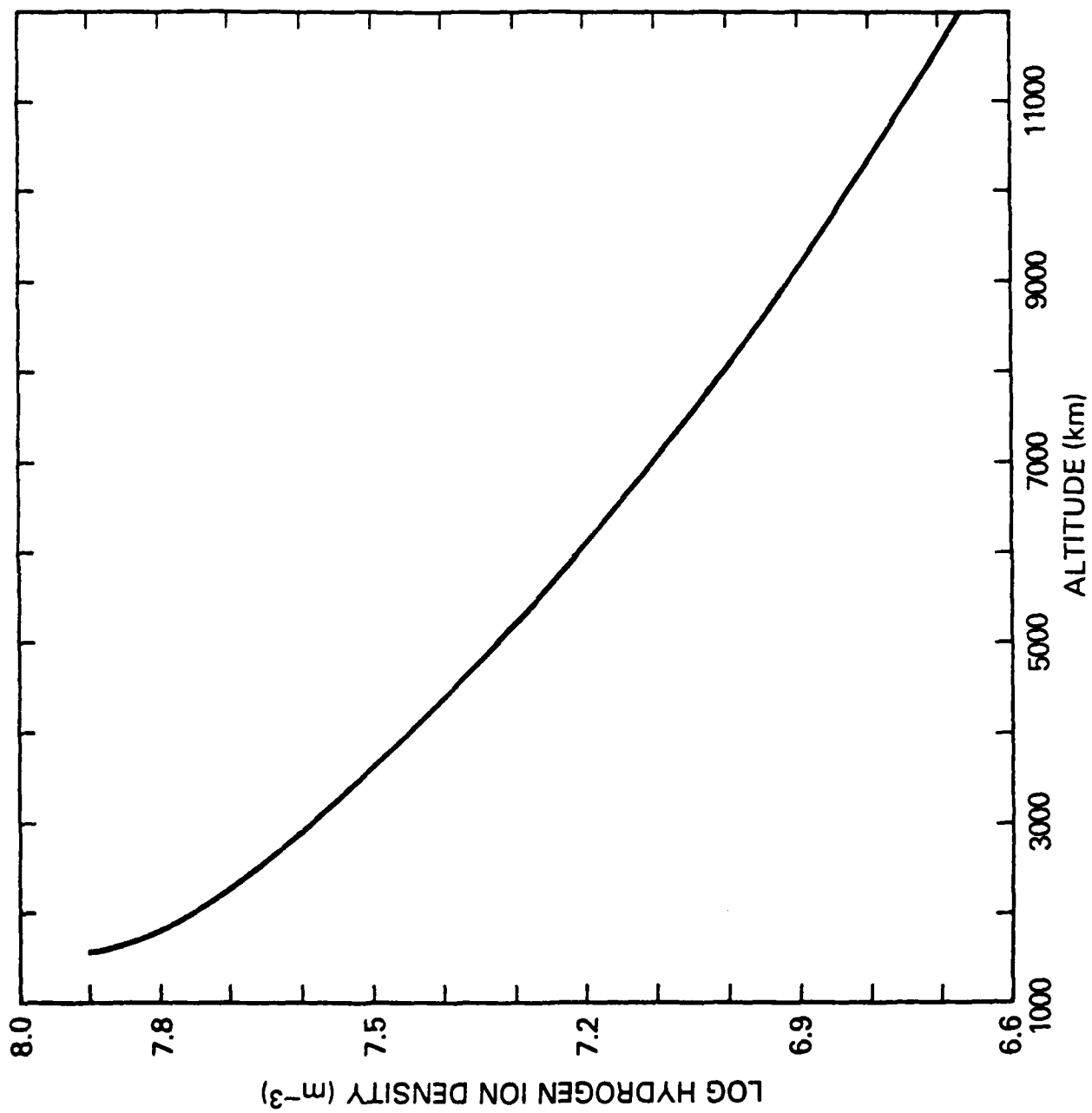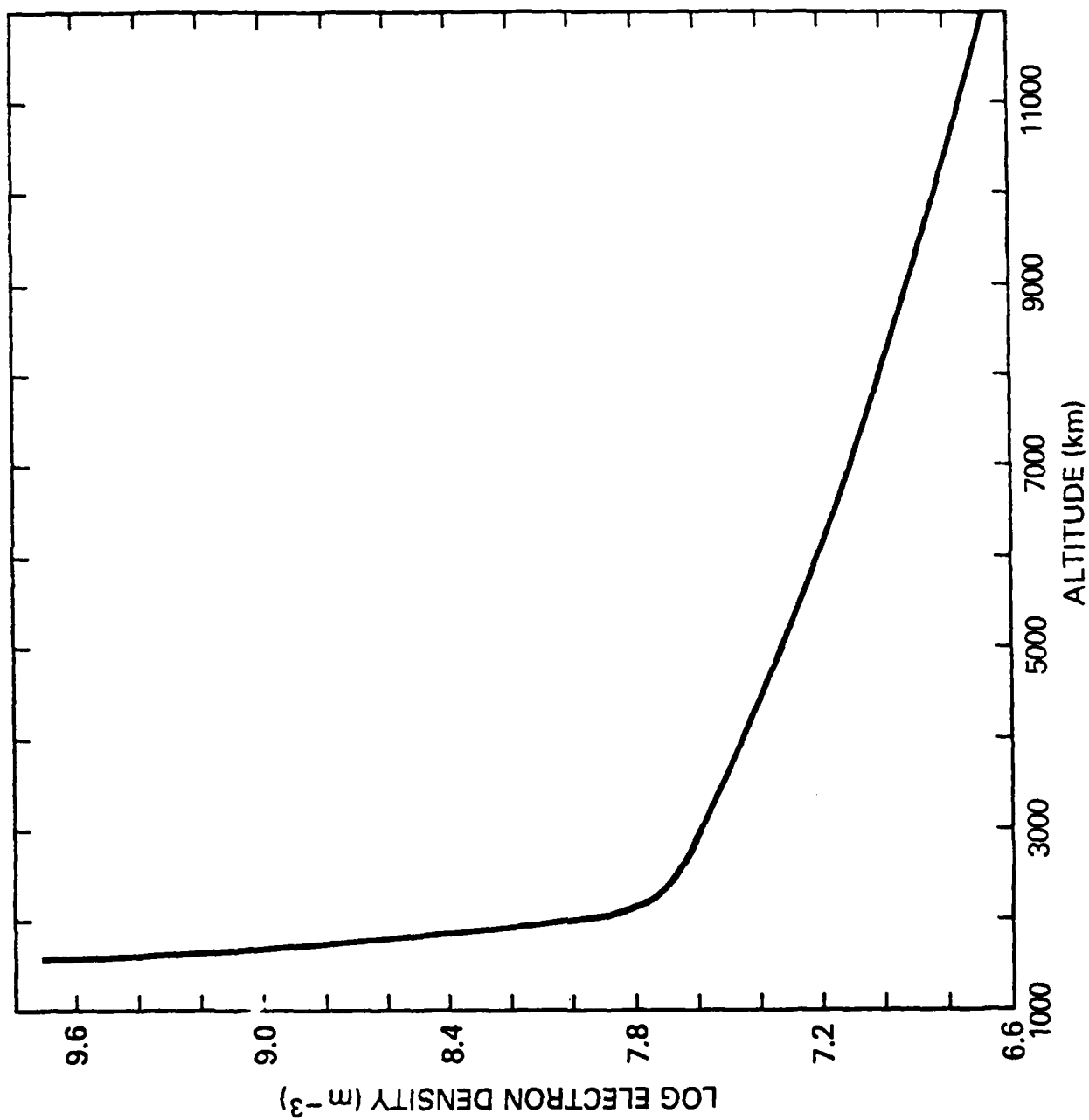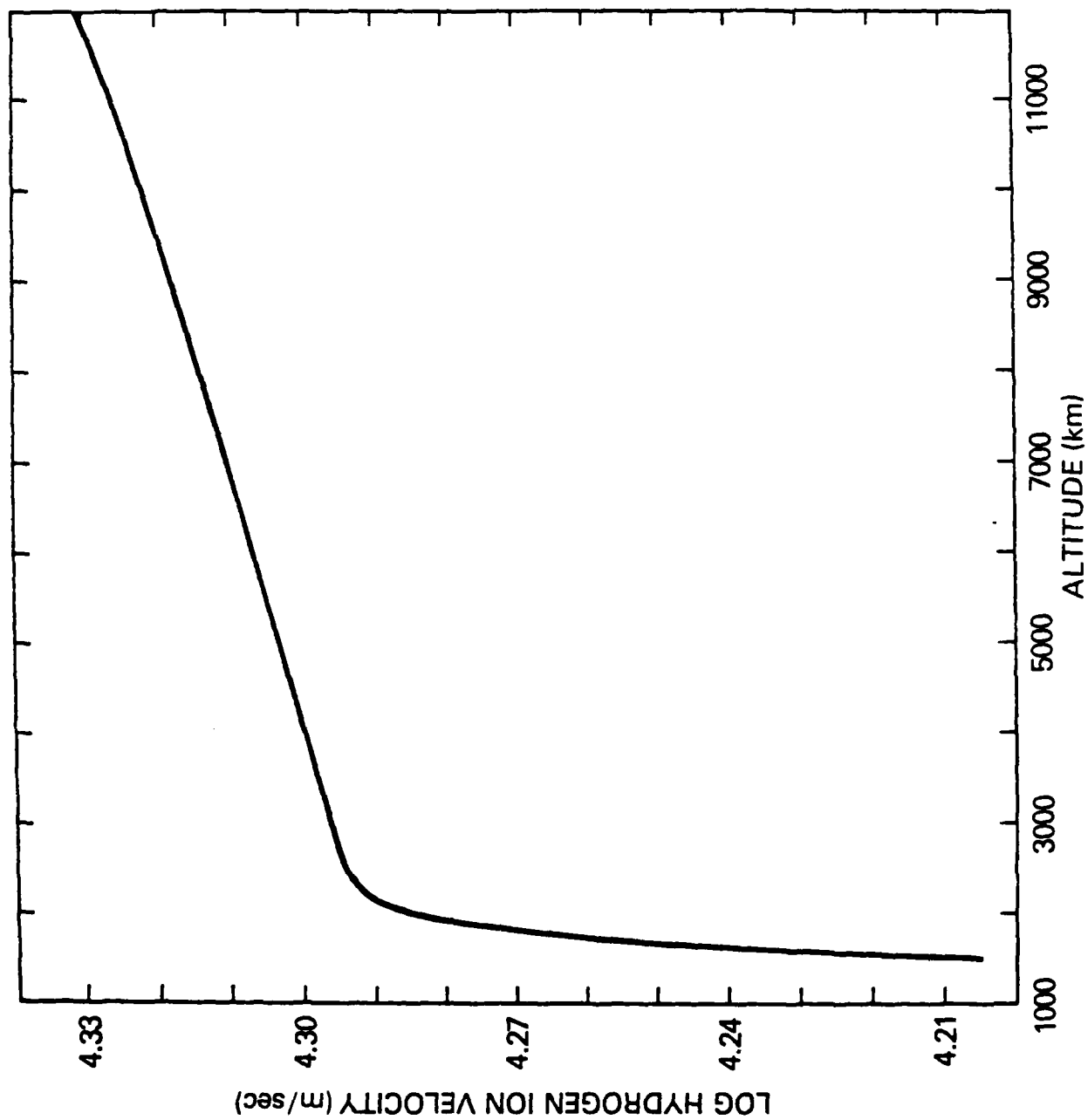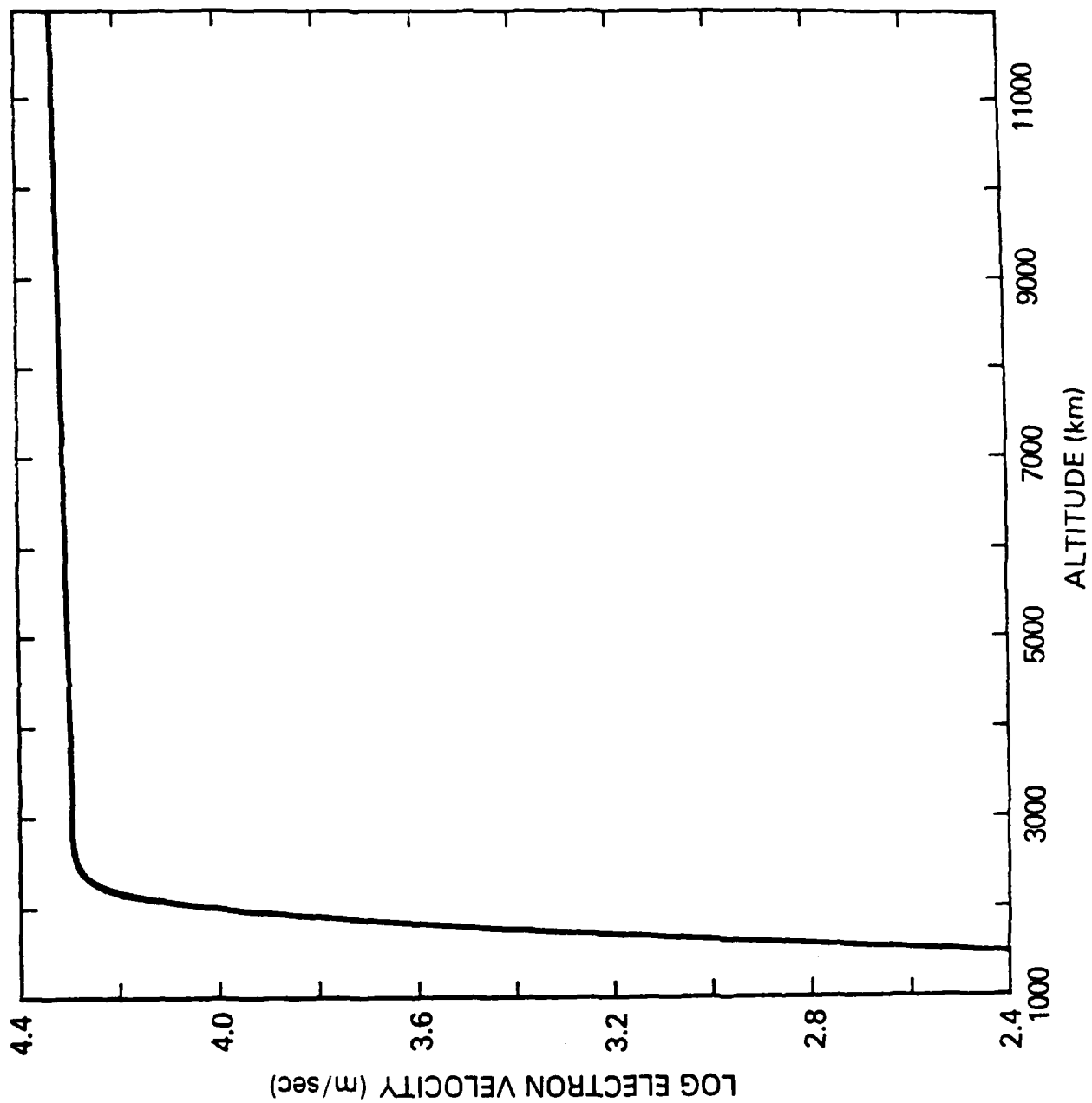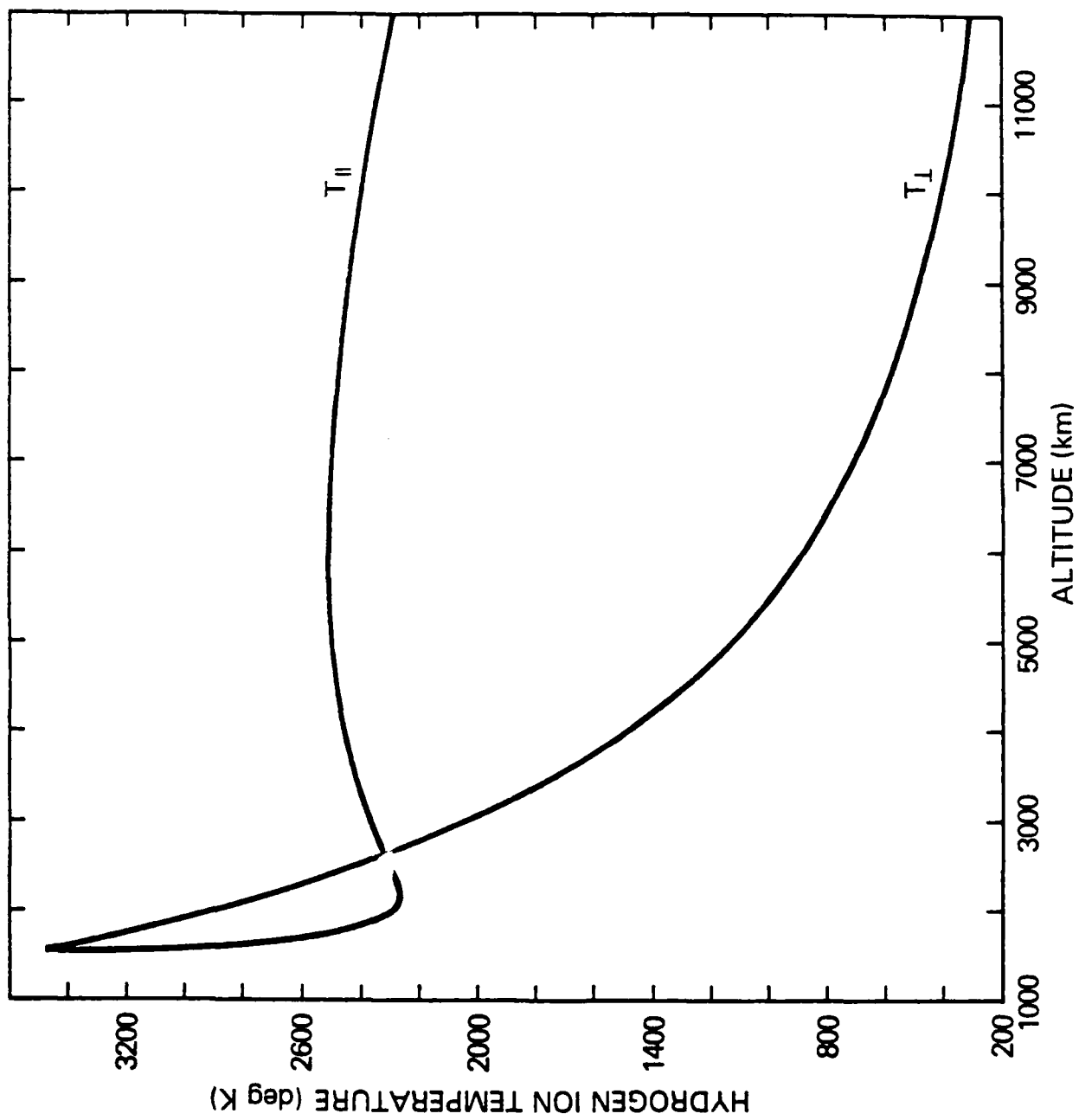
OXYGEN ION DENSITY (m^{-3})

ALTITUDE (km)

Figure 1(b)

ALTITUDE (km)

LOG HYDROGEN ION DENSITY (m−3)

Figure 1(c)

ALTITUDE (km)

LOG ELECTRON DENSITY (m^{-3})

Figure 1 (d)

ALTITUDE (km)

LOG ELECTRON VELOCITY (m/sec)

Figure 1 (e)

F-37

Figure 1(f)

F-38

ALTITUDE (km)

ELECTRON TEMPERATURE (deg K)

Figure 1 (q)

ALTITUDE (km)

LOG HYDROGEN ION DENSITY (m−3)

Figure 2(a)

ALTITUDE (km)

LOG ELECTRON DENSITY (m⁻³)

Figure 2 (b)

F-41

ALTITUDE (km)

LOG HYDROGEN ION VELOCITY (m/sec)

Figure 2 (c)

Figure 2 (d)

F-43 2 (d)

Figure 2 (e)

ALTITUDE (km)

HYDROGEN ION TEMPERATURE (deg K)

ALTITUDE (km)

Figure 2(f)

ELECTRON TEMPERATURE (deg K)
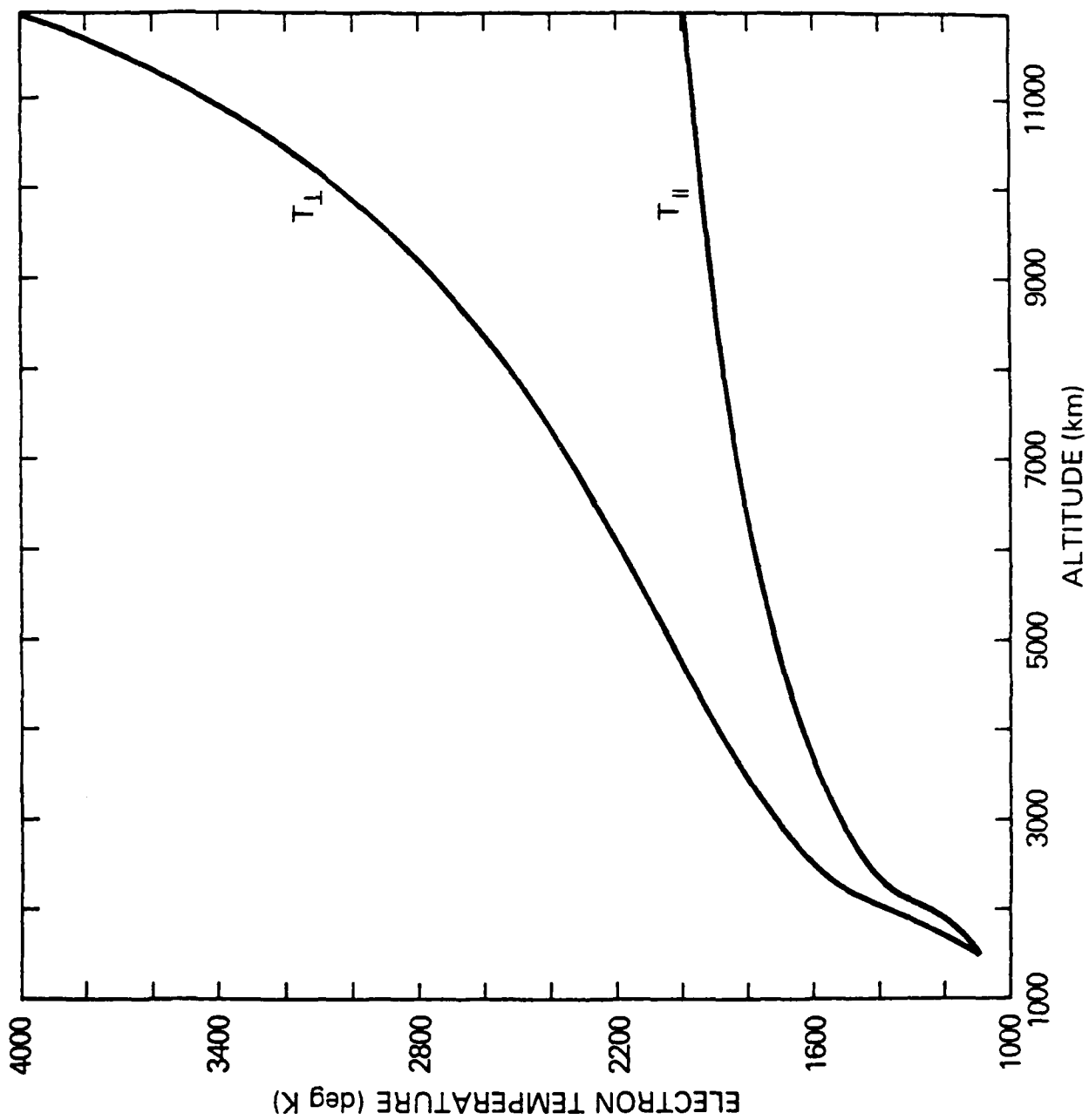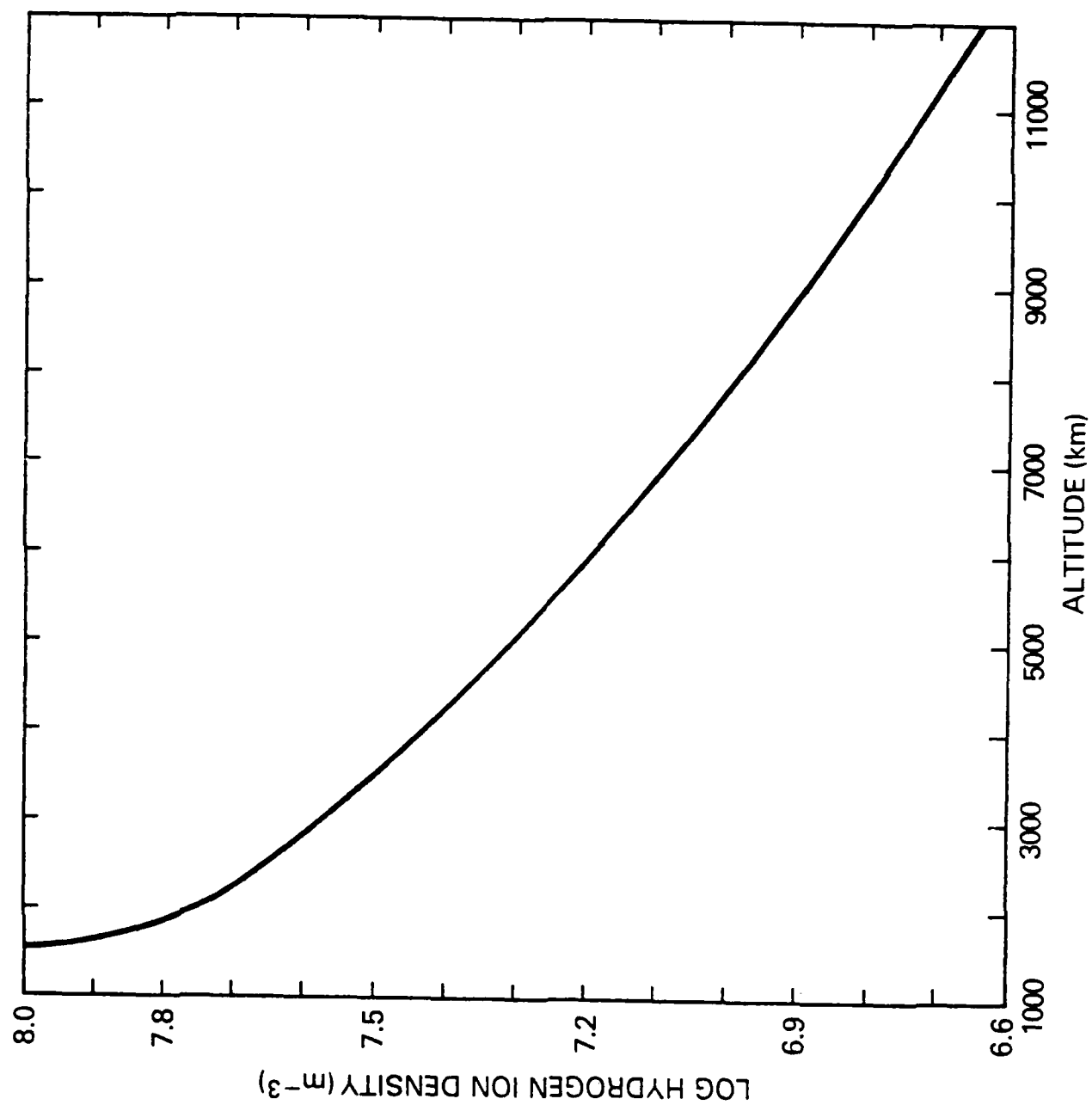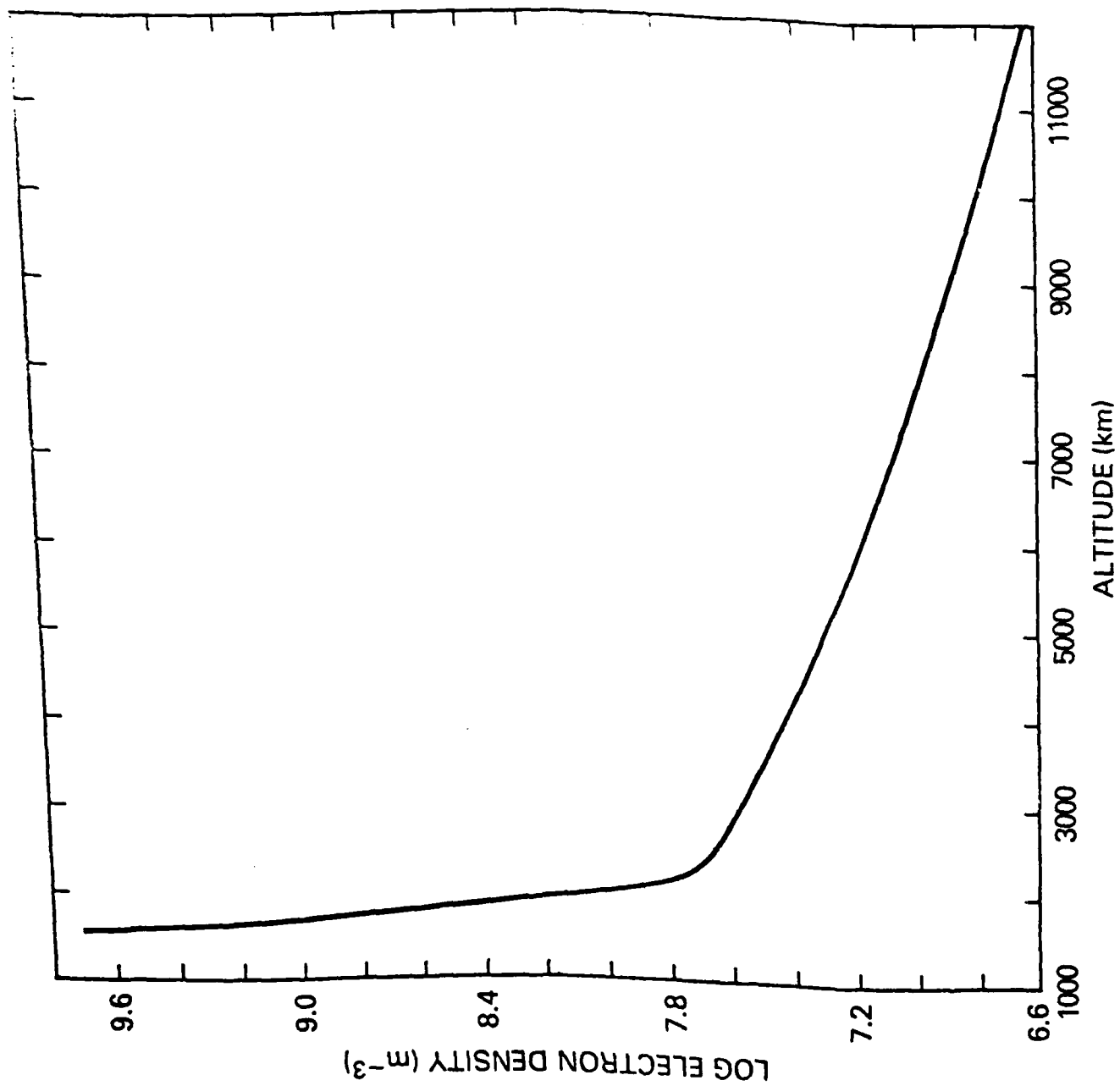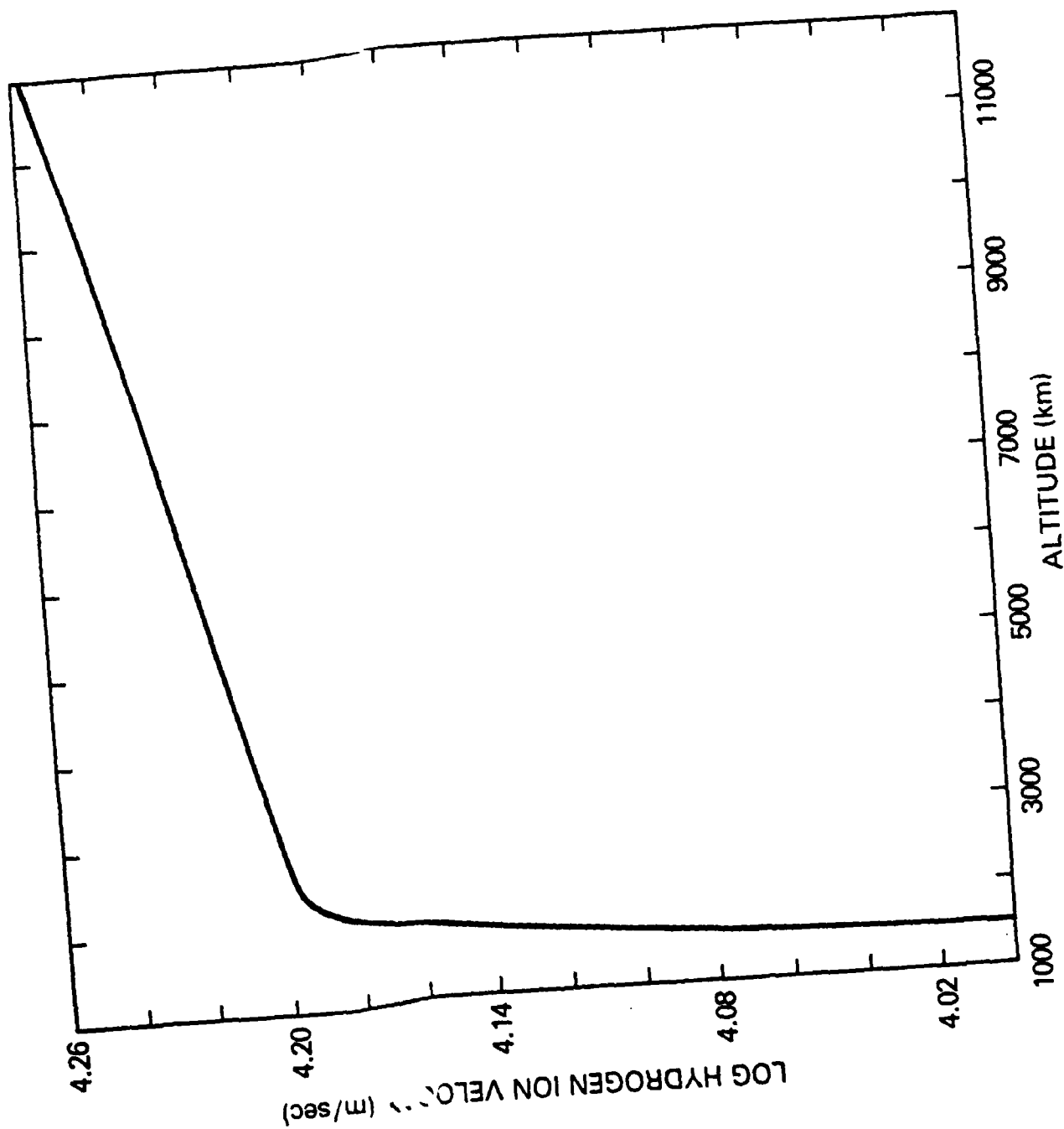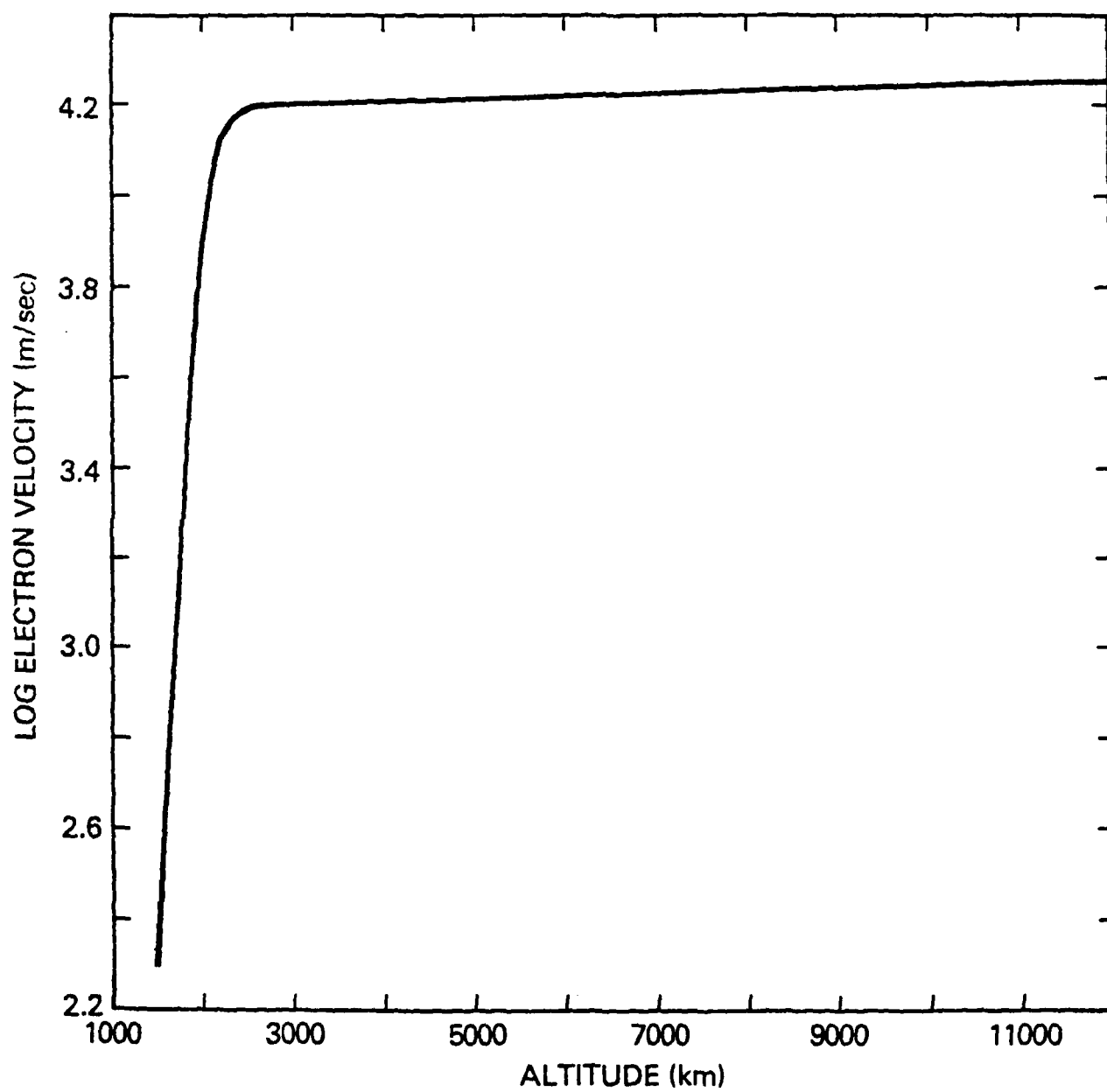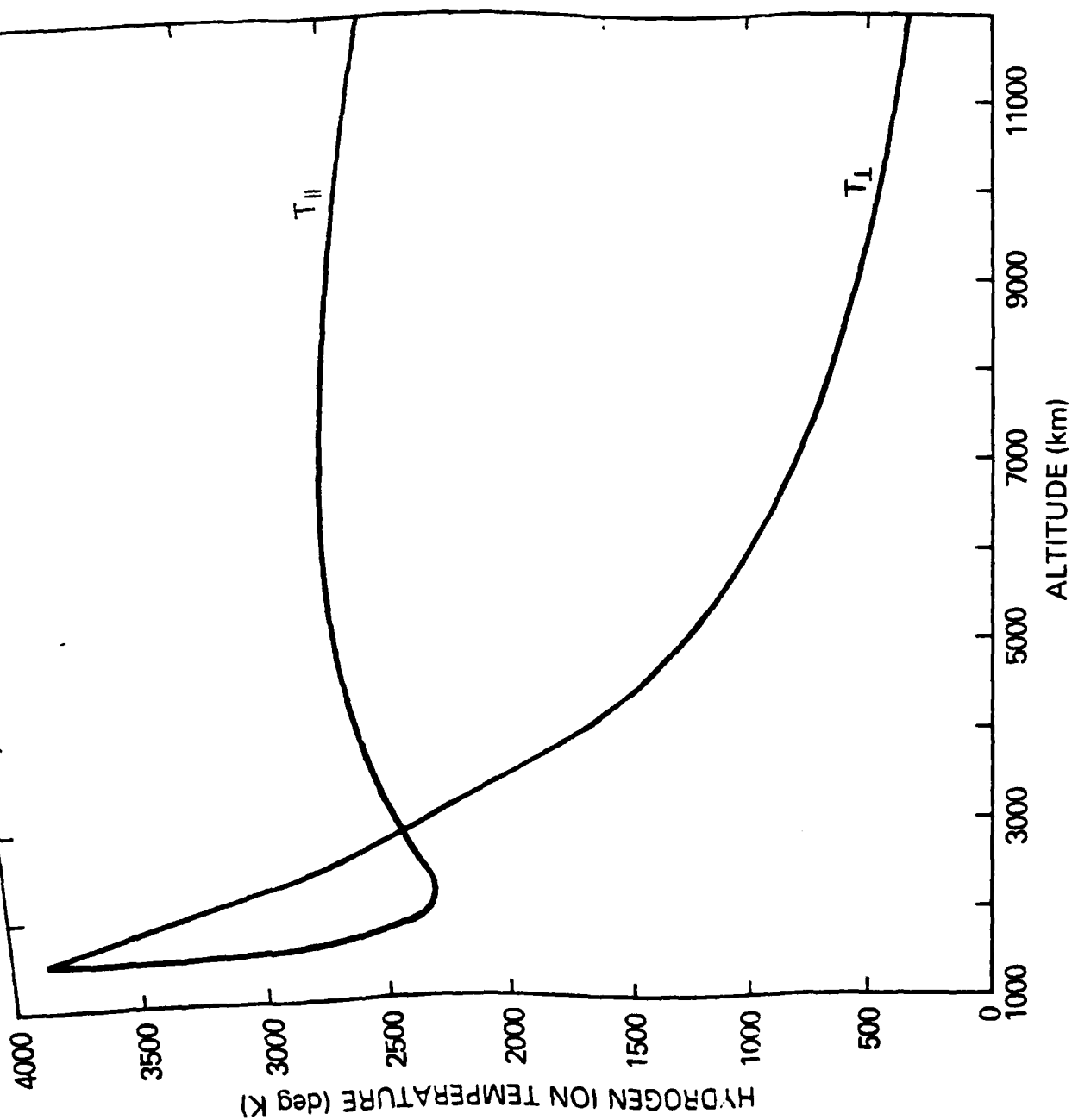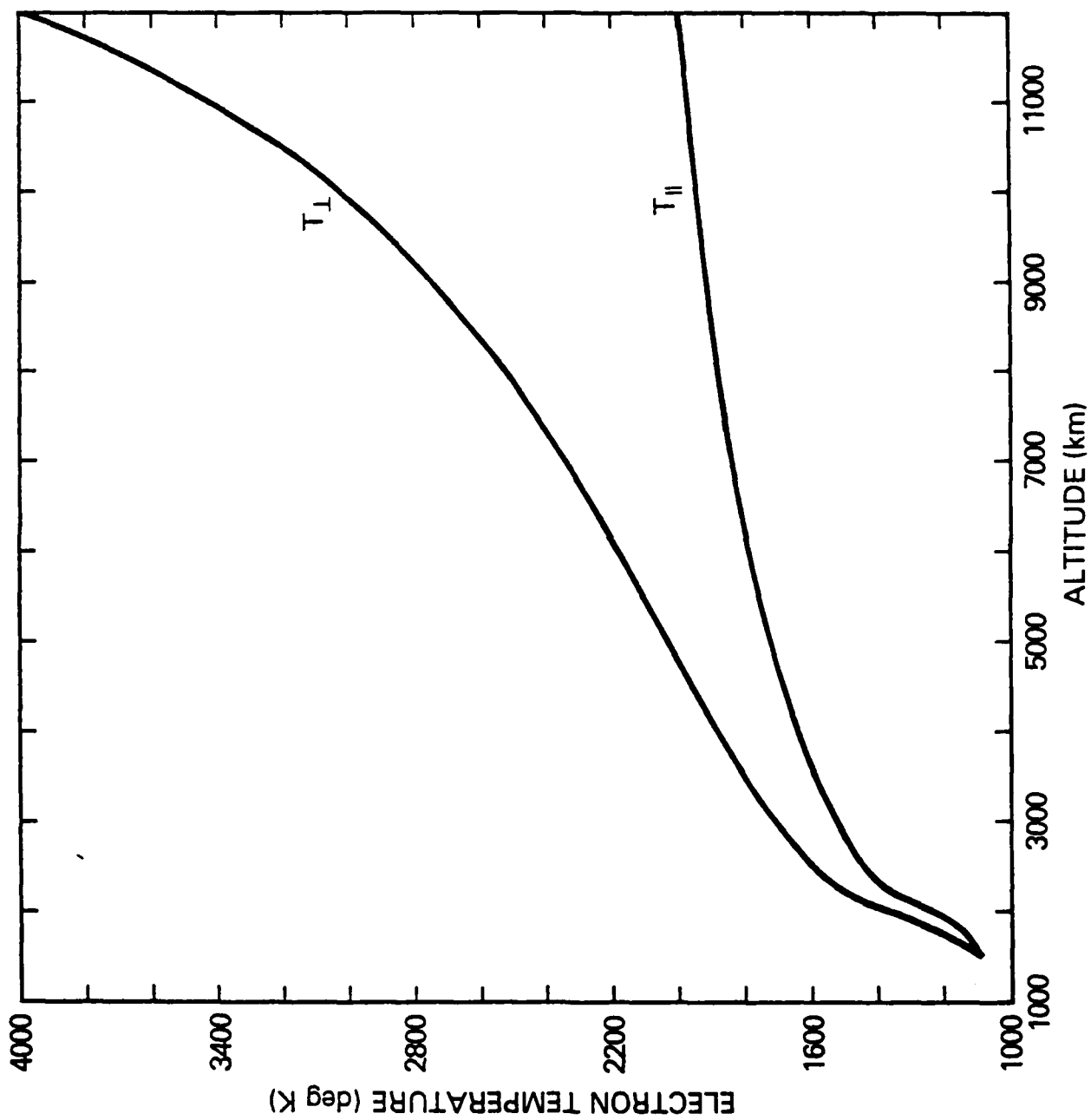
APPENDIX G

Stabilization of the Collisional Current-Driven

Ion Cyclotron Instability

Stabilization of the Collisional Current-Driven Ion Cyclotron Instability

P.K. Chaturvedi
Science Applications, Inc.
McLean, VA 22102

S.L. Ossakow J.D. Huba and M.J. Keskinen
Plasma Physics Division
Naval Research Laboratory
Washington, D.C. 20375

September 1984

Abstract

A stabilization mechanism of the current-driven collisional electrostatic ion-cyclotron instability is considered based upon Dupree's resonance broadening theory. The theory considers kinetic ions $(k_\perp \rho_i \gtrsim 1)$ as well as fluid ions $(k_\perp \rho_i < 1)$. The nonlinear saturated amplitudes are estimated with application to the auroral ionosphere.

G-4

Table of Contents

1. INTRODUCTION

It is well known that obliquely propagating electrostatic ion-cyclotron (EIC) waves may be excited in a collisionless plasma by a relative streaming between electrons and ions parallel to the ambient magnetic field [Drummond and Rosenbluth, 1962]. The effect of weak and strong electron collisions on this instability has been considered by many workers [Kindel and Kennel, 1971; Milich, 1972; Chaturvedi and Kaw, 1975] while the role of ion-ion collisions was examined by Varma and Bhadra (1964). The electron collisions facilitate growth of the wave while ion collisions are stabilizing. Physically, the instability is related to the dissipative effect on electrons in their parallel motion which impedes the "instantaneous" redistribution of the electron fluid to a Boltzman-like distribution in the wave potential. In the collisionless limit, the dissipation is due to the wave-particle (Landau) resonance, while in the collisional case, it is caused by the electron collisions with ions (or neutrals). When the electron drift velocity exceeds the parallel wave phase velocity, the EIC wave becomes unstable. The nonlinear stabilization of the collisionless EIC instability has been presented by Dum and Dupree (1970) based on the resonance broadening mechanism of Dupree (1966). In this work, we extend Dum and Dupree's theory to the case of the collisional EIC instability. Physically, the effect of the turbulence generated by the instability may be interpreted as an enhanced ion viscosity.

Kindel and Kennel (1971) have suggested that the EIC instability has the lowest threshold for excitation among various low frequency ion waves in the topside auroral ionosphere which is characterized by field-aligned currents. The possibility of excitation of EIC waves by field-aligned currents at lower altitudes (such as the upper E- and F-regions) has also

been considered by D'Angelo (1973) and Chaturvedi (1976). There have been some observations which indicate that EIC waves may have been observed in these regions of the auroral ionosphere [Bering et al., 1975; Ogawa et al., 1981; Yau et al., 1983; Bering, 1984; Fejer et al., 1984; Basu et al., 1984. At such altitudes the collisional excitation of EIC waves would obviously be a likely possibility. We present estimates of the saturated amplitudes of EIC waves for the auroral situations. In the next section, we outline the theory and then discuss the result in the ionospheric context in the final section.

2. THEORY

The coordinate frame for the auroral application considered here has the z-axis aligned with the earth's magnetic field $B_0 \hat{z}$, and the y- and x-axes point in the northward and westward directions, respectively. In equilibrium, a field-aligned current $J_0 \hat{z}$ is assumed to flow owing to electrons drifting with a speed $V_0 \hat{z}$ relative to ions. The electron dynamics is considered in the collisional limit and is described by fluid equations. This treatment is valid for $\nu_e > \omega$ and $k_\parallel \lambda_e < 1$, where ν_e is the electron colision frequency, ω the wave frequency, k the wavenumber ($\parallel$ and $\perp$ denote parallel and perpendicular to the magnetic field, respectively), and λ_e is the electron mean free path. Here $\lambda_e = v_e/\nu_e$, where $v_e = (T_e/m_e)^{1/2}$ is the electron thermal speed and we have expressed temperature in energy units. For ions, we use the Vlasov equation, which allows consideration of the transverse wavelengths in the regime $k_\perp \rho_i \sim 1$, where $\rho_i = v_i/\Omega_i$ is the mean ion Larmor radius. The dispersion relation for the ion-cyclotron waves, in the linear approximation, is

$$1 + \epsilon_e^\ell(\underline{k}, \omega) + \epsilon_i^\ell(\underline{k}, \omega) = 0 \tag{1}$$

where $\epsilon_{e,i}^\ell$ are the electron and ion contributions to the plasma dielectric constant in the small amplitude limit.

A derivation of the expression for ϵ_e^ℓ is as follows. The equations used are

$$\frac{\partial n_e}{\partial t} + \nabla \cdot (n_e \underline{v}_e) = 0 \tag{2}$$

$$0 = - \nabla p_e - e n_e \left(- \nabla \phi + \frac{\underline{v}_e \times \underline{B}_0}{c} \right) - m_e n_e \nu_e \underline{v}_e \tag{3}$$

$$p = nT \tag{4}$$

Using the expansions, $n = n_0 + \tilde{n}$, $\underline{v}_e = V_0 \hat{z} + \underline{\tilde{v}}$, $\phi = \tilde{\phi}$, the perturbed electron velocities are given by

$$\underline{\tilde{v}}_\parallel \simeq - i \frac{v_e^2}{\nu_e} \underline{k}_\parallel \left(\frac{\tilde{n}}{n_0} - \frac{e\tilde{\phi}}{T_e} \right) \tag{5}$$

and

$$\underline{\tilde{v}}_\perp \simeq i \frac{v_e^2}{\Omega_e} \left(- \frac{\nu_e}{\Omega_e} \underline{k}_\perp + \underline{k}_\perp \times \hat{z} \right) \left(\frac{\tilde{n}}{n_0} - \frac{e\tilde{\phi}}{T_e} \right) \tag{6}$$

Combining (2), (5), and (6) gives us the desired expression

$$\epsilon_e^\ell = \frac{\omega_e^2}{k^2 v_e^2 \left[1 - i \frac{\tilde{\omega} \, \nu_e}{v_e^2 k_\parallel^2} \left(1 + \frac{v_e^2}{\Omega_e^2} \frac{k_\perp^2}{k_i^2} \right) \right]} \tag{7}$$

where $\omega_e = (4\pi n_0 e^2/m_e)^{1/2}$ is the electron plasma frequency, and

$$\tilde{\omega} = \omega - k_\parallel V_0. \tag{8}$$

We shall use the collisionless expression for the ions which has been derived in many places [e.g., Dum and Dupree, 1970]

$$\varepsilon_i^\ell(\underline{k}, \omega) = \frac{\omega_i^2}{k^2 v_i^2} Z \left[(1 - \Gamma_0(\mu_i)) - \sum_{n=1}^{\infty} \frac{2\omega^2}{\omega^2 - n^2 \Omega_i^2} \Gamma_n(\mu_i) \right.$$

$$\left. - \frac{\Gamma_i(\mu_i)}{2\alpha_i^2} \frac{\omega}{(\omega - \Omega_i)} + i\left(\frac{\pi}{2}\right)^{1/2} \frac{\omega}{|k_\parallel| v_i} \exp\left(-\alpha_i^2\right) \Gamma_i(\mu_i) \right] \tag{9}$$

where $2\alpha_i^2 = |(\omega - \Omega_i)/k_\parallel v_i|^2$, and Z is the ion charge.

Using (7) and (9) in (1) gives the linear dispersion equation for the EIC modes,

$$\frac{(\omega - \Omega_i)}{\Omega_i} \simeq Z \frac{T_e}{T_i} \Gamma_i \left[1 - i \frac{v_e \tilde{\omega}}{k_\parallel^2 v_e^2} \right] \tag{10}$$

where we made the following approximations, $n = 1$, $\alpha_i^2 \gg 1$, $(\omega - \Omega_i)/\Omega_i \ll 1$, $(v_e/\Omega_e)(k_\perp/k_\parallel) \ll 1$. From (10), one obtains the real frequency of the modes, with, $\omega = \omega_r + i\gamma$, and, $|\gamma| \ll \omega_r$,

$$\omega_r - \Omega_i \simeq \frac{Z T_e}{T_i} \Omega_i \Gamma_1 \tag{11}$$

For $\mu_i \ll 1$ (the long transverse wavelength approximation), one obtains the familiar dispersion relation for EIC modes in the fluid limit,

$$\omega_r \simeq \Omega_i \left(1 + \frac{1}{2} \frac{k_\perp^2 c_s^2}{\Omega_i^2} \right) \tag{12}$$

where $C_s = [(T_e + T_i)/m_i]^{1/2}$ is the ion acoustic speed, and $Z = 1$ has been assumed.

Similarly the growth rate is given by

$$\gamma_k^\ell \simeq -\frac{T_e}{T_i} \Omega_1 \Gamma_1 \frac{m_e \nu_e}{T_e k_\parallel^2} \{\omega_r - k_\parallel V_o\} \tag{13}$$

which, for the case $\mu_1 < 1$, becomes [Chaturvedi and Kaw, 1975],

$$\gamma_k^\ell \simeq \{\frac{m_e}{2m_i}\}\frac{k_\perp^2}{k_\parallel^2} \nu_e \{-1 + \frac{k_\parallel V_o}{\omega_r}\}. \tag{14}$$

Thus, the expressions (12) and (14) refer to the long wavelength $\lfloor k_\parallel \lambda_e \ll 1, k_\perp^2 \rho_i^2 \ll 1 \rfloor$ EIC instability in a collisional plasma. An application of this instability has previously been discussed for the auroral E- and F-region situations [Chaturvedi, 1976].

The nonlinear dispersion relation for the electrostatic ion-cyclotron modes, including the effects of resonance broadening, may be obtained by substituting $\bar{\omega} \equiv \omega + i\Delta\omega^w$ in lieu of ω in the ion contribution to the dielectric constant (ϵ_i) in (1) [Dum and Dupree, 1970]. Here $\Delta\omega^w$ is the modification introduced by the effect of a spectrum of finite amplitude modes on the particle orbits (resonance broadening effect). Thus,

$$1 + \epsilon_e^\ell(\underline{k}, \omega) + \epsilon_i^{n\ell}(\underline{k}, \omega + i\Delta\omega^w) = 0 \tag{15}$$

is the nonlinear dispersion relation for the EIC modes. We note that Dum and Dupree [1970] have shown the effect of resonance broadening is important only for ions in the EIC wave case. Hence the contribution coming from the resonance broadening effect on electrons has been ignored

G-11

in the expression (15). An expression for $\Delta\omega^W$ has been given by Dum and Dupree [1970],

$$\Delta\omega_k^W = \frac{k_\perp^2 c^2}{B_0^2} \sum_k |E_{k_\perp}|^2 F_1\left(\frac{k_\perp v_\perp}{\Omega_i}\right)\left(\frac{1}{\omega - \Omega_i}\right)\left[\frac{\Delta\omega_k/(\omega - \Omega_i)}{1 + \left(\frac{\Delta\omega_k}{\omega - \Omega_i}\right)^2}\right] \quad (16)$$

where $\Delta\omega^W/(\omega - \Omega_i) \ll 1$.

A simple expression may be obtained from (15) for EIC modes,

$$1 + \frac{\omega_e^2}{k^2 v_e^2} \frac{1}{\left(1 - i\frac{\nu_e \tilde{\omega}}{v_e^2 k_\parallel^2}\right)} + \frac{\omega_i^2}{k^2 v_i^2}\left[-\frac{\Omega_i \Gamma_1(\mu_i)}{(\omega + i\Delta\omega_k^W - \Omega_i)}\right] = 0 \quad (17)$$

where ion-cyclotron damping has been neglected. One may obtain a nonlinear growth rate $\gamma^{n\ell}$ for EIC modes from (17) which is assumed to vanish at the saturation level,

$$\gamma^{n\ell} = \gamma_k^\ell - \Delta\omega^W = 0 \quad (18)$$

For the EIC case, $\Delta\omega^W$ may be approximated as [Dum and Dupree, 1970],

$$\Delta\omega^W = (\omega - \Omega_i)\left[\left(\frac{n_1}{n_1^0}\right)^2 - 1\right]^{1/2} \quad (19)$$

where $n_1/n_1^0 \gtrsim 1$, and it has been assumed that nonlinear resonance broadening dominates quasilinear and collisional broadening. Here n_1 is the saturated nonlinear amplitude of the wave, and, n_1^0 is the threshold level of the nonlinear amplitude at which the resonance broadening effects assume importance. The expression for n_1^0 is

$$\frac{n_1^0}{n} = \left(\frac{T_i}{2T_e}\right)\left(\frac{\Omega_i}{k_\perp v_i}\right)^2 \frac{\{\omega_k - \Omega_i\}}{\Omega_i \{F_1(\mu_i)\}^{1/2}}$$

$$\simeq \left(\frac{T_i}{2T_e}\right) \frac{1}{\mu_i \{F_1\}^{1/2}} \left(\frac{\omega - \Omega_i}{\Omega_i}\right) \qquad (20)$$

where $\quad F_1(x) \simeq \begin{cases} \frac{1}{4}\left[1 - \frac{1}{4}\left(\frac{x}{2}\right)^4 + \frac{1}{9}\left(\frac{x}{2}\right)^6 + \ldots, \text{ for } x < 2 \right. \\ \frac{1}{\pi x} \qquad\qquad\qquad\qquad\qquad\qquad x > 3 \end{cases} \qquad (21)$

It may be noted that the broadening of resonances above corresponds to an enhancement in the group of ions that can exchange energy with the wave via resonance interaction. Stabilization of the mode results when the resonance is broadened to an extent such that the bulk of the ion distribution interacts with the wave and absorbs energy from it, thereby, leading to a steady finite amplitude nonlinear state. We now use expressions (18)-(20), and (11)-(13) to compute the nonlinear saturated amplitudes for the collisional EIC modes. From (18) and (19), one has

$$\{\omega - \Omega_i\}\left[\left(\frac{n_1}{n_1^0}\right)^2 - 1\right]^{1/2} \simeq \gamma_k^\ell \qquad (22)$$

which leads to

$$\left(\frac{n_1}{n}\right)^2 \simeq \left(\frac{n_1^0}{n}\right)^2\left[1 + \frac{(\gamma_k^\ell)^2}{\{\omega - \Omega_i\}^2}\right]$$

or

$$\left(\frac{n_1}{n}\right)^2 \simeq \frac{\left(\frac{T_i}{T_e}\right)^2\left(\frac{\Omega_i}{k_\perp v_i}\right)^4\left(\frac{\omega_r - \Omega_i}{\Omega_i}\right)^2}{F_1\left(\frac{k_\perp v_\perp}{\Omega_i}\right)}\left[1 + \frac{\left\{\frac{T_e}{T_i}\Omega_i\Gamma_1\frac{\nu_e}{k_\perp^2 v_e^2}\{k_\parallel V_0 - \omega_r\}\right\}^2}{\{\omega_r - \Omega_i\}^2}\right]. \qquad (23)$$

For the case, $T_e \simeq T_i$, one has

$$(\omega - \Omega_i) \simeq \Omega_i \Gamma_i$$

Then

$$\left(\frac{n_i}{n}\right)^2 \simeq \frac{\left(\frac{\Omega_i}{k_\perp v_i}\right)^4 \Gamma_i^2}{\frac{k_\perp v_\perp}{F_i\left(\frac{k_\perp v_\perp}{\Omega_i}\right)}} \left[1 + \left\{\frac{\nu_e}{k_\parallel^2 v_e^2} \left(k_\parallel v_o - \omega_r\right)\right\}^2\right] \qquad (24)$$

The expression (24) gives the saturated nonlinear amplitudes of the collisional ion-cyclotron modes due to resonance broadening effects. A comparison with the collisionless case, discussed by Dum and Dupree [1970], shows that the saturated amplitudes can be higher in the collisional case, by an increment of approximately $\sim \frac{1}{2}\left[\left(v_o/v_e\right)\left(1/k_\parallel \lambda_e\right)\right]^2$. We note that, in the above comparison, it is implied that $\gamma_{kc}/(\omega_k - \Omega_i) \ll 1$, where γ_{kc} is the collisionless growth rate.

3. DISCUSSION

We have considered the saturation of the collisional current-driven electrostatic ion-cyclotron instability due to the resonance broadening mechanism of Dupree [1966]. This work represents an extension of a similar saturation mechanism proposed for the case of current-driven collisionless EIC instability by Dum and Dupree [1970]. For the collisional EIC instability , the nonlinear stabilization may lead to larger saturated amplitudes than in the collisionless case. One may also note that in the collisional case, the linear growth rates are larger than the corresponding collisionless growth rates. The collisional EIC instability considered

here is applicable to the longer parallel wavelengths, while the transverse scale size is in the range $k_\perp \rho_i < 1$ to $k_\perp \rho_i > 1$. It should be noted that the present paper considers kinetic ions, i.e., $k_\perp \rho_i > 1$, in contrast to the previous work of Chaturvedi [1976], which considered fluid ions, i.e., $k_\perp \rho_i \ll 1$. Dupree's resonance broadening theory is valid only for a broad spectrum of waves which are assumed isotropic and incoherent, i.e., the wave coherence time (spectral width) is much shorter than an ion cyclotron period. For a narrow coherent wave spectrum resonance broadening theory must be replaced by an analysis which considers exact ion dynamics in a coherent wave [Davidson, 1972; Aamodt, 1970]. Recent nonlinear numerical simulations [Pritchett et al., 1981; Okuda and Ashour-Abdalla, 1981] of the collisionless ion cyclotron instability indicate a large amplitude coherent wave spectrum in the nonlinear regime. However these simulations also show several modes excited in the saturation phase of the ion cyclotron instability. To our knowledge, there have been no nonlinear simulations of the collisional current-driven ion cyclotron instability. We shall now discuss some particular examples of the auroral ionospheric application of the collisional EIC instability.

In a recent rocket experiment [Bering, 1984], ion-cyclotron waves were observed at the F-region altitudes ($\sim$ 237 kms). For this region of auroral ionosphere, we have $T_e \sim T_i \sim 0.1$ eV, $\Omega_{0^+} \sim 3.0 \times 10^2$ sec^{-1}, $\nu_e \sim 2 \times 10^3$ sec^{-1}, etc. For the collisional excitation of the modes with $\lambda_\perp \sim 10m$ and $\lambda_\parallel \sim 500m$ (100m), one needs $V_0 \gtrsim 2.0 \times 10^6$ cm sec^{-1} for the instability. In this case the growth rate is $\gamma^\ell / \Omega_i \sim 10^{-3}$. Recent DE and Hilat satellite observation has measured the currents of this magnitude in the auroral F-region [Bythrow et al., 1984; Sugiura et al., 1984]. We use the value of $V_0 \sim 3.0 \times 10^6$ cm sec^{-1} from Bythrow et al. data to compute the

saturated amplitude for EIC waves from (24). The saturated amplitude is found to be, $n_1/n_0 \approx 0.25$, or a 25% density fluctuation level. The saturated amplitude estimates presented above is comparable to the experimental observations. We also note that the saturated amplitudes for the parameters cited above are slightly larger for the collisional case than the collisionless case when for the same parameters, the *saturation amplitude would be 22.8%.* Large amplitude saturation has also been reported in the laboratory experiments of the EIC waves [Bohmer and Fornaca, 1979]. Finally, we mention that in the auroral ionosphere, the currents would vary with respect to the altitude $|$ i.e.,$J_1(z)$ or $n_0(z)e \ V_0(z)|$, and that the plasma may also be in transverse motion which may be sheared. We are currently studying these effects on the linear and nonlinear aspects of collisional EIC waves for the auroral ionosphere.

ACKNOWLEDGMENTS

REFERENCES

Aamodt, R.E., Particle motion in the presence of three dimensional finite amplitude harmonic cyclotron waves, Phys. Fluids., 13, 2341, 1970.

Basu, Su., S. Basu, E. MacKenzie, W.R. Coley, W.B. Hanson and C.S. Lin, F region electron density irregularity spectra near auroral acceleration and shear regions, J. Geophys. Res., 89, 5554, 1984.

Bering, E.A., M.C. Kelley and F.S. Mozer, Observations of an intense field-aligned thermal ion flow and associated intense narrow band electric field oscillations, J. Geophys. Res., 80, 4612, 1975.

Bering, E.A., Apparent electrostatic ion cylotron waves in the diffuse aurora, Geophys. Res. Lett., 10, 647, 1983a.

Bering, E.A., The plasma wave environment of an auroral arc: Electrostatic ion cyclotron waves in the diffuse aurora, J. Geophys. Res., 89, 1635, 1984.

Bohmer, H. and S. Fornaca, Experiments on nonlinear effects of strong ion-cyclotron wave turbulence, J. Geophys. Res., 84, 5234, 1979.

Burke, W.B., M. Silevitch and D. Hardy, Observations of small scale auroral vortices by the S3-2 satellite, J. Geophys. Res., 88, 3127, 1983.

Bythrow, P.F., T.A. Potemra, W.B. Hanson, L.J. Zanetti, C.-I. Meng, R.E. Huffmann, F.J. Rich and D.A. Hardy, Earthward directed high density Birkeland currents observed by HILAT, J. Geophys. Res., 89, 9114, 1984.

Chaturvedi, P.K. and P.K. Kaw, Current driven ion cyclotron waves in collisional plasma, Plasma Phys., 17, 447, 1975.

Chaturvedi, P.K., Collisional ion cyclotron waves in the auroral ionosphere, J. Geophys. Res., 81, 6169, 1976.

Davidson, R.C., Methods in Nonlinear Plasma Theory, Academic, New York, 1972.

Drummond, W.E. and M.N. Rosenbluth, Anomalous diffusion arising from microinstabilities in a plasma, Phys. Fluids, 5, 1507, 1962.

Dum, C.T. and T.H. Dupree, Nonlinear stabilization of high frequency instabilities in a magnetic field, Phys. Fluids, 13, 2064, 1970.

Dupree, T.H., A perturbation theory for strong plasma turbulence, Phys. Fluids, 9, 1773, 1966.

D'Angelo, N., Type 3 spectra of the radar aurora, J. Geophys. Res., 78, 3987, 1973.

Fejer, B.G., R.W. Reed, D.T. Farley, W.E. Swartz and M.C. Kelley, Ion cyclotron waves as a possible source of resonant auroral radar echoes, J. Geophys. Res., 89, 187, 1984.

Kelley, M.C., E.A. Bering and F.S. Mozer, Evidence that the electrostatic ion cyclotron instability is saturated by ion heating, Phys. Fluids, 18, 1590, 1975.

Kindel, J.M. and C.F. Kennel, Topside current instabilities, J. Geophys. Res., 76, 3055, 1971.

Milich, B., Spontaneous excitation of the long-wave ion-cyclotron and ion-acoustic oscillations in fully ionized plasmas, Phys. Fluids, 15, 1630, 1972.

Ogawa, T., H. Mori, S. Miyazaki, and H. Yanagishi, Electrostatic plasma instabilities in highly active aurora, Mem. Natl. Inst. Polar Res. Spec. Issue Japan, 18, 312, 1981.

Okuda, H. and M. Ashour-Abdulla, Formation of a conical distribution and intense ion heating in the preence of hydrogen cyclotron waves, Geophys. Res. Lett. 8, 811, 1981.

Pritchett, P.L., M. Ashour-Abdalla, and J.M. Dawson, Simulation of the current-driven electrostatic ion cyclotron instability, Geophys. Res. Lett. 8, 611, 1981.

Sugiura, M., T. Iyemori, R.A. Hoffman, N.C. Maynard, J.L. Burch, and J.D. Winningham, Relationships between field-aligned currents, electric fields, and particle precipitation as observed by Dynamics Explorer-2, in Magnetospheric Currents, Geophys. Monogr. Ser., Vol. 28, pp. 96-103, AGU, edited by T.A. Potemra, Washington, D.C., 1984.

Sugiura, M. et al., Relationships between field-aligned currents, electric fields, and particle precipitation as observed by Dynamics Explorer-2, NASA Memorandum 85025, 1983.

Varma, R.K. and D. Bhadra, Collisional effects in a hot plasma at ion gyro-frequency, Phys. Fluids, 7, 1082, 1964.

Yau, A.W., B.A. Whalen, A.G. McNamara, P.J. Kellog, and W. Bernstein, Particle and wave observations of low-altitude ionospheric acceleration events, J. Geophys. Res., 88, 341, 1983.

APPENDIX H

Production and Control of Ion Cyclotron Instabilities

in the High Latitude Ionosphere by High Power

Radio Waves

PRODUCTION AND CONTROL OF ION CYCLOTRON

INSTABILITIES IN THE HIGH LATITUDE IONOSPHERE

BY HIGH POWER RADIO WAVES

P.K. Chaturvedi
Science Applications International Corporation
McLean, Virginia 22102

M.J. Keskinen
Geophysical and Plasma Dynamics Branch
Plasma Physics Division
Naval Research Laboratory
Washington, D.C. 20375-5000

and

S.L. Ossakow
Plasma Physics Division
Naval Research Laboratory
Washington, D.C. 20375-5000

December 1984

Abstract

The possible generation and suppression of ion cyclotron waves in a collisional plasma by external high power electromagnetic waves with frequency close to the local upper-hybrid frequency is considered. It is shown that the ion-cyclotron instability can be destabilized (stabilized) for $\omega_0 < \omega_{uh}$ ($\omega_0 > \omega_{uh}$). The results are applied to naturally occurring ion cyclotron instabilities in the high latitude ionosphere.
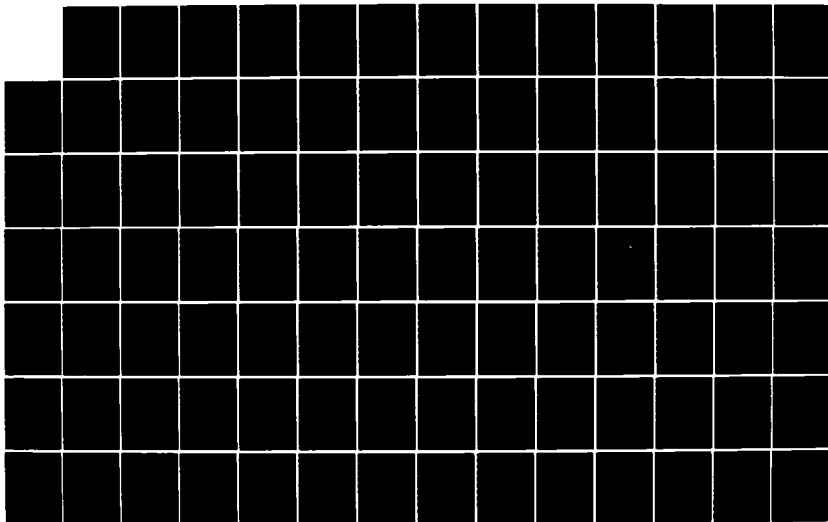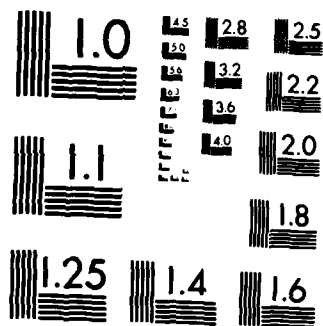
MICROCOPY RESOLUTION TEST CHART
NATIONAL BUREAU OF STANDARDS-1963-A

1. INTRODUCTION

It is now recognized that many of the phenomena occurring in the auroral ionosphere may be associated with the presence of the field-aligned current-systems which are a constant feature at these latitudes [see e.g., Burke, 1981]. In addition to being a key component of the ionosphere-magnetosphere coupling circuit, these currents may also be responsible in generating micro-and/or macro-structures (turbulence) in the ambient plasmas at low altitudes. Such structures have been observed by various measurement techniques (ground based ionosound, VHF radar backscatter, optical measurements, scintillations, in-situ rocket and satellite measurements, etc.) A catalogue of the structure scale sizes spans the domain from a few meters to a few hundred of kilometers [see e.g., Aarons, 1973; Clark and Raitt, 1976; Dyson, 1969; Dyson and Winningham, 1974; Frenouw et al., 1977; Greenwald, 1974; Hanuise et al., 1981; Hower et al., 1966; Kelley et al., 1980; Ogawa et al., 1976; Olesen et al., 1976; Phelps et al., 1976; Sagalyn et al., 1974; Vickrey et al., 1980; Weaver, 1965]. Recent theoretical studies have attempted to interpret these structures in terms of plasma instabilities, neutral turbulence, structured particle precipitation, convection flows, etc. [Keskinen and Ossakow, 1983. Due to the ever-varying conditions prevalent in the auroral ionosphere, it seems likely that all of these processes may be occuring at one time or another. In some instances, different processes can result in similar observable effects which makes the resolution of individual mechanisms difficult and introduces complications in the modelling process. The use of active experiments in the near-earth space offers an attractive complement to the studies of understanding of natural plasma processes occurring in the ionosphere. One technique that has been widely used is

the modification of ionosphere using powerful radio waves (Utlaut, 1970; Fialer, 1974; Thide et al., 1982; Stubbe et al., 1981; Wong et al., 1981] Considerable amount of theoretical work has been done in this field [Perkins and Kaw, 1971; Perkins et al., 1974; Fejer, 1979; Vaskov and Gurevich, 1977; Das and Fejer, 1979; Stenflo, 1983]. One of the possible consequences of the interaction of a large amplitude EM wave with the ionosphere is the generation of structures in the ambient plasma density. This may come about several ways; one of them being the excitation of plasma instabilities by an electromagnetic pump wave under sub-threshold conditions. By the same token, one could use the same principle of parametric coupling of the external pump and the natural plasma modes to suppress a current-driven or gradient-driven plasma instability in the system. Work on basic parametric instability processes in plasmas is exhaustive [Silin, 1965; DuBois and Goldman, 1965; Nishikawa, 1968]. The application of these ideas to the possible control of ionospheric irregularities was originally made by Lee et al. [1972] for the case of equatorial electrojet; and, has since been applied for the equatorial spread F situation [Bujarbarua and Sen, 1978] and the auroral ionosphere [Keskinen et al., 1983]. In this report, we examine the possibility of external control (excitation or suppression) of the current-driven ion-cyclotron instability in the auroral ionosphere. In addition to being excited in the topside ionosphere [Kindel and Kennel, 1971], the current-driven ion cyclotron instability may also be triggered in the collisional bottomside ionosphere [Chaturvedi, 1976; Satyanaryana et al., 1985; Fejer et al., 1984] by a radio-wave at the local upper-hybrid frequency. In the

next section, we outline the theory, and, estimate the incident power density required to stabilize or destabilize the instability. The final section considers application of these results to the bottomside high latitude F region ionosphere.

II. THEORY

We follow the theoretical procedure outlined in Lee et al. [1972] and Keskinen et al. [1983] for the calculation of the dynamic plasma response to an large amplitude electromagnetic pump wave. The equilibrium consists of a field-aligned current $J_0\hat{z}(= - n_0eV_0\hat{z})$ and an oscillating electric field $\underline{E}_0 = \underline{E}_p \cos \omega_0 t$. We have equated the zero-order current to an equilibrium electron drift $v_0\hat{z}$ and have used the so-called dipole approximation for the pump wave which is valid when the wavelength of the perturbations $(\sim k^{-1})$ is considered much smaller than the scalesize of the variation of the pump-field (k_0^{-1}), i.e., $k_0 \ll k$. We shall use the two-fluid equations in describing the electron - and ion - fluid dynamics,

$$\frac{\partial}{\partial t} N_\alpha + \nabla \cdot \left(N_\alpha \underline{v}_\alpha\right) = 0 \tag{1}$$

$$N_\alpha M_\alpha \left(\frac{\partial}{\partial t} + \underline{v}_\alpha \cdot \nabla\right)\underline{v}_\alpha = - \nabla p_\alpha \pm eN_\alpha \left(\underline{E} + \frac{\underline{v}_\alpha \times \underline{B}_0}{c}\right) - \nu_\alpha M_\alpha N_\alpha \underline{v} \tag{2}$$

$$p_\alpha = N_\alpha T_\alpha \tag{3}$$

$$\nabla \cdot \underline{E} = 4\pi e\left(N_i - N_e\right) \tag{4}$$

We initially assume cold ions $\left(T_i = 0\right)$, Later, we will present results that include the ion-temperature effects $\left(T_i \neq 0\right)$. All symbols in Eq. (1)-(4)

retain their conventional meaning. Since we restrict this study to bottom-side altitudes we take $\nu_{ii} \leq \nu_{in}$ where ν_{ii} is the ion-ion collision frequency and ν_{in} the ion-neutral collision frequency. In equilibrium, we have

$$\nabla \cdot N_0 \left(\underline{V}_\alpha + \underline{V}_{\alpha p} \right) = 0 \tag{5}$$

$$0 = \pm \frac{e}{m_\alpha} \left(\underline{E}_0 + \frac{\underline{V}_{\alpha 0} \times \underline{B}}{c} \right) - \nu_\alpha \underline{V}_{\alpha 0} - \nabla p_{\alpha 0} \tag{6}$$

$$\frac{d\underline{V}_{\alpha p}}{dt} = \pm \frac{e}{m_\alpha} \left(\underline{E}_p + \frac{\underline{V}_{\alpha p} \times \underline{B}}{c} \right) - \nu_\alpha \underline{V}_{\alpha p} \tag{7}$$

where $\alpha = e,i$, and $\underline{V}_0$ and $\underline{V}_p$ refer to drifts induced by the ambient and pump fields, respectively. Note that eq. (7) describes the equilibrium oscillatory motion of plasma particles under the action of the RF electromagnetic field. Linearizing (1) – (4) for perturbations, $f_\alpha = f_{\alpha 0} + \delta f_\alpha$, and assuming $\delta f_\alpha \ll f_{\alpha 0}$, we obtain

$$\frac{\partial}{\partial t} \delta n_\alpha + \left(\underline{V}_{\alpha 0} + \underline{V}_{\alpha p} \right) \cdot \nabla \delta n_\alpha + \delta \underline{V}_\alpha \cdot \nabla N_0 + N_0 \nabla \cdot \delta \underline{V}_\alpha = 0 \tag{8}$$

$$\frac{\partial \delta \underline{V}_\alpha}{\partial t} + \left(\underline{V}_{\alpha 0} + \underline{V}_{\alpha p} \right) \cdot \nabla \delta \underline{V}_\alpha = \pm \frac{e}{m_\alpha} \left[\delta \underline{E} + \frac{\delta \underline{V}_\alpha \times \underline{B}}{c} \right] - \frac{\nabla \delta p_\alpha}{m_\alpha N_0} - \nu_\alpha \delta \underline{V}_\alpha \tag{9}$$

$$\nabla \cdot \delta \underline{E} = 4\pi e \left(\delta n_i - \delta n_e \right) \tag{10}$$

It is convenient to transform to an oscillating frame, defined by

$$\underline{r}'_j = \underline{r} - \underline{R}_j(t)$$

H-8

$$\frac{d\underline{R}_j(t)}{dt} = \underline{v}_{\alpha 0}$$

The plasma quantities in the oscillating frame are $\tilde{f}_\alpha'(\tilde{\underline{r}}_\alpha', t) = f_\alpha'(r_\alpha, t)$ where f stands for $(N, \underline{v}_j, \underline{E})$, and tildes denote the oscillating frame quantities. Equations (8) - (9) are similar in the oscillating frame, with substitutions $(V_{\alpha 0} + V_{\alpha p}) \to V_{\alpha 0}$, $\delta n_\alpha \to \delta \tilde{n}_\alpha$, $\delta \underline{V}_\alpha \to \delta \tilde{\underline{v}}_\alpha$, $\delta \underline{E} \to \delta \tilde{\underline{E}}$ and $\underline{r} \to \tilde{r}_\alpha$. Assuming a harmonic perturbation, $\exp[i(\underline{k} \cdot \tilde{\underline{r}}_\alpha - \omega t)]$ with $\underline{k} = (k_x x + k_y y + \kappa_z z)$ and $\omega = \omega_r + i\gamma$, we may combine (8) and (9) as

$$- i\tilde{\omega} \frac{\tilde{N}_\alpha}{N_0} + \frac{1}{(1 + \frac{\Omega_\alpha^2}{\tilde{\nu}_\alpha^2})} \left[i \frac{c}{B_0} \frac{\Omega_\alpha}{\tilde{\nu}_\alpha} \underline{k}_\perp \cdot \tilde{\underline{E}}_\perp' + \frac{ck^2}{B_0 q_\alpha} \frac{\Omega_\alpha}{\tilde{\nu}_\alpha} \frac{\tilde{P}_\alpha'}{N_0} \right.$$

$$- \frac{\tilde{N}_\alpha'}{N_0} i\underline{k}_\perp \cdot \nabla P_{\alpha 0} \frac{\Omega_\alpha}{\tilde{\nu}_\alpha} \frac{c}{q_\alpha B_0} - i \frac{c}{q_\alpha} \frac{\Omega_\alpha^2}{\tilde{\nu}_\alpha^2} \frac{\tilde{N}_\alpha'}{N_0} \left(\frac{\underline{k}_\perp \cdot \nabla P_{\alpha 0} \times \underline{B}_0}{B_0^2} \right) \tag{12}$$

$$+ \frac{c}{B_0} \frac{\Omega_\alpha}{\tilde{\nu}_\alpha} \tilde{\underline{E}}_\perp' \cdot \frac{\nabla N_0}{N_0} + \frac{c\Omega_\alpha^2}{\tilde{\nu}_\alpha^2} \frac{\delta \tilde{\underline{E}} \times \underline{B}_0}{B_0^2} \cdot \frac{\nabla N_0}{N_0} \right] = 0$$

where,

$$\tilde{\nu}_\alpha = \nu_\alpha - i\tilde{\omega}_\alpha, \quad \tilde{\omega}_\alpha = \omega - \underline{k} \cdot \underline{v}_0, \quad q_\alpha = \pm e, \quad \Omega_\alpha = \frac{q_\alpha B_0}{m_\alpha c}$$

Defining electron and ion susceptibilities, χ_e, χ_i, as

$$\delta \tilde{n}_e = \frac{ik\chi_e}{e} \tilde{\delta E},$$

$$\delta n_i = - i \ \frac{k \chi_i}{e} \ \delta \tilde{E}$$

We find that,

$$4\pi \chi_e = \frac{(\omega_{pe}^2/k^2)}{(\tilde{\omega}_e - \frac{v_e^2 k_z^2}{\hat{\omega}} + \omega \frac{v_e^2 k_\perp^2}{\Omega_e^2 - \omega^2}} \ (- \frac{k_z^2}{\omega} + \hat{\omega} \ \frac{k_\perp^2}{\Omega_e^2 - \omega^2}) \tag{13}$$

and

$$4\pi \chi_i = - \frac{\omega_{pi}^2 (1 + i \ \frac{\nu_i}{\omega})}{[(\omega + i\nu_i)^2 - \Omega_i^2]} \tag{14}$$

where

$$\omega_{p\alpha}^2 = \frac{4\pi n_0 e^2}{m_\alpha} \ , \ \omega = \tilde{\omega}_e + i\nu_e, \ v_\alpha^2 = (T_\alpha/m_\alpha).$$

We have used $\nabla N_0 = 0$, $T_i = 0$ in deriving (13) - (14). One now transforms back to the laboratory frame and writes down the dispersion relation for the modes by using the Poisson's equation. This transformation has been discussed in Lee et al. [1972], and the dispersion relation, thus obtained, is

$$[1 + 4\pi(\chi_i + \chi_e)] = - J_1^2(\zeta) 4\pi \ \chi_i (1 + 4\pi \ \chi_e) [\frac{1}{H_e(\omega_+)} + \frac{1}{H_e(\omega_-)}] \tag{15}$$

where $\omega_\pm = \omega \pm \omega_0$ and,

$$J_n(\zeta) = \frac{i^{-n}}{\pi} \int_0^\pi e^{i\zeta \cos\theta} \cos n\theta d\theta \tag{16}$$

and ζ is defined by $\underline{k} \cdot \underline{R} = \zeta \sin(\omega_0 t + \delta)$, and, $H_e = - \frac{1}{(4\pi \chi_e)}(1 + 4\pi \chi_e)$. Note that we have ignored the effect of pump wave on ions and have used the approximation $\zeta \ll 1$ in deriving (15) which states that the electron excursion length in the pump field is smaller than the perturbation wavelength. In absence of the pump field, the left hand side of (15) leads to the dispersion relation for ion-cyclotron waves [Chaturvedi, 1976],

$$(\omega + i\nu_i)^2 - \Omega_i^2 - [C_s^2 k^2 - i \frac{m_e}{m_i} \frac{k^2}{k_z^2} \nu_e(\omega - \kappa_z V_0)](1 + i \frac{\nu_i}{\omega}) = 0 \qquad (17)$$

which describes a resistive ion-cyclotron instability for modes with real frequency,

$$\omega_r^2 = \Omega_i^2 + k^2 C_s^2.$$

and growth rate   (18)

$$\gamma = - \frac{1}{2} \frac{m_e}{m_i} \frac{k^2}{k_z^2} \nu_e(1 - \frac{k_z V_0}{\omega_r}) - \nu_i$$

Here $C_s^2 = T_e/m_i$. An application of this instability for the auroral ionosphere has recently been discussed by Satyanarayana et al. [1985]. Physically, the instability is related to the dissipative effect on electrons in their parallel motion which impedes the "instantaneous" redistribution of the electron fluid to a Boltzmann-like distribution in the wave potential. In the collisionless limit, the dissipation is due to the wave-particle (Landau) resonance [Drummond and Rosenbluth, 1962], while in the collisional case, it is caused by the electron collisions with ions

(or neutrals) [Chaturvedi and Kaw, 1975]. When the electron drift velocity exceeds the parallel wave phase velocity, the EIC wave becomes unstable. In the presence of the pump-wave, the dispersion relation (15) is modified to

$$[(\omega + i\nu_i)^2 - \Omega_i^2 - \{k^2 c_s^2 + (m_e/m_i)(\hat{\omega}^2 - (k_z^2/k^2)\Omega_e^2)^{-1}(\hat{\omega}\,\hat{\omega}_e)(\Omega_e^2 - \hat{\omega}^2)\}]$$

$$\left(1 + i\frac{\nu_i}{\omega}\right) = A \tag{19}$$

which gives

$$\omega_r^2 = \Omega_i^2 + k^2 c_s^2 + A \tag{20}$$

and

$$\gamma = \frac{m_e}{2m_i} \frac{k^2}{k_z^2} \frac{\nu_e}{\bar{\Omega}_i} \left(k_z V_0 - \bar{\Omega}_i - \frac{A}{2\bar{\Omega}_i}\right) - \nu_i \tag{21}$$

where

$$A = 2J_1^2(\zeta)(\omega_{pe}^2 \omega_{pi}^2) \frac{\left(\delta + \frac{\nu_e}{\omega_0}\beta\right)}{(\delta^2 + \beta^2)} \tag{22}$$

$$\bar{\Omega}_i^2 = \Omega_i^2 + C_s^2 k^2,$$

$$\delta = \omega_0^2 - \omega_{UH}^2, \quad \omega_{UH}^2 = \Omega_e^2 + \bar{\omega}_{pe}^2 + \nu_e^2$$

$$\bar{\omega}_{pe}^2 = \omega_{pe}^2 + v_e^2 k^2, \quad \beta = \nu_e \omega_0 \left(2 - \frac{\bar{\omega}_{pe}^2}{\omega_0^2}\right)$$

and,

$$\zeta^2 = \frac{e^2}{m_e^2(\omega_0^2 - \Omega_e^2)^2} \{k_x^2 E_{px}^2 + k_y^2 E_{py}^2 + \frac{\Omega_e^2}{\omega_0^2}(k_y^2 E_{px}^2 + k_x^2 E_{py}^2) +$$

$$2E_{px}E_{py}[k_x k_y \cos\psi(1 - \frac{\Omega_e^2}{\omega_0^2}) - \frac{\Omega_e}{\omega_0} k_\perp^2 \sin\psi] \qquad (23)$$

$$+ \frac{(\omega_0^2 - \Omega_e^2)}{\omega_0^2} k_z E_{pz}[k_x E_{px} - \frac{\Omega_e}{\omega_0} k_x E_{px}\sin\psi + k_y E_{py}\cos\psi]\}$$

Here, the pump wave is taken as [Lee et al., 1972]

$$E_p = \frac{E_{px}}{-2i}\exp(-i\omega_0 t)x + \frac{E_{py}}{-2i}\exp(-i\omega_0 t - i\psi)y + \frac{E_{px}}{-2i}\exp(-i\omega_0 t)z + c_1c \qquad (24)$$

where, E_{pz}, is included as we are considering modes with $k_z \neq 0$. We have
used $\Omega_e/\nu_e > k/k_z$, $\omega_n > \gamma$, ν_{in}, $1 > A/\bar{\Omega}_i^2$, in deriving (16) - (17). We can
rewrite the modified growth rate of the modes as

$$\gamma = [\frac{k^2}{2k_z^2}\frac{\nu_e}{\Omega_e}(k_z V_0 - \bar{\Omega}_i) - \nu_i] - \frac{k^2}{2k_z^2}\frac{\nu_e}{\Omega_0}\frac{(\zeta^2/16)}{\bar{\Omega}_i}\frac{(\omega_{pe}^2\omega_{pi}^2)\delta}{(\delta^2 + \beta^2)} = \gamma^2 - \gamma_s \qquad (25)$$

where γ^2 denotes the linear growth contribution in absence of the pump-
field while γ_s represents the modification introduced by the pump. We have
again used $\zeta \ll 1$ in the above. We see from inspection of (25) that the
presence of the pump can be stabilizing (destabilizing) if $\delta > 0$ (< 0), or,
when $\omega_0 > \omega_{UH}(\omega_0 < \omega_{UH})$. We note that similar criteria were also obtained
by earlier workers [Lee et al., 1972, Bujarbarua and Sen, 1978, Keskinen et
al., 1983].

We can treat the finite ion temperature effects in a similar
fashion. Since the ion-cyclotron instability is likely to have maximum

growth ionosphere near $k_\perp \rho_i \sim 1$, one needs to use the kinetic (collisionless Vlasov-Boltzmann) equation for ions [Dum and Dupree, 1970]. In this case, the modified dispersion relation becomes,

$$\omega = \Omega_i \left[1 + \Gamma_{1i} \tau \left\{ \left(1 - i \frac{\nu_e \bar{\omega}_e}{k_z^2 v_e^2} \right) + 2 J_1^2(\xi) \frac{\omega_{pe}^4}{k^2 v_e^2} \frac{\left(\delta + \frac{\nu_e}{\omega_p} \beta \right)}{\left(\delta^2 + \beta^2 \right)} \right\} \left\{ 1 - i\sqrt{\pi} \frac{\omega t}{\Omega_i} \bar{e}^{t^2} \right\} \right.$$
$$\left. - i(\nu_i / \Omega_i) \right]$$
(26)

where,

$$\tau = \frac{T_e}{T_i}; \quad t = \left(\frac{\omega - \Omega_i}{k_z v_i} \right); \quad \Gamma_n(\mu_\alpha) = I_n(\mu_\alpha) e^{-\mu_\alpha}; \quad \mu_\alpha = \frac{k_\perp^2 v_\alpha^2}{\Omega_\alpha^2}$$
(27)

In the absence of the pump wave, this expression yields the ion-cyclotron wave dispersion relation,

$$\omega = \Omega_i \left[1 + \Gamma_{1i} \tau \left\{ 1 - i \frac{\nu_e \bar{\omega}_e}{k_z^2 v_e^2} - i\sqrt{\pi} \frac{\omega t}{\Omega_i} \bar{e}^{t^2} \right\} \right]$$
(28)

which yields the expressions for the real frequency and the growth rate

$$\omega_r = \Omega_i [1 + \Gamma_{1i} \tau],$$

$$\gamma = \Omega_i \Gamma_{1i} \tau \left[\frac{\nu_e \bar{\omega}_e}{k_z^2 v_e^2} + \sqrt{\pi} \frac{\omega}{k_z v_i} \Gamma_{1i} \bar{e}^{t^2} \right] - \nu_i$$
(29)

where the second term in the expression for γ results from the ion-Landau damping. The collisional ion-cyclotron instability described by equations (29) may have relevance for the short wavelength observations (such

that $k_\perp \rho_i \sim 1$, of ion-cyclotron waves at low ionospheric altitudes [Bering, 1984; Satyanarayana et al., 1985].

The inclusion of pump wave effects in equation (28) leads to modification of (29) in the form given by

$$\omega_r = \Omega_i \left[1 + \Gamma_{1i} \left(\tau + \frac{A}{\kappa^2 v_i^2} \right) \right],$$

$$\gamma = \gamma_L - (\Gamma_{1i})^2 \frac{\tau}{\mu_i} \frac{\nu_e}{k_z^2 v_e^2} A \tag{30}$$

where A and γ_L are given by (22) and (29) respectively. We see that the pump wave is stabilizing (destabilizing) for $\delta > 0$ (< 0), i.e., when $\omega_o > \omega_{uh}$ ($\omega_o < \omega_{uh}$); as in case of fluid ions (eq. (25)). One can readily extend this analysis to the case of kinetic EIC instability [Drummond and Rosenbluth, 1962]. However, in the ionosphere, the kinetic instability is likely to occur at higher altitudes [Kindel and Kennel, 1971] such as above the F peak, whereas the modification experiments have access only to the lower collisional altitudes.

A rough estimate for the threshold amplitude of pump-field required to stabilize or destabilize the EIC instability, reveals that,

$$\frac{c|E_p|^2}{8\pi} = \frac{2B_0^2}{\pi c k_\perp^2} \left(\frac{\nu_e}{\Omega_e} \right) \left[\frac{\omega_0^2 (\omega_0 - \Omega_e)^2}{\omega_{pe}^4} \right] \left[(k_\perp V_0 - \omega_R) \omega_0 \right] \tag{31}$$

where we have considered a circularly-polarized O-mode, so $\psi = -\pi/2$ and $|E_{px}| = |E_{py}|$. For typical high-latitude F-region parameters [Satyanarayana et al., 1985], we have, $B_0 \sim .5$ gauss, $(\nu_e/\Omega_e) \sim 10^{-4}$, $\frac{\kappa_z}{k_\perp} \sim 10^{-2}$, $k_\perp \rho_i \sim 1.5$, $\rho_i (\sim \sqrt{\frac{T_i}{m_i \Omega_i^2}}) \sim 10^3$ cm, $\omega_0 \sim \omega_{pe} \sim 3 \times 10^7 \text{s}^{-1}$, $V_0 \sim 2 \times 10^6$ cm s^{-1}, we find that $c|E_p|^2/8\pi \sim 10^{-4}$ W/m^2.

III. DISCUSSION

We have studied the effects of a high frequency electromagnetic pump
wave on the evolution of ion cyclotron instabilities in a weakly ionized
collisional plasma. We find that an electromagnetic pump wave oscillating
with the upper hybrid frequency can lead to the artificial production or
control of ion cyclotron instabilities in a collisional plasma. The basic
physical mechanism of this process can be expressed as follows. The
electromagnetic pump wave with frequency ω_{UH} interacts with low frequency
ion cyclotron modes ω and drives sidebands at $\omega \pm \omega_{UH}$. These sidebands
can, in turn, couple to the pump fields and nonlinearly affect the ion
cyclotron modes. This interaction is ponderomotive in nature. However,
the partial pressure force (Fejer, 1979) can also play a role depending
upon the k_i of the sidebands. For parameters typical of the high latitude
ionosphere, we find that ion cyclotron modes can be stabilized or
destabilized with an incident pump electric field on the order of 0.1
V/m. The polarization of the pump wave should be O mode. These power
density levels could be accessible using the ionospheric heaters in Alaska
(Wong et al., 1980) and Norway (Stubbe et al., 1981).

We have made several simplifying assumptions in the course of this
paper. We have assumed the dipole approximation, i.e., taken the
wavelength of the pump wave $\sim \kappa_p^{-1}$ to be much larger than the wavelength of
the ion cyclotron modes k^{-1}. Since $\kappa_p^{-1} \sim 100$'s m and $k^{-1} \sim \rho_i \sim 10$ m, this
assumption is valid. In addition, we have neglected pump electric field
swelling near the reflection point (Ginzburg, 1964) and, as a result, our
threshold pump electric fields should be considered as lower bounds.

Acknowledgments

References

Aarons, J.,   1973   J. Geophys. Res., 78, 7441.

Basu, Su., S. Basu,   1984   J. Geophys. Res, 89, 5554.
   E. MacKenzie, W.R. Coley,
   W.B. Hanson and C.S. Lin

Bering, E.A.,   1984   J. Geophys. Res., 89, 1635.

Bujarbarua, S. and Sen, A.   1978   J. Atmos. Terr. Phys. 40, 615.

Burke, W.J.,   1981   Physics of Auroral Arc Formation,
                                                 AGU, Washington, DC, p. 164.

Chaturvedi, P.K., and   1975   Plasma Physics, 17, 447.
   P.K. Kaw

Chaturvedi, P.K.   1976   J. Geophys. Res. 81, 6169.

Clark, D.H., and W.J. Raitt   1976   Planet. Space Sci., 24, 873.

Drummond, W.E., and   1962   Phys. Fluids, 5, 1507.
   M.N. Rosenbluth

DuBois, D.F., and   1965   Phys. Rev. Lett., 14, 544.
   M.V. Goldman

Dum, C.T. and   1970   Phys. Fluids, 13, 2064.
   T.H. Dupree

Dyson, P.L.,   1969   J. Geophys. Res., 74 6291.

Dyson, P.L., and   1974   J. Geophys. Res., 79, 5219.
   J.D. Winningham

Fejer, B.G., Reed, R.W.,   1984   J. Geophys. Res. 89, 187.
   Farley, D.T., Swartz, W.E.,
   and Kelley, M.C.

Fejer J.A.   1979   Rev. Geophys. Space Phys. 17, 135.

Fialer P.A.   1974   Radio Sci. 9, 923.

Fremouw, E.J., C.L. Rino   1977   Geophys. Res. Lett., 4, 539.
    R.C. Livingstone, and
    M.D. Cousins

Ginzburg V.L.   1964   The Propagation of Electromagnetic
                                             Waves in Plasma, Addison Wesley,
                                             Reading, Mass.

Greenwald, R.A.,   1974   J. Geophys. Res., 79, 4807.

Hanuise, C., J.P. Villain   1981   Geophys. Res. Lett., 8, 1083.
    and M. Crochet

Hower, G.L., D.M. Ranz and   1966   J. Geophys. Res., 71, 3215.
    C.L. Allison

Kelley, M.C., K.D. Baker,   1980   Radio Sci., 15, 491.
    C. Rino and J.C. Ulwick

Keskinen, M.J., and   1983   Radio Sci., 18, 1077.
    S.L. Ossakow

Keskinen, M.J.,   1983   J. Geophys. Res. 88, 7239.
    Chaturvedi, P.K. and
    Ossakow, S.L.

Kindel, J.M., and C.F. Kennel   1971   J. Geophys. Res., 76, 3055.

Lee K., Kaw, P.K., and   1972   J. Geophys. Res. 77, 4197.
    Kennel, C.F.

Nishikawa, K.   1968   J. Phys. Soc. Jpn., 24, 916.

Ogawa, T., H. Mori, and   1976   J. Geophys. Res., 81, 4013.
    S. Mayazaki

Olesen, J.K., F. Primdahl,   1976   Geophys. Res. Lett., 3, 399.

   F. Spangslev, E. Ungstrup

   A. Bahnsen, U. Fahlson,

   C. -G. Fälthammer, and

   A. Pedersen

Ossakow, S.L., and   1979   Geophys. Res. Lett., 6, 322.

   P.K. Chaturvedi

Perkins, F.W., and P.K. Kaw   1971   J. Geophys. Res., 76, 282.

Perkins, F.W., C. Oberman, and 1974   J. Geophys. Res., 79 1478.

   E.J. Valeo

Phelps, A.D.R.and R.C. Sagalyn 1976   J. Geophys. Res., 81, 515.

Sagalyn, R.C., M. Smiddy, and   1974   J. Geophys. Res., 79, 4252.

Satynanarayana, P., P.K.   1985   To be submitted to J. Geophys.

   Chaturvedi, M.J. Keskinen,   Res.

   and S.L. Ossakow

Silin, V.P,   1965   Sov. Phys. JETP, 21, 1127.

Stenflo, L.   1983   Radio Sci. 18, 1379.

Stubbe, P., Kopka, H. and   1981   J. Geophys. Res. 86, 9073.

   Dowden, R.L.

Thide, B., Kopka, H. and   1982   Phys. Rev. Lett. 49, 1561.

   Stubbe, P.

Utlaut, W.F.,   1970   J. Geophys. Res., 75, 6402.

Vaskov, V.V., and   1977   Sov. Phys. JETP, 46, 487.

   A.V. Gurevich

Vickrey, J.F., C.L. Rino   1980   Geophys. Res. Lett., 7, 789.

   T.A. Potemra

Weaver, P.F.   1965   J. Geophys. Res., 70, 5425.

Wong, A.Y., Roederer, J.   1981   Effects of the Ionosphere on
    Hunsucker, R., Dimonte, G.,   Radio-wave Systems, ed. J.
Viezbicke, P., Gregorio, J.,   Goodman, U.S. Government
    and Santoru, J.   Printing Office, Washington, D.C.

APPENDIX I

Effects of Finite Current Channel Width on the

Current Convective Instability

Effects of Finite Current
Channel Width on the
Current Convective Instability

P. Satyanarayana and J. Chen
Science Applications, Inc.
McLean, Va. 22102

and

M.J. Keskinen
Geophysical and Plasma Dynamics Branch
Plasma Physics Division
Naval Research Laboratory
Washington, D.C. 20375

August 1984

Abstract

The effects of the finite current channel width on the current convective instability are studied both analytically and numerically. First using a sharp-boundary field-aligned current distribution which has a finite width along the plasma density gradient, the dispersion relation is obtained analytically. It is found that, for the long wavelength modes ($k_y d \ll 1$) where the nonlocal effects are most prominent, the growth rate γ is proportional to $|\overline{V}_d d/L^2|$ in the collisional limit ($\nu_{in} \gg |\omega|$), where d is the half-width of the current channel, L is the plasma density gradient scale length, $\overline{V}_d$ is the field-aligned current velocity, ν_{in} is the ion-neutral collision frequency and ω is the perturbation frequency. For the long wavelength modes in the inertial limit ($\nu_{in} \ll |\omega|$), the growth rate γ scales as $|\overline{V}_d d/L^2|^\alpha$, where $\alpha = 1/2$ (2/3) for $k_z^2/k_y^2 \, \Omega_e/\nu_{ei}$ much less than (greater than) $|\omega|/\Omega_i$ and $k_z (k_y)$ is the wavenumber parallel (perpendicular) to the magnetic field, $\Omega_e (\Omega_i)$ is the electron (ion) gyrofrequency, and ν_{ei} is the electron-ion collision frequency. Numerical results are also presented for a diffuse-boundary current velocity distribution. Applications to the high latitude ionosphere are discussed.

I.   INTRODUCTION

From a variety of experimental observations [see recent reviews by Fejer and Kelley, 1980, Vickrey and Kelley, 1983, and Hanuise, 1983], it is now known that the high latitude ionosphere, from the auroral zone into the polar cap, is a highly structured and nonequilibrium medium containing plasma fluctuations and structures with scale sizes ranging from hundreds of kilometers to meters. Several processes, e.g., particle precipitation, plasma instabilities, and neutral fluid dynamics, have been proposed to account for high latitude ionospheric plasma structure [Keskinen and Ossakow, 1983a]. The plasma instabilities that have received the most attention thus far are the ExB instability [Simon, 1963; Linson and Workman, 1970; Keskinen and Ossakow, 1982, 1983b; Huba et al; 1983, Keskinen, 1984] and the current convective instability [Lehnert, 1958; Kadomtsev and Nedospasov, 1960; Ossakow and Chaturvedi, 1979; Huba and Ossakow, 1980; Keskinen et al., 1980; Chaturvedi and Ossakow, 1981, 1983; Satyanarayana and Ossakow, 1984; Gary, 1984; Huba, 1984]. The current convective instability results from the coupling of a magnetic field-aligned current and a plasma density gradient transverse to the magnetic field — a configuration likely to occur in the auroral zone ionosphere [Vickrey et al., 1980]. All of the previous studies of the current convective instability have assumed that the width of the current transverse to the magnetic field is infinite. However, recent observational results [see, for example, Bythrow et al., (1984)] indicate that the transverse dimension of the field-aligned current distributions may be comparable to or less than the density gradient scale length. Since the instability requires both a density gradient and a field-aligned current, the properties of the instability may be modified if one uses a more realistic geometry with a current channel of finite width. Indeed, physical intuition would lead one to expect reduction in the growth rate and modification in the stability boundary for narrow current channels. In this analysis we remove the infinite-width current simplification and study the effects of finite current channel width on the current convective instability. The analytical and numerical results will show that, in the long wavelength limit, $k_y d \ll 1$, where the nonlocal results are most prominent, the growth rate depends on the global quantities such as $(\overline{V}_d d / L^2)$, where $\overline{V}_d$ is the current velocity, d is the half-width of the current channel and L is the density gradient scale length. These intrinsically nonlocal effects may be of interest for interpretation of the

observational data. We discuss the nonlocal results and apply them to the high latitude ionosphere.

The organization of the paper is as follows. In Section II we derive the general dispersion relation describing the mode structure of the current convective instability with a finite current channel width. In Section III we present a theoretical analysis of the mode structure equation while in Section IV we give numerical results. Finally, in Section V we summarize our findings and discuss applications to the high latitude ionosphere.

II. MODE STRUCTURE EQUATION

In this paper we use a slab model shown in Fig. (1). The plasma is assumed inhomogeneous along the north-south direction ($\hat{x}$) and is assumed to support equilibrium currents along the magnetic field. The magnetic field is uniform and vertical ($\hat{z}$) with the field-aligned currents taken to be of the form $\underline{J} = J_o(x) \, \hat{z}$. The primary objective of this paper is to confine the field-aligned currents to a finite region along the direction of the density gradient ($\hat{x}$) and to study the effects of finite current width on the current convective instability. We neglect weak altitude dependent density gradients as well as east-west ($\hat{y}$) gradients and transverse equilibrium electric fields. The temperature effects responsible for diffusive damping are ignored as is magnetic field shear. Electron inertia is neglected since current convective instability is a low frequency instability $\left(\omega \ll \Omega_e \right)$. Furthermore, we confine ourselves to the F-region of the ionosphere and ignore the electron-neutral collision frequency $\left(\nu_{en} \right)$ compared to the electron-ion collision frequency $\left(\nu_{ei} \right)$. Due to the variation of the field-aligned currents and the background density along x, we perform a nonlocal analysis and derive a mode structure equation for the perturbed potential. This procedure allows us to study short wavelength and long wavelength modes. The basic two-fluid equations describing the electron and ion dynamics in the rest frame of the neutrals are

$$\frac{\partial n_\alpha}{\partial t} + \nabla \cdot \left(n_\alpha \underline{V}_\alpha \right) = 0 , \tag{1}$$

I-5

$$m_\alpha n_\alpha \left(\frac{\partial}{\partial t} + \underline{V}_\alpha \cdot \nabla\right) \underline{V}_\alpha = q_\alpha n_\alpha \left(\underline{E} + \frac{\underline{V}_\alpha \times \underline{B}}{c}\right) - m_\alpha n_\alpha \nu_{\alpha n} \underline{V}_\alpha - \underline{R}_\alpha , \qquad (2)$$

where α denotes species (e for electrons; i for ions), n_α is the plasma density, $\underline{V}$ is the fluid velocity, m_α is the mass of the species, q_α is the charge of the species, c is the speed of light, $\underline{E}$ is the electric field, $\nu_{\alpha n}$ is the plasma particle collision frequency with neutrals, and $\underline{R}_\alpha$ is the friction force given by

$$R_i = m_i n_i \nu_{ie} \left(\underline{V}_i - \underline{V}_e\right) , \qquad (3)$$

$$R_e = m_e n_e \nu_{ei} \left(\underline{V}_e - V_i\right). \qquad (4)$$

The equilibrium velocities are given by

$$V_{ez}^0 = -\frac{e\, E_{0z}}{m_e \nu_{ei}} \qquad (5)$$

$$V_{iz}^0 = 0 \qquad (6)$$

In obtaining these equations, terms proportional to $\nu_{en}/\Omega_e \ll 1$ have been neglected. By setting $\underline{E}_{0\perp} = 0$, it can be easily shown that $\underline{V}_{e\perp} = \underline{V}_{i\perp} = 0$. We choose the friction force to be $R_e = -R_i$ so that momentum conservation demands $\nu_{ie} m_i = \nu_{ei} m_e$ and thus $V_{iz}^0 = 0$. The net drift velocity $V_d \equiv V_{ez}^0 - V_{iz}^0$ then becomes $V_d = V_{ez}^0$. More generally, however, neutral particles also participate in momentum conservation, and V_{iz}^0 need not be zero. The above simplification implies that the electrons are the primary current carriers.

In order to derive the nonlocal mode structure equation, we use a perturbation of the form $\hat{f} \sim f(x) \exp\left[-i\left(\omega t - k_y y - k_z z\right)\right]$, where $\omega = \omega_r + i\gamma$, $\gamma > 0$ for growth and k_y and k_z are the mode numbers in y and z directions. We then linearize Eqs. (1) and (2), and finally we subtract the electron continuity equation from the ion continuity equation [Eq. (1)] and use quasi-neutrality condition to derive the mode structure equation.

We consider only electrostatic perturbations and do not perturb the magnetic field [Ossakow and Chaturvedi, 1979]. By perturbing Eq. (2) for both electrons and ions, we obtain the perturbed velocities in the z direction

$$\hat{V}_{ez} = - \frac{e \, \hat{E}_z}{m_e \nu_{ei}} \tag{7}$$

$$\hat{V}_{iz} = 0 \tag{8}$$

The perpendicular perturbed velocities are given as

$$\hat{V}_{e\perp} = \frac{c}{B} \left[\hat{\underline{E}}_\perp \times \hat{\underline{z}} - (\nu_{ei}/\Omega_e) \hat{\underline{E}}_\perp \right] \tag{9}$$

$$\hat{\underline{V}}_{i\perp} = \frac{c}{B} \left[\hat{\underline{E}}_\perp \times \hat{\underline{z}} - i \, \frac{(\omega + i\nu_{in})}{\Omega_i} \, \hat{\underline{E}}_\perp \right] \tag{10}$$

We substitute Eqs. (7)-(11) in Eq. (1) and use $\underline{E} = - \nabla\phi$ in the electrostatic limit. Then we subtract the electron continuity equation from the ion continuity equation and impose quasineutrality to obtain

$$\frac{\partial^2 \hat{\phi}}{\partial x^2} + p(x) \frac{\partial \hat{\phi}}{\partial x} + q(x)\hat{\phi} = 0, \tag{11}$$

where

$$p(x) = n_o'/n_o \tag{12}$$

$$q(x) = - k_y^2 - \frac{i \, k_z^2 \, (\Omega_e/\nu_{ei}) \, \Omega_i}{(\omega + i\nu_{in})}$$

$$+ \frac{k_z V_d(x)}{(\omega - k_z V_d(x))} \frac{\Omega_i}{(\omega + i\nu_{in})} \left[k_y(n_o'/n_o) - i(\Omega_e/\nu_{ei}) \, k_z^2 \right] \tag{13}$$

This equation agrees with the nonlocal mode structure equation derived earlier by Satyanarayana and Ossakow (1984) and Huba (1984).

The effects of finite current width are contained in the third term in Eq. (13). We solve Eq. (11) exactly for two specific profiles of the current velocity $V_d(x)$. In the next section, we obtain the analytic dispersion relation for a "waterbag" distribution.

$$V_d(x) = \begin{cases} \bar{V}_d, & |x| \leq d \\ 0, & |x| > d \end{cases} \tag{14}$$

where 2d is the current channel width. We choose an exponential plasma density profile $n_o(x) = \bar{n}_o \exp(x/L)$ so that $n_o'/n_o = 1/L$. In section IV we present the numerical results for both the waterbag current model and the diffuse Gaussian current model.

III. DISPERSION RELATION

The dispersion relation is obtained by matching the logarithmic derivatives of the wavefunction inside and outside the waterbag at the boundaries, $x = \pm d$, and requiring that the solution be evanescent for $x \rightarrow \pm \infty$. First, we will cast Eq. (11) into a Schrödinger type equation by using the transformation

$$\hat{\phi} = \psi(x) \exp\left[-\frac{1}{2} \int p(x)dx\right]. \tag{15}$$

Then, we have

$$\frac{\partial^2 \psi}{\partial x^2} + Q^2(x)\, \psi = 0 \tag{16}$$

where

$$Q^2(x) = q(x) - p^2/4 - p'/2 \tag{17}$$

and $p' = \partial p/\partial x$. For an exponential density profile, $n_o = \bar{n}_o \exp(x/L)$, $p = 1/L$ and $p' = 0$. Thus, for the waterbag profile $V_d(x)$ given by Eq. (14) and for the exponential density profile, Eq. (16) can be written as

$$\frac{\partial^2 \psi_{out}}{\partial x^2} - Q_o^2\, \psi_{out} = 0 \qquad |x| > d \tag{18}$$

$$\frac{\partial^2 \psi_{in}}{\partial x^2} + Q_i^2 \; \psi_{in} = 0 \qquad |x| \leq d \qquad (19)$$

with

$$Q_i^2 = - \left[k_y^2 + 1/(4L^2) \right] - \frac{i \; k_z^2 (\Omega_e/\nu_{ei}) \Omega_i}{(\omega + i\nu_{in})}$$

$$+ \frac{k_z \bar{V}_d}{(\omega - k_z \bar{V}_d)} \frac{\Omega_i}{(\omega + i\nu_{in})} \left[k_y/L - i \; k_z^2 \; (\Omega_e/\nu_{ei}) \right] \qquad (20)$$

and

$$Q_o^2 = \left[k_y^2 + 1/(4L^2) \right] + \frac{i \; k_z^2 \; (\Omega_e/\nu_{ei}) \Omega_i}{(\omega + i\nu_{in})} \qquad (21)$$

where primes indicate derivatives with respect to x. The current convective instability is a nearly purely growing mode with $\omega = \omega_r + i\gamma \sim i\gamma$. This will be shown to be true _a posteriori_ in the next section. For $\omega_r < \gamma$, the sign convention applicable in Eqs. (18) and (19) is such that $Q_o^2 > 0$ and $Q_i^2 > 0$. In Eq. (20) the sign of $\bar{V}_d/L$ (< 0) is chosen so that $Q_i^2 > 0$ and the growth rate is positive for positive k_y. Furthermore, in the following we assume that $|k_z \bar{V}_d| \ll |\omega|$ in the denominator and $k_z^2 \; (\Omega_e/\nu_{ei}) < k_y/L$. First, we rewrite Q_i^2 and Q_o^2 as follows:

$$\hat{Q}_o^2 = \frac{\hat{k}^2 (\omega + i\bar{\nu})}{(\omega + i\nu_{in})} \qquad (22)$$

$$\hat{Q}_i^2 = - \frac{\hat{k}^2 (\omega - \omega_+)(\omega - \omega_-)}{\omega (\omega + i\nu_{in})} \qquad (23)$$

where

$$\bar{\nu} = \nu_{in} + (\hat{k}_z^2 / \hat{k}^2)(\Omega_e/\nu_{ei})\Omega_i \qquad (24)$$

$$\omega_o^2 = \omega_+ \omega_- = (\hat{k}_z \hat{k}_y/\hat{k}^2)|\bar{V}_d/L|\Omega_i \qquad (25)$$

$$\omega_\pm = - (i\bar{\nu}/2)\left[1 \pm (1 + 4(\omega_o^2/\bar{\nu}^2))^{1/2} \right] \qquad (26)$$

I-9

$$\hat{k}^2 = \hat{k}_y^2 + 1/4 \qquad (27)$$

and $\hat{k}_y$, $\hat{k}_z$, and $\hat{d}$ are the normalized quantities $k_y L$, $k_z L$, and d/L respectively. We note that $\omega_{\pm}$ are the two roots of the local dispersion relation $(Q_i = 0)$. Since the potential, $\hat{Q}_i^2(x)$, in Eq. (16) is symmetric about $x = 0$, we can restrict our analysis to eigenfunctions of definite parity.

In the region $|x| < d$ we have

$$\psi_{in} = A \cos\left(\hat{Q}_i x/L\right) \qquad \text{for even parity} \qquad (28)$$

$$\psi_{in} = B \sin\left(\hat{Q}_i x/L\right) \qquad \text{for odd parity} \qquad (29)$$

where A and B are constants. In the region $|x| > d$, we have an exponentially decreasing solution for either case

$$\psi_{out} = C \, e^{-\hat{Q}_o \left|\frac{x}{L}\right|} \qquad (30)$$

where C is a constant. The matching condition in the case where $V_{iz}^0 = 0$ is that the logarithmic derivative be continuous at $x = \pm d$

$$\left(\psi_{in}'/\psi_{in}\right)_{d_-} = \left(\psi_{out}'/\psi_{out}\right)_{d_+}$$

where $d_{\pm} = \lim_{\varepsilon \to o}(d \pm \varepsilon)$. This condition yields the dispersion relation

$$\hat{Q}_i \tan\left(\hat{Q}_i \hat{d}\right) = \hat{Q}_o \qquad \text{even modes} \qquad (31a)$$

$$\hat{Q}_i \cot\left(\hat{Q}_i \hat{d}\right) = -\hat{Q}_o \qquad \text{odd modes} \qquad (31b)$$

The effect of finite current channel width are contained in the argument of the tangent (cotangent) function for the even modes (odd modes). We analyze the dispersion relation for the even modes by first inverting Eq. (31a) to obtain

$$\hat{Q}_i = \frac{1}{\hat{d}} \left[\text{Arc tan}\left(\hat{Q}_o/\hat{Q}_i\right)\right] \qquad (32)$$

We can rewrite Eq. (32) as

$$\hat{Q}_i = \frac{1}{d}\left[\tan^{-1}\left(\hat{Q}_o/\hat{Q}_i\right) + m\pi\right] \tag{33}$$

where $\tan^{-1}\left(\hat{Q}_o/\hat{Q}_i\right)$ is the principal value of Arc tan $\left(\hat{Q}_o/\hat{Q}_i\right)$ and m is an integer. Equation (33) is the fundamental nonlocal dispersion relation. We note that when d = 0, the dispersion relation $Q_o = 0$ from Eq. (31a) does not give instability since the currents driving the instability vanish.

We can compare Eq. (33) and Eq. (19) to understand the local and nonlocal limits. We recall that the local limit means that the current channel width is infinite so that Eq. (19) describes the mode structure throughout the space. In the local theory, Eq. (19) is also Fourier analyzed with respect to x to obtain

$$Q_i^2 = k_x^2 \tag{34}$$

and if we assume $k_y^2 \gg k_x^2$ we regain the earlier results of <u>Ossakow and Chaturvedi</u> (1979), $Q_i \sim 0$, corresponding to $\omega \sim \omega_+$. Comparing Eqs. (33) and (34) we see that in the nonlocal analysis, the right hand side of Eq. (33) provides the inverse scale length, L_x^{-1}. The role played by the current channel, then, is to form a wavepacket of width of the order of L_x localized within the current channel.

In the limit $|\hat{Q}_o/\hat{Q}_i| \gg 1$, $\tan^{-1}\left(Q_o/Q_i\right)$ approaches $\pi/2$. This happens in the local limit when $\omega \simeq \omega_\pm$ as can be seen by dividing Eq. (22) by Eq. (23) to obtain

$$\frac{\hat{Q}_o^2}{\hat{Q}_i^2} = -\frac{\omega\left(\omega + i\bar{\nu}\right)}{\left(\omega - \omega_+\right)\left(\omega - \omega_-\right)}$$

As we approach the local limit we have from Eq. (33)

$$\hat{Q}_i = \left(m + 1/2\right)\pi/\hat{d} \tag{35}$$

We set $m = 0$ and consider the fastest growing mode. Then, with the definition of $\hat{Q}_i$ from Eq. (23), Eq. (35) becomes

$$- \hat{k}^2 \frac{(1 - \omega_+/\omega)(1 - \omega_-/\omega)}{(1 + i\hat{\nu}_{in}/\omega)} = \frac{\pi^2}{4\hat{d}^2} \qquad (36)$$

Thus, as we approach the local limit, we have $L_x = 2d/\pi$ and L_x plays the role of the wavelength in the x direction. For $\nu_{in}/|\omega| \ll 1$ the new roots are

$$\omega = \frac{- (i\bar{\nu}/2) \left[1 \pm \left(1 + 4 \, \omega_o^2 \, (1 + \pi^2/4\hat{k}^2\hat{d}^2)/\bar{\nu}^2 \right)^{1/2} \right]}{\left(1 + \pi^2/4\hat{k}^2\hat{d}^2 \right)} \qquad (37)$$

Furthermore, we regain the local growth rates for $k_y d \to \infty$, namely,

$$\omega \equiv \omega_\pm = (-i\bar{\nu}/2)\left\{ 1 \stackrel{+}{-} \left[1 + 4(\omega_o^2/\bar{\nu}^2) \right]^{1/2} \right\} \qquad (38)$$

In the limit $|\hat{Q}_o/\hat{Q}_i| \ll 1$, the inverse tangent function is approximately equal to $\hat{Q}_o/\hat{Q}_i$. Then Eq. (33) becomes

$$\hat{Q}_o/\hat{Q}_i = \hat{Q}_i \, \hat{d} \qquad (39)$$

Using Eqs. (22) and (23) we obtain

$$(\omega - \omega_+)(\omega - \omega_-) = - \omega(\omega + i\nu_{in})\left[1 + i\hat{k}_{z1}^2 \nu_{in}/(\omega + i\nu_{in}) \right]^{1/2}/\hat{k}\hat{d} \qquad (40)$$

where $\hat{k}_{z1}^2 = (\hat{k}_z^2/\hat{k}^2)(\Omega_e/\nu_{ei})(\Omega_i/\nu_{in})$. The above equation is valid for $(\hat{Q}_o/\hat{Q}_i) \ll 1$ or $|\hat{Q}_i\hat{d}| \ll 1$ which is essentially the long wavelength limit, $k_y d \ll 1$. Equation (40) can then be solved both in the highly collisional and weakly collisional domains. Using Eqs. (24) and (25), Eq. (40) can be written as

$$\omega^2 + i\bar{\nu} \, \omega + \omega_o^2 \approx \pm \, \omega(\omega + i\nu_{in})\left[1 + i \, \hat{k}_{z1}^2 \nu_{in}/(\omega + i\nu_{in}) \right]^{1/2}/\hat{k}\hat{d} \qquad (41)$$

The negative (positive) sign on the right hand side yields a growing (damped) mode. In the following anlaysis we consider the growing modes.

Collisional limit

In this limit where $\nu_{in} \gg |\omega|$, Eq.(41) has the following roots:

$$\omega_> = -(i\nu_>/2) \left\{ 1 \pm \left[1 + 4 \omega_o^2 (1 + \kappa_1)/\nu_>^2 \right]^{1/2} \right\}/(1 + \kappa_1) \tag{42}$$

where $\kappa_1 = (1 + \hat{k}_{z1}^2)^{1/2}/k_y d$ and $\nu_> = \bar{\nu} + \nu_{in}\kappa_1$. A simple expression for the growth rate can be obtained by examining the small channel width limit, $d \ll L$, where the growth rate is much less than the local growth rate. Thus for $\omega \ll \omega_\pm$, Eq. (40) or (41) yields

$$\omega_+ \omega_- \hat{k}\hat{d} = - i\omega\nu_{in} (1 + \hat{k}_{z1}^2)^{1/2}$$

from which the growth rate $(\omega = \omega_r + i\gamma)$ is given as

$$\gamma = (\hat{k}_z \hat{k}_y/\hat{k}) (1 + \hat{k}_{z1}^2)^{-1/2} (\Omega_i/\nu_{in}) |\bar{V}_d/L| \; (d/L) \tag{43}$$

It is worthwhile to compare the growth rate in nonlocal long wavelength limit as given by Eq. (43) with the local result as given by <u>Chaturvedi and Ossakow</u>, (1981)

$$\gamma_L = (k_z/k_y) (\Omega_i/\nu_{in}) (\bar{V}_d/L) (1 + \hat{k}_{z1}^2)^{-1} \tag{44}$$

We then find the simple result

$$\gamma = k_y d (1 + \hat{k}_{z1}^2)^{1/2} \gamma_L \tag{45}$$

Since $k_y d < 1$ in the nonlocal long wavelength limit, the nonlocal growth rate is less than the local growth rate. Several important conclusions can be drawn from this nonlocal analysis. In this collisional long wavelength limit, (i) the growth rate depends on the product of the magnitude of the drift velocity, $\bar{V}_d$, and the current channel width, d; (ii) the growth rate scales inversely with ν_{in}, the ion-neutral collision frequency; and (iii), the growth rate scales inversely with the gradient scale length, L.

Inertial limit

In the inertial limit where $\nu_{in} \ll |\omega|$, the solutions of Eq. (41) are

$$\omega_< = -(i\nu_</2) \left\{1 \pm \left[1 + 4\,\omega_o^2\,(1 + \kappa_2)/\nu_<^2\right]^{1/2}\right\}/(1 + \kappa_2) \qquad (46)$$

where $\kappa_2 = (1/k_y d)$ and $\nu_< = \bar{\nu} + \nu_{in}\hat{k}_{z1}^2 \kappa_2^2/2$. To obtain a simple expression for the growth rate, we consider small channel widths, $(d \ll L)$, where the growth rate is much smaller than the local growth rate. Thus for $\omega \ll \omega_+$ Eq. (40) yields in the inertial limit

$$\omega_+ \omega_- \hat{k}d = -\omega^2 \left(1 + i\hat{k}_{z1}^2 \nu_{in}/\omega\right)^{1/2} \qquad (47)$$

Equation (47) can be simplified for the case $\hat{k}_{z1}^2\,\nu_{in} \gg |\omega|$, i.e., $(\hat{k}_z^2/\hat{k}^2)(\Omega_e/\nu_{ei}) \gg |\omega|/\Omega_i$. The growth rate can then be written as

$$\gamma = \left(\nu_{ei}\Omega_i/\Omega_e\right)^{1/3} \left(\hat{k}_y\hat{d}\right)^{2/3} \left(|\bar{V}_d|/L\right)^{2/3} \qquad (48)$$

From __Chaturvedi and Ossakow__, (1981) we have, in the local inertial limit the maximum growth rate

$$\gamma_L = \left(\hat{\nu}_{ei}\Omega_i/\Omega_e\right)^{1/3} \left(|\bar{V}_d|/L\right)^{2/3} \qquad (49)$$

As a result, we have for the nonlocal long wavelength inertial limit,

$$\gamma = \left(k_y d\right)^{2/3}\gamma_L \qquad (50)$$

Equation (50) shows that the nonlocal growth rate in the inertial limit γ is less than the local growth rate since $k_y d \ll 1$ in the long wavelength limit. For $k_{z1}^2 \nu_{in} \ll |\omega|$, i.e., $(\hat{k}_z^2/\hat{k}^2)(\Omega_e/\nu_{ei}) \ll |\omega|/\Omega_i$, Eq. (47) yields

$$\gamma = \left(\omega_+ \omega_- \hat{k}\hat{d}\right)^{1/2} \qquad (51)$$

By using Eqs. (24) - (27), this expression can be rewritten as

$$\gamma = \left(\hat{k}_z\hat{k}_y/\hat{k}\right)^{1/2} \left(\Omega_i\right)^{1/2} |\bar{V}_d/L|^{1/2}(d/L)^{1/2} \qquad (52)$$

In this limit where $|Q_o/Q_i| \ll 1$, $\nu_{in} \ll |\omega|$ and $k_{z1}^2 \nu_{in} \ll |\omega|$, the growth rate depends on the square root of the product of $\overline{V}_d$ and d, and is independent of the ion-neutral collision frequency. An important conclusion is that in both limits discussed above the growth rate scales as $(\overline{V}_d d/L^2)^\alpha$, $\alpha < 1$. We note that the growth rates given in Eqs. (42)-(46) can be shown to be less than the local growth rate, $|\omega_+|$, as assumed earlier. In the next section we solve numerically the full nonlocal dispersion relation [Eq. (33)] in order to study the growth rate over a larger range of $k_y L$ and d/L.

IV. NUMERICAL RESULTS

In order to illustrate the properties of Eq. (33) and the scaling properties of the growth rate in the collisional and inertial domains, we have chosen, for convenience, the case where $k_{z1} = 1$. This choice corresponds to $k_z = k_y (\nu_{ei}/\Omega_e)(\nu_{in}/\Omega_i) \ll k_y$. With this choice, the local dispersion relation (equation (38)) exhibits a maximum at $\nu_{in}/\Omega_i = (1/24)^{2/3} (\omega_o^2/\Omega_i^2)^{2/3}$. This is shown in Fig. 2 where we plot γ/Ω_i versus ν_{in}/Ω_i. As a numerical example, we choose $\nu_{ei}/\Omega_e = 10^{-4}$, $|\overline{V}_d/L| = 5$, $d/L = 0.3$ and $k_y L = 1$ (Bythrow et al., 1984). Curve A shows the exact solution of Eq. (33) obtained by solving it numerically. Curves B and C represent the growth rates given by the analytical expressions in Eqs. (46) and Eq. (42) in the inertial and collisional domains, respectively. These curves show that there is good agreement between the numerical results and the analytical expressions given in Eqs. (42) and (46). Curves B´ and C´ show the simplified analytical expressions given by Eqs. (43) and Eq. (52). Curve D gives the local growth rate, ω_-, given by Eq. (38). The figure shows that for small current channel widths, $d \sim 0.3 \ \lambda/2\pi$, where λ is the wavelength of the perturbation, the growth rate is reduced by an order of magnitude. For the particular choice of the parallel wavenumber the growth rate peaks at $\nu_{in}/\Omega_i \sim 2.0 \ 10^{-3}$ whereas it is maximized at $\nu_{in}/\Omega_i \sim 5.0 \ 10^{-3}$ in the nonlocal limit. In addition, curves B´ and C´ show that the Eqs. (43) and (52), which contain the scaling properties of the growth rate, agree fairly well with the exact numerical results in $\nu_{in} \gg \Omega_i$ and $\nu_{in} \ll \Omega_i$ regimes, respectively. Based on this agreement we can say that the growth rate scales as $(\nu_{in}/\Omega_i)^{1/2}$ in the collisional

domain and as $(\nu_{in}/\Omega_i)^{-1/2}$ in the inertial limit. A more important result is that for $d \ll \lambda$ the growth rate scales as $(V_d d/L^2)^\alpha$, where $\alpha < 1$. This result shows that in the long wavelength limit the growth rate depends on the total current in the region where the wave packet is localized rather than on V_d as is true in the local case.

In solving equation (33), we consider the fastest growing mode ($m = 0$) and use the following parameter values: $\nu_{in}/|\overline{V}_d/L| = 1$, $\Omega_i/|\overline{V}_d/L| = 10^4$, $\nu_{ei}/\Omega_e = 10^{-4}$ and $k_z/k_y = (\nu_{ei}\nu_{in}/\Omega_e\Omega_i)$ (Chaturvedi and Ossakow, 1981; Satyanarayana and Ossakow, 1984). In Fig. 3, we plot the normalized growth rate $\hat{\gamma} \equiv \gamma/|\overline{V}_d/L|$ as a function of $\hat{k} = k_y L$ for various values of the width of the current channel normalized to density gradient scale length $\hat{d} \equiv d/L$ = 0.1, 1.0, and 10.0. First, we see the nonlocal behaviour of the instability where the growth rate is reduced for $\hat{k} \equiv k_y L < 1$ and slowly increases and saturates to the local limit at $\hat{k} \gg 1$ (Huba, 1984). Second, the larger the value of $\hat{d}$, the smaller is the $\hat{k}$ value for which the local limit $\hat{\gamma}_L$ is achieved; for $\hat{d} = 10$, $\hat{\gamma}$ approaches $\hat{\gamma}_L$ for $\hat{k} \gtrsim 2$ whereas for $\hat{d} = 0.1$, $\hat{\gamma}$ approaches $\hat{\gamma}_L$ for $\hat{k} \sim 100$(not shown in figure). The local limit, $\hat{\gamma}_L$, is given by the imaginary part of Eq. (38) normalized to $|\overline{V}_d/L|$. Thus we can conclude that the current channel width has be to small ($\hat{d} \lesssim 1$) to substantially reduce the growth rate of the short wavelength modes ($\hat{k} > 1$).

In Figure 4 we plot $\hat{\gamma}$ as a function of $\hat{d}$ for $\hat{k}$ = 0.5, 1.0, 10.0, and 100.0. As we discussed earlier, we see that as $\hat{d} \to \infty$ we recover the conventional current convective growth rate ($\hat{\gamma}_L$ given in Eq. (38)). The second point is that, as $\hat{d}$ is decreased, the growth rate decreases, eventually going to zero for $\hat{d} \to 0$. The quenching of the instability should be expected, because as $\hat{d} \to 0$ the currents that are driving the current convective instability become highly localized and thus do not sample the entire density gradient. Since the instability is driven by the density gradient in the presence of field aligned currents, as the current channel width (d) is reduced in relation to the density gradient scale length (L), the growth rate of the instability is reduced. The instability is most sensitive to the finite width of the current channel when the current channel width, d, is comparable to or less than the gradient scale length, L. In fact, when the wavelength is comparable to the current

channel width, $\lambda \sim d$ implying $kd \sim 2\pi$, the growth rate drops by at least 50%. Furthermore, we notice that the longer wavelength modes are more easily stabilized. That is, a wider channel ($\hat{d} \geq 10$) significantly reduces the growth rate of modes with wavelength of $4\pi L$ ($\hat{k} = 0.5$), whereas channel width of $\hat{d} = 0.1$ reduces the growth rate of modes with wavelengths of $0.2\pi L(\hat{k} = 10)$ by the same amount. From figures 3 and 4, we can conclude that the growth rate of the current convective instability is reduced if the current channel width is such that $kd \lesssim 1$. Similar results were noticed in the context of collisionless current driven ion-cyclotron waves by Bakshi et al. (1983). We note that we find the real part of the frequency to be much smaller than the growth rate, $\hat{\omega}_r \sim 10^{-4} \ll \hat{\gamma}$.

We have also numerically solved equation (11) for a more realistic diffuse profile of density and current. We choose a density profile given by

$$n(x) = n_o \frac{1 + \varepsilon \tanh (x/L)}{1 - \varepsilon} \tag{53}$$

so that

$$\frac{n'}{n} = \frac{1}{L} \frac{\varepsilon \operatorname{sech}^2(x/L)}{1 + \varepsilon \tanh (x/L)}$$

We take $\varepsilon = 0.8$ so that n'/n is a maximum at $x/L \equiv x_o = -0.55$. We find then that $(n'/n)_{max} \simeq 1/L$. In addition we consider a smooth profile for the current velocity $V_d(x)\hat{z}$ with

$$V_d(x) = \overline{V}_d \exp \left[- (x-x_o)^2/d^2\right] \tag{54}$$

We take the same parameters as in the sharp boundary case. In Fig. 5 we plot $\hat{\gamma}$ versus $k_y L$ for several values of d/L. Similar nonlocal behavior is seen for the growth rate $\hat{\gamma}$. In Fig. 6, we plot $\hat{\gamma}$ versus d/L. The results shown in these figures are similar to those obtained by using a simple waterbag model (Figs. 3 and 4) leading us to believe that the simple waterbag model adequately models the essential physics, namely that the finite current channel width has a stabilizing influence on the current convective instability.

V. DISCUSSION AND SUMMARY

We have presented an analysis of the effects of finite current channel width on the current convective instability. The current convective instability results from the coupling of a magnetic field aligned current and a density gradient perpendicular to the magnetic field. For a current with perpendicular scale size 2d and a plasma density gradient scale length L, our analytical results indicate a monotonic decrease in the growth rate γ of the current convective instability for d/L < 1 both in the collisional $(\nu_{in} \gg \omega)$ and inertial limits $(\nu_{in} \ll \omega)$. For d/L $\ll$ 1 , we find $\gamma \propto \overline{V}_d d/L^2$ in the collisional limit while $\gamma \propto (\hat{V}_d d/L^2)^\alpha$, $\alpha < 1$ in the inertial limit. In general, the growth rate of the current convective instability is reduced by the finite width of the current channel from that of the local case in which the current distribution is infinite in extent.

It is significant to note that, in the long wavelength limit $k_y d \ll 1$ where the nonlocal effects are most prominent, the dependence on $V_d(x)$ enters the nonlocal results in the sharp-boundary case in the form of $(\overline{V}_d d)$, the "area" under the function $V_d(x)$ in the current channel. It is clear that this quantity is proportional to the total current in the channel per unit length in the y-directin (divided by the density of the current carriers and the electric charge). This point is to be contrasted with the local dispersion relation (34) in which the growth rate depends on the current velocity itself, a local quantity. In addition, the nonlocal growth rate depends on the fractional plasma density gradient across the current channel (i.e. d/L). The growth rate is reduced because in a growth period $\left(\sim (V_d/L)^{-1}\right)$ the fluid element does not sample the entire gradient (1/L) but a smaller fraction of the density gradient (f/L , f = d/L). Furthermore, a single value of γ corresponds to the entire wavepacket which occupies the current channel. These nonlocal features are well-known and general to all intrinsically nonlocal perturbations such as the tearing mode (see, for example, Chen and Palmadesso, 1984). With respect to perturbations that have valid local limits, certain differences in the interpretation of theoretical and observational results must be kept in mind as one goes from the local to nonlocal regime. First, with finite current channels, observations must provide global quantities such as the total integrated currents in order to predict the behaviour of the plasma

at any point. Second, because there is no plane wave in the x direction, an observer passing through the current channel in the x direction does not see the usual Doppler shift $k_x V_0$ that would be predicted by a local theory, where V_0 is the velocity of the observer. This point has also been noted by Ganguli et al. (1984) in connection with the current driven ion cyclotron instability. The two perpendicular directions, x and y, are no longer equivalent.

An important result is that in the long wavelength limit, the growth rate scales as some power of the product of the magnitude of the drift velocity and the current channel width $(\overline{V}_d d/L^2)^\alpha$, $\alpha < 1$. This suggests that the growth rate would be the same whether a weaker current is distributed over a larger channel or a stronger current is concentrated in a narrow channel. With regard to the auroral ionosphere, if the density gradient scale length is around 20 kms, then we see from Fig. 4, that the growth rate of smaller scale modes, say $\lambda \sim 1$ km corresponding to $k_y L \sim 100$, is reduced from $0.3\ \overline{V}_d/L$ to $0.15\ \overline{V}_d/L$ by a current channel of width $2d = 40$ km. The above growth rate corresponds to $0.75\ 10^{-3}\ s^{-1}$ if $\overline{V}_d = 50$ m/s (corresponding to currents of order $\mu A/m^2$). Since $\nu_{in} \sim \overline{V}_d/L$, these parameters correspond to the high latitude F region. We also point out that the short wavelength modes ($k_y L < 1$) are not affected by the current channels of 40 kms width.

Vickrey et al. (1980) have computed the growth rates from the current convective instability to explain small scale plasma density fluctuations near high latitude F region large scale plasma enhancements. However, their data indicate that the transverse dimensions of the currents driving the instability are comparable to the perpendicular (to the geomagnetic field) scale sizes of the plasma enhancements. Our results suggest that their growth rates are overestimates. From our analysis we would predict that both the long and short wavelength modes driven by the current convective instability should have longer growth times than previously estimated. Other data sets have also shown very narrow high latitude F-region field-aligned currents. From the results of this paper, we expect the nonlocal nature to have an important impact.

Recently Bythrow et al. (1984) using HILAT satellite data have measured very large downward currents (~ 100 $\mu A/m^2$), presumably carried by cold upward drifting electrons, in the high latitude topside F-region ionosphere. The dimensions of these currents perpendicular to the magnetic field is of order the transverse scale size (~ 3 km) of precipitation induced density structures. Turbulent horizontal ion drifts were also measured in conjunction with the large currents and transverse density gradients. Their data shows that $d \sim 1.9$ km, $L = 6$ km, and $\overline{V}_d = 30$ km/sec. In the case of ionospheric F region, $\nu_{ei}/\Omega_e \sim 10^{-4}$ and $\nu_n/\Omega_i \sim 10^{-3}$. The growth rate for different values of λ are as follows. For $\lambda = 1$, 2, and 10 km $\gamma \sim 0.0028$ Ω_i, $0.002640\Omega_i$, and 0.00146 Ω_i, respectively. Whereas, for $d/L \gg 1$, the local growth rate is ~ 0.0031 Ω_i. For narrower current channel and large density gradients or longer wavelength modes the growth rate could be substantially lower.

Finally, several aspects of the theory of the effects of finite current channel width on the current convective instability have not been discussed here. For very large currents, the self-consistent role of magnetic shear must be included [Huba and Ossakow, 1980]. An approximate value of the scale length for magnetic shear is $L_s = cB/4\pi J$ with c, the speed of light, B the magnetic field, and J the current density. For $J = 10^{-6} A/m^2$ and $B \sim 0.5$ G we find $L_s \sim 10^4$ km. For $d \ll L_s$ where d is the current channel width we do not expect magnetic shear effects to play an important role. In addition, we have not considered self-consistent velocity shear and its effects on the current convective instability with a finite current channel width, the finite parallel extent of the auroral ionosphere, electromagnetic effects, or nonlinear aspects. We are presently investigating several of these aforementioned effects.

REFERENCES

Bakshi, P., G. Ganguli, and P. Palmadesso, Finite width currents, magnetic shear, and the current driven ion cyclotron instability, Phys. Fluids, 26, 1808, 1983.

Bythrow, P.F., T.A. Potemra, L.J. Zanetti, C. Meng, R.E. Huffman, F.J. Rich, D.A. Hardy, W.B. Hanson, R.A. Heelis, Earthward directed high density Birkeland currents observed by HILAT, J. Geophys. Res. (in press, 1984).

Chaturvedi, P.K., and S.L. Ossakow, Nonlinear stabilization of the current convective instability in the diffuse aurora, Geophys. Res. Lett., 6, 957, 1979.

Chaturvedi, P.K., and S.L. Ossakow, The current convective instability as applied to the auroral ionosphere, J. Geophys. Res., 86, 4811, 1981.

Chaturvedi, P.K., and S.L. Ossakow, Effect of an electron beam on the current convective instability, J. Geophys. Res., 88, 4114, 1983.

Chen, J., and P. Palmadesso, Tearing instability in an anisotropic neutral sheet, Phys. Fluids, 27, 1198, 1984.

Ganguli, G., P. Bakshi, and P. Palmadesso, Electrostatic Ion-Cyclotron Waves in Magnetospheric Plasmas: Nonlocal Aspects, J. Geophys. Res., 89, 945, 1984.

Gary, S.P., Kinetic theory of current and density drift instabilities with weak charged-neutral collisions, J. Geophys. Res., 89, 179, 1984.

Huba, J.D., and S.L. Ossakow, Influence of magnetic shear on the current convective instability in the diffuse aurora, J. Geophys. Res., 85, 6874, 1980.

Huba, J.D., Long wavelength limit of the current convective instability, J. Geophys. Res., 89, 2913, 1984.

Huba, J.D., S.L. Ossakow, P.Satyanarayana, and P. N. Guzdar, Linear theory of the $E \times B$ instability with an inhomogeneous electric field, J. Geophy. Res., 88, 425, 1983.

Kadomtsev, B.B. and A.V. Nedospasov, Instability of the positive column in a magnetic field and the "anomalous diffusion effect," J. Nucl. Energy, Part C, 1, 230, 1960.

Keskinen, M.J., S.L. Ossakow, and B.E. McDonald, Nonlinear evolution of diffuse auroral F region ionospheric irregularities, Geophys. Res. Lett., 7, 573, 1980.

Keskinen, M.J., and S.L. Ossakow, Nonlinear evolution of plasma enhancements in the auroral ionosphere I: long wavelength irregularities, J. Geophys. Res., 87, 144, 1982.

Keskinen, M.J., and S.L. Ossakow, Nonlinear evolution of convecting plasma enhancements in the auroral ionosphere II: small scale irregulrities, J. Geophys. Res., 88, 474, 1983a.

Keskinen, M.J. and S.L. Ossakow, Theories of high latitude ionospheric irreguarities: A review, Radio Sci., 18, 1077, 1983b.

Keskinen, M.J., Nonlinear theory of the $\underline{E} \times \underline{B}$ instability with an inhomogeneous electric field, J. Geophys. Res., 89, 3913, 1984.

Lehnert, B., Diffusion processes in the positive column in a longitudinal magnetic field, in Proceedings of the Second Geneva Conference on the Peaceful Uses of Atomic Energy, 32, 349, 1958.

Linson, L.M., and J.B. Workman, Formation of striations in ionospheric plasma clouds, J. Geophys. Res., 75, 3211, 1970.

Ossakow, S.L. and P.K. Chaturvedi, Current convective instability in the diffuse aurora, Geophys. Res. Lett., 6, 332, 1979.

Satyanarayana, P., and S.L. Ossakow, Influence of velocity shear on the current convective instability, J. Geophys. Res., 89, 3019, 1983.

Vickrey, J.F., C.L. Rino, and T.A. Potemra, Chatanika/Triad observations of unstable ionization enhancements in the auroral F-region, Geophys. Res. Lett., 7, 789, 1980.

Vickrey, J.F., and M.C. Kelley, Irregularities and instabilities in the auroral F-region, High Latitude Space Plasma Physics, ed. B. Hultquist and T. Hagfors, Plenum, New York, 1983.

FIGURE CAPTIONS

1. Schematic of the geometry used displaying the finite current channel of width 2d along $\hat{x}$.

2. Plot of growth rate $\left(\gamma/\Omega_i\right)$ versus the ion-neutral collision frequency $\left(\nu_{in}/\Omega_i\right)$ for $k_y d = 0.3$, $\hat{V}_d/L = 5.0$, and $\nu_{ei}/\Omega_e = 10^{-4}$. Curve A shows the exact numerical solutions of Eq. (33). Curves B and C represent Eqs. (46) and (42) which are solutions in the inertial and collisional limits for long wavelength modes. Curves B´ and C´ represent the simplified analytical expressions, Eqs. (52) and (43), in the same limits. Curve D is the local solution, ω_-, given by Eq. (38).

3. Plot of growth rate $\hat{\gamma}$ versus $\hat{k}$ for $\hat{d} = 0.1$, 1.0, and 10.0 for sharp boundary case. The parameters chosen are $\nu_{in}/|\bar{V}_d/L| = 1$, $\Omega_i/|\bar{V}_d/L| = 10^4$, and $\nu_{ei}/|\bar{V}_d/L| = 10^{-4}$.

4. Plot of growth rate $\hat{\gamma}$ versus $\hat{d}$ for $\hat{k} = 0.5$, 1.0, 10.0 and 100.0, and for the same parameters as in Fig. 3. Note that $\hat{\gamma} \rightarrow \hat{\gamma}_L$ (Eq. 38) for $\hat{d} \rightarrow \infty$.

5. Plot of growth rate $\hat{\gamma}$ versus wavenumber $\hat{k}$ in the collisional limit for diffuse boundary case. The profiles used for the current and the density are given in Eqs. (53) and (54), respectively. The parameters used are the same as in Fig. 3.

6. Plot of growth rate $\hat{\gamma}$ versus finite current channel width $\hat{d}$ for diffuse boundary case and for the same parameters as in Fig. 3.
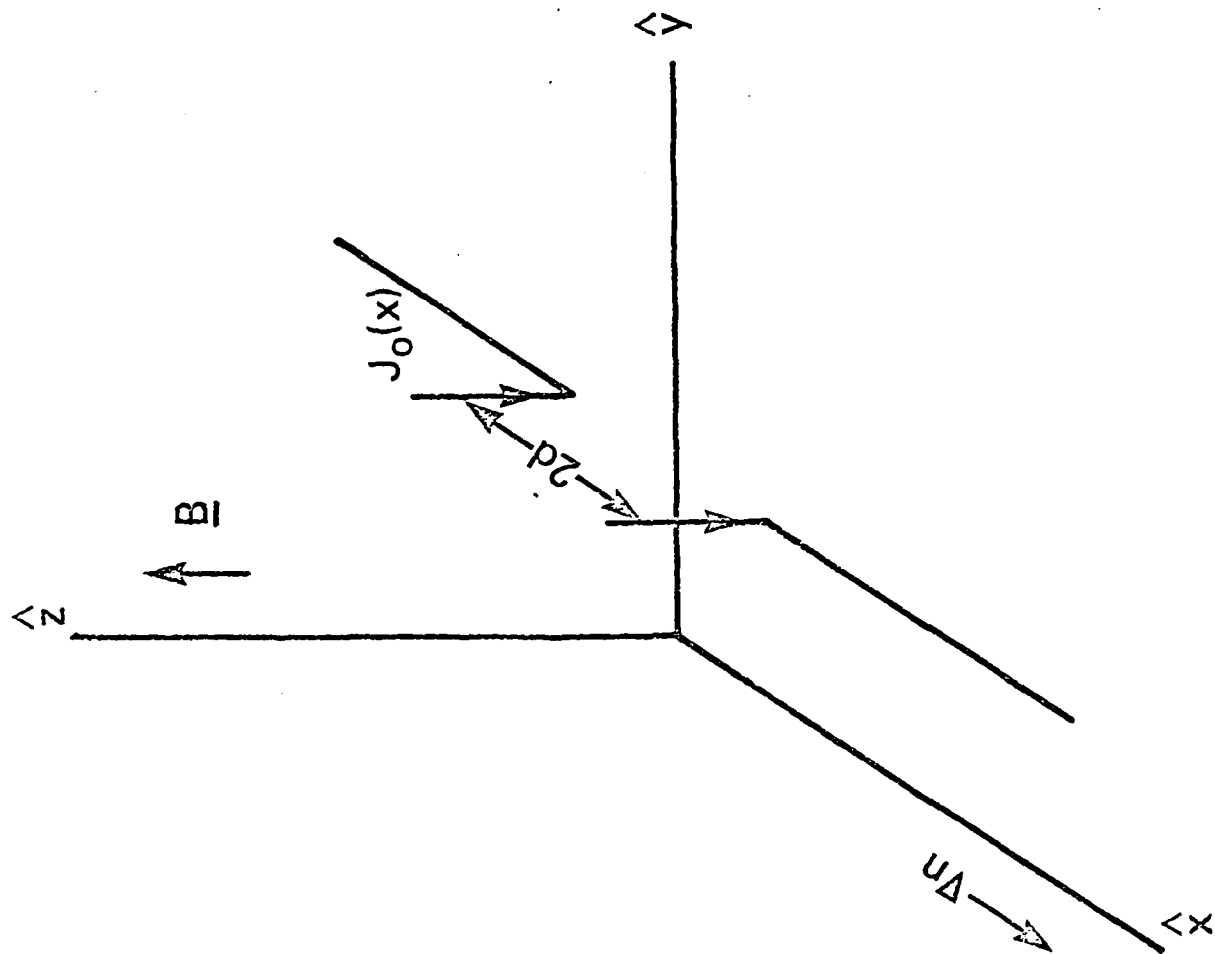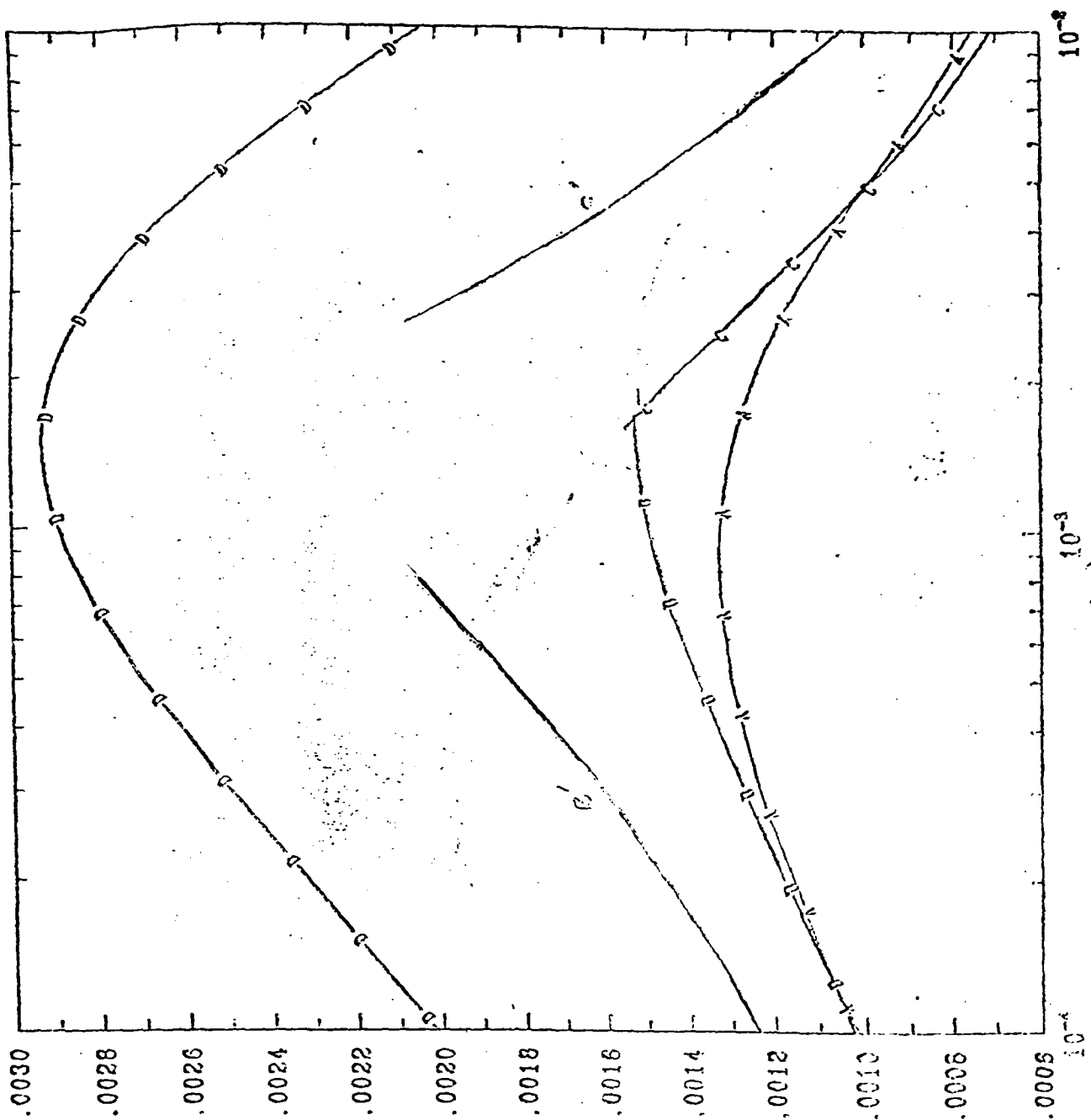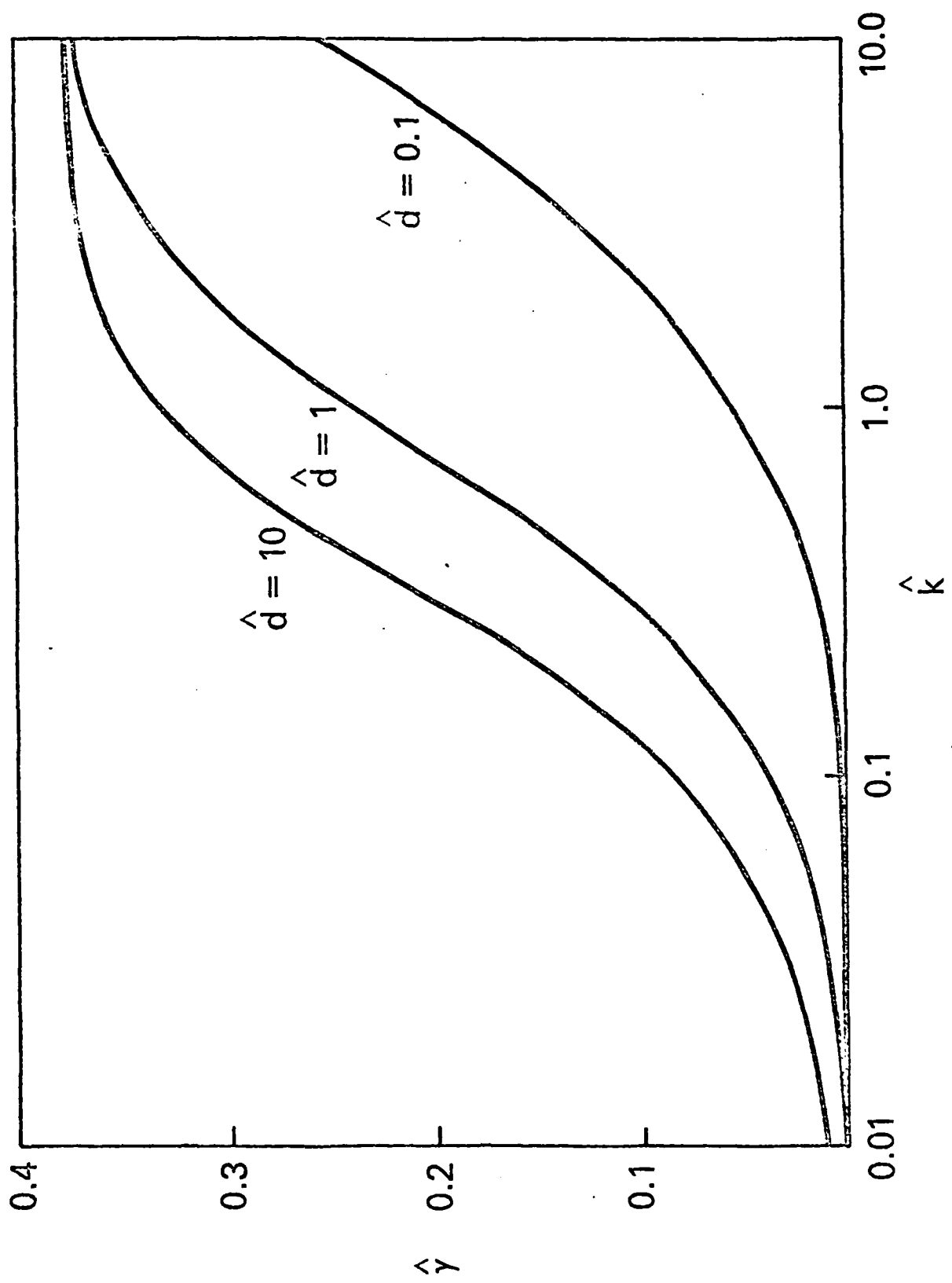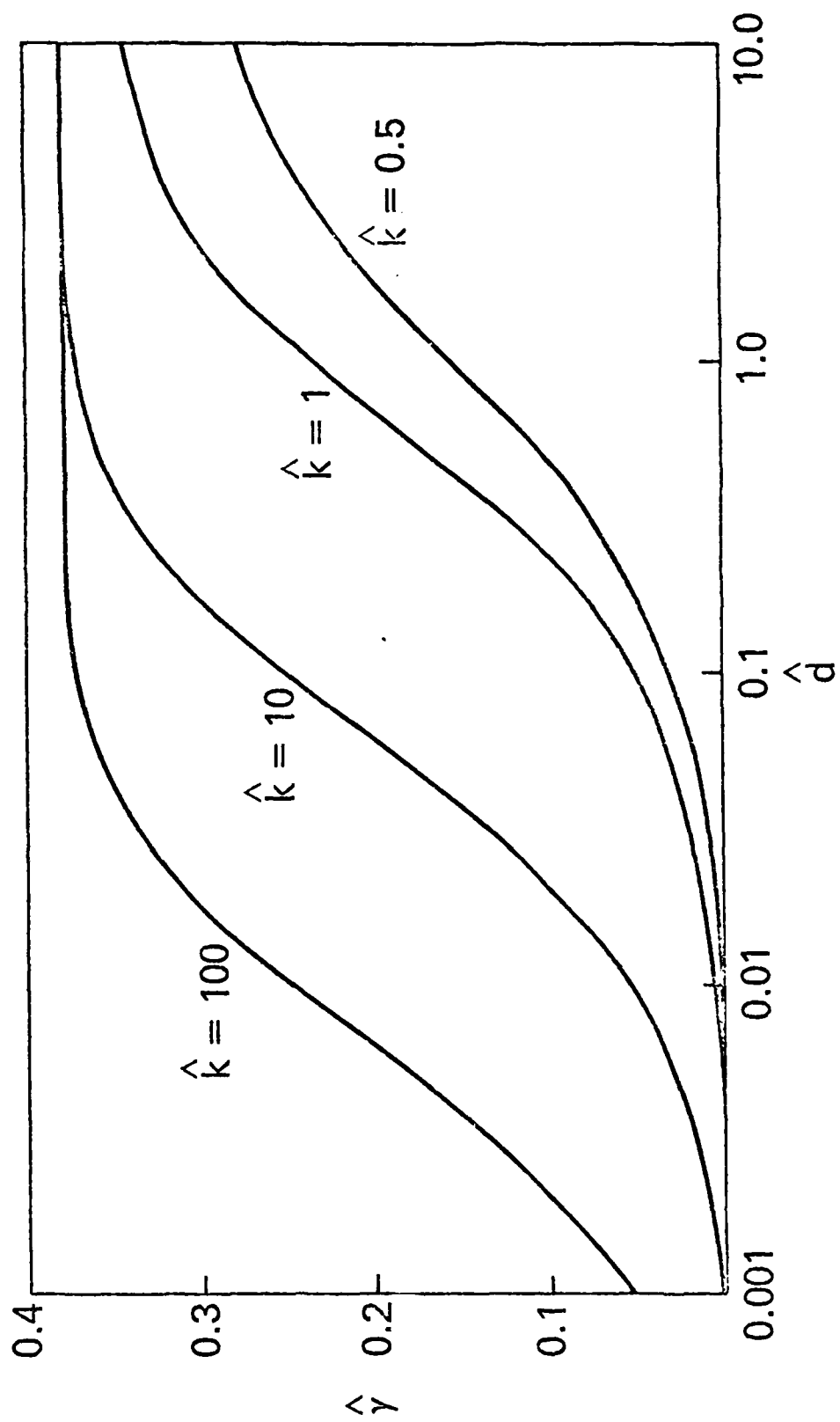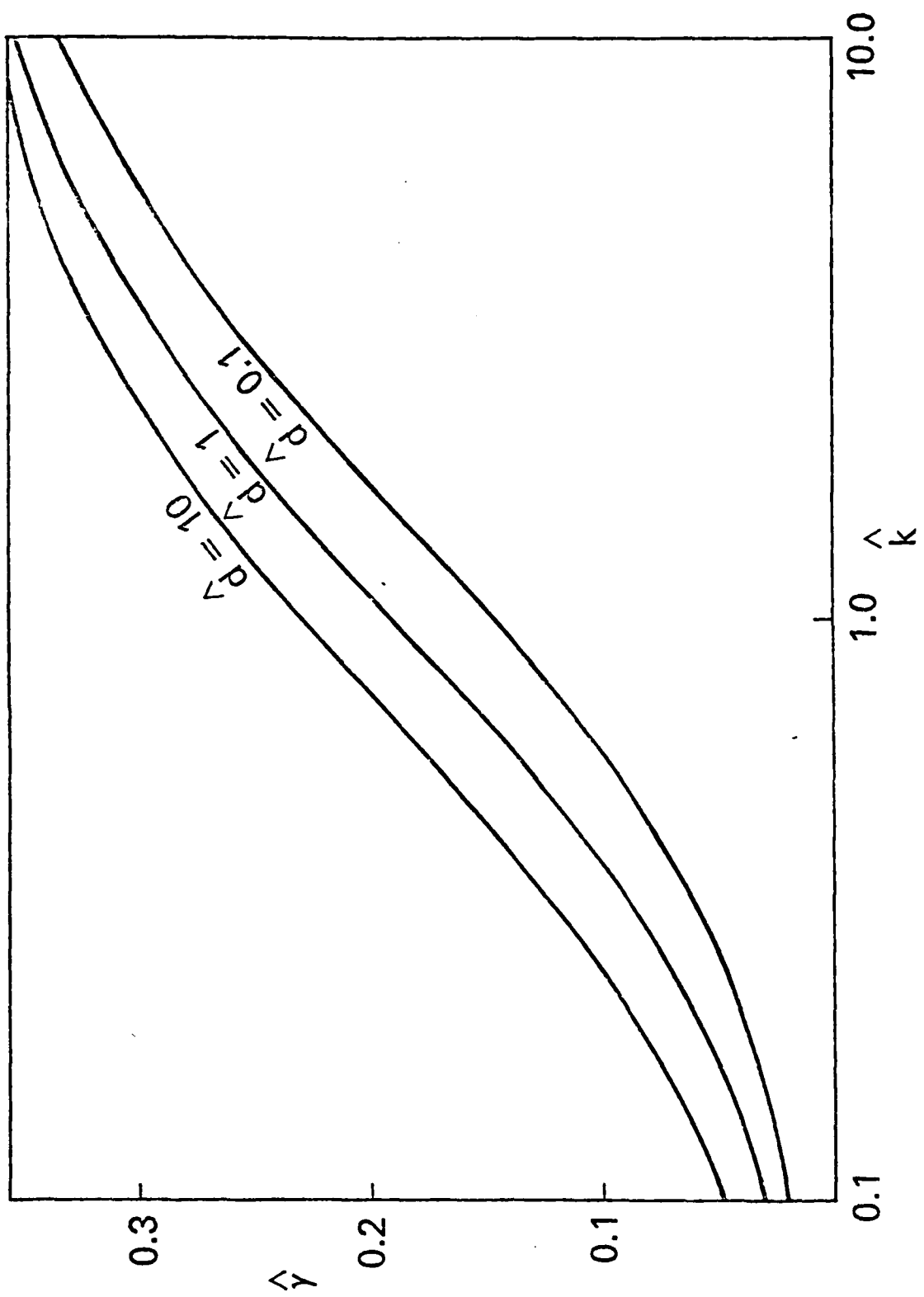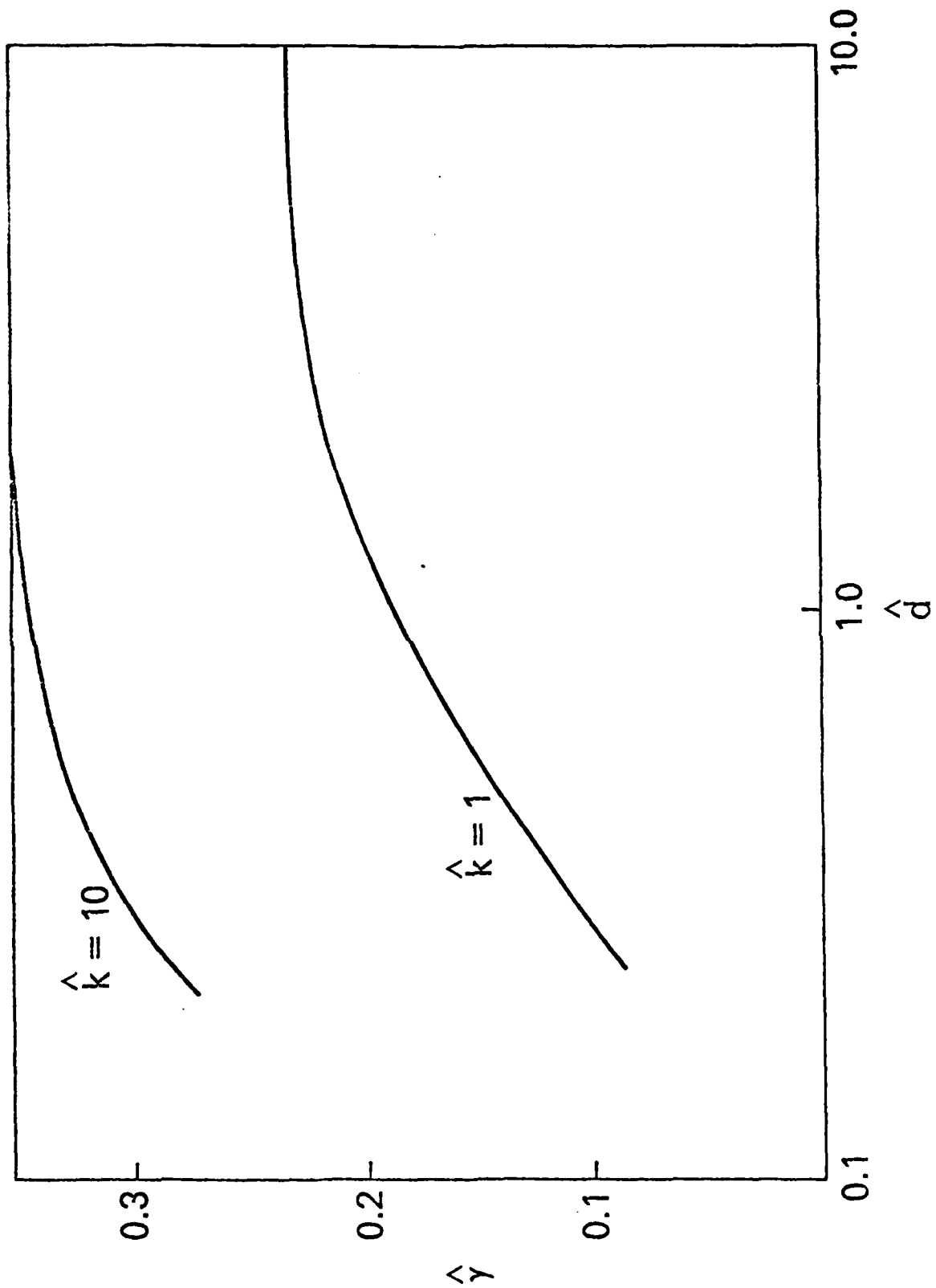
APPENDIX J

Ionospheric Turbulence: Interchange Instabilities and

Chaotic Fluid Behavior

IONOSPHERIC TURBULENCE: INTERCHANGE INSTABILITIES AND CHAOTIC FLUID BEHAVIOR

J.D. Huba[1], A.B. Hassam[2], I.B. Schwartz[1], and M.J. Keskinen[1]

[1]Naval Research Laboratory, Washington, D.C. 20375

[2]Science Applications, Inc., McLean, Virginia 22102

Abstract We develop a set of mode coupling equations which describe the nonlinear evolution of the Rayleigh-Taylor and $E \times B$ gradient drift instabilities which are relevant to the ionosphere. We show that for a three mode system, the nonlinear equations describing these instabilities correspond exactly to the Lorenz equations which approximately describe the Rayleigh-Benard instability. It is shown that the three mode system can exhibit a strange attractor with chaotic behavior. Ion inertia plays a critical role in this phenomenon in that if it is neglected, as in the collisional limit, the three mode system does not exhibit chaos and a stable convection pattern results.

Introduction

It is well-known that interchange instabilities produce turbulence in the ionosphere [Ossakow, 1979; Fejer and Kelley, 1980]. The Rayleigh-Taylor instability is believed to cause the intense nighttime equatorial F region turbulence known as equatorial spread F [Ossakow, 1981; Kelley and McClure, 1981], while the $E \times B$ gradient drift instability has been invoked to explain high-latitude ionospheric irregularities [Keskinen and Ossakow, 1983], the rapid structuring of barium clouds [Linson and Workman, 1970], and turbulence in equatorial electrojet [Ossakow, 1979]. These instabilities are fundamentally similar in nature in that they require a density gradient, and they act to interchange the high and low plasma density regions. However, they have different driving mechanisms: the Rayleigh-Taylor instability is driven by the gravitational force, while the $E \times B$ gradient drift instability is driven by an ambient electric field or neutral wind. A considerable amount of research has been devoted to the study of these instabilities and their application to ionospheric turbulence. Since, in general, it is the nonlinear phase of the instabilities that is observed, it is important to identify the salient characteristics of this phase (e.g., wave amplitude at saturation, power spectra, etc.).

Interchange instabilities, as they are applied to the ionosphere, can be divided into two categories: collisional and inertial. The collisional limit considers $\nu_{in} \gg \omega$ (where ν_{in} is the ion-neutral collision frequency and ω is the wave frequency) while the inertial limit considers $\omega \gg \nu_{in}$. In the ionosphere, the transition from the collisional limit to the inertial limit typically occurs in the altitude regime ~ 500 km. The bulk of the nonlinear research on inter-

change instabilities in the ionosphere (both theory and simulation) has been restricted to the collisional domain. The purpose of this paper is to extend the nonlinear theory of interchange instabilities into the inertial regime.

The organization of this letter is as follows. In the next section we present the geometry, assumptions, and derivation of the nonlinear mode coupling equations. In the following section we present our results for a three mode system and show the correspondence to the Rayleigh-Benard problem. We derive a criterion for the onset of chaotic turbulence involving the dissipation parameters (i.e., diffusion coefficient, ion-neutral collision frequency). Finally, in the last section we summarize our findings and discuss the implications for ionospheric turbulence.

Derivation of Nonlinear Equations

The plasma configuration and assumptions used in the analysis are described as follows. We consider an ambient magnetic field in the z-direction $(B = B_0 e_z)$, a gravitational acceleration in the -x-direction $(g = -g e_x)$, a density gradient in the x-direction $(n = n_0(x)$ and $\partial n_0/\partial x > 0)$, and an ambient electric field in the y direction $(E = E_0 e_y)$. We assume two dimensional perturbations in the x-y plane (transverse to B) such that $k = k_x e_x + k_y e_y$ with $k_x L \gg 1$ and $k_y L \gg 1$ where $L = [\partial \ln n/\partial x]^{-1}$ is the density gradient scale length. For simplicity we assume a cold ion plasma $(T_i = 0)$. We consider low frequency turbulence in a weakly collisional plasma such that $\partial/\partial t \ll \Omega_i$, $\nu_{in} \ll \Omega_i$, $\nu_{ie} \ll \Omega_i$, and $\nu_{ei} \ll \Omega_e$ where $\Omega_\alpha = eB/m_\alpha c$ is the cyclotron frequency of species α, ν_{in} is the ion-neutral collision frequency, ν_{ie} is the ion-electron collision frequency, and ν_{ei} is the electron-ion collision frequency. We neglect electron-neutral collisions since $\nu_{en}/\Omega_e \ll \nu_{in}/\Omega_i$ in the F region. Finally, we consider electrostatic turbulence and assume quasi-neutrality $(n_e = n_i)$.

The equations used in the analysis are continuity, momentum transfer, and charge conservation:

$$\frac{\partial n_\alpha}{\partial t} + \nabla \cdot (n V_\alpha) = 0 \qquad (1)$$

$$0 = -\frac{e}{m_e}(E + \frac{1}{c} V_e \times B) - \frac{T_e}{m_e}\frac{\nabla n}{n} - \nu_{ei}(V_e - V_i) \qquad (2)$$

$$\frac{dV_i}{dt} = \frac{e}{m_i}(E + \frac{1}{c} V_i \times B) - \nu_{ie}(V_i - V_e)$$
$$- \nu_{in} V_i + g \qquad (3)$$

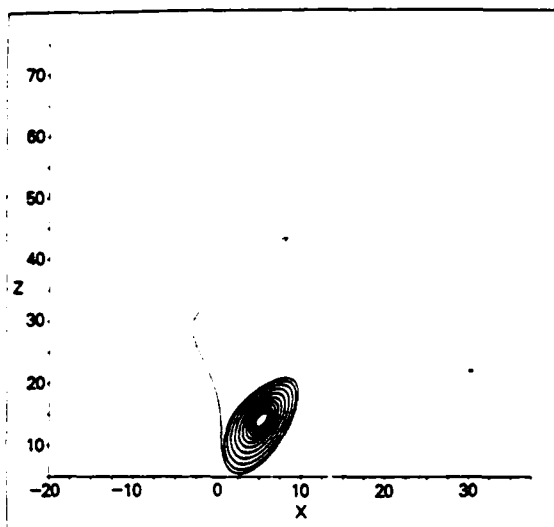$$\nabla \cdot J = \nabla \cdot [n(V_i - V_e)] = 0 \qquad (4)$$

Fig. 1.   Depicted is an approach to the non-trivial steady state attractor to (9)-(11) projected onto the X-Z plane. The parameters used for the numerical simulation are $\sigma = 10$ and $r = 15$; note that $r_c = 21.4$ so that $1 < r < r_c$.

We perturb (1)-(4) about an equilibrium and let $n = n_0 + \tilde{n}$, $E = E_0 - \nabla\tilde{\phi}$, and $V = V_0 + \tilde{V}$. To lowest order in ν_α/Ω_α, the equilibrium drifts are given by $V_{e0} = -(cT_e/eB)|\partial\ell n\, n/\partial x|^{-1} e_y$ (the electron diamagnetic drift) and $V_{i0} = (g/\Omega_i + (\nu_{in}/\Omega_i)(cE_0/B))e_y$ (the ion gravitational drift and ion Pedersen drift, respectively). Note we have chosen $V_{0x} + V_{0x} - cE_{0y}/B$. We solve (2) and (3) for $\tilde{V}_e$ and $\tilde{V}_i$, and substitute these values into (1) and (4). We arrive at the coupled set of equations for $\tilde{n}$ and $\tilde{\phi}$:

$$\frac{\partial}{\partial t}\frac{\tilde{n}}{n_0} - \frac{c}{B}\nabla\tilde{\phi} \times \hat{e}_z \cdot \frac{\nabla n_0}{n_0} - D_e \nabla^2 \frac{\tilde{n}}{n_0}$$
$$= \frac{c}{Bn_0}\nabla\tilde{\phi} \times \hat{e}_z \cdot \nabla\tilde{n} \qquad (5)$$

and

$$\left[\frac{g}{\Omega_i} \times \hat{e}_z + \frac{\nu_{in}}{\Omega_i}\frac{cE}{B}\right] \cdot -\frac{\tilde{n}}{n_0}$$

$$-\frac{c}{B}\frac{1}{\Omega_i}\left[\frac{\partial}{\partial t} + \hat{e}_z \times \nabla\tilde{\phi} \cdot \nabla + \nu_{in}\right]\nabla^2\tilde{\phi} = 0 \qquad (6)$$

where $D_e = \nu_{ei}\rho_e^2$ is the electron diffusion coefficient and we have assumed $\partial/\partial t \gg V_{i0}$. It may be seen that (5) and (6) are mathematically the same as the Rayleigh-Benard equations [Eqs. (17) and (18) of Lorenz (1963)] provided the substitution $\nu_{in} \rightarrow \nu\nabla^2$ is made in (6).

Results

We now present results of our analysis for a three mode configuration. Prior to this we cast (5) and (6) into dimensionless form. Specifically, we find that (5) and (6) can be written as

$$\frac{\partial\tilde{n}_1}{\partial t_1} = \hat{D}_e\nabla^2 \tilde{n}_1 + \hat{\partial}_y\tilde{\phi}_1 + \nabla\tilde{n}_1 \cdot \nabla\tilde{\phi}_1 \times \hat{e}_z \qquad (7)$$

and

$$\left[\frac{\partial}{\partial t_1} + \hat{e}_z \times \nabla\tilde{\phi}_1 \cdot \nabla\right]\nabla^2\tilde{\phi}_1 = -\hat{\nu}_{in}\nabla^2\tilde{\phi}_1 + \hat{\partial}_y\tilde{n}_1 \qquad (8)$$

where $t_1 = \gamma_0 t$, $\hat{\nu}_{in} = \nu_{in}/\gamma_0$, $\tilde{n}_1 = (\tilde{n}/n_0)(L/\lambda)$, $\tilde{\phi}_1 = \tilde{\phi}(c/B\lambda^2\gamma_0)$, $\hat{\nabla} = \lambda\nabla$, $\hat{D}_e = D_e/\lambda^2\gamma_0$, $\gamma_0 = [g + \nu_{in}cE_0/B]/L]^{1/2}$, and λ is half of the maximum wavelength permitted (i.e., $\lambda < 2L$).

We consider the following perturbations for $\tilde{\phi}_1$ and $\tilde{n}_1$: $\tilde{\phi}_1 = X_1 \sin x \sin y$ and $\tilde{n}_1 = Y_1 \sin x \cos y + Z_1 \sin 2x$ where we have taken $k_x = k_y$ with $k_x = 1/\lambda$ and $k_y = 1/\lambda$ for simplicity. Here, x and y represent the x and y spatial coordinate normalized to λ, and only the coefficients X_1, Y_1, and Z_1 are assumed to be time dependent. Substituting $\tilde{n}_1$ and $\tilde{\phi}_1$ into (7) and (8) we obtain the following set of coupled ordinary differential equations:

$$\dot{X} = -\sigma X + \sigma Y \qquad (9)$$

$$\dot{Y} = -Y + rX - XZ \qquad (10)$$

$$\dot{Z} = -2Z + XY \qquad (11)$$

where the dot over a variable indicates a time derivative, $X = X_1\sqrt{r\sigma}$, $Y = Y_1\sqrt{r\sigma}/2\nu_{in}$, $Z = rZ_1$, $\tau = 2D_e t_1$, $\sigma = \nu_{in}/2D_e$ and $r = [4D_e\nu_{in}]^{-1}$. Equations (9)-(11) correspond exactly to the equations solved by Lorenz (1963) for the Rayleigh-Benard instability (with the exception that Lorenz' parameter b is equal to 2 in our case).

Following Lorenz (1963), (9)-(11) can be analyzed to determine (i) the nonlinear fixed states of the system, and (ii) the stability of these fixed states as a function of r and σ. The fixed states are determined by the condition $\dot{X} = \dot{Y} = \dot{Z} = 0$. If $r < 1$, the only stable steady state is given by $X_0 = Y_0 = Z_0 = 0$. This represents the state of no convection, i.e., the usual equilibrium state upon which linear stability analysis is performed; in fact, $r = 1$ is the point of marginal linear stability of the equilibrium. For $r > 1$, the equilibrium is unstable resulting in convection and the interchange of high and low density regions. However, $r > 1$ allows two additional fixed states, given by $X_0 = Y_0 = \pm [2(r - 1)]^{1/2}$ and $Z_0 = r - 1$; these correspond to convection cells of either positive or negative vorticity. The linear instability may thus "saturate" by attracting to one of these new fixed states with X_0, Y_0, and Z_0 providing estimates for the saturation amplitudes of $\tilde{n}$ and $\tilde{\phi}$. This is indeed the case for $1 < r < r_c \equiv \sigma(\sigma + 5)/(\sigma - 3)$ or $\sigma < 3$. In this range of r, the fixed states are stable and the orbit in X, Y, Z phase space asymptotes to one of the nontrivial fixed points. An example is shown in Figure 1 ($\sigma = 10$, $r = 15$) where the projection of the orbit on to the X-Z plane is plotted.

For $\sigma > 3$ and $r > r_c$, the saturated convection pattern described above is itself unstable. No other fixed stable states exist; this means that the amplitudes X, Y, and Z oscillate in intensity in periodic or chaotic fashion. The magnitude of these oscillations cannot be determined analytically and numerical analysis of (9) - (11) is required. Nevertheless, some general features may be discerned: even though the phase space orbit does not approach a single point, it does lie in a bounded, or "attracting", region of phase space. Figure 2 illustrates such an orbit for $\sigma = 10$ and $r = 30$. This orbit in fact tends

to encircle either one or the other of the two non-trivial fixed states. There is, however, no periodicity for the case shown: the transition from encircling one or the other fixed points is seemingly random. In such a case the orbit is "chaotic" and the attracting region is a strange attractor. Since all orbits are unstable, one sees chaotic behavior in the amplitudes of X, Y, and Z [Ruelle and Takens, 1971]. Note that the amplitudes of X and Z in Figure 2 can fluctuate by more than a factor of 2.

An important point to be recognized concerning the application of this theory to interchange instabilities is the following. As noted earlier, we consider two limits: collisional and inertial. In the collisional limit $(\nu_{in} \gg \partial/\partial t)$, $\tilde{X} = 0$ in (9) so that $X = Y$ and the problem reduces to solving only two coupled differential equations. For this case, the convection states are always stable. This is the situation that has been considered in most previous analytic treatments of ionospheric interchange instabilities [Rognlien and Weinstock, 1974; Chaturvedi and Ossakow, 1977, 1979] although the stability of the convection states was not analyzed. Thus, for this simple three mode system, we find that ion inertia is required for unstable convection patterns to occur. We comment that the nonlinear behavior of Rayleigh-Taylor instability in the inertial limit has been considered by Hudson (1978). However, Hudson (1978) did not find chaotic behavior because it was assumed that $\partial/\partial t = -i\omega$ where ω is the linear eigen-frequency in (6). This ad hoc assumption effectively reduces the problem to two differential equations and leads to results similar to the collisional limit.

Conclusions

We have shown that interchange instabilities relevant to ionospheric turbulence (Rayleigh-Taylor and $E \times B$ gradient drift), can be studied in the context of chaotic attractor theory. In particular, we demonstrate that for a simple system (three modes) the equations governing these instabilities are exactly the same as those that govern the Rayleigh-Benard instability [Saltzman, 1962; Lorenz, 1963]. The analogy between these two instabilities is the following. The Rayleigh-Benard instability is driven by a temperature gradient and convects "hot and cold" fluid elements; the temperature gradient is maintained by a heat source at one end and a heat sink at the other. The Rayleigh-Taylor and $E \times B$ gradient drift instabilities are driven by a density gradient and convect "heavy and light" fluid elements; in the case of the ionosphere, the density gradient could be maintained by photoionization at one end and recombination at the other. We have shown that these interchange instabilities can exhibit both stable and unstable convection patterns in this system. A crucial point is that unstable convection only results if inertial effects are important, i.e., $\nu_{in} \lesssim \partial/\partial t$.

For application to the ionosphere, we consider the stability of the fixed states of the Rayleigh-Taylor instability in the equatorial ionosphere, and the $E \times B$ gradient drift instability in the high latitude auroral ionosphere. Three observations may be made. First, the nonlinear fixed states given by X_0, Y_0, and Z_0
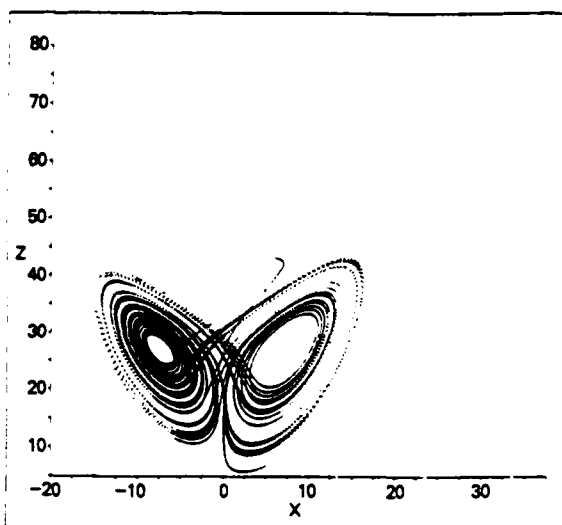

Fig. 2. A strange attractor for (9)-(11) is illustrated as a projection onto the X-Z plane. The parameters used are $\sigma = 10$ and $r = 30$. Note that $r_c = 21.4$ so that $r > r_c$. All periodic orbits are unstable, as well as the three equilibrium points. The attractor lies in a finite volume of space.

correspond to the saturated potential and density fluctuation amplitudes. We note the density fluctuation amplitude associated with Y_0 is $\tilde{n}/n_0 = 4(\rho_e/L)(\nu_{in}\nu_{ei}/\gamma_0^2)^{1/2}$, while the amplitude associated with Z_0 is $\tilde{n}/n_0 = \lambda/L$. These estimates agree with previous results [Chaturvedi and Ossakow, 1977, 1979] and yield density fluctuations of several percent for typical F region parameters. These estimates can vary by more than a factor of 2 when the instabilities are in the "chaotic regime" (see Figure 2). Second, since $\sigma = \lambda^2\nu_{in}/2\nu_{ei}\rho_e^2$ using the normalizations listed after (8), we find that $10^3 \leq \sigma \leq 10^5$ for the F region ionosphere (200-800 km) where we have taken $\lambda = 500$ m, $\rho_e = 1.5$ cm, $\nu_{in} = 2.4 \times 10^{11} T_n^{1/2} n_n \ sec^{-1}$ [Strobel and McElroy, 1970], $\nu_{ei} = (\lambda_{ei}/3.5 \times 10^5)(n_e/T_e^{3/2}) \ sec^{-1}$ [Braginskii, 1965; Johnson, 1961] where T_e is the electron temperature in eV, n_n is the neutral gas density, n_e is the electron density, $\lambda_{ei} = 23.4 - 1.15 \log n_e + 3.45 \log T_e$, and the neutral densities were obtained from a Jacchia (1975) model neutral atmosphere. Third, since $\sigma \gg 1$, the critical value of r is given by $r_c = \sigma$. For the Rayleigh-Taylor instability, the condition for unstable fixed states can thus be written as $\nu_{in} < (g/2L)^{1/2}$. For $g = 9.8$ m/sec^2 and $L = 10$ km, we find that unstable behavior can occur for $\nu_{in} < 0.02 \ sec^{-1}$ which corresponds to altitudes greater than 400-500 km in the equatorial F region ionosphere. For the $E \times B$ gradient drift instability, the condition for an unstable fixed state is $\nu_{in} \lesssim cE_0/2RL$. Taking $cE_0/R = 6 \times 10^2$ m/sec and $L = 10^2$ km [Weber et al., 1984], we find that chaotic behavior can occur for $\nu_{in} < 6 \times 10^{-3} \ sec^{-1}$ which corresponds to altitudes greater than roughly 500 km in the high latitude F region.

Finally, we have only considered a simple three mode system which could be argued to be unrealistic. It is known that the nonlinear

behavior of the Lorenz equations for more than
three modes can be different from the three mode
system [Ott, 1981]. For example, we have shown
that for three modes, the nonlinear fixed states
are always stable in the collisional limit (i.e.,
$\nu_{in} > \nu_0$). However, we have also developed a
pseudo-spectral code which follows the evolution
of a many mode system ($\sim$ 120 modes). Preliminary
results indicate that chaotic fluid behavior can
also occur in the collisional limit, in sharp
contrast to the simple three mode result. A
report on the nonlinear dynamics of the many mode
system will follow shortly.

References

Braginskii, S.I., Transport processes in a
  plasma, in Reviews of Plasma Physics, ed. M.
  Leontovich, Vol. 1, Consultants Bureau, New
  York, 1965.
Chaturvedi, P.K. and S.L. Ossakow, Nonlinear
  Theory of the Collisional Rayleigh-Taylor
  Instability in Equatorial Spread F, Geophys.
  Res. Lett., 4, 558, 1977.
Chaturvedi, P.K. and S.L. Ossakow, Nonlinear
  Stabilization of the $E \times B$ Gradient Drift
  Instability in Ionospheric Plasma Clouds, J.
  Geophys. Res., 84, 419, 1979.
Fejer, B.G. and M.C. Kelley, Ionospheric
  Irregularities, Rev. Geophys. Space Phys., 18,
  401, 1980.
Hudson, M.K., Spread F Bubbles: Nonlinear
  Rayleigh-Taylor Mode in Two Dimensions, J.
  Geophys. Res., 83, 3189, 1978.
Jacchia, L.G., Static Diffusion Models of the
  Upper Atmosphere with Empirical Temperature
  Profiles, Smithson. Contrib. Astrophys., 8,
  215, 1965.
Johnson, F.S., Satellite Environment Handbook,
  ed. F.S. Johnson, Stanford University Press,
  Stanford, Calif., 1961.

Kelley, M.C. and J.P. McClure, Equatorial Spread
  F: A Review of Recent Experimental Results,
  J. Atm. Terr. Phys., 43, 427, 1981.
Keskinen, M.J. and S.L. Ossakow, Theories of
  High-Latitude Ionospheric Irregularities: A
  Review, Radio Sci., 18, 1077, 1983.
Linson, L.M. and J.B. Workman, Formation of
  Striations in Ionospheric Plasma Clouds, J.
  Geophys. Res., 75, 3211, 1970.
Lorenz, E.N., Deterministic Nonperiodic Flow, J.
  Atmos. Sci., 20, 130, 1963.
Ossakow, S.L., Ionospheric Irregularities, Rev.
  Geophys. Space Phys., 17, 521, 1979.
Ossakow, S.L., Spread F Theories - A Review, J.
  Atm. Terr. Phys., 43, 437, 1981.
Ott, E., Strange Attractors and Chaotic Motions
  of Dynamical Systems, Rev. Mod. Phys., 53,
  655, 1981.
Rognlien, T.D. and J. Weinstock, Theory of the
  Nonlinear Spectrum of the Gradient Drift
  Instability in the Equatorial Electrojet, J.
  Geophys. Res., 79, 4733, 1974.
Ruelle, D. and F. Takens, On the Nature of
  Turbulence, Comm. Math. Phys., 20, 167, 1971.
Saltzman, B., Finite Amplitude Free Convection as
  an Initial Value Problem-I, J. Atmos. Sci.,
  19, 329, 1962.
Strobel, D.F. and M.B. McElroy, The F2-layer at
  Middle Latitudes, Planet. Space Sci., 18,
  1181, 1970.
Weber, E.J., J. Buchau, J.G. Moore, J.R. Sharber,
  R.C. Livingston, J.D. Winningham, and B.
  Reinisch, F layer Ionization Patches in the
  Polar Cap, J. Geophys. Res., 89, 1683, 1984.

A.B. Hassam, Science Applications, Inc.,
McLean, VA 22102.
J.D. Huba, M.J. Keskinen, and I.B. Schwartz,
Naval Research Laboratory, Washington, D.C.
20375-5000.

APPENDIX K

Estimating Spectral Indices from Transforms of

Discrete Representations of Density Functions

Estimating Spectral Indices from Transforms of Discrete Representations of Density Functions

M. MULBRANDON, N.J. ZABUSKY* AND E. HYMAN**

Geophysical and Plasma Dynamics Branch
Plasma Physics Division

*Fluid Sciences, Inc.
Pittsburgh, PA 15217

**Science Applications, Inc.
McLean, VA 22102

March 30, 1984

NAVAL RESEARCH LABORATORY
Washington, D.C.

REPORT DOCUMENTATION PAGE

1a. REPORT SECURITY CLASSIFICATION		1b. RESTRICTIVE MARKINGS			
UNCLASSIFIED					
2a. SECURITY CLASSIFICATION AUTHORITY		3. DISTRIBUTION/AVAILABILITY OF REPORT			
2b. DECLASSIFICATION/DOWNGRADING SCHEDULE		Approved for public release; distribution unlimited.			
4. PERFORMING ORGANIZATION REPORT NUMBER(S)		5. MONITORING ORGANIZATION REPORT NUMBERS			
NRL Memorandum Report 5298					
6a. NAME OF PERFORMING ORGANIZATION	6b. OFFICE SYMBOL (If applicable)	7a. NAME OF MONITORING ORGANIZATION			
Naval Research Laboratory					
6c. ADDRESS (City, State, and ZIP Code)		7b. ADDRESS (City, State and ZIP Code)			
Washington, DC 20375					
8a. NAME OF FUNDING/SPONSORING ORGANIZATION	8b. OFFICE SYMBOL (If applicable)	9. PROCUREMENT INSTRUMENT IDENTIFICATION NUMBER			
Defense Nuclear Agency					
8c. ADDRESS (City, State and ZIP Code)		10. SOURCE OF FUNDING NOS			
Washington, DC 20305		PROGRAM ELEMENT NO	PROJECT NO	TASK NO	WORK UNIT NO
11. TITLE (Include Security Classification)		62715H			47-0917-04
(See Page ii)					

12. PERSONAL AUTHORS
M. Mulbrandon, N.J. Zabusky* and E. Hyman**

13a. TYPE OF REPORT	13b. TIME COVERED		14. DATE OF REPORT (Yr. Mo. Day)	15. PAGE COUNT
Interim	FROM	TO	March 30, 1984	41

16. SUPPLEMENTARY NOTATION   *Fluid Sciences, Inc., Pittsburgh, PA 15217
**Science Applications, Inc., McLean, VA 22102   (Continues)

17. COSATI CODES			18. SUBJECT TERMS (Continue on reverse if necessary and identify by block number)	
FIELD	GROUP	SUB GR	Power Spectral Density (PSD) Spatial irregularities	
			Optical scans Plasma striations (Continues)	

19. ABSTRACT (Continue on reverse if necessary and identify by block number)

   Structuring of plasma in the high altitude disturbed atmosphere can adversely impact the operation of optical detectors. In this paper we consider idealized functions of one variable that may represent "scan" functions that are obtained from three-dimensional optical sources observed by remote sensors. We establish the relationship between singular properties of these functions or their derivatives and the spectral index of their transforms, and describe the limitations on obtaining reliable spectral indices where there is no clear *separation of scales* in a spatial profile. The ability to extract a good estimate of the spectral index depends on the complexity of the spatial emission profile, the adequacy of resolution, and aliasing errors that necessarily result from the analysis. We illustrate these competitive effects by numerical examples using spatial profiles of a top hat, circular arc and trapezoid.

20. DISTRIBUTION/AVAILABILITY OF ABSTRACT	21. ABSTRACT SECURITY CLASSIFICATION	
UNCLASSIFIED/UNLIMITED ☒ SAME AS RPT ☐ DTIC USERS ☐	UNCLASSIFIED	
22a. NAME OF RESPONSIBLE INDIVIDUAL	22b. TELEPHONE NUMBER (Include Area Code)	22c. OFFICE SYMBOL
M. Mulbrandon	(202) 767-6781	Code 4780

DD FORM 1473, 83 APR   EDITION OF 1 JAN 73 IS OBSOLETE

11. TITLE (Include Security Classification)

ESTIMATING SPECTRAL INDICES FROM TRANSFORMS OF DISCRETE REPRESENTATIONS OF DENSITY FUNCTIONS

16. SUPPLEMENTARY NOTATION (Continued)

18. SUBJECT TERMS (Continued)

Spectral indices
Separation of scales

CONTENTS

iii

ESTIMATING SPECTRAL INDICES FROM TRANSFORMS OF
DISCRETE REPRESENTATIONS OF DENSITY FUNCTIONS

1.   INTRODUCTION

One of the important needs of the defense community is to be able to
evaluate reliably the effect on optical sensors of the disturbed atmosphere
resulting from a high altitude nuclear event (HANE). If we can understand
the structure and emission characteristics of the disturbed atmosphere it
will be possible to design detectors which avoid particular wavelength
regions and can discriminate between targets and artifactual atmospheric
phenomena.

A great deal has been learned in the past several years from the
research programs at the Naval Research Laboratory (NRL) and elsewhere
about the instability mechanisms that lead to ionospheric plasma structures
and the space-time characteristics of the resulting striations. In the
near future we hope to clarify the cause of the so-called "freezing"
phenomenon for striations, make predictions about their inner scale length,
etc. However, to use this information to design better detectors, we must
relate the observed spectral characteristics of the density fluctuations of
the emitting medium to the structures that numerical simulations and other
forms of data (besides optical) predict, and vice-versa. This is an
"inverse" problem and can be ill-posed and yield nonunique solutions. The
motivation for our studies is to reduce nonuniqueness, etc. through a
detailed consideration of the procedures used in relating observed spectral
quantities to striation properties.

We will address several aspects of this problem in a series of papers
that are currently in preparation. In this paper we consider idealized
"scan" functions, namely functions of one variable that can arise from

three-dimensional optical sources that are observed by remote sensors. We will establish the relationship between continuity properties of these functions or their derivatives and the spectral index of their transforms. We will show how inadequate resolution, whether in measured data or numerical simulations, introduces errors in estimates of spectral indices. Specifically, we will discuss the errors that arise from "aliasing" and the number of data samples required to obtain an adequate separation of scales. We will illustrate these effects with numerical examples.

In a second paper in preparation we relate spectral properties of multidimensional emitting sources to spectral properties of the scan functions. Sources of constant emission intensity and sources with finite gradients viewed from different directions will be considered.

In a third paper, a simple model of a realistic nonaxisymmetric ionospheric striation is constructed, which incorporates the properties of emitting structures established in the NRL research programs. Using this model, we examine the variation in spectral properties that would be observed by scans obtained from different viewing directions. We also investigate the sensitivity of the spectral index to variations in model parameters. Subsequent papers will investigate multiple striation effects and other properties needed to further clarify the relationship between emitting sources and measured spectral indices.

A preliminary investigation of these topics has been given by Wortman and Klb [1]. They have added the additional feature of a self-similar and probabilistic distribution of scale sizes in the density function and a thorough comparison with available data. However, they do not focus on uncertainties in the spectral indices resulting from inadequate resolution and the inadequate separation of scales.

2. NOTATION AND TRANSFORMS

2.1 Notation

We define the direct and inverse Fourier transforms

$$\hat{f} = \mathscr{F}f \quad \text{and} \quad f = \mathscr{F}^{-1}\hat{f}.$$

Three forms of f are considered. The continuous function on $x \in [-\infty, \infty]$; the periodic function on $x \in [-L, L]$; and the sampled periodic function on $x \in [-L, L]$, with $2N$ samples and spacing h. These and the relevant forms of Parseval's relation are:

$$\hat{f}(k) = \int_{-\infty}^{+\infty} f(x) \, e^{-ikx} dx, \qquad\qquad x \in [-\infty, +\infty], \qquad (2.1a)$$

$$f(x) = (2\pi)^{-1} \int_{-\infty}^{+\infty} \hat{f}(k) \, e^{+ikx} dx, \qquad\qquad (2.1b)$$

$$\int_{-\infty}^{+\infty} |\hat{f}|^2 \, dk = 2\pi \int_{-\infty}^{+\infty} f^2(x) \, dx; \qquad\qquad (2.1c)$$

$$\hat{f}_\nu \equiv \hat{f}(k_\nu) = (2L)^{-1} \int_{-L}^{L} f(x) \, e^{-ik_\nu x} \, dx, \qquad x \in [-L, L]; \qquad (2.2a)$$

$$f(x) = \sum_{-\infty}^{+\infty} \hat{f}(k_\nu) \, e^{+ik_\nu x}, \qquad\qquad \nu \in [-\infty, +\infty] \qquad (2.2b)$$

$$\sum_{-\infty}^{+\infty} |\hat{f}_\nu|^2 = (2L)^{-1} \int_{-\infty}^{+\infty} f^2(x) \, dx \qquad\qquad (2.2c)$$

$$\hat{F} \equiv \hat{F}(k_\nu) = (2N)^{-1} \sum_{n=-N+1}^{n=N} f(nh) \, e^{-inhk_\nu}, \; n \in [-N+1, N]; \qquad (2.3a)$$

$$f(nh) = \sum_{\nu=-N+1}^{N} \hat{F}(k_\nu) \, e^{+inhk_\nu}, \qquad\qquad \nu \in [-N+1, N], \qquad (2.3b)$$

$$\sum_{\nu=-N+1}^{N} |\hat{F}|^2 = (2N)^{-1} \sum_{n=-N+1}^{N} |f(nh)|^2, \qquad\qquad (2.3c)$$

where $k_\nu = (\pi\nu/L) \equiv (\pi\nu/Nh)$, and ν is the mode number. Note if $f(x)$ in (2.2a) is a function that vanishes identically outside a region contained within $(-L, L)$, (a function of compact support), then

$$\hat{f}(k)\big|_{k=k_\nu} = (2L) \, \hat{f}_\nu.$$

That is, they have the same form.

We have displayed these forms so as to clarify relationships. Brigham [2] shows analytically and with lucid graphics that a periodic function $f(x) = f(x+2L)$ can be obtained from a function of compact support on $x \in [-L, L]$ by convolving it with the series

$$\sum_{n=-\infty}^{+\infty} \delta(x-2nL).$$

In the transform domain this convolution becomes a product of $\hat{f}(k)$ with $\sum_L \delta(k-n/2L)$ which amounts to selecting discrete lines from the continuous Fourier transform. Finally, we sample the physical space by multiplying by $\sum \delta(x-nh)$ and integrating. In the transform domain this becomes a convolution which causes the leakage or "aliasing" phenomenon that arises in discrete systems.

2.2 Transforms of Elementary Continuous Functions of Compact Support

One of our goals is to characterize physical space functions by spectral indices. That is, the power density $|\hat{f}|^2$ (or $|\hat{F}|^2$, etc.) has an envelope that may be characterized by k^{-p_j} in various regions j and we seek to define these regions and find accurate estimates of p_j. For convenience in illustrating separation of scales and asymptotic properties, we will use a function $f(x)$ that is composed of piecewise-constant, linear, quadratic, etc. functions and fractional powers of these functions. We believe these functions are sufficiently general to include the essential features of real scans. The spectral index p will be determined by the particular functions that are chosen and by the manner in which they intersect.

First, consider the transform of $(\partial_x f)$ on $x \in [-\infty, \infty]$

$$\mathcal{F}(\partial_x f) = \int_{-\infty}^{+\infty} (\partial_x f) e^{-ikx} dx = (ik) \hat{f}(k). \qquad (2.4)$$

In general, if $\partial_x^q f$ vanishes sufficiently rapidly, then

$$(\partial_x^q f) = (ik)^q \hat{f}(k). \qquad (2.5)$$
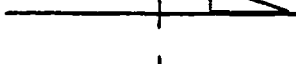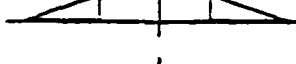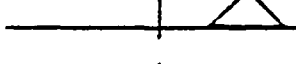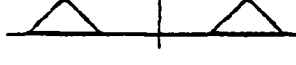
In the sense of generalized functions, the derivative of a Heaviside step function

$$H(x) = \begin{cases} 1 & x > 0 \\ 1 & x < 0 \end{cases},$$

is the delta function $\delta(x)$. Their transforms are related by $\mathcal{F}(\delta(x)) = 1 = (ik) \hat{H}$. Thus, for functions of compact support that are composed of

K-13

piecewise polynomials, one differentiates a sufficient number of times until delta and more singular generalized functions are obtained. (For example, for a trapezoid one differentiates twice). To obtain the transform of f, we divide the transforms of these singular functions with singularities located at x_{sj} by the appropriate power of (ik) (the number of differentiations) and combine with appropriate phase shift factors, $\exp(ikx_{sj})$. Some typical results are given in Table I.

Table 1 — Fourier transforms of elementary figures

	$\underline{p}$	Transform
	(2)	$2Ak^{-1} e^{-iz_+} \sin z_-$ (I.1)
	(2)	$4Ak^{-1} \cos z_+ \sin z_-$ (I.2)
	(2)	$4Ak^{-1} \sin z_+ \sin z_-$ (I.3)
	(2)	$iA\left[-k^{-1} e^{-ika} + 2\Delta^{-1} k^{-2} e^{-iz_+} \sin z_-\right]$ (I.4)
	(2)	$-2Ak^{-1} \sin ka + 4A\Delta^{-1} k^{-2} \sin z_+ \sin z_-$ (I.5)
	(4)	$8A\Delta^{-1} k^{-2} e^{-iz_+} \sin^2(z_-/2)$ (I.6)
	(4)	$16A\Delta^{-1} k^{-2} \cos z_+ \sin^2(z_-/2)$ (I.7)
	(4)	$i16A\Delta^{-1} k^{-2} \sin z_+ \sin^2(z_-/2)$ (I.8)

$$z_\pm = \frac{1}{2} k(b \pm a) \; , \; \Delta = (b - a)$$

The symmetrical trapezoid of amplitude A is obtained by combining (I.1) with (I.2) where in the latter, $a = 0$ and $b = a$. Thus

$$\hat{f} = A(b + a)(\sin z_+ \sin z_-)/(z_+ z_-), \tag{2.6}$$

where

$$z_{\pm} = \frac{1}{2} k(b \pm a). \tag{2.7}$$

The half-width of the trapezoid may be defined as $\ell_{1/2} = (b + a)/2$, and the first null of (2.6) is at $\pi/\ell_{1/2}$. This is also the interval between nulls associated with $\sin z_+$. In a similar fashion, if f is

$$f(x) = 1, \qquad\qquad |x| < a,$$

$$f(x) = [1 - (|x| - a)^2/\Delta^2]^\tau, \qquad a < |x| < b, \tag{2.8}$$

$$f(x) = 0, \qquad\qquad |x| > b,$$

where $\Delta = (b - a)$, $\tau > -1$. Note, f is singular at $|x| = b$ if $-1 < \tau < 0$ and f has a singular slope at $|x| = b$ if $0 < \tau < 1$. The transform is given in Appendix A and for $\tau = 1/2$ (an elliptical arc) it is

$$\hat{f}(k) = k^{-1} \sin ka\{2 - \pi H_1(k\Delta)\} + \pi k^{-1} J_1(k\Delta), \tag{2.9}$$

where H_1 is a Struve function, as discussed, for example, in Reference 3, and J_1 is the Bessel function of the first kind. If $k\Delta \gg 1$,

$$H_1(k\Delta) = Y_1(k\Delta) + \frac{2}{\pi} + O(k\Delta)^{-2},$$

where Y_1 is the Bessel function of the second kind. Thus

$$\lim_{k\Delta \,\gg\, 1} \hat{f}(k) = (2\pi)^{1/2}\Delta(k\Delta)^{-3/2}\left[\cos\left(k\Delta - \frac{3\pi}{4}\right) - \sin\left(k\Delta - \frac{3\pi}{4}\right)\sin k a\right].$$

$$(2.10)$$

Further properties of these functions are discussed below.

3. ASYMPTOTIC SPECTRA AND SEPARATION OF SCALES

    3.1 Functions on the Infinite Line

    In this section, quantitative results for special functions are presented and general rules are induced. Particularly, that the asymptotic spectrum of continuous functions is determined by the physical space regions where slopes of f change in the most singular manner.

    The spectral representation of variables, $|\hat{f}|^2$, in nonlinear dynamical processes often can be represented by a power-law function k^{-p_j} in the region $k_{j-1} < k < k_j$, where p_j is called the spectral index in region j. (This excludes the dissipative range where some exponential variation with k usually occurs). These representations are often obtained by least-squares fitting procedures which suppress oscillatory effects. For example, the _envelope_ of _maxima_ of piecewise polynomials discussed previously can be fitted by $|\hat{f}_e|^2 \propto k^{-p}$ when length scales are sufficiently "separated". For $k \to \infty$, p is called the asymptotic spectral index.

    For the trapezoid (2.6), the asymptotic spectrum is $(4/\Delta)^2 k^{-4}$, or $p = 4$ and for (2.8), the asymptotic spectral index is obtained from Appendix A as

$$p = 2(\tau + 1), \quad \tau > -1.$$

$$(3.1)$$

For $\tau = 1/2$ (see Equation (2.10)) $p = 3$ which is intermediate between 2 and 4, the values for the top hat and the trapezoid, respectively. For $-1 < \tau < 0$, f is singular at $x = b$ and $0 < p < 2$ (that is, shallower than a top hat). For $0 < \tau < 1$, $f'(x)$ is singular at $x = b$ and for $\tau \geq 1$, $f'(x)$ is everywhere continuous and vanishes at $x = b$. From these results, we induce a rule for piecewise polynomials and powers of piecewise polynomials: the asymptotic spectral index is determined by the nature of the singularities of $\partial^q f / \partial x^q$, where these piecewise polynomials intersect. For example, if the first derivative ($q = 1$) has a singular slope somewhere, then

$$2 < p < 4;$$

if $q = 1$ does not have a singular slope but $q = 2$ does have a singularity, then

$$4 < p < 6; \text{ etc.}$$

Let us now consider the separation of scales, namely different spectral indices p_j in different regions of k, $k_{j-1} < k < k_j$. For the trapezoid (2.6) we have three regions:

$$\hat{f}_e(k) \approx (b + a), \qquad\qquad k \ll k_1,$$

$$\hat{f}_e(k) \approx 2k^{-1}, \qquad\qquad k_1 \ll k \ll k_2, \qquad\qquad (3.2)$$

$$\hat{f}_e(k) \approx (b - a)^{-1} k^{-2}, \qquad k_2 \ll k,$$

where $k_1 = 2\pi/(b + a)$ and $k_2 = 2\pi/(b - a)$. Thus if $(b + a)/(b - a) \gg 1$ we have a good separation of scales. For the trapezoid-plus-top hat with $\mu \ll 1$ shown in Figure 1,

$$\hat{f} = (1 - \mu)(b + a)(\sin z_+ \sin z_-)/(z_+ z_-) + 2\mu b(\sin kb)/(kb), \qquad (3.3)$$

and we have four regions

$$\hat{f}_e = (1 - \mu)(b + a), \qquad\qquad k \ll k_1,$$

$$\hat{f}_e = 2k^{-1}, \qquad\qquad k_1 \ll k \ll k_2,$$

$$\qquad\qquad\qquad\qquad\qquad\qquad\qquad\qquad\qquad (3.4)$$

$$\hat{f}_e = (b - a)^{-1} k^{-2}, \qquad\qquad k_2 \ll k \ll k_3,$$

$$\hat{f}_e = 2\mu k^{-1}, \qquad\qquad k_3 \ll k;$$

where

$$k_1 = 2\pi/(b + a), \ k_2 = 2\pi/(b - a),$$

$$\qquad\qquad\qquad\qquad\qquad\qquad\qquad\qquad\qquad (3.5)$$

$$k_3 = (1 - \mu) \, \mu^{-1} \, \pi/(b - a),$$

and where we have assumed $\mu \ll 1$. The asymptotic spectral index is 2 because of the small but finite jump. Note that the last region begins at a point dependent on the size of the discontinuity, which in practice could be related to a data artifact.

K-18

3.2 Periodic Continuous and Discrete Functions

Because of the computational efficiency of the fast Fourier transform algorithm, one usually imbeds functions in a periodic domain, $-L < x < L$. If the functions have compact support over a range $< 2L$, then from (2.2a) the transforms have the same form but the continuous k is replaced by $k_\nu = \pi\nu/L$, where ν takes on all positive and negative integers. As a rule, if one wishes many harmonics between nulls, one requires $(L/\ell_{1/2}) \gg 1$, where $\ell_{1/2}$ is the "half-width" of the function. If we satisfy this criterion we will obtain a reasonable approximation to the continuous transform function but it may not yield a good estimate for the spectral index, as we will see in Section 3.3.

For discrete functions, defined at intervals $h = L/N$, Eq. (2.3a) is applicable. The discrete system has $2N$ independent harmonics $\nu = (-N+1)$, $(-N+2)\dots-1,0,1,\dots N$. The lowest harmonic is (π/Nh) and the highest is (π/h). For the symmetric trapezoid, Eq. (2.3a) yields

$$\hat{F}(\theta) = A\,\frac{(\beta+\alpha)}{2N}\left\{\frac{\sin\frac{1}{2}\theta(\beta+\alpha)}{(\beta+\alpha)\sin(\frac{1}{2}\theta)}\ \frac{\sin\frac{1}{2}\theta(\beta-\alpha)}{(\beta-\alpha)\sin(\frac{1}{2}\theta)}\right\} \tag{3.6}$$

where

$$b = \beta h \text{ and } a = \alpha h, \tag{3.7a}$$

$$\theta = kh = \pi\nu/N, \quad \nu \in [-N+1, N], \tag{3.7b}$$

and $\theta_{max} = \pi$. The essential difference between (3.7) and (2.6) is the presence in the denominator of $(\sin\theta/2)^2$ instead of $(\theta/2)^2$. This difference is called "aliasing" [4] and is the result of "folding" the discrete spectrum of the Fourier series around the highest mode. Thus

aliasing, an unavoidable result of dealing with discrete data, modifies the asymptotic spectral index.

To obtain a quantitative measure of the error we define a ratio of local "indices" and subtract one, or

$$\varepsilon_p(\theta) \equiv \left\{ \frac{d\left[\ln|\hat{f}_e|^2\right]/d(\ln\theta)}{d\left[\ln|\hat{F}_e|^2\right]/d(\ln\theta)} - 1 \right\}. \tag{3.8}$$

where $\hat{f}_e$ and $\hat{F}_e$ are the envelope functions corresponding to $\hat{f}$ and $\hat{F}$, respectively. Thus if $\varepsilon_p(\theta) > 0$, $\hat{F}_e$ has a smaller effective p than does $\hat{f}_e$. An approximate result for the trapezoid is obtained by setting

$$|\hat{f}_e|^2 = \left(\tfrac{1}{2}\theta\right)^{-p_j} \text{ and } |\hat{F}_e|^2 = \left(\sin\tfrac{1}{2}\theta\right)^{-p_j},$$

where

$$p_2 = 2 \text{ for } 2\pi/(b+a) \ll k \ll 2\pi/(b-a)$$

$$p_3 = 4 \text{ for } k \gg 2\pi/(b-a).$$

Thus

$$\varepsilon_p = \left[\left(\tan\tfrac{1}{2}\theta\right)/\left(\tfrac{1}{2}\theta\right)\right] - 1 = \left(\theta^2/12\right) + O\left(\theta^4\right). \tag{3.9}$$

is positive and independent of p_j and is: 0.024 at $\theta = \pi/6$; 0.055 at $\theta = \pi/4$; 0.103 at $\theta = \pi/3$; and 0.273 at $\pi/2$. That is, aliasing errors decrease the measured spectral index. Thus, if we use a nonlocal fitting

procedure to estimate p (as described below) and we wish to avoid using data that contributes local errors > 27% (or > 10.3%), we must <u>discard</u> half (or two-thirds) of the modes!

3.3 Estimating Spectral Indices of the Trapezoid

As discussed in Sec. 4, a least-squares (nonlocal) fitting procedure is used to estimate spectral indices. The essential caveats are: avoid using data near a transition between spectral ranges; and discard data above $k_{max}/2$ (or $k_{max}/3$). We discuss the choice of appropriate data fitting regions for the trapezoid, if we wish to obtain estimates of $p_2 = 2$ and $p_3 = 4$.

We wish to fit μ_3 peaks of the slow oscillation associated with sin $k(b-a)/2$ in the last region (No. 3). The last data mode will be

$$\gamma k_{max} \equiv \gamma\pi/h, \tag{3.10}$$

where, for example, to avoid aliasing errors $\gamma < 1/2$. If we start at $3\ k_2/2$, the condition for μ_3 peaks beyond the transition yields a range condition

$$\left(\frac{3}{2} + \mu_3\right)\left(2\pi/(b-a)\right) = \gamma\pi/h$$

or

$$(b - a) = h\left(3 + 2\mu_3\right)/\gamma. \tag{3.11}$$

The intermediate fitting region (No. 2) starts after k_1, the first null, and proceeds to k_1^*. Here k_1^* is chosen according to the error made as one approaches k_2, that is according to the departure of $[\sin (k(b - a)/2)/(k(b - a)/2)]^2$ from unity as given in

$$\left[\sin \tfrac{1}{2} k_1^*(b - a)/ \tfrac{1}{2} k_1^*(b-a)\right]^2 = 1 - \epsilon_1^2 + 0\left(\epsilon_1^4\right),$$

or

$$\epsilon_1 = (3)^{-1/2} k_1^*(b - a)/2, \qquad\qquad (3.12)$$

We proceed as in the highest range, and require that we fit μ_2 peaks associated with $\sin k(b+a)/2$, or

$$\left(\tfrac{3}{2} + \mu_2\right)\left(2\pi/(b + a)\right) = (12)^{1/2} \epsilon_1/(b - a), \qquad\qquad (3.13)$$

or using (3.11)

$$(b + a) = h\left(3 + 2\mu_2\right)\left(3 + 2\mu_3\right) \pi/\gamma\epsilon_1(12)^{1/2}. \qquad\qquad (3.14)$$

Finally, we wish to have sufficient data in the first region before the first null at $2N/(S+\alpha)$. Thus

$$N = \mu_1(3 + \alpha)/2, \qquad\qquad (3.15)$$

where a minimal requirement is $\mu_1 > 4$. If we take $\mu_1 = 4$ and requirements in the other regions, as follows:

$$\mu_2 = \mu_3 = 3, \ \gamma = 1/2 \text{ and } \epsilon_1^2 = 0.1, \qquad\qquad (3.16)$$

then we obtain

$$(b - a)/h = 18, \quad (b + a)/h = 464.6 \text{ and } N = 929,$$

where the last is obtained from (3.15). In Section 4.2 we will compare methods of fitting the data from the trapezoid $(b-a)/h = 16$ and $(b+a)/h = 464$ for $N = 512, 1024,$ and 2048, which straddle the value $N = 929$.

4. FITTING DISCRETE DATA

4.1 Least Squares Fits

In this section we illustrate errors in a weighted least-squares fit of discrete data $|\hat{F}(k_\nu)|^2$ over specified ranges with

$$|\hat{F}_a|^2 = \overline{F}_a^2 \, k^{-\bar{p}} = E_0 \, \nu^{-\bar{p}}, \qquad \nu \in [-N+1, N]. \tag{4.1}$$

Thus, $\bar{p}$ and E_0 are obtained from the pair of linear equations

$$\sum_\nu w_\nu \log_{10}|\hat{F}|^2 - \log_{10} E_0 \sum_\nu w_\nu + \bar{p} \sum_\nu w_\nu z_\nu = 0 \tag{4.2}$$

$$\sum_\nu w_\nu z_\nu \log_{10}|\hat{F}|^2 - \log_{10} E_0 \sum_\nu w_\nu z_\nu + \bar{p} \sum_\nu w_\nu z_\nu^2 = 0 \tag{4.3}$$

where $z_\nu = \log_{10}\nu$ and the weighting w_ν that yields good fits is

$$w_\nu = \frac{1}{2}\, |z_{\nu+1} - z_{\nu-1}| \approx \frac{1}{\nu} + O(\frac{1}{\nu^2}), \tag{4.4}$$

because it emphasizes the lower modes.

The fitting range for spectral region j is defined as

$$\nu \in [\nu_{jI}, \nu_{jF}]$$

where ν_{jI} and ν_{jF} are the initial and final mode values included in the fit for region j, and are chosen where $|\hat{F}(k_\nu)|^2$ has a <u>local maximum</u>, and such that they are not too close to transition points. This procedure was found to give a good estimate of $\tilde{p}$ for <u>single</u> figures. No consistent improvements were obtained when spectra for single figures were smoothed. However, when many figures were placed on a line (including overlapping figures), we found that the precise ν_{jI} and ν_{jF} were less critical. This follows because the point-to-point variation of $|\hat{F}|^2$ was large (i.e., poorly correlated). It is possible that an algorithm that fits $\log_{10}|\hat{F}|^2$ with a polynomial in z_ν would give a better estimate of a local spectral index.

Table 2 contains summary information on the top hat (a = b), circle (Eq. 2.8 with a = 0 and τ = 1/2) and trapezoid. This table illustrates the errors made in obtaining $\tilde{p}$, when parameters are varied including the fitting interval $[\nu_{jI} \ \nu_{jF}]$ or n_{max}, the total number of data maxima in the interval. Measures of the quality of fit are given by $\delta_p = (\tilde{p} - p_j)/p_j \times 100$ and by

$$\bar{\sigma} = \frac{\{(\nu_{jF} - \nu_{jI})^{-1} \sum_\nu w_\nu (\log_{10}|\hat{F}|^2 - \log_{10} E_0 \nu^{-\tilde{p}})^2\}^{1/2}}{[\sum_\nu w_\nu (z_\nu - \bar{z})^2]^{1/2}} \qquad (4.5)$$

where $\bar{z} = \sum_\nu w_\nu z_\nu / \sum_\nu w_\nu$. Note: In statistical fitting procedures $\bar{\sigma}$ is the square root of the variance of $\tilde{p}$.

Table 2 -- Results of fitting simple figures

Type	Case	N	a/h	b/h	ν_I	ν_F	n_{max}	J	$\tilde{p}_J$	δ_P	$\bar{\sigma}$
Top flat	1	2048	232	232	14	1038	111	2	2.06	3.0	0.04
	2	2048	232	232	14	526	56	2	2.10	5.0	0.07
	3	1024	232	232	8	528	99	2	2.04	2.0	0.06
	4	1024	232	232	8	268	50	2	2.09	4.5	0.11
	5	256	58	58	8	140	26	2	2.08	4.0	0.18
	6	256	58	58	8	74	13	2	2.23	11.5	0.34
Circle	7	1024	0	232	8	528	99	2	3.06	2.0	0.06
	8	1024	0	232	8	268	50	2	3.16	5.3	0.11
	9	256	0	58	8	140	26	2	3.09	3.0	0.18
	10	256	0	58	8	74	13	2	3.30	10.0	0.34
Trapezoid	11	2048	224	240	14	120	12	2	2.53	26.5	0.25
	12	2048	224	240	14	85	9	2	2.48	24.	0.35
	13	2048	224	240	388	900	3	3	4.01	0.25	0.45
	14	2048	224	240	388	644	2	3	4.82	21.	1.06
	15	1024	224	240	8	61	11	2	2.47	23.5	0.36
	16	1024	224	240	8	43	8	2	2.35	17.5	0.50
	17	1024	224	240	194	450	3	3	4.06	1.5	0.68
	18	1024	224	240	194	322	2	3	5.02	25.0	1.6
	19	512	112	120	8	43	8	2	2.35	17.5	0.52
	20	512	112	120	8	25	4	2	2.58	29.0	1.1
	21	512	112	120	194	322	2	3	4.38	9.5	1.6

K-25

4.2   Discussion of Fitted Results.

The results given in Table 2 are for the top hat (cases 1-6), the circle (cases 7-10) and the trapezoid (cases 11-21). To assure a good value of $\tilde{p}$ (to minimize δ_p), the figures were well resolved and occupied a small extent of the total interval (to yield well-defined oscillations). These requirements dictate a large total mesh size. The cases illustrated in the table show the effect of satisfying these criteria to a greater or lesser degree.

If we compare the errors in the least squares results for region 2 we find that for the top hat and circle (two-region functions) $\overset{\sim}{p_2}$ is much closer to p_2 than for the trapezoid (a three-region function), for a given mesh size. Thus, even with large-mesh sizes a least squares fit to the data produces substantial errors in the prediction of a spectral index if there are several distinct regions of k-space with different spectral indices.

Cases 1 and 2 show results for a mesh (2N = 4096) much larger than is being used presently in numerical simulations. A plot of $\log_{10}|\hat{F}|^2$ vs. $\log_{10}\nu$ for these cases is shown in Figure 2. The ordinate is normalized so that the area under the profile is unity. The lower scale on the abscissa is defined in such a way as to provide a measure of the size of the object relative to the mesh. The number given at the origin is the ratio of the mesh size to the size of the figure (here it is 8.8 = 2048/232). The first null (which is not, in general, a point of the plot) occurs at 1 on this scale, the second at 1/2, the third at 1/3, etc. In Table 2 we see errors, δ_p, in $\tilde{p}$ of 3% and 5%, respectively, and a consistent variation in $\overline{\sigma}$. Note that the fitting procedure always yields a $\tilde{p} > p$. This is due to our algorithm for choosing the fitting regions. We are not certain

whether the increase in error from case 1 to case 2 is related to the decrease in sample size (14-1038 to 14-526) or has to do with ν_{2F} in case 2 being farther from the aliasing region, since aliasing tends to spuriously reduce $\bar{p}$. In any event, the errors are acceptably small. In cases 3 and 4 the same top hat is placed on a mesh half the size of that in cases 1 and 2. We obtain slightly better results, with errors of 2% and 4.5% respectively. The minor improvement is due to the particular choices of ν_{2I} and ν_{2F} determined by our algorithms. In fact, choosing ν_T in cases 1 and 2 to be 15 instead of 14 improves the fit enough that cases 1 and 2 then show smaller errors than cases 3 and 4, respectively.

With a smaller top hat in a smaller box ($2N = 512$, cases 5 and 6, Figure 3) the errors are larger, 4% for case 5 and 11.5% for case 6. The normalized standard deviation, $\bar{\sigma}$, has also increased. For the circular arc the results are consistent with the top hat results. For example, cases 7 and 8 give δ_p of 2% and 5%, respectively. The errors for cases 9 and 10 compare closely, also, with the analogous top hat cases 5 and 6.

For the trapezoid (see Figure 4), the errors in p_2 range from 17.5% to 29%. Generally, as the data set increases, δ_p and $\bar{\sigma}$ decrease if we do not approach too close to transitional points or aliasing regions. The smaller errors in region 3 are the result of aliasing errors competing with the errors introduced by the fitting procedure. The variation in δ_p for different meshes among comparable regions (e.g. 26.5%, 23.5% and 17.5%) is an indication of the magnitude of the variability obtained by such procedures when data with aliasing errors are included. These larger errors result because the configuration of "minimal" parameters (3.16) does

not yield a sufficient number of oscillations of data far from the transitional points. If we choose a more conservative set of parameters, e.g.

$$\mu_1 = 8, \qquad \mu_2 = \mu_3 = 4, \qquad \gamma = \frac{1}{3} \qquad \text{and} \qquad \epsilon_1^2 = 0.01$$

then we obtain

$$(b - a)/h = 33, \qquad (b + a)/h = 3290 \qquad \text{and} \qquad N = 13,170.$$

This large value of N cannot be used conveniently or routinely with present-day computers.

In addition to the trapezoid runs in Table 2 we have made runs with randomly placed multiple (three) identical trapezoids. In a mesh with $N = 2048$, analogous to the single trapezoid cases 11-14, we found only small differences in the resulting values of $\tilde{p}_j$. This suggests that single figures can provide a good estimate of variability due to fitting procedures in a situation where multiple figures occur. However, a proper statistical theory for multiple figures is needed to generalize our limited findings.

5. CONCLUSIONS

We have demonstrated the essential elements which are required to determine accurate estimates of spectral indices. We have presented both analytical arguments and numerical experiments, which use least squares procedures for simple geometric representations of scan functions. For two-region figures, such as the top hat or circular arc, we find that an accurate estimate of the spectral index can be obtained with 256 or larger mode numbers, over a dynamical range of 30-50 db. However, for three-spectral region figures, even with a moderate separation of scales, an excess of 2048 modes is required to obtain good estimates of the spectral indices. Here, a typical dynamical range is 80 db. We have investigated various sources of errors including, for example, the number of modes in the data set, aliasing, and transitional nulls. It is possible that fitting functions, which are based on physical considerations, will reduce the data set required to obtain accurate estimates of spectral indices.

There is a practical lesson to be learned from this study. Spectral indices determined from data cannot safely be used beyond the range in k for which they have been measured. We have shown that even under well controlled conditions large errors in spectral indices can occur. To extrapolate these indices beyond the dynamical range for which they were obtained can produce power level predictions that are incorrect by orders of magnitude. From a systems perspective one could conceivably take a very conservative point of view, a worst case hypothesis, and assume that wherever the atmosphere structures, the spatial power spectrum of irregularities falls off like k^{-2}. However, this would be unduly constraining to instrument designers. The fact is that we do know a fair amount about the likely shapes of striations under HANE conditions. We

should, therefore, be able to construct analytical models of striations that sufficiently mimic reality so that we can investigate the sensitivity of spectral indices both to model parameters and to the direction of observation. Their validity could not go to larger k values than is warranted by the details of striation structures as predicted by our physical theories. These studies are being embarked upon now and will be reported on presently.

Acknowledgment
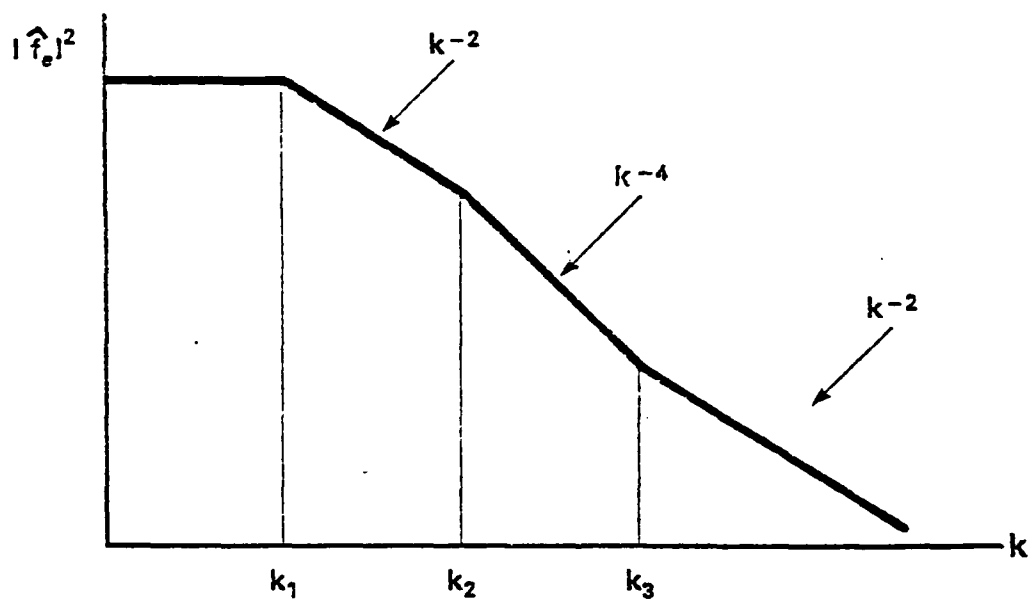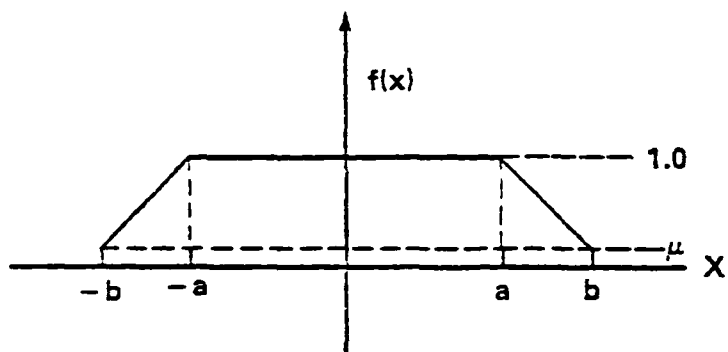
Fig. 1. An example of a function with four spectral regions.

Fig. 2. Plot of $\log_{10}|\hat{F}|^2$ vs. $\log_{10}\nu$ for a top hat with N = 2048, a = b = 232. A straight line with slope −2 has been drawn through the second maximum.
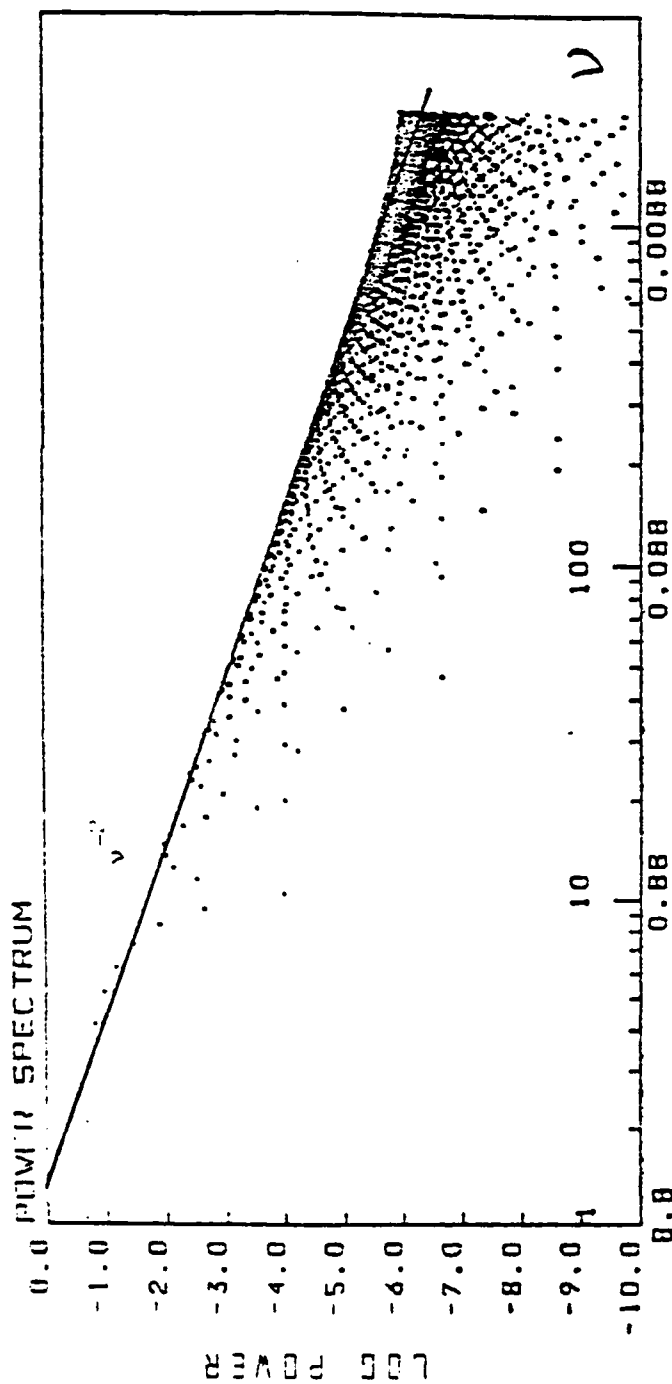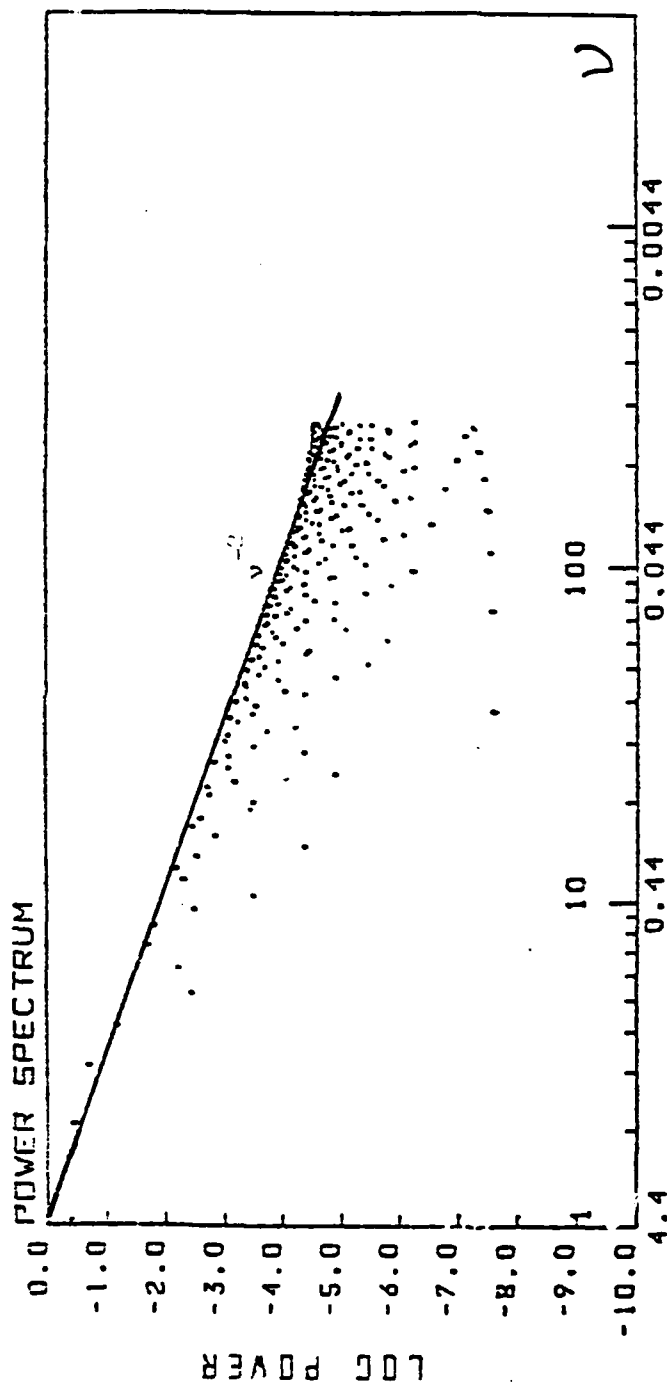
Fig. 3. Plot of $\log_{10}|\hat{F}|^2$ vs. $\log_{10}\nu$ for a top hat with $N = 256$, $a =$ b = 58. A straight line with slope -2 has been drawn through the second maximum.
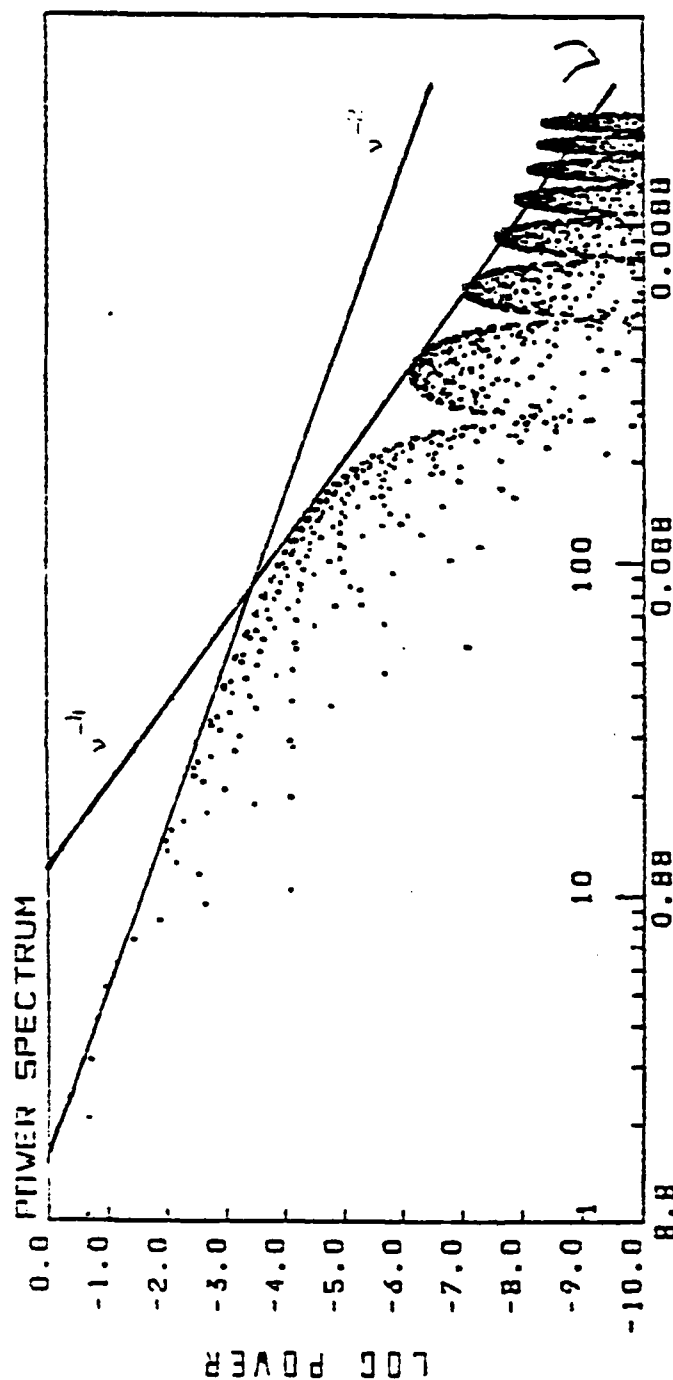
Fig. 4. Plot of $\log_{10}|\hat{F}|^2$ vs. $\log_{10}\nu$ for a trapezoid with $N = 2048$, $a =$ 224, and $b = 240$. Straight lines with slopes of -2 and -4 have been drawn through the relevant second maxima.

APPENDIX A. TRANSFORM OF A SPECIAL FUNCTION

We consider the function

$$f(x) = 1 \qquad\qquad\qquad\qquad |x| < a,$$

$$f(x) = \left(1 - \Delta^{-2}(x - a)^2\right)^{\tau}, \qquad a < |x| < b,$$

$$f(x) = 0 \qquad\qquad\qquad\qquad |x| > b, \qquad\qquad (A1)$$

where $\Delta = b - a$ and $\tau > 1$. Since it is symmetric the transform can be written as

$$\hat{f}(k) = I + I* + 2k^{-1} \sin ka, \qquad\qquad (A2)$$

where the last term is associated with the region $|x| < a$ and

$$I = \left\{\left(\tfrac{1}{2}\, \Delta\right)^{-\tau+1/2} \pi^{1/2} \Gamma(\tau+1)\, k^{-(\tau+1/2)}\, e^{-ika}\right\} \times$$

$$\left\{J_{\tau+1/2}(k\Delta) - i\, H_{\tau+1/2}(k\Delta)\right\}. \qquad\qquad (A3)$$

The last is obtained from [5] Sec. 4.3, Eq. 12 and the use of

$$I_{\tau+1/2}(k\Delta) = i^{\tau+1/2}\, J_{\tau+1/2}(k\Delta),$$

and

$$L_{\tau+1/2}(ik\Delta) = i^{\tau+3/2}\, H_{\tau+1/2}(k\Delta),$$

where J_m and I_m are the usual Bessel functions and L_m and H_m are the Struve functions.

It can be shown that if $\Delta \gg (b+a)/2$, $|\hat{f}(k)|^2$ has two well-separated spectral regions where the spectral index of the envelope is $p_1 = 2$ and $p_2 = 2(\tau+1)$, respectively. Thus, if $\tau = -1 + \varepsilon$ then $p_2 = 2\varepsilon$, nearly a flat spectrum.

REFERENCES

1. Wortman, W.R. and Kilb, R.W., Contact Geophysical and Plasma Dynamics Branch, Code 4780, NRL for Reference.

2. Brigham, E.O., The Fast Fourier Transform, Prentice Hall, Englewood Cliffs, N.J., 1974.

3. Abramowitz, M. and Stegun, I.A., Handbook of Mathematical Functions. See Sec. 12, and Eq. 12.1.31, National Bureau of Standards Applied Mathematical Series #55, 1964.

4. Koopmans, L.H., The Spectral Analysis of Time Series, Academic Press, N.Y., 1974. Aliasing is discussed in Chapter 3. It is also discussed in Reference 2, Chapter 6.

5. Erdelyi, A. (ed.), Tables of Integral Transforms, I., McGraw-Hill Book Co., Inc., N.Y., 1954.

APPENDIX L

Projections of Plasma Structures and Their Spectra

Projections of Plasma Structures and their Spectra

N. J. ZABUSKY

Fluid Sciences, Inc.
Pittsburgh, PA 15217

E. HYMAN

Science Applications International Corporation
McLean, VA 22102

M. MULBRANDON

Geophysical and Plasma Dynamics Branch
Plasma Physics Division

NAVAL RESEARCH LABORATORY
Washington, D.C.

We have established a relationship between the asymptotic spectral index of idealized piecewise-constant (pc) optically-thin radiating sources and their scans. For piecewise-constant clouds, where the one-dimensional asymptotic spectrum of the power is proportional to k^{-2}, we have shown that the asymptotic spectrum of the scan depends upon the character of the contour at the point $x_0 \equiv (x_0, y_0)$ where it is tangent to the extremal ray. If the contour at (x_0) behaves like $y - y_0 = \gamma (x - x_0)^\tau$ then the asymptotic spectral envelope of the PSD of the scan varies as $k^{-2(\tau + 1)}$. For a convex curve with finite curvature at x_0, we have $\tau = 1/2$ and obtain the well-known result, k^{-3}. In addition, if the radiating density in such a cloud flank varies with a power law m, then the asymptotic spectral envelope of the scan's PSD varies as $k^{-2(1 + \tau + m)}$. We also apply the results to the interpretation of optical scans from two PLACES events. These are insufficiently resolved and their estimated spectral index of 2.5 is associated with a composite of effects and not the nonlinear dynamics of striation evolution.

1. INTRODUCTION

Observation of unstable and turbulent geophysical fluid dynamical processes are often indirect and made from remote sensors. Many processes are observed optically from several vantage points and the spatial radiance distribution is recorded photographically or electronically. From successive frames, one hopes to deduce the location and morphology of evolving hierarchies of structures. Unfortunately, a detailed reconstruction is impossible because of the lack of precise control of the processes that govern the radiation, the paucity of recording locations, and the lack of detailed in-situ (rocket borne) diagnostics. That is, compared to the progress in laboratory tomography, our problem is highly underdetermined.[1,2]

A long-range goal of the present investigation is to construct simple models of radiating ionospheric or HANE plasma clouds that are useful to communication and tracking systems engineers. We are interested in the: intercloud distances, scale sizes, gradients and asymmetries with respect to the earth's magnetic field and ambient winds and the evolution of these structural features. We will distill the bits of information available from field experiments and large-scale nonlinear dynamical computer simulations into cogent models. Conventionally, one discretizes field data and uses the computed power spectral densities (PSD's) to compare with realistic turbulent or wave steepening numerical simulations. However, PSD's and their spectral exponents are subject to errors because of the inadequacy of resolution and dynamical range in experimental and numerical simulation data. Some considerations of the latter were given in the first report of this series[3] and are applied here.

In Section 2 we discuss the relation between radiation from an idealized (piecewise-constant, pc) cloud and its projection functions, $f(x)$. These are intensity scans through a "slice" of the cloud. For simplicity, the cloud is taken to be sufficiently remote so that parallax effects are negligible. That is, all rays emitted by the cloud are perpendicular to the projection plane. We will show that essential properties of $f(x)$ are related to properties of the cloud's boundary curve (e.g., curvature, etc.) at points where projection rays are tangent to the boundary curve. We also examine the competition between local curvature

and density gradient at a tangent ray to clouds. In Section 3 we relate PSD's of clouds to the PSD's of their projection functions. In Section 4 we analyze measured scans from two "PLACES" experiments in light of the above results, and Section 5 presents our conclusions.

2. PROJECTIONS OF 3D CLOUDS

2.1 Introduction

Ionospheric plasma cloud densities may be approximated by the separable function

$$n(\underline{x}',t) = n_\perp(x',y',t)g_\parallel(z',t) \tag{1}$$

where z' is along the earth's magnetic field. Thus $n_\perp$ exhibits a steep "backside" and $g_\parallel$ may be approximated by $\exp - \{(z'-z_0)/\ell\}^2$ where $\ell^2 = \ell_0^2 + (\nu t)$ approximates a diffusive spreading along z' with diffusivity ν and $z_0(t)$ decreases in time as the cloud settles from its high altitude release point. There is evidence that the symmetry in $z' - z_0$ may be broken in time, that is, the higher altitude regions may be more diffuse.[4] However, to illustrate the nature of projections and the essential issues involved in computing PSD's we suppress the time variable and consider an idealized cloud with piecewise constant (pc) density in a bounded domain D, namely

$$n = \begin{cases} F_0 & \underline{x} \ \epsilon \ D \\ 0 & \underline{x} \ \cancel{\epsilon} \ D \end{cases} \tag{2}$$

2.2 Piecewise-Constant Clouds.

Figure 1 shows a segment of a pc cloud, the curve $C(x,y) = 0$ (which is the intersection of domain D and $P(\underline{x})$, the perpendicular intersection plane) and the projection plane on which the radiance image is recorded. The sketch to the right of the plane is an intensity plot $f(x)$ associated with a "slice", the line a-b on the projection plane. For an optically thin cloud, $f(x)$ is obtained by integrating the intersection intensity, $f_I(x,y)$, along the y direction (perpendicular to the projection plane). The limits of integration $y_+(x)$ and $y_-(x)$ are the intersections of a line perpendicular to the projection plane with $C(x,y) = 0$. That is

$$f(x) = \int_{-y_-(x)}^{+y_+(x)} dy \; f_I(x,y) = F_0\{y_+(x) + y_-(x)\} \equiv F_0 v(x). \qquad (3)$$

Generally, for non-pc clouds $f_I(x,y)$ will not be constant and will depend on the orientation angle of the viewer with respect to the magnetic field and ambient wind.

Consider $f(x)$ near $x = x_0$ where a projection ray is tangent on the left to $C(x,y) = 0$, (e.g., point a in Fig. 1). Thus, for $x > x_0$ we represent the curve <u>locally</u> for $y > y_0$ by

$$x - x_0 = t, \qquad (4a)$$

$$y - y_0 = \gamma t^\tau, \qquad (4b)$$

where $t \to (0+)$. That is, the right side of (4a) and (4b) may be considered the leading terms in a series in t, which represent an arbitrary curve. Thus,

$$y_x \equiv y_t / x_t = \tau \gamma t^{\tau-1}, \qquad (5)$$

is singular, constant, or zero as $t \to 0$ if $\tau < 1.0$, $\tau = 1.0$ or $\tau > 1.0$, respectively. Similarly, the curvature

$$\kappa \equiv \frac{y_{tt} x_t - x_{tt} y_t}{\{x_t^2 + y_t^2\}^{3/2}} = \frac{\gamma \tau(\tau-1) t^{(-2\tau + 1)}}{\{t^{2-2\tau} + \tau^2 \gamma^2\}^{3/2}}, \qquad (\tau < 1) \qquad (6)$$

is singular, constant or zero as $t \to 0$ if $\tau > 1/2$, $\tau = 1/2$, or $\tau < 1/2$, respectively. The table below summarizes some cases in the vicinity of $x = x_0$.
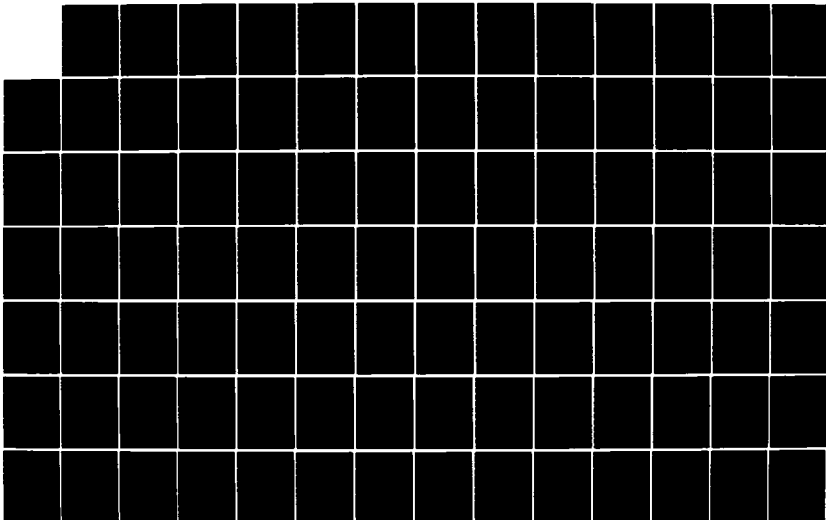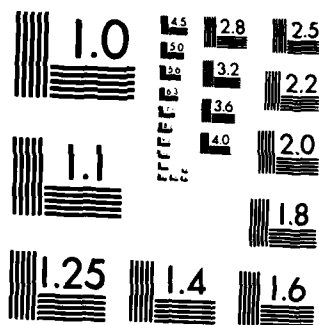
Table 1. Various Curves, (Equation 4) Near an Extremal Ray and The Asymptotic Behavior of the PSD for Piecewise-Constant Regions

τ	LOCAL FUNCTIONAL FORM	$y_x(x_0)$	$\kappa(x_0)$	FIG. 2	ASYMPTOTIC BEHAVIOR OF PSD FOR PC REGIONS
2.0	$y-y_0 = \pm\gamma(x-x_0)^2$	0	∞	(NOT SHOWN)	k^{-6}
4/3	$y-y_0 = \pm\gamma(x-x_0)^{4/3}$	0	∞	CUSP (NOT SHOWN)	$k^{-14/3}$
1.0	$y-y_0 = \pm\gamma(x-x_0)$	γ	∞	CORNER (NOT SHOWN)	k^{-4}
2/3	$y-y_0 = \pm\gamma(x-x_0)^{2/3}$	∞	∞	(NOT SHOWN)	$k^{-10/3}$
1/2	$y-y_0 = \pm\gamma(x-x_0)^{1/2}$	∞	$-2/\gamma^2$	●	k^{-3}
1/3*	$y-y_0 = \gamma(x-x_0)^{1/3}$	∞	0	$\triangle$	$k^{-8/3}$
1/4	$y-y_0 = \pm\gamma(x-x_0)^{1/4}$	∞	0	▢	$k^{-5/2}$
$\epsilon\ll 1$	$y-y_0 = \pm\gamma(x-x_0)^{\epsilon}$	∞	0	(NOT SHOWN)	$k^{-(2+2\epsilon)}$

*All cases are for $x > x_0$ except $\tau = 1/3$ which applies for $-\infty < x < \infty$

The next to last column refers to illustrations given in Figure 2. The last column gives the asymptotic behavior of the PSD for pc densities (i.e $m = 0$, as discussed in Sec 3.2).

For example, the elliptical limacon

$$\{x,y\} = \{1-\mu \cos \theta\}\{\alpha \cos \theta, \beta \sin \theta\}, \tag{7}$$

has a curvature

$$\kappa = \alpha\beta\{1 + 2\mu^2 - 3\mu \cos \theta\}/D^{3/2}, \tag{8}$$

where

L-8

$$D = \alpha^2 \{\sin \theta - \mu \sin 2\theta\}^2 + \beta^2 \{\cos \theta - \cos 2\theta\}^2. \qquad (9)$$

From (8) one obtains $\kappa = 0$ at $\theta = 0$ if $\mu = 1/2$ and

$$\{y/\beta\} = \{2\}^{-1/4} \{\frac{\alpha}{2} - x\}^{1/4} + \dots , \qquad (10)$$

which corresponds to the $\tau = 1/4$ entry in Table 1. More realistic clouds may be composed by summing many nested pc clouds and each one will contribute its own projection function.

2.3 Finite-gradient Clouds.

We now consider more realistic $n(\underset{\sim}{x})$ with finite gradients near the edge of the boundary of the domain. Hence $f_I(x,y)$ is no longer constant within the contour of intersection $C(x,y)$ and we have two competing space scales at the tangency points, namely, the local radius of curvature and the local gradient scale, $\ell = f_I/|\nabla f_I|$.

To elucidate this competition, we perform a local analysis for a structure with a polynomial flank of degree m

$$f_I = x_0^{-m} [(x_b - x)^2 + (y_b - y)^2]^{m/2} F_0, \qquad x_0 - |\epsilon| < x < x_0 , \qquad (11)$$

where (x_b, y_b) are on the boundary such that

$$\frac{y}{x} = \frac{(y_b - y)}{(x_b - x)},$$

or

$$x_b = x_0 - \{\frac{x_b y}{x \gamma}\}^{\frac{1}{\tau}}. \qquad (12)$$

To lowest order this is

$$x_b = x_0 - \{\frac{x_0 y}{x \gamma}\}^{\frac{1}{\tau}}.$$

At fixed x, one evaluates

$$f = 2\int_0^{y_+} f_I(x,y)dy,$$

where $y_+ = \gamma(x_0 - x)^\tau$. Near $x = x_0$, one expands the terms in parenthesis and retains only the lowest order in y, $O(y^2)$, and after some algebra obtains

$$f \approx 2x_0^{-m} F_0 \gamma (x_0 - x)^{m+\tau} + O(x_0 - x)^{m+\tau+1} \tag{13}$$

Thus, to leading order the exponent increases from τ to $(m + \tau)$ if a piecewise-constant cloud is replaced by one with a m-th degree polynomial flank. Note this indicates that by examining projections, one cannot distinguish between local gradients of density and the local shape of the boundary curve of the cloud.

3. Power Spectral Densities of Piecewise-Constant Clouds and Projections
   3.1 Clouds

   We define the direct and inverse Fourier transforms of an n-dimensional cloud as

$$\hat{f}(\underset{\sim}{k}) \equiv \hat{f}(k_1, k_2, \ldots, k_n) = \int_{(n)} f(\underset{\sim}{x}) e^{-i\underset{\sim}{k}\cdot\underset{\sim}{x}} d\underset{\sim}{x} , \quad \underset{\sim}{x} \in \mathbb{R}^n \tag{14}$$

$$f(\underset{\sim}{x}) = f(x_1, x_2, \ldots, x_n) = (2\pi)^{-n} \int_{(n)} \hat{f}(\underset{\sim}{k}) e^{+i\underset{\sim}{k}\cdot\underset{\sim}{x}} d\underset{\sim}{k} , \quad \underset{\sim}{k} \in \mathbb{R}^n \tag{15}$$

where $\int_{(n)}$ symbolizes n integrations that cover the entire domain and $d\underset{\sim}{x} \equiv dx_1 dx_2 \ldots dx_n$ and $d\underset{\sim}{k} \equiv dk_1 dk_2 \ldots dk_n$. The last can be written as $d\underset{\sim}{k} = dk \, d\sigma_k$, where $k = |\underset{\sim}{k}|$ and $d\sigma_k$ is an (n-1)-dimensional surface differential such that $\int_{(n-1)} d\sigma_k = 2\pi^{n/2}/\Gamma(n/2)$. The functions f and $\hat{f}$ satisfy Parseval's formula

$$E_T \equiv \int |\hat{f}|^2 \, d\underset{\sim}{k} = (2\pi)^n \int |f(\underset{\sim}{x})|^2 \, d\underset{\sim}{x}, \tag{16}$$

where $|\hat{f}|^2$ is the PSD.

Gelfand et al.[5] show that if the boundary ∂D of a pc cloud of density F_0 is a convex surface (i.e., at each point on ∂D the product of the principal radii of curvature $\neq 0$), and if ∂D is centrally symmetric about the origin (e.g., like an ellipsoid), then the asymptotic spectrum is

$$\hat{f}(\underset{\sim}{k}) = 2F_0(2\pi)^{(n-1)/2}\{\rho_1\rho_2\cdots\rho_{n-1}\}^{(1/2)}k^{-(n+1)/2}$$

$$\times \cos\left\{k\hat{a} - \frac{1}{4}(n+1)\pi\right\}\{1 + O\{k^{-1/2}\}\}, \qquad (17)$$

where $k = |\underset{\sim}{k}|$, $2\hat{a}$ is the "diameter" of D perpendicular to the direction $\underset{\sim}{k}/k$ (which is associated with the index n) and $\rho_1, \rho_2, \cdots, \rho_{n-1}$ are the principal radii of curvature at points A and A′ on ∂D, namely the extremal points. Figure 3 illustrates these quantities for an ellipse (n = 2) where $\underset{\sim}{k}/k = \underset{\sim}{e}_y$, and the curvatures $\kappa = 1/\rho_1$ at A and A′ are the same, since the ellipse is centrally symmetric. The two-dimensional PSD obtained from (17) is

$$E(\underset{\sim}{k}) \equiv |\hat{f}(\underset{\sim}{k})|^2 = 8\pi F_0^2\rho_1 k^{-3}\cos^2\left\{k\hat{a} - \frac{3\pi}{4}\right\}\{1 + O\{k^{-1/2}\}\}. \qquad (18)$$

We define the one-dimensional PSD as

$$E_1(k) \equiv k^{n-1}\int_{(n-1)}d\sigma_k\, E(\underset{\sim}{k}) = k^{n-1}\int_{(n-1)}d\sigma_k|\hat{f}|^2, \qquad (19)$$

and thus $E_T = \int_{-\infty}^{+\infty}dk\, E_1(k)$. From (19) with (17) the dominant term in $E_1(k)$ is

$$E_1(k) = \{2^{n+2}\pi^{(\frac{3n}{2} - 1)}/\Gamma(\tfrac{n}{2})\}F_0^2 k^{-2}\{\rho_1\rho_2\cdots\rho_{n-1}\}\cos^2\left\{k\hat{a} - \frac{1}{4}(n+1)\pi\right\} + \cdots. \qquad (20)$$

That is, the asymptotic dependence of the one-dimensional PSD of an n-dimensional piecewise constant cloud with convex boundaries is proportional to k^{-2} and the quantity in brackets is $(4\pi)^2$ or $(4\pi)^3$ for n = 2 or 3, respectively. The amplitude of the asymptotic spectrum is inversely proportional to the product of the curvatures at the extremal points.

3.2 Projections

In Section 2 we have shown that in a small region near the tangent ray (e.g., the origin x = 0), we can represent the projection function as

$$f(x) = x^\tau h(x), \quad x > 0, \qquad (21)$$

where $h(x)$ is an analytic function for $x > 0$ and $\tau > 0$. The simplest

L-11

projection function for a convex cloud is

$$f(x) = x^{\tau_1}\{1 - \{x/a_2\}\}^{\tau_2} h_{12}(x), \quad 0 < x < a_2,$$

where h_{12} is analytic and greater than zero between $0 < x < a_2$, and τ_1, τ_2 are > 0. The asymptotic spectrum will depend on which exponent is most singular, that is, smaller. For simplicity, we consider one such point and examine the Fourier transform

$$\hat{f}(k) = \int_0^\infty e^{-ikx} x^\tau h(x)\, dx$$

or

$$\hat{f}(k) = k^{-(\tau+1)} \int_0^\infty e^{-i\xi} \xi^\tau h(\xi/k)\, d\xi \qquad (22)$$

where $kx = \xi$. If one applies the method of stationary phase[6] for $k \gg 1$ we can show that the integral is $O(1)$ and the asymptotic spectral index of $\hat{f}$ is $- (\tau + 1)$. The result agrees with that presented in our previous report,[3] namely for the function

$$f = 1, \; |x| < a, \; f = 0, \; |x| > b$$

$$\qquad\qquad\qquad\qquad\qquad\qquad\qquad\qquad (23)$$

$$f = \{1 - (x-a)^2(b-a)^{-2}\}^\tau, \; a < |x| < b,$$

the asymptotic spectrum is $- (\tau + 1)$ or the spectral index of the PSD of f is $p = 2(\tau + 1)$.

We conclude with the results: For clouds contained in a finite domain and having a polynomial flank of degree m (see Equation (11)), the asymptotic spectral index of $|\hat{f}|^2$ (the PSD of the projection function $f(x)$) is

$$p = 2(1 + \tau + m).$$

For pc densities ($m = 0$) the asymptotic spectral behavior is given in the last column of Table 1. Note the well-known result, a k^{-3} dependence occurs when the curvature at the extremal ray is

finite ($\tau = 1/2$). Furthermore, the asymptotic spectral index varies continuously from slightly greater than 2 ($\tau = \epsilon$) to indefinitely large values depending upon the nature of the cusp. Note, a linear flank on a convex curve gives an asymptotic PSD $\alpha \, k^{-5}$.

4. Application of Results

We apply the results of the present and previous[3] papers to data from the recent "PLACES" high-altitude barium cloud releases.[7] We will show that the PSD results in Reference 7 for events GAIL and IRIS are valid only for the small wavenumber region, $K < 1.5 \, km^{-1}$ which is the region associated with the mean size of the cloud. These spectra do not yield any information about the asymptotic spectral index. Such exponents arise in a Rufenach fit to a nonlinear dynamical process, namely

$$PSD(K) = [1 + (KL_o)^2]^{-p/2}$$

where $(KL_o) \gg 1$. In this section $K =$ radians/km $= (length)^{-1}$ (i.e. not the conventional $2\pi/(length)$) and L_o is the outer scale length, typically 1 km to 3 km.

Optical emission data for events GAIL and IRIS are given in reference 7 in several forms: non field-aligned photographs of optical emission; smoothed optical radiance contours (e.g., Fig. 4a and 5a); several scans of the contours in a direction transverse to the local magnetic field (e.g. Fig. 4b and 5b); and a PSD of a "windowed" scan (e.g. Fig. 4c and 5c). Several features of the data reduction process deserve comment.[8] In windowing, the given data is multiplied by a prescribed function (a Kaiser-Bessel window) which makes the resulting function nearly periodic. This avoids discontinuities and large contributions to the high-wave number spectrum at the expense of introducing a frequency domain "smoothing" by convolution.[9] In Figs. 4a and 5a three rectangular regions are shown. The scans or profiles in Figs. 4b and 5b and their standard deviations are obtained by averaging 21 separate scans in each rectangular region. Typically this involves fewer than $256\sqrt{2} \approx 362$ points per scan. This data is then reinterpolated with 250 to 500 points (twice the ratio of the highest to the lowest mode number) so as to obtain a reasonable fit to the oscillations, which are attributed to striations. These reasonable but

ad hoc procedures lead one to question the validity of the highest 50% of the modes as a representation of the nonlinear dynamics of striation evolution. The following table presents pertinent information obtained from the small figures in Ref. 7.

FIG.	EVENT	REF. 7	HIGHEST MODE (km^{-1})	LOWEST MODE (km^{-1})	HIGHEST MODE / LOWEST MODE	EST. SPECTRAL INDEX (REF. 7)
4C	IRIS	FIG. 66 (LOWEST)	6.6	0.066	100	2.5
5C	GAIL	FIG. 51 (LOWEST)	7.6	0.038	200	2.5

For an approximation consistent with the location of the first two nulls, the data in Figures 4c and 5c are conveniently fit with trapezoids. For example, the symmetric trapezoid with altitude A, upper and lower parallel sides 2a and 2b, respectively, has a PSD[3]

$$|\hat{f}|^2 = \left[A(b + a) (\sin z_+ \sin z_-)/(z_+ z_-) \right]^2 ,$$

where

$$z_\pm = \pi K(b \pm a).$$

Thus, if the scales are well-separated, $(b + a)/(b - a) \gg 1$, then we have a k^{-2} envelope for $K_{11} \equiv 2/(b + a) < K < K_{21} \equiv 2/(b - a)$ and a k^{-4} envelope for $K > K_{21}$. From our asymptotic theory given in Section 2, the k^{-4} region would occur, no matter what the shape of the function in the region $(b - a)$, where the trapezoid is linear. This linear behavior corresponds to $\tau = 1$ in Table 1. If other exponents, τ , describe the function in this narrow region then the appropriate spectral index envelope would be $2(\tau + 1)$.

The first two nulls in Fig. 4c are consistent with fitting the scan in Fig. 4b with a _symmetrical_ trapezoid whose upper and lower parallel sides are 2a = 1.8 km and 2b = 6.2 km. The first null of the discrete Fourier transform, $K_{11} = 2/(b + a) = 0.5$ is associated with the first transition. The first null of the second transition is at $K_{21} = 2/(b-a) = 1.1$ and is consistent with the second null in Fig. 4c. Hence we conclude that the scales are _not_ well separated. The only information available concerning the asymptotic spectrum lies in the range $K > 1.5$. This region represents a composite of effects resulting from: the K^{-4} trapezoidal spectrum; the small-scale structures on the trapezoid (their widths and separations); film grain noise; and aliasing. One cannot see the spectral index of individual striations.

Event GAIL had steeper gradients as shown in Fig. 5b. One could approximate this scan function by an unsymmetric trapezoid with an upper parallel side 2a = 14.5 km and a base composed of a right segment b_1 = 8.45 km and a left segment b_2 = 9.45 km. The lack of symmetry causes an interference of the nulls and they aren't as clean as in the discussion of Fig. 4b. However, it is reasonable to approximate the unsymmetric trapezoid with a symmetric one with 2b = 17.9 then K_{11} = 0.123 and K_{21} = 1.18, a good separation of scales. Thus, between 0.123 and 1.18 the spectral index is changing from 2 to 4. For $K > 1.2$ a comment similar to that given in the above paragraph applies.

As discussed in reference 3, to make a good esimate of the asymptotic spectral index from a scan with no noise, one needs at least:

256 modes   for a scan function with two k-space regions

10,000 modes   for a scan function with three well separated k-space
                 regions.

Thus, we conclude the data presented do not allow one to deduce the spectral index of striations. It is obvious that a single unqualified PSD index can be misleading.

5. CONCLUSIONS

In this report we have considered the relationship between a radiating cloud and the power spectral density of a scan of its photographic image. To allow us to focus on the uncertainties associated with geometrical aspects, we have assumed idealized conditions, namely: optically thin clouds, no parallax effects and no distortion due to camera, lenses and film grain.. We have considered clouds with a piecewise constant and power law radiating density. We have not attempted to correlate this radiant density with the ion density.

For convex piecewise-constant clouds, where the <u>one-dimensional</u> asymptotic spectrum of the power is proportional to k^{-2}, we have shown that the asymptotic spectrum of the scan depends upon the character of the contour at the point where it is tangent to the extremal ray. If the contour at (x_0, y_0) behaves like $y - y_0 = \gamma(x - x_0)^\tau$ then the asymptotic spectral envelope of the PSD of the scan varies as $k^{-2(\tau + 1)}$. In addition, if the radiating density in a cloud flank varies with a power law m then the asymptotic spectral envelope of the scan's PSD varies as $k^{-2(1 + \tau + m)}$.

We have applied these considerations to data from PLACES events IRIS and GAIL. We have shown that the spectral index obtained in Ref. 8 is associated with a fit to an intermediate region with several competing effects and is not associated with the asymptotic spectral index that arises in nonlinear turbulent or wave steepening dynamical processes.

Acknowledgements

References

1. L.A. Shepp and J.B. Kruskal, Computerized tomography: the new medical x-ray technology, Amer. Math. Monthly, 420-439, June-July, 1978.

2. S.R. Deans, The Radon transform and some of its applications, Wiley, New York, 1983.

3. M. Mulbrandon, N.J. Zabusky and E. Hyman, Estimating Spectral Indices from Transforms of Discrete Representations of Density Functions, NRL Memo Report No. 5298, 1984.

4. C. Lebeda, S.P. Gary, and M.B. Pongratz, Density Spectra as a Function of Altitude in an Ionospheric Barium Release," Geophys. Res. Lett. 11, 591-594, 1984.

5. I.M. Gelfand, M.I. Graev, M. Ya. Vilenkin, Generalized Functions, Vol. 5, Integral Geometry and Representation Theory. Academic Press, NY, 1966. See Sec. 1.7, p. 19.

6. F.W.J. Olver, Asymptotics and Special Functions, Academic Press, NY, 1974. The method of stationary phase is discussed in Section 11 and theorems for finite range Fourier transforms are given in Section 13. The Riemann-Lebesgue lemma, discussed in Sec 4.2, plays an important role in obtaining these asymptotic results.

7. D.J. Simons, C.F. Lebeda, M.B. Pongratz, T.J. Fitzgerald, R.R. Dupre, Evolution of Structure in the PLACES Barium Clouds, Los Alamos National Laboratory LA 9648-MS, February 1984.

8. The procedures for transforming the photographs into PSD are described in C.F. Lebeda, "Procedures for analysis of photographic records of striated clouds," EGG report No. EGG 10282-5008, June 1983. In a telephone conversation (8/27/84), L. Testerman of EGG described pertinent numbers. The smoothed radiance contours were obtained from a 256 x 256 digitization of a selected portion of a 35 mm frame. To obtain the fitted radiance profiles with deviations (3 curves), 21 scans were made in each rectangular region and averaged. Each profile was then digitized with 250-500 points (125-250 modes) depending on the resolution of the small scale oscillations which are attributed to striations. Usually 7 to 10 points per oscillation was considered "reasonable".

9. F.J. Harris, On the use of windows for harmonic analysis with discrete Fourier transform, Proc. IEEE, 66, 51-83, 1978.

Figure Captions

1 Schematic of a remote radiating cloud and the projection function $f(x)$ through a slice of the cloud.

2 Two projections of a realistic two-finger cloud showing the effects of tangency points (□ and △) where $\kappa = 0$.

3 Parameters used to define the asymptotic spectrum of a convex centrally symmetric piecewise-constant 2D cloud.

4 Event IRIS. PSD contains 100 modes. (Reference 7, Figs. 65 and 66).

  (a) Smoothed radiance contours and three rectangular regions in which scans are made.

  (b) Fitted radiance profiles with upper and lower standard deviation corresponding to the lowest scanning rectangle.   Small scale oscillations in arrowed circle indicate striations.   (These are resolved with about 10 points per period.)

  (c) PSD of information in (b) above after using a Kaiser-Bessel window.

   EVENT GAIL.   PSD contains 200 modes.   (Reference 7, Figs. 50 and 51).
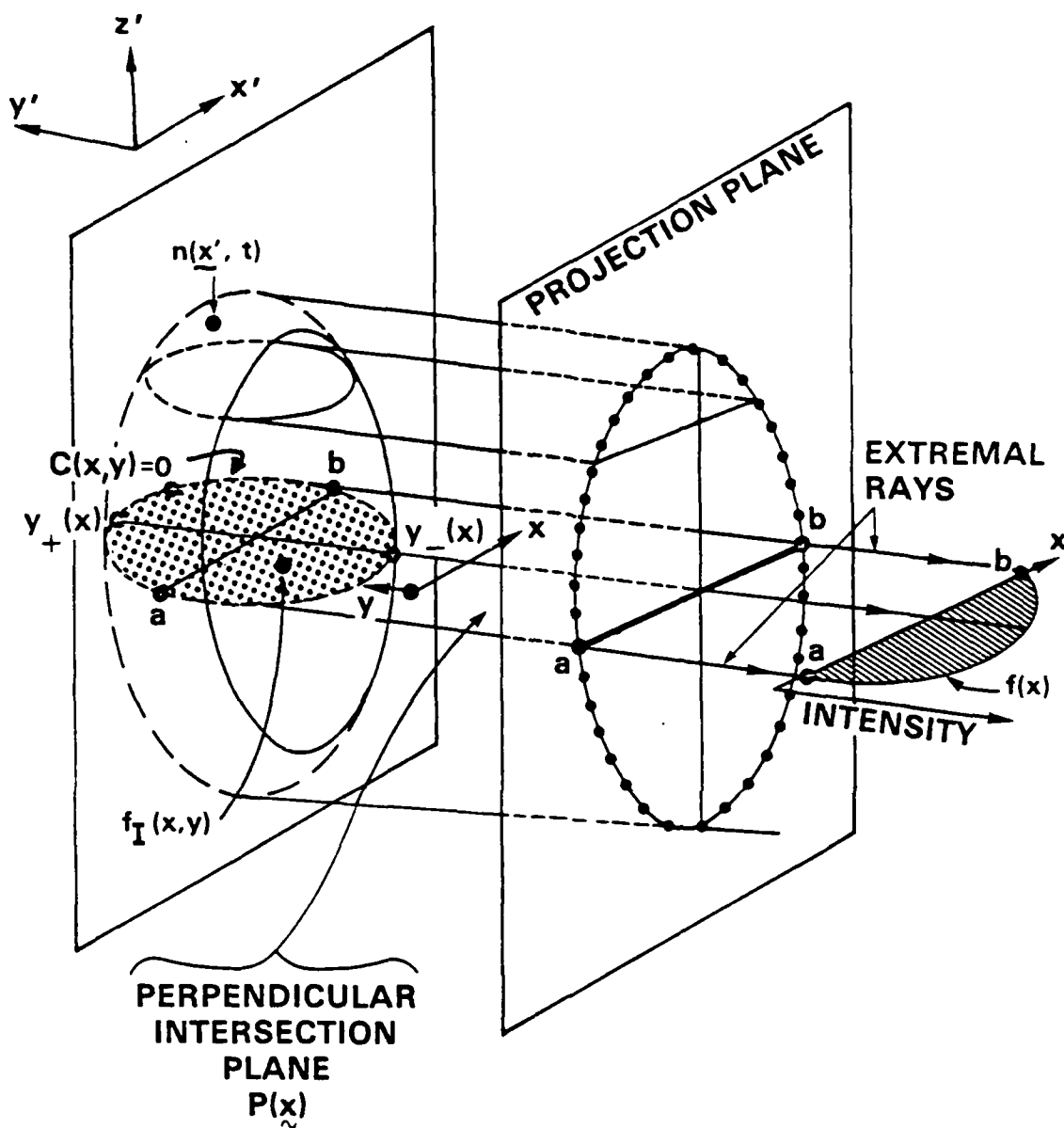
  Captions on (a) (b) (c) same as in Fig. 4.

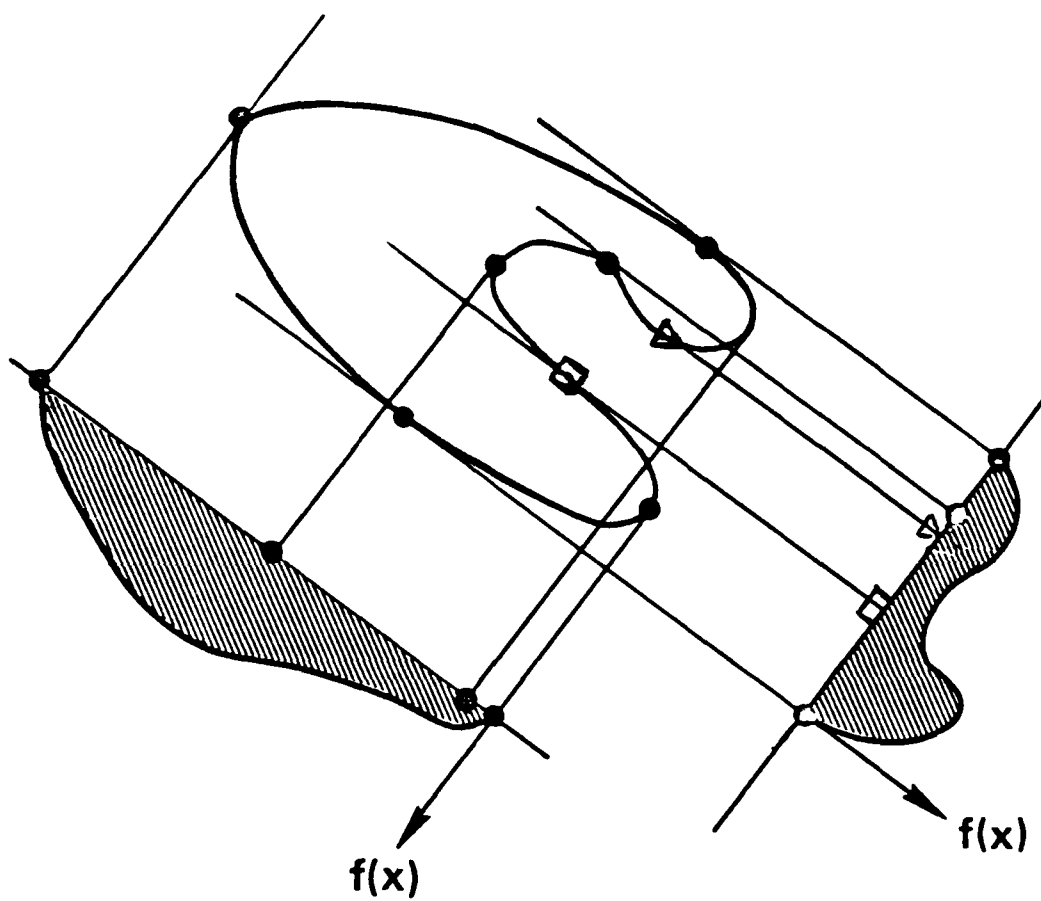**FIGURE 1.**

FIGURE 2.
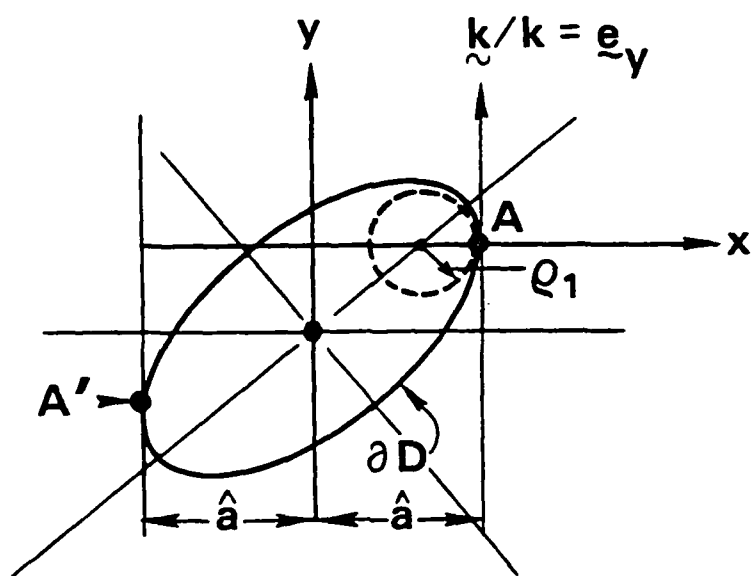
FIGURE 3.
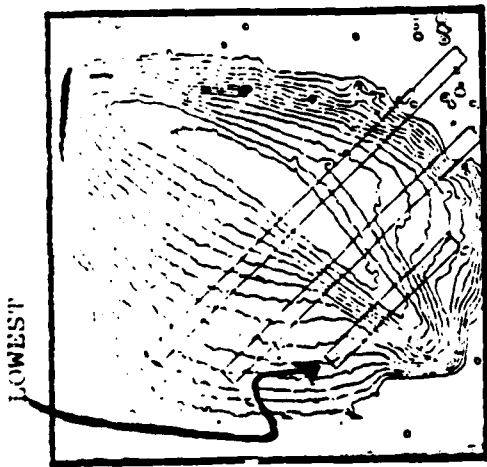
Fig. 4 (c)

Spatial Frequency (km^{-1})

Power Spectral Estimate

1E-15
1E-16
1E-17
1E-18
1E-19
1E-20
1E-21
1E-22
1E-23
1E-24
1E-25

.01 .1 1 10

Fig. 4 (b)

Distance (km)

Radiance (10^{-9} W/cm^2-sr)

5.5
5.0
4.5
4.0
3.5
3.0
2.5
2.0
1.5
1.0
0.5
0.0

0 2 4 6 8 10 12 14 16

Fig. 4 (a)

LOWEST

Smoothed radiance contour showing
areas where profiles were extracted.

Fig. 5 (c)

Spatial Frequency (km^{-1})

Power Spectral Estimate

1E-16
1E-17
1E-18
1E-19
1E-20
1E-21
1E-22
1E-23
1E-24
1E-25
1E-26

.01 .1 1 10

Fig. 5 (b)

Distance (km)

Radiance (10^{-9} W/cm^2-sr)

1.8
1.6
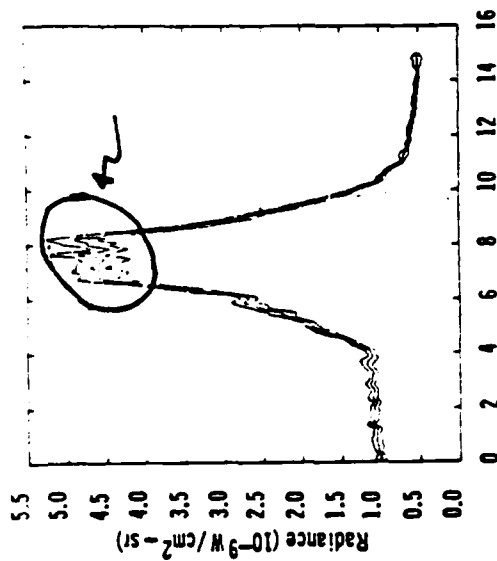1.4
1.2
1.0
0.8
0.6
0.4
0.2
0.0

0 5 10 15 20 25 30
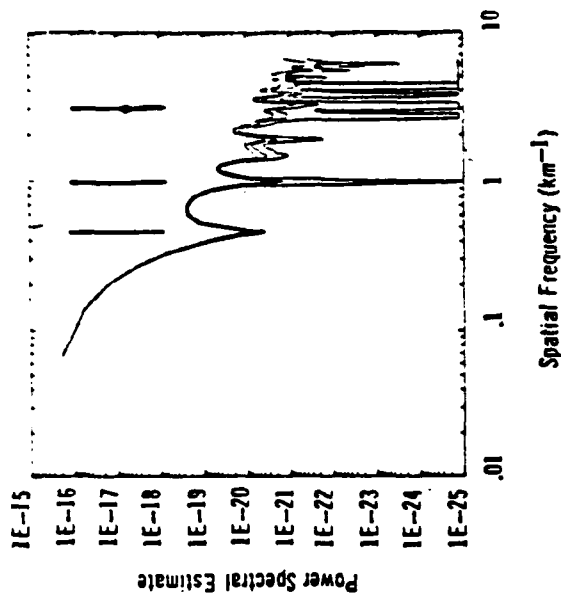
Fig. 5 (a)

LOWEST
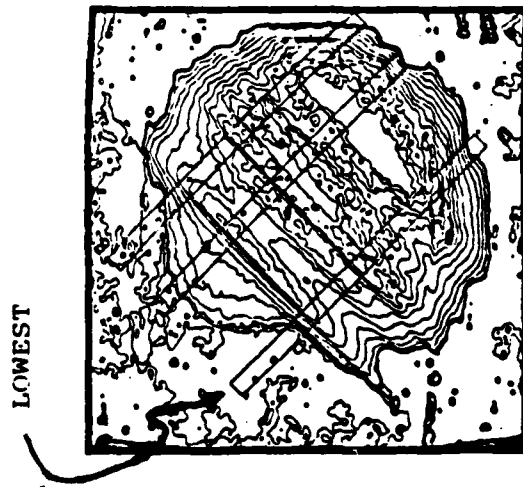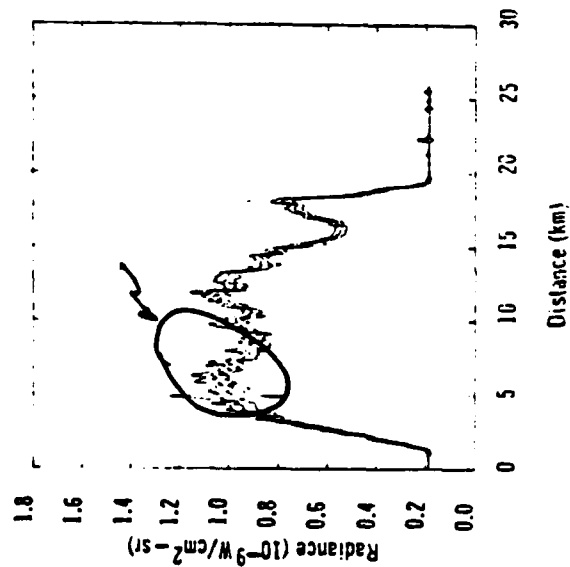
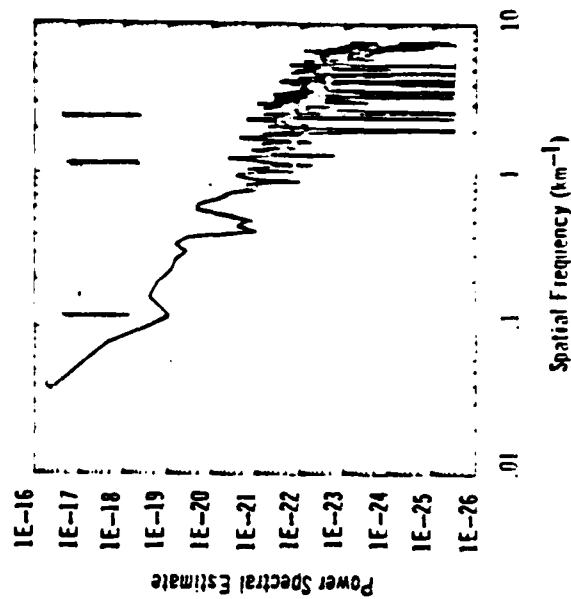Smoothed radiance contour showing
areas where profiles were extracted.

APPENDIX M

The Role of Finite Parallel Length on the

Stability of Barium Clouds

The Role of Finite Parallel Length on the Stability of Barium Clouds

J. L. Sperling

JAYCOR, San Diego, California

J. F. Drake[1]

Science Applications, Inc., McLean, Virginia

S. T. Zalesak and J. D. Huba

*Geophysical and Plasma Dynamics Branch, Plasma Physics Division
Naval Research Laboratory, Washington, D. C.*

A simple model is used to show that the finite parallel length of ionospheric plasma clouds can affect the growth rate of striation instabilities (e.g., gradient drift). The finite parallel length of plasma clouds tends to favor the growth of striations with short perpendicular wavelengths.

1. Introduction

In the disturbed ionosphere, Rayleigh-Taylor [*Scannapieco and Ossakow*, 1976; *Ott*, 1978; *Ossakow et al.*, 1979; *Zalesak and Ossakow*, 1980] and gradient drift instabilities [*Simon*, 1963; *Linson and Workman*, 1970; *McDonald et al.*, 1980, 1981] are considered to be primary sources for fluid structuring. These instabilities are predicted to be aligned along magnetic field lines with the result that analysis and numerical simulation have emphasized the flute approximation, which neglects the explicit dependence of modes on the coordinate parallel to the ambient magnetic field; when considered, it has been taken into account, in a gross sense, by averaging plasma parameters over magnetic field lines, but without considering the implications on the ionosphere of accompanying mode variation along magnetic field lines. One exception to this generality is the paper by *Goldman et al.* [1976], which calculates eigenmodes in the electrostatic approximation, recognizing that modes must vary along the magnetic field lines as one moves away from the source of instability, an artificial plasma cloud.

Artificial plasma clouds in the ionosphere have a finite spatial extent that can influence the development and properties of plasma instabilities. In this paper, particular emphasis is placed on determining certain effects on the gradient drift instability resulting from the finite length of plasma clouds along the geomagnetic field. It is demonstrated, with a rather simple plasma geometry, that finite plasma length implies parallel currents and electric fields which contribute to the development of eigenmode structure along the geomagnetic field. Specifically, the finite field line integrated electron density of ionospheric plasma clouds can play a role in reducing the growth rate of striation instabilities. This point is subsequently quantified. The finite parallel length of ionospheric plasma clouds tends to favor the growth of striations with short perpendicular wavelengths.

In section 2 the calculation model and general equations are discussed. Section 3 contains a derivative of the dispersion equation. Section 4 describes the quantitative evaluation of the model for parameters appropriate to barium releases. Concluding remarks are given in section 5.

2. General Equations

We first derive a set of nonlinear equations to describe the evolution of a cold plasma cloud ($T = 0$) in a uniform magnetic field $\mathbf{B} = B_0 \hat{z}$ with a background neutral wind $\mathbf{V}_n = V_n \hat{x}$ (see Figure 1a). For simplicity we consider only low frequency $\partial/\partial t \ll v_z$ motion of the cloud and take the electron collisions to be sufficiently weak so that $v_e \Omega_e \ll 1$ but allow $v_i \Omega_i$ to be arbitrary. The collision frequency and gyrofrequency of the α species are given by v_α and Ω_α, respectively. In this limit the fundamental equations of our analysis are continuity, momentum transfer, charge neutrality and Ampere's law:

$$\frac{\partial n_\alpha}{\partial t} - \nabla \cdot (n \mathbf{v}_\alpha) = 0 \tag{1}$$

$$0 = -e\mathbf{E} - \frac{e}{c} \mathbf{v}_e \times \mathbf{B} - m_e v_{en}(\mathbf{v}_e - \mathbf{V}_n) - m_e v_{ei}(\mathbf{v}_e - \mathbf{v}_i) \tag{2}$$

$$0 = e\mathbf{E} + \frac{e}{c} \mathbf{v}_i \times \mathbf{B} - m_i v_{in}(\mathbf{v}_i - \mathbf{V}_n) - m_i v_{ie}(\mathbf{v}_i - \mathbf{v}_e) \tag{3}$$

$$\nabla \cdot \mathbf{J} = \nabla \cdot [n_e(\mathbf{v}_i - \mathbf{v}_e)] = 0 \tag{4}$$

$$\nabla \times \mathbf{B} = \frac{4\pi}{c} \mathbf{J} \tag{5}$$

where the variables have their usual meaning. We take the electric and magnetic fields to be represented by potentials as

$$\mathbf{E} = -\nabla \phi - \frac{1}{c} \frac{\partial A_z}{\partial t} \hat{z} \tag{6}$$

$$\mathbf{B} = B_0 \hat{z} + \nabla A_z \times \hat{z} \tag{7}$$

where ϕ is the electrostatic potential and A_z is the vector potential associated with the magnetic field produced by the self-consistent plasma currents. We consider only A_z since $J_\parallel \gg J_\perp$ and we assume

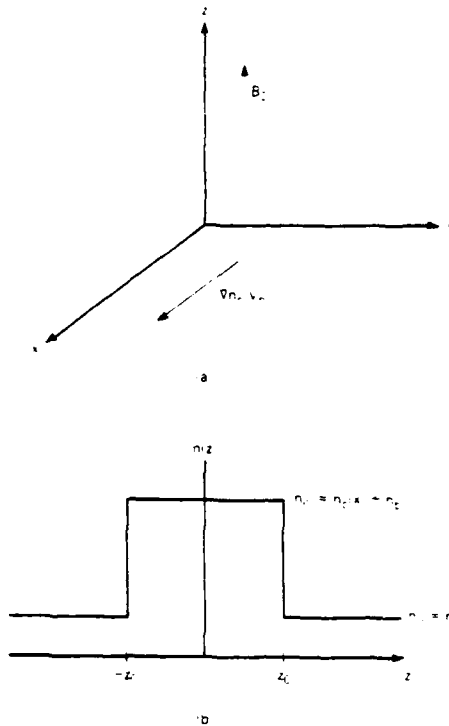$$|\nabla A_z \times \hat{z}| \ll B_0$$

Fig. 1. Plasma configuration and geometry. (a) Coordinate system. (b) Density profile parallel to B_0.

The electron cross-field motion is given by

$$\mathbf{v}_{e\perp} = -\frac{c}{B} \nabla_\perp \phi \times \hat{z} \qquad (8)$$

while the parallel motion is given by

$$v_{e\parallel} = \frac{e}{m_e \nu_e} \left[(\hat{b} \cdot \nabla)\phi - \frac{1}{c} \frac{\partial A_z}{\partial t} \right] \qquad (9)$$

where $\mathbf{v}_e = \mathbf{v}_{e\perp} + \mathbf{v}_{e\parallel}$ and $\hat{b} = \mathbf{B}/B_0$.

The ion cross-field motion is given by

$$\mathbf{v}_{i\perp} = \delta \left[-\frac{c}{B} \nabla_\perp \phi \times \hat{z} - \frac{\nu_{in}}{\Omega_i} \mathbf{V}_n \times \hat{z} \right.$$

$$\left. - \frac{\nu_{in}}{\Omega_i} \frac{c}{B} \nabla_\perp \phi - \left(\frac{\nu_{in}}{\Omega_i}\right)^2 \mathbf{V}_n \right] \qquad (10)$$

where $\delta = (1 + \nu_{in}^2 \Omega_i^{-2})^{-1}$, and the parallel motion is given by

$$v_{i\parallel} = -\frac{e}{m_i \nu_{in}} \frac{\nu_{en}}{\nu_e} \left[(\hat{b} \cdot \nabla)\phi - \frac{1}{c} \frac{\partial A_z}{\partial t} \right] \qquad (11)$$

In (10) we have included both the Pedersen and Hall responses to the electric field and neutral wind, while in (11) we have assumed $m_e \nu_{en} \ll m_i \nu_{in}$.

Substituting (8)–(11) into (1), (4), and (5), we find that

$$\frac{dn}{dt} - \frac{c}{B} \nabla \phi \times \hat{z} \cdot \nabla n + \frac{c}{4\pi e} (\hat{b} \cdot \nabla) \nabla_\perp^2 A_z = 0 \qquad (12)$$

$$\delta \frac{\nu_{in}}{\Omega_i^2} \frac{c}{B} \nabla n \cdot \nabla \phi \times \hat{e}_z - \delta \frac{\nu_{in}}{\Omega_i} \frac{c}{B} \nabla \cdot n \nabla \phi$$

$$- \frac{\nu_{in}}{\Omega_i} \nabla n \cdot \mathbf{V}_n \times \hat{e}_z - \frac{c}{4\pi e} (\hat{b} \cdot \nabla) \nabla_\perp^2 A_z = 0 \qquad (13)$$

$$\nabla_\perp^2 A_z = \frac{4\pi}{c \eta_e} \left[(\hat{b} \cdot \nabla)\dot{\phi} + \frac{1}{c} \frac{dA_z}{dt} \right] \qquad (14)$$

where

$$\dot{\phi} = \phi - (B c/\nu_{in} \Omega_i)\mathbf{V}_n \cdot \mathbf{x}$$

$$d/dt = \partial/\partial t + (\nu_{in}/\Omega_i)\hat{z} \times \mathbf{V}_n \cdot \nabla$$

$$\eta_e = m_e \nu_e /ne^2$$

Equation (12) is the electron continuity equation, (13) is the charge conservation equation, and (14) is Ampere's law. Thus, (12)–(14) provide a complete description of the evolution of a three-dimensional, cold plasma cloud.

We will only consider the linear stability of a two-dimensional cloud which is localized both along and across the magnetic field B_0: $n_c = n_c(x, z)$ with $|x| \lesssim x_0$ and $|z| \lesssim z_0$. The background plasma is taken to be uniform throughout all space. The equations describing this two-dimensional equilibrium are given by

$$\frac{\partial n}{\partial t} + \frac{1}{e} \frac{\partial}{\partial z} \frac{1}{\eta_e} \left(\frac{1}{c} \frac{\partial A_z}{\partial t} + \frac{\partial \phi}{\partial z} \right) = 0 \qquad (15)$$

$$\delta \frac{\nu_{in}}{\Omega_i} \frac{c}{B} \frac{\partial}{\partial x} n \frac{\partial \phi}{\partial x} + \frac{c}{4\pi e} \frac{\partial}{\partial z} \frac{\partial^2 A_z}{\partial x^2} = 0 \qquad (16)$$

$$\frac{\partial^2 A_z}{\partial x^2} = \frac{4\pi}{c \eta_e} \left(\frac{1}{c} \frac{\partial A_z}{\partial t} + \frac{\partial \phi}{\partial z} \right) \qquad (17)$$

From (15)–(17) we find that the equilibrium is given by $A_z = \phi = 0$ with $n_c(x, z)$ an arbitrary function. For simplicity we consider the plasma density to be given by (similar to that used by Sperling [1983a])

$$n(x, z) = n_c = n_c(x) + n_b \qquad |z| < z_0$$

$$n(x, z) = n_b = n_b \qquad |z| > z_c \qquad (18)$$

where the subscripts c and b refer to cloud and background, respectively (see Figure 1b).

We note that if we had retained a finite plasma temperature then the density equation would be

$$\frac{\partial n}{\partial t} - \frac{\partial}{\partial z} \frac{T}{m_i \nu_{in}} \frac{\partial n}{\partial z} = 0 \qquad (19)$$

where $T = T_i + T_e$ and we have taken $\partial/\partial x = 0$. Equation (19) describes the diffusion of the cloud along z with a diffusion coefficient, $D_z = T/m_i \nu_{in}$. Thus, in general (15)–(17) will not have equilibrium solutions when $\partial/\partial z \neq 0$ and $T \neq 0$. However, in calculating the growth rates of unstable modes with growth times which are short compared with the diffusion time $t_z = z_0^2/D_z$, we would expect the evolution of the equilibrium to have very little influence on the stability calculation for this situation. Consideration of finite temperature effects will be deferred to a later report.

3. LINEARIZED EQUATIONS AND DISPERSION RELATION

To find the influence of the parallel dynamics on the instability, we linearize (7)–(9) where the perturbed quantities vary as $\tilde{p} \sim \tilde{p}(z) \exp(\gamma t - ik_y y)$. After eliminating the equation for $\tilde{n}$ algebraically, we obtain two coupled differential equations for $\tilde{A}_z$ and $\tilde{\phi}$.

$$(\gamma + k_y^2 D_z)\tilde{A}_z = -c \frac{\partial \tilde{\phi}}{\partial z} \qquad (20)$$

$$(\tilde{\gamma} - \gamma_0)\tilde{\phi} = -\gamma \alpha D_r \frac{1}{c} \frac{\partial \tilde{A}_z}{\partial z} \qquad (21)$$

where $\gamma_0 = -n_< V_n n_< \delta$. $n_< = \partial n_< / \partial x$. $\tilde{\gamma} = \gamma - ik_y V_n v_{in} \Omega_i$. $D_r = v_{i} c^2 / \omega_{pe}^2$ is the resistive diffusion coefficient, and $\alpha = \Omega_e \Omega_i / v_e v_{in} \delta$.

Prior to solving (20) and (21) for the density profile given by (18), we first consider a cloud of infinite extent $(z_0 \to \infty$ in (18)) and Fourier expand modes parallel to B_0, i.e., $\tilde{p}(z) \sim \tilde{p} \exp (ik_z z)$. We consider the local approximation $(k_y (n'/n)^{-1} \gg 1)$ so that (20) and (21) can be solved algebraically. This allows comparison with previous results [Sperling, 1983b; Basu and Coppi, 1983] and insight into the effects of finite parallel wavelengths. The local dispersion equation is given by

$$(\tilde{\gamma} - \gamma_0)(\tilde{\gamma} + k_y^2 D_r) = -\gamma \alpha k_z^2 D_r \qquad (22)$$

We note that the right-hand side of (22) can be expressed as $-\gamma k_z^2 V_A^2 v_{in} \delta$, where $V_A = B/(4\pi n m_i)^{1/2}$ is the Alfvén velocity. This form explicitly shows the coupling to an Alfvén wave which is the dominant finite k_z effect. For simplicity we assume $\gamma \gg k_y V_n (v_{in} \Omega_i)$ and solve (22) in two limits: $\gamma \gg k_y^2 D_r$ (electromagnetic limit) and $\gamma \ll k_y^2 D_r$ (electrostatic limit). It is found that

$$\hat{\gamma} = 1 - \hat{k}_z^2 = 1 - k_z^2 V_A^2 \gamma_0 v_{in} \delta, \qquad \gamma \gg k_y^2 D_r \qquad (23)$$

$$\hat{\gamma} = (1 + \hat{k}_z^2 \hat{k}_y^2)^{-1} \qquad \gamma \ll k_y^2 D_r \qquad (24)$$

where $\hat{\gamma} = \gamma / \gamma_0$, $\hat{k}_y = k_y L_r$, $\hat{k}_z = k_z z_r$, and L_r and z_r are the perpendicular and parallel resistive length scales given by $L_r^2 = D_r / \gamma_0$ and $z_r^2 = \alpha D_r / \gamma_0$. In the ideal limit $(D_r = 0)$, (23) indicates that electromagnetic effects stabilize the instability when $\hat{k}_z^2 > 1$ (i.e., $k_z^2 V_A^2 > \gamma_0 v_{in} \delta$) by coupling to an Alfvén wave. This result is similar to that of Basu and Coppi [1983] who investigated the collisional Rayleigh-Taylor instability. On the other hand, (24) indicates that in the electrostatic limit there is only a reduction in growth rate. This is because resistive diffusion across the magnetic field lines is sufficiently rapid to dissipate the Alfvén wave. Finally, in the limit $k_z \to 0$ we recover from (22) the standard result $\gamma = \gamma_0 - ik_y V_n (v_{in} \Omega_i)$, where the real frequency is caused by the equilibrium electric field in the x direction; in a frame of reference moving with the electrons, however, the mode has no real frequency. A second mode, which is damped, is given by $\gamma = -k_y^2 D_r - ik_y V_n (v_{in} \Omega_i)$ [Chu et al., 1978; Sperling, 1983b].

For a general profile $n(x, z)$ the coupled equations for $\tilde{\phi}$ and $\tilde{A}_z$ must be solved subject to the boundary conditions $\tilde{\phi}, \tilde{A}_z \to 0$ as $|z| \to \infty$. For the step profile for $n(x, z)$ given in (18), the solutions to (20) and (21) in the region $|z| > z_0$ can be written as plane waves.

$$\tilde{A}_z = \tilde{A}_{z,>} \exp[-k_>|z|] \qquad (25a)$$

$$\tilde{\phi} = \tilde{\phi}_> \exp[-k_>|z|] \qquad (25b)$$

with

$$(\tilde{\gamma}_> - k_y^2 D_{r,>})\tilde{A}_{z,>} = k_> c \tilde{\phi}_> \qquad (25c)$$

$$\frac{k_>^2}{k_y^2} = \left(\frac{\tilde{\gamma}}{\gamma} \frac{1}{\alpha R}\right)_> \qquad (25d)$$

where

$$R = \frac{k_y^2 D_r}{\tilde{\gamma} - k_y^2 D_r} \qquad (25e)$$

and the subscript $>$ on a given parameter indicates that it is to be evaluated in the region $|z| > z_0$. Note that the solutions

which diverge as $z \to \pm\infty$ have been omitted in (25a) and (25b). The parameter R is a measure of the electrostatic or electromagnetic nature of the mode. For $k_y^2 D_r \gg \gamma$, we note that $R \sim 1$ and the mode is essentially electrostatic. In the opposite limit $k_y^2 D_r \ll \gamma$, the mode is electromagnetic and $R \ll 1$.

In the region $|z| < z_0$, the solutions for $\tilde{\phi}$ and $\tilde{A}_z$ are

$$\tilde{A}_z = \tilde{A}_{z,<}^1 \sin(k_< z) - \tilde{A}_{z,<}^2 \cos(k_< z) \qquad (26a)$$

$$\tilde{\phi} = \tilde{\phi}_<^1 \cos(k_< z) + \tilde{\phi}_<^2 \sin(k_< z) \qquad (26b)$$

with

$$(\tilde{\gamma}_< + k_y^2 D_{r,<})\tilde{A}_{z,<}^{1,2} = k_< c \tilde{\phi}_<^{1,2} \qquad (26c)$$

$$\frac{k_<^2}{k_y^2} = \left(\frac{\gamma_0 - \tilde{\gamma}}{\gamma} \frac{1}{\alpha R}\right)_< \qquad (26d)$$

To complete the dispersion relation, we must match the various plane wave solutions at $z = \pm z_0$. The appropriate matching conditions are obtained from (20) and (21). Integrating these two equations across the discontinuity in the density at $z = \pm z_0$, we find that $\tilde{\phi}$ and $\tilde{A}_z$ must be continuous. For the even $\tilde{\phi}$ solution $(\tilde{\phi}_<^2 = 0)$, we obtain the dispersion relation for the growth rate γ.

$$k_< z_0 = \tan^{-1}\left[\frac{k_>}{k_<} \frac{\tilde{\gamma} + k_y^2 D_{r,<}}{\tilde{\gamma} + k_y^2 D_{r,>}}\right] + m\pi \qquad (27)$$

where m is an integer. The dispersion relation for the odd $\tilde{\phi}$ mode $(\tilde{\phi}_<^1 = 0)$ is similar to (27) except $\tan^{-1}$ is replaced by $-\cot^{-1}$.

In general, the dispersion equation (27) has an infinite number of solutions for a given set of physical parameters, corresponding to eigenmodes with an increasing number of modes (m) along z. The dispersion equation (27) can be solved numerically for arbitrary values of the background and cloud parameters. However, to gain an understanding of the general scaling of the growth rate γ with the parallel extent of the cloud, it is useful to solve (27) analytically. To do this we make a number of simplifying assumptions. We consider only the lowest order mode (i.e., $m = 0$ which implies $0 < k_< z_0 < \pi/2$; it is easily shown that this mode has the largest growth rate); take $v_{in} \Omega_i$ to be small so that $\delta \simeq 1$ and the real frequency $k_y V_n v_{in} / \Omega_i$ can be neglected; and finally, take all parameters but the density to be the same inside and outside of the cloud. In this limit the expressions for $k_\gtrless$ reduce to

$$\frac{k_>^2}{k_y^2} = (\alpha R)_>^{-1} \qquad (28a)$$

$$\frac{k_<^2}{k_y^2} = \frac{\gamma_0 - \tilde{\gamma}}{\tilde{\gamma}} (\alpha R)_<^{-1} \qquad (28b)$$

We separate our analysis into two separate cases $v_e \gtrless v_{en}$. In the limit $v_e \gg v_{en}$, the resistive diffusion coefficient D_r is continuous across the cloud boundary and $R_> = R_<$.

With these assumptions the dispersion equation (27) becomes

$$k_< z_0 = \tan^{-1}\left[\left(\frac{\tilde{\gamma}}{1 - \tilde{\gamma}} \frac{n_>}{n_<}\right)^{1/2}\right] \qquad (29a)$$

with

$$k_<^2 z_0^2 = [(1 - \tilde{\gamma})/\tilde{\gamma}](n_< n_>)(\tilde{\gamma} + \hat{k}_y^2)\hat{z}_0^2 \qquad (29b)$$

and $\hat{z}_0 = z_0 z_r$, $\hat{k}_y = k_y L$, where $L_r^2 = D_{r,>} / \gamma_0$ and $z_r^2 = \alpha$.
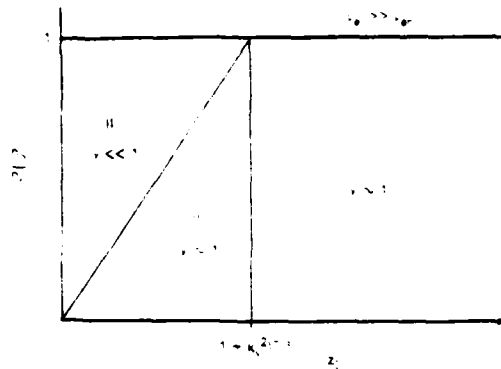
Fig. 2. Regions of validity for the growth rates given by (33), (36), and (37). The growth rates are listed in Appendix A and are based upon the assumption that $\nu_{ei} \gg \nu_{en}$.

L_r^2. The dispersion relation in (29) is now a function of only three parameters: $\bar{z}_0$, $n_>$, $n_<$ and k_y.

In the limit

$$[(1 - \bar{\gamma})\bar{\gamma}](n_< n_>) \ll 1 \qquad (30)$$

the arctan function approaches $\pi/2$ so that $k_< \bar{z}_0 \simeq \pi/2$ is the dispersion equation. Furthermore, since $n_< n_> = (n_c - n_b) n_b > 1$, the inequality in (30) can only be satisfied for $\bar{\gamma} \simeq 1$. Thus, the growth rate is given by

$$\bar{\gamma} \simeq 1 - \frac{\pi^2}{4\bar{z}_0^2} \frac{n_>}{n_<} \qquad \bar{\gamma} \gg k_y^2 \qquad (31a)$$

$$\bar{\gamma} \simeq \left(1 - \frac{\pi^2}{4\bar{z}_0^2} \frac{n_>}{n_<} \frac{1}{k_y^2}\right)^{-1} \qquad \bar{\gamma} \ll k_y^2 \qquad (31b)$$

We note that (31a) and (31b) can be compared to the local growth rates (23) and (24) if we define an effective k_{zeff}.

$$k_{zeff}^2 \equiv \frac{\pi^2}{4\bar{z}_0^2} \frac{n_>}{n_<} \qquad (32)$$

Thus, taking $k_z^2 = k_{zeff}^2$ in (23) and (24) we recover (31a) and (31b). For $m \neq 0$ modes, k_{zeff} becomes $(m + \frac{1}{2})^2 \pi^2 / 4\bar{z}_0^2 (n_> n_<)$ indicating a spectrum of modes parallel to B. Finally, since $\bar{\gamma} \sim 1$ from (31a) and (31b) we can write a generalized dispersion relation given by

$$\bar{\gamma} = 1 - \frac{\pi^2}{4\bar{z}_0^2}(1 + k_y^2)^{-1}\frac{n_>}{n_<} \qquad (33a)$$

and is valid for (based on (30))

$$(1 + k_y^2)\bar{z}_0^2 \gg 1 \qquad (33b)$$

In the opposite limit, i.e.,

$$[(1 - \bar{\gamma})\bar{\gamma}](n_< n_>) \gg 1 \qquad (34)$$

arctan function approaches $k_< \bar{z}_0$. The dispersion relation becomes

$$(1 - \bar{\gamma})(\bar{\gamma} + k_y^2)^{1/2} = (n_< n_> \bar{z}_0) \qquad (35)$$

The solution of the equation is

$$\bar{\gamma} = 1 - (n_< n_>)\bar{z}_0^{-1}(1 + k_y^2)^{-1/2} \simeq 1 \qquad (36a)$$

for

$$(n_< n_>)^2 \ll (1 + k_y^2)\bar{z}_0^2 \ll 1 \qquad (36b)$$

where the inequalities follow from (34) and the condition $\bar{\gamma} \simeq 1$. When $\bar{\gamma} \ll 1$, (35) becomes a quadratic equation with the solution

$$\bar{\gamma} = \bar{z}_0^{-2}(n_< n_>)^2[1 + (1 - 4k_y^2\bar{z}_0^2 n_<^2 n_>^2)^{1/2}]/2 \qquad (37a)$$

which is valid for (from $\bar{\gamma} \ll 1$)

$$(1 + k_y^2)\bar{z}_0^2 \ll n_<^2 n_>^2 \qquad (37b)$$

For $\bar{z}_0$ very small the growth rate approaches zero as

$$\bar{\gamma} \simeq k_y \bar{z}_0 n_< n_> \qquad (38)$$

Equation (38) also implies that the growth rate increases with k_y in this region. The physical reason for this behavior will be discussed shortly.

The growth rates and inequalities in (33), (36) and (37) can be summarized rather succinctly in the $(n_>, n_<) - \bar{z}_0$ phase space plot shown in Figure 2. Note that $n_>, n_< = n_b (n_b - n_c) < 1$. Regions I, II and III indicate the range of validity of the growth rates in (33), (36) and (37), respectively. Expressions for the growth rate in these three regions are given in Appendix A. For large $\bar{z}_0$, in regions I and II, the finite length of the cloud along B has very little influence on the growth rate and $\bar{\gamma} \sim \gamma/\gamma_0 \sim 1$. For small $\bar{z}_0$, in region III, $\bar{\gamma} \ll 1$ so that the finite extent of the cloud strongly reduces the growth rate. As k_y increases, region III shrinks in size so that the growth rates for short wavelength modes are less affected by the parallel dynamics than are the growth rates for long wavelength modes. Nevertheless, (25d) shows that the short wavelength modes are more localized along the magnetic field than long wavelength modes [Sperling and Glassman, 1983; Sperling, 1984].

In Figure 3 we schematically show the growth rate $\bar{\gamma}$ as a function of $\bar{z}_0$ for $n_>, n_<$ and $k_y \ll 1$ held fixed. In region III the growth rate first increases linearly with $\bar{z}_0$ and then quadratically until $\bar{\gamma} \sim 1$, where it enters region II. The transition from $\bar{\gamma} \sim \bar{z}_0$ to $\bar{\gamma} \sim \bar{z}_0^2$ in region III is a consequence of the change in character of the mode from being dominantly electrostatic ($\bar{\gamma} < k_y^2 D_r$) for $\bar{z}_0 < k_y n_< n_>$ to electromagnetic ($\bar{\gamma} > k_y^2 D_r$) for $\bar{z}_0 > k_y n_< n_>$.

The dependence of the growth rate on k_y can also be readily obtained from Figure 2 and Appendix A. For parameters $\bar{z}_0$ and $n_>, n_<$ such that modes with $k_y \ll 1$ are in regions I and II ($\bar{z}_0 > n_> n_<$), $\bar{\gamma} \sim 1$ for all k_y since increasing k_y simply pushes the mode further into regions I and II. For the case where modes with $k_y \ll 1$ fall in region III ($\bar{z}_0 < n_> n_<$), the depen-

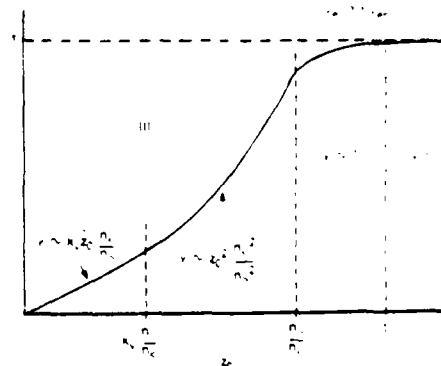Fig. 3. Schematic of the growth rate $\bar{\gamma}$ versus parallel length $\bar{z}_0$ for fixed $n_>, n_<$ and k_y. This curve is based on the assumption that $\nu_{ei} \gg \nu_{en}$.

M-6

dence of γ on k_γ is more interesting. In Figure 4 the growth rate is shown versus k_γ with $n_>$, $n_<$ and z_0 held fixed. For small k_γ the mode falls in region III and has a growth rate nearly independent of k_γ. When $k_\gamma > z_0 n_< n_>$, the mode becomes electrostatic and the growth rate increases with k_γ until $k_\gamma \sim n_> n_< z_0$ when $\gamma \sim 1$ and the mode enters region II. We again conclude from this figure that the growth rates for short wavelength modes are less affected by the parallel dynamics than the growth rates for long wavelength modes.

Up to this point we have discussed only the case where $v_{ei} \gg v_{en}$. The dispersion equation (27) can be solved in a similar manner in the opposite limit $v_{ei} \ll v_{en}$. In this limit the resistive diffusion coefficient is not continuous across the cloud boundaries at $\pm z_0$. The results differ only slightly from those just presented so we skip the details and simply present the analogues of Figure 2 and Appendix A for this case. In Figure 5 we show the $(n_>, n_< \vdash z_0)$ phase space plot showing the three regions of the instability for $v_{en} \gg v_{ei}$. The growth rates for these three regions are listed in Appendix B. The only difference between phase space plots in Figures 2 and 5 is the boundary between regions I and II. which falls at larger z_0 when $v_{en} \gg v_{ei}$. The growth rates for $v_{en} \gtrsim \gtrsim v_{ei}$ differ only in region I. Since $\gamma \sim 1$ in both regions I and II, these differences are not particularly significant so the previous discussion of the instability in the limit $v_{ei} \gg v_{en}$ also applies to the opposite limit.

We have shown that the finite length z_0 of the plasma cloud reduces the growth rate of the gradient drift instability compared with its value when z_0 is infinite. The growth rates of long wavelength modes are more strongly reduced than those of short wavelength modes. The essential physics which underlies these results can be understood by integrating (21) for the perturbed potential $\tilde\phi$ along z,

$$\gamma \int_{-\infty}^{\infty} dz \, n(z)\tilde\phi(z) = \gamma_0 \int_{-z_0}^{z_0} dz \, n(z)\tilde\phi(z)$$

$$\simeq 2\gamma_0 n_< z_0 \tilde\phi_< \qquad (39)$$

where we have again taken $v_{in} \Omega_i$ small and we have assumed that $\tilde\phi(z) \simeq const$ in the region $|z| < z_0$, which is approximately correct for the lowest order mode. The integral on the left side of (39) represents the integrated Pederson conductivity along the entire field line, weighted by the potential $\tilde\phi$. The integral on the right side of this equation is the integrated
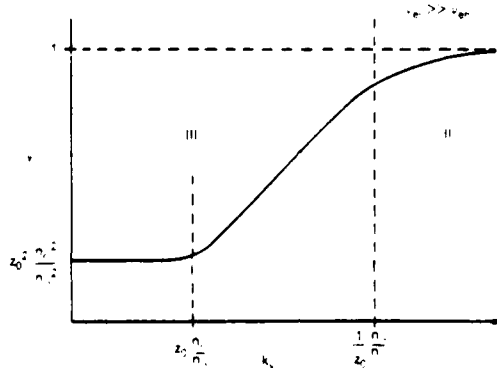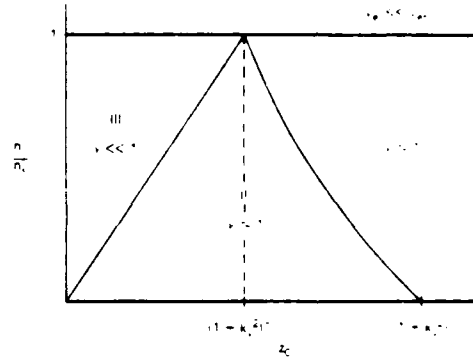

Fig. 5. Regions of validity for the growth rates in the regime $v_{ei} \ll v_{en}$. The growth rates are listed in Appendix B. This curve is similar to Figure 2 but the boundary between regions I and II is shifted to larger z_0

Pederson conductivity of the cloud. Carrying out the remaining integral. we find

$$\gamma \simeq \gamma_0 n_< z_0 \tilde\phi_< (n_< z_0 \tilde\phi_< + n_> k_> {}^{-1}\tilde\phi_>)$$

$$\simeq \gamma_0 n_< z_0 (n_< z_0 + n_> k_> {}^{-1}) \qquad (40)$$

where we have used the results of our previous calculation: $\tilde\phi_< \simeq \tilde\phi_>$ and $\tilde\phi \to 0$ when $k_>|z| > 1$. Substituting the expression for $k_>$ in (25d) into (40), we obtain the dispersion relation

$$\gamma = \gamma_0 \frac{n_< z_0}{n_< z_0 + n_> k_\gamma {}^{-1}(\pi R)_>^{1/2}} \qquad (41)$$

When the result is written in the normalized variables presented previously, it reduces precisely to the dispersion relation presented in (35). The reduction of the growth rates due to finite z_0 occurs because the integrated Pederson conductivity over the extent of the mode along z becomes comparable to that of the cloud. The distance the mode extends along z ($\sim k_>^{-1}$) increases as k_γ decreases (see (25d)) so that long wavelength modes have greater reductions in their growth rates. The electromagnetic effects prevent the mode from extending an infinite distance along the magnetic field line as $k_\gamma \to 0$. In this limit $R_> \to 0$ and (41) becomes

$$\gamma = \gamma_0 \frac{n_< z_0}{n_< z_0 + n_>(\pi D_r \gamma)_>} \qquad (42)$$

so that the growth rate is independent of k_γ as shown in Figure 4.

4. RESULTS

The plasma model outlined in sections 2 and 3 is rather simple, and admittedly does not include all the intricacies and inhomogeneities of the real ionosphere. Nevertheless, the model does show that the growth rate is a function of the parallel length. We now present quantitative results of our model for typical ionospheric parameters. In particular, we take $n_< = 10^7$ cm^{-3}, $n_> = 10^5$ cm^{-3}, $B = 0.4$ G, $T_i = T_e = 0.1$ eV, and consider two values of γ_0: $\gamma_0 = 0.01$ s^{-1} and $\gamma_0 = 0.10$ s^{-1}. The ions for $|z| < z_0$ are assumed to be barium (i.e., $m_{i<} = 137 m_p$, with m_p the proton mass) and the ions for $|z| > z_0$ are assumed to be air with $m_{i>} = 20 m_p$. The mass of an atmospheric neutral particle, $m_{0<i>}$, is also assumed to be $20 m_p$. The neutral density. $n_{0<} = n_{0>} = 8.3 \times 10^9$ cm^{-3}. is appropriate to an altitude of ~ 200 km [Knapp and Schwartz.

Fig. 4. Schematic of the growth rate γ versus perpendicular wave number k_γ for fixed $n_>$, $n_<$ and z_0. This curve is based upon the assumption that $v_{ei} \gg v_{en}$.

TABLE 1.   Resistive Scale Lengths

	$\nu_0 = 0.01$ s⁻¹	$\nu_0 = 0.10$ s⁻¹
Perpendicular $L_\perp$	2.5	0.8
Parallel $z_\parallel$	2370	750

Scale lengths are in kilometers

1975]. The collision frequencies are determined from [*Braginskii*, 1965; *Kilb*, 1977]

$$\nu_{i,n} = 2.5 \times 10^{12} m_i n_0 \qquad (43a)$$

$$\nu_{i,e} = 2.5 \times 10^{13} m_0 n_0 \qquad (43b)$$

$$\nu_{e(i,n)} = 0.51 \nu_{e(i,n)} - 1.9 \times 10^{-8} n_0 \qquad (43c)$$

$$\nu_{e(i,n)} = 1.1 \times 10^{-3} n_{e(i,n)} \qquad (43d)$$

In (43) all parameters are in cgs units. Based upon these parameters and equations we can calculate the perpendicular and parallel resistive scale lengths which are given in Table 1 for $\nu_0 = 0.01$ s⁻¹ and 0.1 s⁻¹.

An important result to be considered is the boundary between regions II and III in Figures 2 and 5. The boundary is defined by the equation

$$n_> n_< = (1 - k_\perp^2)^{1/2} z_{0c} \qquad (44)$$

and marks the transition between strong and weak growth. For $z_0 < z_{0c}$ the theory predicts very weak growth, and it is clear that the long wavelength modes ($k_\perp \ll 1$) have the weakest growth for a given value of z_0 and $n_> n_<$. In Figure 6 we plot z_{0c} (km) versus $k_\perp$ (km⁻¹) based on (44) for $n_> n_< = 0.01$ and the parameters described above and in Table 1. The regions below each curve indicate weak growth, while regions above each curve indicate strong growth. As expected, the value of z_{0c} is largest for $k_\perp \ll 1$. Also, we note that the dependence of z_{0c} on $k_\perp$ is stronger for smaller values of wave number ($k_\perp < 1$ km⁻¹) and ν_0.

In Figure 7 we plot $\gamma = \gamma_{z0}$ versus $k_\perp$ (km⁻¹) for the parameters given above and different values of z_0. The solid lines are based on $\nu_0 = 0.10$ s⁻¹ while the dashed lines are for $\nu_0 = 0.01$ s⁻¹. These figures are based upon (35). Again, these curves quantitatively reflect the growth rate dependence on $k_\perp$ and z_0 which is presented qualitatively in Figure 4. For $k_\perp > 2$ km⁻¹, the normalized growth rate γ is independent of z_0. This is consistent with Figure 6 which shows that z_{0c} is independent of γ_0 for $k_\perp > 2$ km⁻¹. On the other hand, for $k_\perp < 2$ km⁻¹ the difference between the curves becomes larger, especially for z_0 large. Again, this is consistent with Figure 6 which indicates a strong dependence of z_{0c} on γ_0 for $k_\perp < 2$ km⁻¹. It is clear from Figure 7 that the finite parallel extent of the cloud favors the growth of short wavelength modes.

5. CONCLUDING REMARKS

We have presented a linear analysis of the gradient drift instability appropriate to ionospheric plasma clouds of finite spatial extent, both perpendicular and parallel to the ambient magnetic field. Based on a simple model for the cloud (see (18)), we find that the parallel extent of the cloud along **B** can significantly alter the growth rate of the instability. Specifically, we find that long wavelength modes ($k_\perp$ small) tend to have much smaller growth rates than short wavelength modes ($k_\perp$ large). This reduction in growth due to finite z_0 occurs because the integrated Pedersen conductivity of the background plasma over the extent of the mode along z becomes greater than that of the cloud (see (40)). The distance the mode extends along z increases as $k_\perp$ decreases (see (25d)) so that the long wavelength modes are more strongly affected. A more detailed numerical analysis of this effect is given by *Sperling and Glassman* [1983]. We mention that these results also apply to the $E \times B$ gradient drift [*McDonald et al.*, 1980, 1981] and Rayleigh-Taylor [*Ossakow et al.*, 1979; *Sperling*, 1982] instabilities.

A question which naturally arises is, how does the growth rate change as the cloud diffuses along the magnetic field or, more generally, as the cloud evolves in time? It is tempting to conclude that the growth rate simply increases with z_0 as the cloud diffuses along z as shown in Figures 3 and 6. However, as the cloud diffuses along z we expect the electron density inside the cloud to decrease such that $n_\perp z_0 \sim$ const. Loosely

Fig. 7. Plot of perpendicular wave number $k_\perp$ (km⁻¹) versus growth rate $\gamma(\nu, z_0)$ for $\gamma_0 = 0.10$ s⁻¹ (solid curves), $\gamma_0 = 0.01$ s⁻¹ (dashed curves), and several values of z_0 (km). Curve is based upon (27) for $m = 0$. The ionospheric parameters used are given in the text (section 4).
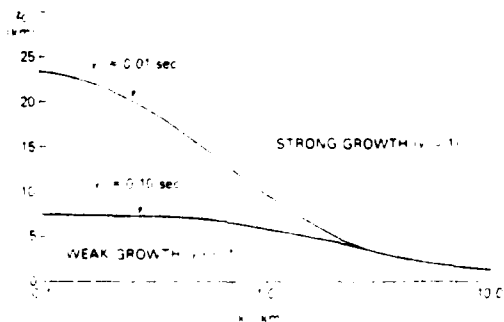
Fig. 6. Plot of "critical" parallel length z_{0c} (km) versus perpendicular wave number $k_\perp$ (km⁻¹) based upon (44) for typical ionospheric parameters. The parameters used are given in the text (section 4). These curves denote the boundary between region II (above curves—strong growth ($\gamma > 1$)) and region III (below curves—weak growth ($\gamma < 1$)).
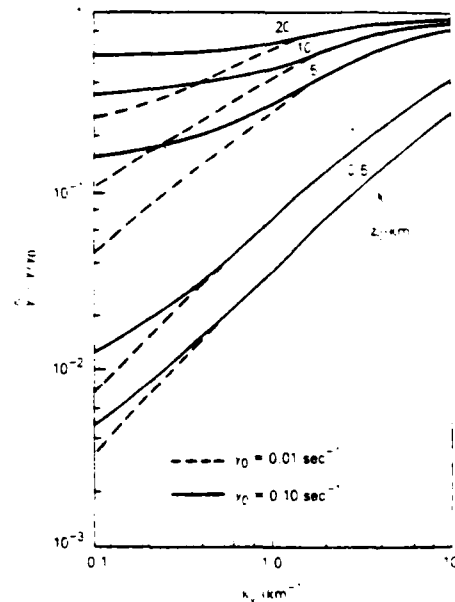
speaking, the total number of cloud electrons along a given magnetic field line should not change, or at least, not change significantly. Since the growth rates of the instability in the weak (region III) and strong (region II) growth regions depend only on the product $n_< z_0$, parallel diffusion along z does not cause the growth rate to increase. The expansion of the cloud along z also does not enable the mode to change from weak to strong growth. This is clearly seen from (44) which indicates that the boundary between regions II and III does not change in time as long as $n_< z_0 \sim$ const. Thus, we conclude that just diffusion of the cloud along z does not change the growth rate in an important way.

On the other hand, the gross evolution of the cloud involves not only diffusion along z but, for example. steepening of the "backside" of the cloud which increases the growth rate γ_0. As shown in Figure 6. for a given value of z_0 more modes are in the strong growth regime when γ_0 is larger. Thus. the parallel dynamics will significantly change the spectrum of unstable modes as the cloud evolves in time. This feature may be related to the observation of the delayed onset of striations. That is, the onset of striations in barium clouds occurs several minutes after the detonation of the barium release. Specifically for larger barium clouds. like Spruce [Linson and Meltz, 1972], the onset time for striations is estimated to be generally greater than approximately 5 min [McDonald et al., 1980]. Linson and Meltz [1972] have estimated that the Spruce and Olive ion clouds had an extent approximately 30–40 km along the magnetic field at about 5 min. This parallel extent corresponds to $z_0 \approx 15$–20 km. It is possible then that plasma clouds need to evolve in time so that they have a sufficiently steepened backside. as well as a sufficient length along **B**, before the striations can occur rapidly.

APPENDIX A

The following equations are growth rates for $v_{ei} \gg v_{en}$:

Region I

$$\gamma = 1 - \left(\frac{\pi^2}{4}\right) \frac{1}{z_0^2} \frac{1}{(1 + k_y^2)} \frac{n_>}{n_<} \approx 1$$

Region II

$$\gamma = 1 - \frac{1}{z_0} \frac{1}{(1 + k_y^2)^{1/2}} \frac{n_>}{n_<} \approx 1$$

Region III

$$\gamma = z_0^2 \left(\frac{n_<}{n_>}\right)^2 \left[1 + \left(1 - \frac{4 k_y^2}{z_0^2} \frac{n_>^2}{n_<^2}\right)^{1/2}\right] \ll 1$$

APPENDIX B

The following equations are growth rates for $v_{ei} \ll v_{en}$:

Region I

$$\gamma = 1 - \frac{\pi^2}{4} \frac{1}{z_0^2} \frac{1}{[1 + k_y^2(n_> n_<)]} \frac{n_>}{n_<} \approx 1$$

Region II

$$\gamma = 1 - \frac{1}{z_0} \frac{1}{(1 + k_y^2)^{1/2}} \frac{n_>}{n_<} \approx 1$$

Region III

$$\gamma = z_0^2 \left(\frac{n_<}{n_>}\right)^2 \left[1 + \left(1 - \frac{4 k_y^2}{z_0^2} \frac{n_>^2}{n_<^2}\right)^{1/2}\right] \ll 1$$

REFERENCES

Basu, B., and B. Coppi, Localized plasma depletion in the ionosphere and the equatorial spread F, *Geophys. Res. Lett.*, *10*, 900, 1983.

Braginskii, S. I., Transport processes in plasmas, in *Reviews of Plasma Physics*, vol. 1. edited by M. A. Leontovich. Consultants Bureau, New York, 1965.

Chu. C., M. S. Chu. and T. Ohkawa, Magnetostatic mode and cross-field transport, *Phys. Rev. Lett.*, *41*, 653, 1978.

Goldman, S. R., L. Baker, S. L. Ossakow, and A. J. Scannapieco, Striation formation associated with barium clouds in an inhomogeneous ionosphere, *J. Geophys. Res.*, *81*, 5097, 1976.

Kilb, R. W., Striation formation. Physics of High-Altitude Nuclear Bursts, *Rep. DNA 4501F*, Def. Nucl. Agency, Washington, D. C., 1977.

Knapp, W. S., and K. Schwartz, Aids for the study of electromagnetic blackout, *Rep. DNA 3499H*, p. 8-5. Def. Nucl. Agency, Washington, D. C., 1975.

Linson, L. M., and G. Meltz, Theory of ion dynamics and morphology. Analysis of Barium Clouds, *Rep. RADC-TR-72-736*, vol. 1, chap. 5, Avco Everett Res. Lab., Everett. Mass., 1972.

Linson, L. M., and J. B. Workman, Formation of striations in ionospheric clouds, *J. Geophys. Res.*, *75*, 3211, 1970.

McDonald, B. E., M. J. Keskinen, S. L. Ossakow, and S. T. Zalesak. Computer simulation of gradient drift instability processes in Operation Avefria, *J. Geophys. Res.*, *85*, 2143, 1980.

McDonald, B. E., S. L. Ossakow, S. T. Zalesak, and N. J. Zabusky. Scale sizes and lifetimes of F region plasma cloud striations as determined by the condition of marginal stability, *J. Geophys. Res.*, *86*, 5775, 1981.

Ossakow, S. L., S. T. Zalesak, B. E. McDonald, and P. K. Chaturvedi. Nonlinear equatorial spread F. Dependence on altitude of the F peak and bottomside background density gradient scale length, *J. Geophys. Res.*, *84*, 17, 1979.

Ott. E., Theory of Rayleigh-Taylor bubbles in the equatorial ionosphere, *J. Geophys. Res.*, *83*, 2066, 1978.

Scannapieco. A. J., and S. L. Ossakow. Nonlinear equatorial spread F, *Geophys. Res. Lett.*, *3*, 451, 1976.

Simon. A., Instability of a partially ionized plasma in crossed electric and magnetic fields. *Phys. Fluids*, *6*, 382, 1963.

Sperling, J. L., Role of Rayleigh-Taylor instabilities on prompt striation evolution. *J. Geophys. Res.*, *87*, 10,514, 1982.

Sperling, J. L., On the effect of finite, field-aligned plasma length on a loss-cone instability, *J. Geophys. Res.*, *88*, 927, 1983a.

Sperling, J. L., Finite parallel wavelengths and ionospheric structuring. *J. Geophys. Res.*, *88*, 4075, 1983b.

Sperling, J. L., The evanescence of striation parameters along the geomagnetic field, *J. Geophys. Res.*, *89*, 6793, 1984.

Sperling, J. L., and A. J. Glassman, Striation eigenmodes along the geomagnetic field and eigenvalues in the limit of strong ion-neutral collisions, *Rep. J530-83-135*, JAYCOR, San Diego, Calif., 1983.

Zalesak, S. T., and S. L. Ossakow, Nonlinear equatorial spread F. Spatially large bubbles resulting from horizontal scale initial perturbations, *J. Geophys. Res.*, *85*, 2131, 1980.

_____

J. F. Drake, University of Maryland, College Park, MD 20742

J. D. Huba and S. T. Zalesak, Geophysical and Plasma Dynamics Branch, Plasma Physics Division, Naval Research Laboratory, Code 4780, Washington, DC 20375

J. L. Sperling, JAYCOR, 11011 Torreyana Road, P. O. Box 85154, San Diego, CA 92138

APPENDIX N

Finite Temperature Stabilization of the
Gradient Drift Instability in Barium Clouds

FINITE TEMPERATURE STABILIZATION OF THE
GRADIENT DRIFT INSTABILITY IN BARIUM CLOUDS

J.F. Drake
Science Applications, Inc.
McLean, Virginia 22102

J.D. Huba and S.T. Zalesak
Geophysical and Plasma Dynamics Branch
Plasma Physics Division
Naval Research Laboratory
Washington, D.C. 20375

December 1984

Abstract

We present a relatively simple analysis of the gradient drift instability in barium clouds which includes the effects of both finite temperature and finite parallel length. It is found that short wavelength modes are stabilized as the electrons redistribute parallel to the magnetic field and neutralize the charge imbalance set up by the instability. An analytical expression for the critical wavenumber for stabilization is given, as well as numerical results. We discuss the application of these results to the structuring of barium clouds.

I. INTRODUCTION

The study of the dynamic evolution of artificial plasma clouds (e.g., barium clouds) in the earth's ionosphere and magnetosphere has been an active area of research for more than two decades. The initial motivation for these active space experiments was to use the plasma cloud as a diagnostic to determine ambient plasma conditions (e.g., electric fields, neutral winds). However, it was soon discovered that the interaction of an artificial plasma cloud and the near-earth space plasma was very complex, and that plasma clouds undergo a complicated and dynamic evolution. One of the prominent features of cloud evolution in the ionosphere is the development of field-aligned striations on the cloud's steepened "backside". These striations have been attributed to the onset of the gradient drift instability (Linson and Workman, 1970). This instability can occur in a weakly collisional plasma which contains a density gradient and a neutral wind (or ambient electric field) (Simon, 1963; Hoh, 1963).

A substantial amount of theoretical and computational research has been invested in understanding the linear and nonlinear development of the gradient drift instability and its relevance to plasma cloud structure (Volk and Haerendel, 1971; Perkins et al., 1973; Zabusky et al., 1973; Shiau and Simon, 1972; Perkins and Doles, 1975; Scannapieco et al., 1976; Chaturvedi and Ossakow, 1979; Keskinen et al., 1980; McDonald et al., 1980; McDonald et al., 1981; Huba et al., 1983). The bulk of analyses to date have neglected the effects of plasma dynamics parallel to the ambient magnetic field B_0 (i.e., considered perturbations only in the plane transverse to B_0) or have incorporated parallel effects in a crude way. Francis and Perkins (1975), for example, assume that the ambient and perturbed potentials map uniformly along B_0 thereby connecting the cloud

dynamics to that of the conducting background at different altitudes. In this model finite thermal effects have a stabilizing influence on short wavelength modes. However, several studies have been performed which attempt to include parallel dynamics self-consistently in the stability analysis (Goldman et al., 1976; Sperling and Glassman, 1984; Sperling et al., 1984). These studies incorporate the parallel length of the cloud along the ambient field into the stability analysis and have shown that parallel effects can play an important role in the development of the gradient drift instability as it relates to ionospheric plasma clouds.

In particular, Sperling et al. (1984) have recently shown that when the finite size of the cloud along $\underset{\sim}{B}_0$ is self-consistently incorporated in the linear stability analysis, the long wavelength modes tend to have much smaller growth rates than short wavelength modes. This reduction in growth due to finite cloud length occurs because the integrated Pedersen conductivity of the background plasma over the extent of the mode along the field becomes greater than the cloud. The distance the mode extends along the field is proportional to the perpendicular wavelength of the mode so that long wavelength modes are more strongly affected. However, this analysis neglected the effects of finite temperature. Sperling and Glassman (1984) included finite temperature in the analysis and found that short wavelength modes became propagating rather than purely growing modes. Moreover, for sufficiently short wavelengths there was some evidence that the modes were be completely stabilized. A drawback of this work though is that a relatively complex, second-order differential equation is solved numerically to obtain results. The underlying physics of the stabilization mechanism is therefore somewhat obscure and not addressed in the paper. Nonetheless, it is evident that finite temperature

and finite cloud length effects can impact the development of the gradient drift instability.

The purpose of this paper is to present a linear stability analysis of the gradient drift instability which incorporates both finite temperature and finite parallel length effects. A simple plasma model is used (similar to the one used in Sperling et al. (1984)) which permits an analytical solution to the dispersion equation. It is found that the short wavelength modes are stabilized by redistribution of electrons parallel to $\underset{\sim}{B}_0$ (i.e., parallel electron diffusion or parallel electron response to the perturbed fields) which neutralize the charge imbalance set up by the instability. An analytical expression for the critical wavenumber for the stabilization of instability is given, as well as numerical results.

The organization of the paper is as follows. In the next section we derive a set of general nonlinear equations which describe the evolution of a three dimensional plasma cloud. In Section III we discuss the equilibrium to be used in the instability analysis. In Section IV we derive a general dispersion equation, and present both analytical and numerical results. Finally, in the last section we summarize our findings and discuss the relevance of our results to cloud structure.

II. GENERAL EQUATIONS

We first derive a set of nonlinear equations to describe the evolution of a warm plasma cloud in a uniform magnetic field $\underset{\sim}{B} = B_0 \hat{z}$ with a background neutral wind $\underset{\sim}{V}_n = V_n \hat{x}$ [see Fig. 1a]. For simplicity we consider only low frequency $\partial/\partial t \ll \nu_\alpha$ motion of the cloud and take the electron collisions to be sufficiently weak so that $\nu_e/\Omega_e \ll 1$ but allow ν_i/Ω_i to be arbitrary. The collision frequency and gyrofrequency of

the α species are given by ν_α and Ω_α, respectively. Both electrons and ions are taken to be warm and for simplicity we consider the isothermal limit. In this case the fundamental equations of our analysis are continuity, momentum transfer, charge neutrality and Ampere's law:

$$\frac{\partial n}{\partial t} + \nabla \cdot \left(n \underset{\sim}{v}_e\right) = 0 \tag{1}$$

$$0 = -e\underset{\sim}{E} - \frac{e}{c} \underset{\sim}{v}_e \times \underset{\sim}{B} - m_e \nu_{en}\left(\underset{\sim}{v}_e - \underset{\sim}{V}_n\right) - m_e \nu_{ei}\left(\underset{\sim}{v}_e - \underset{\sim}{v}_i\right) - \frac{T_e}{n} \nabla n \tag{2}$$

$$0 = e\underset{\sim}{E} + \frac{e}{c} \underset{\sim}{v}_i \times \underset{\sim}{B} - m_i \nu_{in}\left(\underset{\sim}{v}_i - \underset{\sim}{V}_n\right) - m_i \nu_{ie}\left(\underset{\sim}{v}_i - \underset{\sim}{v}_e\right) - \frac{T_i}{n} \nabla n \tag{3}$$

$$\nabla \cdot \underset{\sim}{J} = \nabla \cdot \left[n\left(\underset{\sim}{v}_i - \underset{\sim}{v}_e\right)\right] = 0 \tag{4}$$

$$\nabla \times \underset{\sim}{B} = \frac{4\pi}{c} \underset{\sim}{J} \tag{5}$$

where $\underset{\sim}{v}_\alpha$ and T_α are the fluid velocity and temperature of species α, respectively, $\nu_{\alpha n}$ is the α specie-neutral collision frequency, ν_{ei} is the electron-ion collision frequency, ν_{ie} is the ion-electron collision frequency, and α refers to electrons (e) or ions (i). We take the electric and magnetic fields to be represented by potentials as

$$\underset{\sim}{E} = -\nabla \phi - \frac{1}{c} \frac{\partial A_z}{\partial t} \hat{z} \tag{6}$$

and

$$\underset{\sim}{B} = B_0 \hat{z} + \nabla A_z \times \hat{z} \tag{7}$$

where ϕ is the electrostatic potential and A_z is the vector potential associated with the magnetic field produced by the self-consistent plasma currents. We consider only A_z since $J_\parallel \gg J_\perp$ and assume $|\nabla A_z \times \hat{z}| \ll B_0$.

The electron cross-field motion is given by

$$\underset{\sim}{v}_{e\perp} = -\frac{c}{B} \nabla_\perp \phi \times \hat{z} + \frac{cT_e}{eBn} \nabla_\perp n \times \hat{z} \tag{8}$$

while the parallel motion is given by

$$v_{\parallel e} = -\left[eE_\parallel + T_e \nabla_\parallel \ln(n) + f(\nu_{ei}/\nu_{en})T\nabla_\parallel \ln(n)\right]/\left[m_e(\nu_e + f\nu_{ei})\right] \tag{9}$$

with

$$E_\parallel = -\nabla_\parallel \phi - \frac{1}{c}\frac{\partial A_z}{\partial t}, \tag{10}$$

where $\nu_e = \nu_{ei} + \nu_{en}$, $\nabla_\parallel = \hat{b} \cdot \nabla$, $\hat{b} = \underset{\sim}{B}/|\underset{\sim}{B}_0|$, and $T = T_e + T_i$. The assumption that $\nu_e/\Omega_e \ll 1$ while $\nu_{in}/\Omega_i \sim 1$ requires that $f \equiv m_e\nu_{en}/m_i\nu_{in} \ll 1$.

The ion cross-field motion is given by

$$\underset{\sim}{v}_{i\perp} = \delta_i\left[-\frac{c}{B}\nabla_\perp\phi \times \hat{z} + \frac{\nu_{in}}{\Omega_i}\underset{\sim}{V}_n \times \hat{z} - \frac{cT_i}{eBn}\nabla n \times \hat{z}\right.$$

$$\left. -\frac{\nu_{in}}{\Omega_i}\frac{c}{B}\nabla_\perp\phi + \left(\frac{\nu_{in}}{\Omega_i}\right)^2\underset{\sim}{V}_n - \frac{\nu_{in}}{\Omega_i}\frac{cT_i}{eBn}\nabla_\perp n\right], \tag{11}$$

where $\delta_i = \left(1 + \nu_{in}^2/\Omega_i^2\right)^{-1}$, and the parallel motion is given by

$$v_{\parallel i} = \left\{\left[eE_\parallel + T_e\nabla_\parallel \ln(n)\right]\nu_{en} - \nu_e T\nabla_\parallel \ln(n)\right\}/\left[m_i\nu_{in}(\nu_e + f\nu_{ei})\right]. \tag{12}$$

In (11) we have included both the Pedersen and Hall responses to the electric field, neutral wind and pressure.

Substituting (8)-(12) into (1), (4) and (5) we find that

$$\frac{dn}{dt} - \frac{c}{B} \nabla\hat{\phi} \times \hat{z} \cdot \nabla n + \nabla_\parallel \left(\frac{c}{4\pi e} \nabla_\perp^2 A_z - D_\parallel \nabla_\parallel n\right) = 0, \tag{13}$$

$$\delta_i \frac{c}{B} \frac{\nu_{in}}{\Omega_i} \nabla_\perp \cdot n\nabla_\perp\hat{\phi} + \delta_i \frac{c}{B} \frac{\nu_{in}^2}{\Omega_i^2} \hat{z} \times \nabla\hat{\phi} \cdot \nabla n + \frac{\nu_{in}}{\Omega_i} \hat{z} \times \underset{\sim}{V}_n \cdot \nabla n$$

$$+ D_\perp \nabla_\perp^2 n + \frac{c}{4\pi e} \nabla_\parallel \nabla_\perp^2 A_z = 0, \tag{14}$$

$$\nabla_\perp^2 A_z = \frac{4\pi}{c\eta_e} \left(\nabla_\parallel\hat{\phi} + \frac{1}{c} \frac{dA_z}{dt}\right), \tag{15}$$

where $\eta_e = m_e\nu_e/ne^2$ is the parallel resistivity, $D_\parallel = T/m_i\nu_{in}$ and $D_\perp = \delta_i\left(\nu_{in}/\Omega_i\right)cT/eB$ are the parallel and perpendicular ion transport coefficients, $T = T_e + T_i$, and

$$\hat{\phi} \equiv \phi - \frac{T_e}{e} \ln(n) - \frac{B}{c} \frac{\nu_{in}}{\Omega_i} \underset{\sim}{V}_n \cdot \underset{\sim}{x}, \tag{16}$$

$$\frac{d}{dt} \equiv \frac{\partial}{\partial t} + \frac{\nu_{in}}{\Omega_i} \hat{z} \times \underset{\sim}{V}_n \cdot \nabla, \tag{17}$$

$$\nabla_\parallel = \frac{\partial}{\partial z} + B_0^{-1} \nabla A_z \times \hat{z} \cdot \nabla. \tag{18}$$

Equation (13) is the electron continuity equation, (14) is the charge conservation equation and (15) is Ampere's law. Note that the electron

pressure has been absorbed into $\hat{\phi}$ in (16) and that terms of order $f \ll 1$ have been discarded compared with those of order unity. Equations (13)–(18) constitute a complete description of the evolution of a three-dimensional warm plasma cloud.

III. EQUILIBRIUM

We will consider the linear stability of a two-dimensional cloud which is localized both along and across the magnetic field $\underline{B}_0$: $n_c = n_c(x, z)$ with $n_c \neq 0$ for $|x| \lesssim x_c$ and $|z| \lesssim z_c$. The background plasma is taken to be uniform throughout the region $|z| < z_b$ between two insulating plates at $z = \pm z_b$. The location of the plates, enables us to control the ratio of the total magnetic-field-line integrated Pedersen conductivity of the cloud to that of the background, $n_c z_c / (n_c z_c + n_b z_b)$. This ratio is an important parameter of the equilibrium configuration.

The equations describing the two dimensional plasma cloud are given by

$$\frac{\partial n}{\partial t} - D_\parallel \frac{\partial^2 n}{\partial z^2} + \frac{c}{4\pi e} \frac{\partial}{\partial z} \frac{\partial^2 A_z}{\partial x^2} = 0, \tag{19}$$

$$\delta_1 \frac{c}{B} \frac{\nu_{in}}{\Omega_i} \frac{\partial}{\partial x} n \frac{\partial}{\partial x} \hat{\phi} + D_\perp \frac{\partial^2 n}{\partial x^2} + \frac{c}{4\pi e} \frac{\partial}{\partial z} \frac{\partial^2 A_z}{\partial x^2} = 0, \tag{20}$$

$$\frac{\partial^2 A_z}{\partial x^2} = \frac{4\pi}{c n_e} \left(\frac{\partial \hat{\phi}}{\partial z} + \frac{1}{c} \frac{\partial A_z}{\partial t} \right). \tag{21}$$

When there are no density gradients in the x direction, the solution to these equations is $\hat{\phi} = - (B/c) \left(\nu_{in} / \Omega_i \right) V_n x$ so that

$$\phi = \left(T_e / e \right) \ell n \left\lceil n(z)/n_b \right\rceil \tag{22}$$

with $A_z = 0$, i.e., the potential adjusts itself so that the electrons are in force balance along the magnetic field as the cloud diffuses along $\underset{\sim}{B}_0$. In writing the solution for ϕ in (22) we have required $\phi \to 0$ for $|z| > z_c$ since we have assumed that only the charge accumulations associated with the motion of the plasma cloud itself are responsible for the development of ϕ. There is no charge at $z = \pm z_b$. The density satisfies

$$\partial n/\partial t - D_{\parallel}\partial^2 n/\partial z^2 = 0 \qquad (23)$$

so that n diffuses along $\underset{\sim}{B}_0$. In the opposite limit, where there are no density gradients in the z direction ($\partial/\partial z = 0$), $A_z = 0$ and $\hat{\phi} = - (T/e)\ln(n) - (B/c)(\nu_{in}/\Omega_i)V_n \int_{-\infty}^{x}dx(n_b/n)$ so that

$$\phi = - \frac{T_i}{e} \ln[\frac{n(x)}{n_b}] + \frac{B}{c} \frac{\nu_{in}}{\Omega_i} V_n \int_{-\infty}^{x}dx(1 - \frac{n_b}{n}), \qquad (24)$$

where we have required $\phi \to 0$ as $|x| \to \infty$. In Eq. (24) the potential adjusts itself so that the perpendicular ion pressure gradient is balanced by the electrostatic field. In comparing the expressions for ϕ in (22) and (24), it is important to note that the electron and ion pressures push the potential in the opposite direction (compare the signs of the terms proportional to T_e and T_i).

We now return to the more general two dimensional equations in (19)–(21). These equations describe three time scales: the resistive flux diffusion time, $\tau_r = 4\pi x_c^2/\eta_e c^2$; the parallel diffusion time, $\tau_{\parallel} = z_c^2/D_{\parallel}$; and the perpendicular diffusion time, $\tau_{\perp} = x_c^2/D_{\perp}$. We assume that the flux

diffusion time is the shortest time scale so that inductive effects are not important in the equilibrium, i.e., in Eq. (21) $\partial A_z/\partial t \ll c\, \partial\hat{\phi}/\partial z$. The equations then simplify to

$$\frac{\partial n}{\partial t} - D_{\parallel} \frac{\partial^2 n}{\partial z^2} - D_{\perp} \frac{\partial^2 n}{\partial x^2} - \delta_i \frac{c}{B} \frac{\partial}{\partial x}\, n\, \frac{\partial\hat{\phi}}{\partial x} = 0, \tag{25}$$

$$\delta_i \frac{c}{B} \frac{\nu_{in}}{\Omega_i} \frac{\partial}{\partial x}\, n\, \frac{\partial\hat{\phi}}{\partial x} + \frac{1}{en_e} \frac{\partial^2\hat{\phi}}{\partial z^2} + D_{\perp} \frac{\partial^2 n}{\partial x^2} = 0. \tag{26}$$

Equation (25) governs the time evolution of n while (26) determines $\hat{\phi}$. For $z_b^2 \ll x_c^2\, \Omega_e\Omega_i/\nu_e\nu_{in}$, the second term in (26) is much larger than the remaining terms unless $\partial\hat{\phi}/\partial z \approx 0$. Thus, $\hat{\phi}$ is nearly constant along $\underset{\sim}{B}_0$. An equation for $\overline{\hat{\phi}}$ can then be obtained by averaging (25) and (26) along $\underset{\sim}{B}_0$. The resulting equations are

$$\partial\overline{n}/\partial t = 0 \tag{27}$$

$$\frac{\partial}{\partial x}\, \overline{n}\, \frac{\partial\overline{\hat{\phi}}}{\partial x} + \frac{T}{e} \frac{\partial^2\overline{n}}{\partial x^2} = 0 \tag{28}$$

where the average $\overline{p}$ of a function $p(z)$ is defined as

$$\overline{p} = \int_{-z_b}^{z_b} dz\, p(z)/2z_b. \tag{29}$$

Thus, the integrated density $\overline{n}$ is a constant in time. From (28), we obtain an expression for the potential,

$$\phi = \frac{T_e}{e}\, \ell n\, \left(\frac{n}{n_b}\right) - \frac{T}{e}\, \ell n\, \left(\frac{\overline{n}}{n_b}\right) + \frac{B}{c} \frac{\nu_{in}}{\Omega_i} V_n \int_{-\infty}^{x} dx \left(1 - \frac{n_b}{n}\right). \tag{30}$$

The first and second terms in (30) compete in forcing the potential to balance the parallel electron pressure and ion perpendicular pressure, respectively. In the limit in which n is constant along $\underset{\sim}{B}_0$, $\bar{n} = n$ and $\phi \sim - (T_i/e) \ln (n/n_b)$ so that ϕ balances the ion pressure. In opposite limit, where $z_b/z_c \rightarrow \infty$, $\bar{n} = n_b$ and $\phi \sim (T_e/e) \ln (n/n_b)$ so ϕ balances the electron pressure.

Finally, subtracting the field line average of (25) and (26) from itself, we obtain an equation for $\Delta n = n - \bar{n}$ and $\hat{\Delta \phi} = \hat{\phi} - \bar{\phi}$,

$$\frac{\partial \Delta n}{\partial t} - D_\parallel \frac{\partial^2 \Delta n}{\partial z^2} - D_\perp \frac{\partial^2 \Delta n}{\partial x^2} - \delta_i \frac{c}{B} \frac{\partial}{\partial x} \Delta n \frac{\partial \bar{\phi}}{\partial x} = 0,$$

$$\frac{1}{e \eta_e} \frac{\partial^2 \hat{\Delta \phi}}{\partial z^2} = - D_\perp \frac{\partial^2 \Delta n}{\partial x^2} - \delta_i \frac{c}{B} \frac{\nu_i}{\Omega_i} \frac{\partial}{\partial x} \Delta n \frac{\partial \bar{\phi}}{\partial x},$$

where $\hat{\Delta \phi} \ll \bar{\phi}$. The equation for Δn has no steady state solution so Δn will generally evolve on a time scale of order $\tau_\parallel \sim \tau_\perp$. The z dependent potential $\hat{\Delta \phi}$ drives an equilibrium current $J_z = \eta_e^{-1} \partial \hat{\Delta \phi}/\partial z$ which is required so that $\nabla \cdot \underset{\sim}{J} = 0$. The time variation of the equilibrium and the equilibrium parallel current J_z will be neglected when we carry out the linear stability analysis.

Specifically, in the linear stability analysis we formally take the limit $D_\parallel \rightarrow 0$ and choose

$$n(x,z) = \begin{cases} n_c(x) + n_b & |z| < z_c \\ \\ n_b & z_b > |z| > z_c \end{cases} \tag{31}$$

as shown in Fig. 1b. The perpendicular diffusion coefficient is retained in the stability analysis. The step function model for the density is valid as long as the parallel wavelengths of the modes of interest are much longer than the actual parallel equilibrium density scale length, i.e.,

$$k_\parallel^2 \, z_c^2 \ll 1.$$

The neglect of the equilibrium parallel current and parallel diffusion can similarly be justified for

$$k_\parallel J_z / ne \ll \omega$$

$$k_\parallel^2 D_\parallel \ll \omega,$$

When the electron parallel conductivity is large, $k_\parallel$ is typically quite small so that these inequalities are easily satisfied. Finally, the time evolution of the equilibrium should have a negligible influence on the stability analysis providing

$$|\gamma \tau_\parallel|, \ |\gamma \tau_\perp| \ll 1$$

where γ is the growth (damping) rate of the mode of interest.

IV. LINEARIZED EQUATIONS AND DISPERSION EQUATION

To determine the influence of finite temperature and parallel dynamics on the gradient drift instability we linearize (13)-(15) using the equilibrium discussed in the preceding section. We assume perturbed quantities to vary as $\tilde{p} \sim \tilde{p}(z) \exp(\gamma t + ik_y y)$. After eliminating $\tilde{n}$ algebraically from (13)-(15), we obtain two coupled differential equations for $\tilde{\phi}$ and $\tilde{A}_z$:

$$\left(\gamma + k_y^2 D_r\right)\tilde{A}_z = -c\frac{\partial \tilde{\tilde{\phi}}}{\partial z} \tag{32}$$

$$\left(\gamma - i\omega_* - \gamma_0\right)\tilde{\tilde{\phi}} = -\alpha D_r\left(\gamma - ik_y\overline{V}_i + k_y^2 D_\perp\right)\frac{1}{c}\frac{\partial \tilde{A}_z}{\partial z} \tag{33}$$

where $\overline{\gamma} = \gamma + i(c/B)k_y\hat{\phi}_0'$, $\tilde{\tilde{\phi}} = \tilde{\phi} - (T_e/e)\ln\tilde{n}$, $D_r = \nu_e c^2/\omega_{pe}^2$, $\overline{V}_i = (\nu_{in}/\Omega_i)\delta_i\overline{V}_n$, $\alpha = (\Omega_e/\nu_e)(\Omega_i/\nu_{in})\delta_i^{-1}$, $\omega_* = -k_y(cT/eB)(n_c'/n_c)$, $\overline{V}_n = V_n + (c/B)(\nu_{in}/\Omega_i)\hat{\phi}_0'$, $\gamma_0 = -(n_c'/n_c)\overline{V}_n$, and

$$\hat{\phi}_0' = \left(\frac{B}{c}\frac{\nu_{in}}{\Omega_i}V_n - \frac{T}{e}\frac{n_c'}{n_c}\right)\frac{n_c z_c}{n_c z_c + n_b z_b} \ .$$

In deriving (32) and (33) we have neglected parallel ion diffusion as discussed previously and assumed $n_c \gg n_b$. The primes denote a derivative with respect to x. The important finite temperature effects that appear in (32) and (33) are the diamagnetic drift frequency (ω_*), perpendicular ion diffusion $(D_\perp)$, and modification of the equilibrium $(\hat{\phi}_0')$. In the limit $T_i = T_e = 0$, Eqs. (32) and (33) reduce to those previously derived by Sperling et al. (1984). The eigenvalue $\overline{\gamma}$ is in a frame of reference moving with the electron fluid.

Prior to solving (32) and (33) for the density profile shown in Fig. 1b, we first consider a cloud of infinite extent $[z_c \to \infty]$ and Fourier expand in the direction parallel to $\underset{\sim}{B}_0$, i.e., $\tilde{p}(z) \sim \tilde{p} \exp[ik_z z]$. This allows insight into the influence of finite temperature and parallel dynamics on the instability. The local dispersion equation is given by

$$(\overline{\gamma} - i\omega_* - \gamma_0)(\overline{\gamma} + k_y^2 D_r) = -\frac{k_z^2 V_A^2}{\nu_{in}\delta_i}(\overline{\gamma} - ik_y\overline{V}_i + k_y^2 D_\perp), \tag{34}$$

where $V_A = B/(4\pi n m_i)^{1/2}$ is the Alfvén velocity. This dispersion relation illustrates the coupling between the gradient drift instability and the Alfvén wave when $k_z \neq 0$.

For simplicity, we neglect the terms in (34) which cause the mode to propagate $(\omega_r, k_y\overline{V}_i \to 0$ and $\overline{\gamma} \to \gamma)$ and note that $D_r \gg D_\perp$ in ionospheric applications. The growth rate can be easily obtained in two limits: in the electromagnetic limit $(\gamma \gg k_y^2 D_r)$,

$$\gamma = \gamma_0 - k_z^2 V_A^2/\nu_{in}\delta_i, \tag{35}$$

while in the electrostatic limit $(\gamma \ll k_y^2 D_r)$

$$\gamma = \left(\gamma_0 - \frac{k_z^2 T}{m_e \nu_e}\right)\left(\frac{k_y^2 D_r}{k_y^2 D_r + k_z^2 V_A^2/\nu_{in}\delta_i}\right) \tag{36}$$

The Alfvén wave has a stabilizing influence on the instability in the electromagnetic limit but thermal effects do not affect the growth rate.

Of course, the gradient drift instability is not stable when $k_z V_A^2 / \nu_{in} \delta_i >$ γ_0 as might be construed from (35) since the expression for γ given in (35) breaks down when $\gamma < k_y^2 D_r$. Thermal effects can have a significant influence on the growth rate when $\gamma < k_y^2 D_r$ (electrostatic limit). Namely, for

$$k_z^2 T / m_e \nu_e < \gamma_0, \tag{37}$$

the electrons can move a wavelength along $\underset{\sim}{B}$ during the growth time of the instability, and the mode is stable. In the limit of $k_z \to \infty$ in (36),

$$\gamma \approx - k_y^2 D_\perp \tag{38}$$

so that the mode damps at the ion diffusion rate.

The stabilization mechanism can be understood by examining the electron and ion density perturbations in the electrostatic limit,

$$\tilde{n}_e = \frac{\left(i k_y c n' / B + k_z^2 / e \eta_e \right)}{\gamma + k_z^2 T_e / m_e \nu_e} \tilde{\phi} \tag{39a}$$

$$\tilde{n}_i = \frac{\left[i k_y c n' / B - k_y^2 c \left(\nu_{in} / \Omega_i \right) n / B \right]}{\gamma + k_y^2 D_{\perp i} - i k_y V_n \nu_{in} / \Omega_i} \tilde{\phi} \tag{39b}$$

where $D_{\perp i} = \delta_i \left(\nu_{in} / \Omega_i \right) c T_i / eB$. In the limit $k_z = 0$, $\tilde{n}_e = \left(i k_y c n' / \gamma B \right) \tilde{\phi}$ and the usual growth rate of the instability is obtained by equating $\tilde{n}_e$ and $\tilde{n}_i$. In this case the density perturbation $\tilde{n}_e$ and the electric field perturbation, $\tilde{E}_y = - i k_y \tilde{\phi}$, are in phase and the usual physical description

of instability applies. However, in the limit of large k_z with $T_e \neq 0$, $\tilde{n}_e = n_0 e \tilde{\phi}/T_e$, i.e., the electrons are adiabatic and neutralize the ions by moving along $\underset{\sim}{B}$ rather than across $\underset{\sim}{B}$. In this case $\tilde{n}_e$ is out of phase with $\tilde{E}_y$ and there is no instability. When $T_e = 0$ and k_z is large, the mechanism is somewhat different although the mode is also stable. In this case, the electrons bunch parallel to $\underset{\sim}{B}$, and $\tilde{n}_e = (k_z^2/e n_e \gamma)\tilde{\phi}$. For k_z large the ions can only neutralize the electrons if $\gamma = - k_y^2 D_{\perp i} + i k_y V_n \nu_{in}/\Omega_i$. Namely, the electrons bunch parallel to $\underset{\sim}{B}$ and the ions diffuse across $\underset{\sim}{B}$ to neutralize the charge imbalance. Finally, we note that while electron parallel diffusion or ion perpendicular diffusion stabilizes the mode when the perturbation is periodic along $\underset{\sim}{B}$, when the spatial dependence of the mode is exponential, i.e., $\tilde{p}(z) \sim \tilde{p} \exp (\pm k_z z)$, the thermal effects are not stabilizing. The distinction between a periodic and a nonperiodic solution is important in interpreting the dispersion relation which is obtained for the equilibrium shown in Fig. 1b.

We now solve (32) and (33) for the profile given by (19). The boundary conditions used are $\tilde{\phi}$, $\tilde{A}_z \rightarrow 0$ as $|z| \rightarrow z_m$. For the step profile for $n(x,z)$ the solutions to (32) and (33) in the region $|z| > z_c$ can be written as plane waves

$$\tilde{A}_z = \tilde{A}_{zb} \exp \left[- k_b |z| \right] \tag{40a}$$

$$\tilde{\phi} = \tilde{\phi}_b \exp \left[- k_b |z| \right] \tag{40b}$$

with

$$(\gamma_b + k_y^2 D_{rb})\tilde{A}_{zb} = k_b c \tilde{\phi}_b \tag{40c}$$

$$k_b^2 = \frac{\overline{\gamma}(\gamma + k_y^2 D_r)}{\alpha\, D_r\left(\gamma + k_y^2 D_\perp\right)}\Bigg|_b \qquad\qquad (40d)$$

where the subscript b on a given parameter indicates that it is to be evaluated in the region $|z| > z_c$. Note that we have assumed $k_b z_b \gg 1$ and that solutions which diverge as z becomes large have been omitted from (40). This assumption is consistent with the approximation $z_b \ll \alpha^{1/2} x_c$ made in deriving the equilibrium potential ϕ as long as $k_b z_b \gg 1$.

In the region $|z| < z_c$ the solutions for $\hat{\phi}$ and $\tilde{A}_z$ are

$$\tilde{A}_z = \tilde{A}_{zc}^{\,1} \sin\left(k_c z\right) - \tilde{A}_{zc}^{\,2} \cos\left(k_c z\right) \qquad\qquad (41a)$$

$$\tilde{\phi} = \tilde{\phi}_c^{\,1} \cos\left(k_c z\right) + \tilde{\phi}_c^{\,2} \sin\left(k_c z\right) \qquad\qquad (41b)$$

with

$$\left(\gamma_c + k_y^2\, D_{rc}\right)\tilde{A}_{zc}^{\,1,2} = k_c c\, \tilde{\phi}_c^{\,1,2} \qquad\qquad (41c)$$

$$k_c^2 = -\frac{\left(\gamma - i\omega_* - \gamma_0\right)\left(\gamma + k_y^2 D_r\right)}{\alpha D_r\left(\gamma + k_y^2 D_\perp\right)}\Bigg|_c \qquad\qquad (41d)$$

We note that in writing (40d) and (41d) we have assumed $\overline{\gamma} \gg k_y \overline{V}_i$ for simplicity.

To complete the dispersion relation, we must match the various plane wave solutions at $z = \pm z_c$. The appropriate matching conditions are obtained from (32) and (33). Integrating these two equations across the discontinuity in the density at $z = \pm z_c$, we find that $\tilde{\phi}$ and $\tilde{A}_z$ must be continuous. For the even $\tilde{\phi}$ solution $\left(\tilde{\phi}_c^{\,2} = 0\right)$, we obtain the dispersion

continuous. For the even $\tilde{\phi}$ solution $\left(\tilde{\phi}_c^2 = 0\right)$, we obtain the dispersion equation

$$k_c z_c = \tan^{-1}\left[\frac{k_b}{k_c} \frac{\overline{\gamma} + k_y^2 D_{rc}}{\overline{\gamma} + k_y^2 D_{rb}}\right] + m\pi \qquad (42)$$

where m is an integer. The dispersion relation for the odd $\tilde{\phi}$ mode $\left(\tilde{\phi}_c^1 = 0\right)$ is similar to (42) except $\tan^{-1}$ is replaced by $-\cot^{-1}$. The result in (42) is identical to the dispersion relation obtained previously by Sperling et al. (1984) except that the expressions for k_b and k_c given in (40d) and (41d) now contain thermal effects which were previously neglected.

In general, the dispersion equation (42) has an infinite number of solutions for a given set of physical parameters, corresponding to eigenmodes with an increasing number of nodes (m) along z. The dispersion equation (42) can be solved numerically for arbitrary values of the background and cloud parameters. However, to gain an understanding of the general scaling of the growth rate γ with the parallel extent of the cloud and temperature, it is useful to solve (42) analytically. To do this we make a number of simplifying assumptions. We consider only the lowest order mode (i.e., m = 0 which implies $0 < k_c z_c < \pi/2$; it is easily shown that this mode has the largest growth rate); take ν_{in}/Ω_i to be small so that take all parameters but the density to be the same inside and outside of the cloud; assume $n_c \gg n_b$; and $\nu_{ei} \gg \nu_{en}$ so that the resistive diffusion coefficient is continuous across the boundary $z = z_c$ (i.e. $D_{rb} = D_{rc}$). With these assumptions the dispersion equation becomes

$$k_c z_c = \tan^{-1}\left(k_b/k_c\right) \qquad (43)$$

where

$$\frac{k_b}{k_c} = [\frac{n_b}{n_c} \frac{\overline{\gamma}}{\gamma_0 - \overline{\gamma} + i\omega_*}]^{1/2}. \tag{44}$$

In Sperling et al. (1984), the dispersion relation was carefully solved in all possible limits of the various parameters. In order to clearly emphasize the role of finite temperature in stabilizing short wavelength modes, we will focus our analysis primarily on modes with growth rates less than γ_0 for which $k_b/k_c \ll 1$. In this limit (43) becomes

$$k_c^2 z_c \approx k_b \tag{45}$$

or

$$n_c z_c (\overline{\gamma} - i\omega_* - \gamma_0) + n_b k_b^{-1} \overline{\gamma} = 0. \tag{46}$$

In the form shown in (46), the nature of the dispersion relation can be simply understood. The first (second) term is the magnetic field line integrated contribution from the cloud (background). The background contribution arises only from the region $|z| < k_b^{-1}$ since the perturbed potential $\widetilde{\phi}$ is small outside of this interval. The result in (46) can be directly obtained by integrating (33) for $\widetilde{\phi}$ along z.

The dispersion relation in (45) or (46) can be solved analytically for various values of k_y. In the limit $k_y \to 0$, $k_b^2 = \overline{\gamma}/cD_r$ and the dispersion relation is given by

$$(\gamma_0 - \bar{\gamma})^2 = \alpha \frac{n_b^2 D_r}{n_c^2 z_c^2} \bar{\gamma}, \tag{47}$$

and is independent of the plasma temperature. For $z_c^2 \gg \alpha D_r n_b^2/n_c^2 \gamma_0$,

$$\bar{\gamma} \approx \gamma_0 \tag{48}$$

while in the opposite limit $z_c^2 \ll \alpha D_r n_b^2/n_c^2 \gamma_0$,

$$\bar{\gamma} = \frac{\gamma_0^2 n_c^2 z_c^2}{\alpha n_b^2 D_r} . \tag{49}$$

These results have been obtained previously [Sperling et al. (1984)].

When k_y becomes very large, $k_b^2 \simeq \bar{\gamma}/\alpha D_\perp$ and the dispersion relation becomes

$$(\bar{\gamma} - i\omega_* - \gamma_0)^2 = \alpha D_\perp \frac{n_b^2}{n_c^2 z_c^2} \bar{\gamma}. \tag{50}$$

For large k_y, we have $\omega_* \gg \gamma_0$ since $\omega_* \propto k_y$ and therefore to lowest order

$$\bar{\gamma} = i\omega_*, \tag{51}$$

the mode simply propagates at the diamagnetic frequency. To investigate whether the mode is stable or unstable in this limit, corrections to this result must be calculated. These corrections arise from the right side of (50) and yield the eigenvalue

$$\bar{\gamma} = i\omega_* \pm \frac{n_b}{n_c z_c} \left(\alpha D_\perp \omega_* \right)^{1/2} e^{i\pi/4}. \tag{52}$$

Two significant features of (52) are first that γ_0 does not enter the equation, and second that there appears to be an instability even in the absence of γ_0. However, the unstable root is invalid. In order for $\tilde{\phi}$ to remain bounded as $|z|$ becomes large, we require $Re(k_b) > 0$. Thus, for $\bar{\gamma} = i\omega_*$ we find

$$k_b = \left(\omega_*/\alpha D_\perp\right)^{1/2} e^{i\pi/4}. \tag{53}$$

The root with the opposite sign must be discarded. Inserting this expression for k_b into (46), we obtain the damped root in (52). Thus, when thermal effects are retained, the gradient-drift mode is stable for large k_y.

The stabilization mechanism can be understood in terms of our earlier discussion of the local dispersion relation. When ω_* is discarded in (45) and (46), the parallel wavevector k_b remains real (the mode is evanescent in the outer region) and the instability survives even as $k_y \to \infty$. However, when ω_* is retained, the parallel wavevector k_b becomes complex (the mode is evanescent and propagating in the outer region) and the mode is stable for large k_y. In other words, ω_* causes the mode to become oscillatory along $\underset{\sim}{B}$, and the electrons can now move along rather than across $\underset{\sim}{B}$ to neutralize the ions; the mode is therefore stable.

To obtain an expression for the critical wavelength k_c where the mode becomes stable, we take $\bar{\gamma} = - i\omega_r$ and solve (46) directly. The critical wavelength is given by

$$k_c^2 \rho_s^2 = \frac{v_n^2}{c_s^2} \left[\left(1 + \frac{2n_c^2 z_c^2}{n_b^2} \frac{v_n}{\alpha D_\perp L_n}\right)^2 + \frac{4n_c^2 z_c^2}{n_b^2} \frac{\rho_s^2 c_s^2}{\alpha D_\perp^2 L_n^2} \right] \tag{54}$$

with

$$\omega_r = \omega_* \left(1 + \frac{n_c^2}{n_b^2} \frac{2\gamma_0 z_c^2}{\omega D_\perp}\right)^{-1} \tag{55}$$

where $L_n = -\left(n_c'/n_c\right)^{-1}$ and $\rho_s = c_s/\Omega_i$ is the Larmor radius based on the sound speed $c_s = \left(T/m_i\right)^{1/2}$. Note from (54) that in the limit $T \to 0$, then $k_c \to \infty$ so the mode is not stabilized for a zero temperature plasma [Sperling et al. (1984)]. Equation (54) also appears to imply that k_c becomes very large as the integrated cloud density n_c increases. This result is misleading. In a cloud which is finite in the y direction, the neutral wind velocity V_n in (54) should be replaced by the effective slip velocity V_{eff} of the cloud and the neutral wind. For a circular cloud, the effective velocity is given by [Ossakow and Chaturvedi, 1978]

$$V_{eff} = 2V_n \, n_b z_b / \left(n_b z_b + n_c z_c\right). \tag{56}$$

In the limit of very large $n_c z_c$, Eq. (54) yields the critical wavelength

$$k_c^2 L_n^2 = \frac{4V_n^2 z_b^2}{2D_\perp^2} \left(1 + \frac{4z_b^2 V_n^2}{\alpha \rho_s^2 c_s^2}\right), \tag{57}$$

which is independent of $n_c z_c$. Thus, short wavelength modes are stable even in large ionospheric clouds.

V. NUMERICAL RESULTS

We now present quantitative results for the wave frequency of the gradient drift instability by solving (43) numerically. In Fig. 2 we plot γ/γ_0 (solid curve) and ω_r/γ_0 (dashed curve) vs. $k_y\rho_s$ where $\omega = \omega_r + i\gamma$ is the wave frequency. We consider the following typical parameters for a barium cloud at 180 km: $n_c/n_b = 10.0$, $T_e = T_i = 0.1$ eV, $m_i = 16\ m_p$ (O^+ background), $z_c = 10$ km, $B = 0.3$ G, $\alpha = 10^6$, $D_\perp = 100$ m^2/sec, $V_n = V_{eff} = 20$ m/sec and $L_n = 1$ km. From these values we note that $c_s = 10^3$ m/sec and $\rho_s = 6$ m. The main features of Fig. 2 are described as follows. First, the growth rate has a maximum value at $k_y\rho_s = k_{ym}\rho_s = 0.08$. For $k_y < k_{ym}$ the growth rate decreases because of coupling to the background plasma as described in Sperling et al. (1984). For $k_y > k_{ym}$ the growth rate decreases rapidly and becomes stable (i.e., $\gamma < 0$). This is due to parallel electron motion as described in the preceding section and is the dominant finite temperature effect. Second, the critical wavenumber for stabilization as given by (54) is denoted by the arrow along the $k_y\rho_s$ axis ($k_y\rho_s \simeq 0.26$). It is seen that (54) gives a very good approximation to the critical wavenumber obtained numerically ($k_y\rho_s = 0.28$). For the parameters used the critical wavelength is given by $\lambda_c \simeq 135$ m. Third, the real frequency is linear in k_y and is proportional to the diamagnetic drift velocity $V_d = (cT/eB)(n_c'/n_c)$.

The results shown in Fig. 2 appear to be in qualitative agreement with the numerical work of Sperling and Glassman (1984). They consider a plasma cloud with a Gaussian distribution along the magnetic field rather than a waterbag model. The shape of the curve of γ vs k_y shown in Fig. 2 is similar to corresponding curves presented in their report. Moreover, they also find that $\omega_r \propto k_y$ for large k_y.

VI. CONCLUDING REMARKS

We have presented a relatively simple analysis of the gradient drift instability in barium clouds which includes both finite temperature and finite parallel length effects. We have derived a general set of nonlinear equations which describe the evolution of a three dimensional plasma cloud in the ionosphere. We then investigate the stability of a two dimensional plasma cloud in which the density varies in the direction of the neutral wind and along the ambient magnetic field $\underset{\sim}{B}_0$. By modeling the density variation along $\underset{\sim}{B}_0$ as a waterbag, we are able to obtain an analytic dispersion relation for the gradient drift instability. There is no static equilibrium since the cloud diffuses both perpendicular and parallel to $\underset{\sim}{B}_0$ so that we restrict our analysis to time scales short compared to the cloud diffusion time scales.

In recent work Sperling et al. (1984) found that the finite length of the cloud suppressed the growth of long wavelength modes because of "good" coupling to the background plasma. However, the growth rate of short wavelength modes is unaffected by the finite size of the cloud since they do not couple to the background in a zero temperature plasma. In contrast to this result, we find that in a finite temperature plasma the short wavelength modes do couple to the background plasma and that for sufficiently short wavelengths the modes are completely stabilized. Stabilization results as the electrons redistribute parallel to $\underset{\sim}{B}_0$ and neutralize the charge imbalance set up by the instability. The parallel electron motion results from diffusion and/or the response to the perturbed fields. We have also derived a simple analytic expression (see (54)) for the wavenumber corresponding to marginal stability (i.e., $\gamma = 0$). Our results are consistent with previous numerical computations of Sperling and

Glassman (1984) who also noted the importance of finite temperature on the stability of the gradient drift mode.

The extent to which the work described here may have relevance to the barium cloud "freezing" phenomenon deserves some discussion. Briefly, it is observed that barium ion clouds released at ionospheric altitudes will, through the nonlinear evolution of the gradient drift instability, break into smaller pieces. This process, known as bifurcation, continues until a certain minimum transverse dimension is reached, at which point further bifurcation ceases. This frozen scale size is observed to be approximately 400 m. Simple two dimensional models of barium cloud evolution fail to explain frozen scale sizes this large [McDonald et al, 1981]. One explanation which has been advanced to explain freezing is that of end-shorting [Francis and Perkins, 1975; Zalesak et al., 1984] which takes into account the distribution of plasma along magnetic field lines, finite plasma temperature, and parallel currents, as we have done here. However end-shorting depends on the "mapping" of transverse electric fields over relatively large distances along $\underset{\sim}{B}$; this becomes increasingly more difficult as k increases. Indeed, as shown here, and in Sperling et al. (1984), end-shorting fails to provide stabilization of the very high k modes (at least for the simple profiles of n_c, n_b and ν_{in} considered). If nothing else, the present work shows the existence of a viable stabilization mechanism (i.e., finite temperature) in the gap missed by the end-shorting mechanism. It should also be pointed out, however, that we are not that far removed (135 m stabilization wavelength) from offering a mechanism that by itself may stabilize a 400 m diameter barium striation.

<div align="center">ACKNOWLEDGMENT</div>

REFERENCES

Chaturvedi, P.K., and S.L. Ossakow, Nonlinear stabilization of the E B gradient drift instability in ionospheric plasma clouds, J. Geophys. Res., 84, 419, 1979.

Francis, S.H., and F.W. Perkins, Determination of striation scale sizes for plasma clouds in the ionosphere, J. Geophys. Res.. 80, 3111, 1975.

Goldman, S.R., L. Baker, S.L. Ossakow, and A.J. Scannapieco, Striation formation associated with barium clouds in an inhomogeneous ionosphere, J. Geophys. Res., 81, 5097, 1976.

Hoh, F.C., Instability of Penning-type discharges, Phys. Fluids, 6, 1184, 1963.

Huba, J.D., S.L. Ossakow, P. Satyanarayana, and P.N. Guzdar, Linear theory of the E × B instability with an inhomogeneous electric field, J. Geophys. Res., 88, 425, 1983.

Keskinen, M.J., S.L. Ossakow, and P.K. Chaturvedi, Preliminary report of numerical simulations of intermediate wavelength E × B gradient drift instability in ionospheric plasma clouds, J. Geophys. Res., 85, 3485, 1980.

Linson, L.M., and J.B. Workman, Formation of striations in ionospheric plasma clouds, J. Geophys. Res., 75, 321, 1970.

McDonald, B.E., M.J. Keskinen, S.L. Ossakow, and S.T. Zalesak, Computer simulation of gradient drift instability processes in Operation Avefria, J. Geophys. Res., 85, 2143, 1980.

McDonald, B.E., S.L. Ossakow, S.T. Zalesak, and N.J. Zabusky, Scale sizes and lifetimes of F region plasma cloud striations as determined by the condition of marginal stability, J. Geophys. Res., 86, 5775, 1981.

Ossakow, S.L. and P.K. Chaturvedi, Morphological studies of rising equatorial spread F bubbles, J. Geophys. Res., 83, 2085, 1978.

Perkins, F.W., and J.H. Doles III, Velocity shear and the E × B instability, J. Geophys. Res., 80, 211, 1975.

Perkins, F.W., N.J. Zabusky, and J.H. Doles III, Deformation and striation of plasma clouds in the ionosphere, 1, J. Geophys. Res., 78, 697, 1973.

Scannapieco, A.J., S.L. Ossakow, S.R. Goldman, and J.M. Pierre, Plasma cloud late time striation spectra, J. Geophys. Res., 81, 6037, 1976.

Shiau, J.N., and A. Simon, Onset of striations in barium clouds, Phys. Rev. Lett., 29, 1664, 1972.

Simon, A., Instability of a partially ionized plasma in crossed electric and magnetic fields, Phys. Fluids, 6, 382, 1963.

Sperling, J.L., and A.J. Glassman, Striation eigenmodes along the geomagnetic field and eigenvalues in the limit of strong ion-neutral collisions, JAYCOR Report J530-83-135, JAYCOR, San Diego, CA, 1983.

Sperling, J.L., J.F. Drake, S.T. Zalesak, and J.D. Huba, "The role of finite parallel length on the stability of barium clouds," submitted to J. Geophys. Res., 1984.

Volk, H.J., and G. Haerendel, Striation in ionospheric clouds, J. Geophys. Res., 76, 454, 1971.

Zabusky, N.J., J.H. Doles III, and F.W. Perkins, Deformation and striation of plasma clouds in the ionosphere, 2, Numerical simulation of a nonlinear two-dimensional model, J. Geophys. Res., 78, 711, 1973.

Zalesak, S.T., P.K. Chaturvedi, S.L. Ossakow, and J.A. Fedder, Finite temperature effects on the evolution of ionospheric barium clouds in the presence of a conducting background ionosphere I. A high altitude incompressible background ionosphere, _Memo Report 5346_, Naval Res. Lab., Washington, D.C., July 1984.
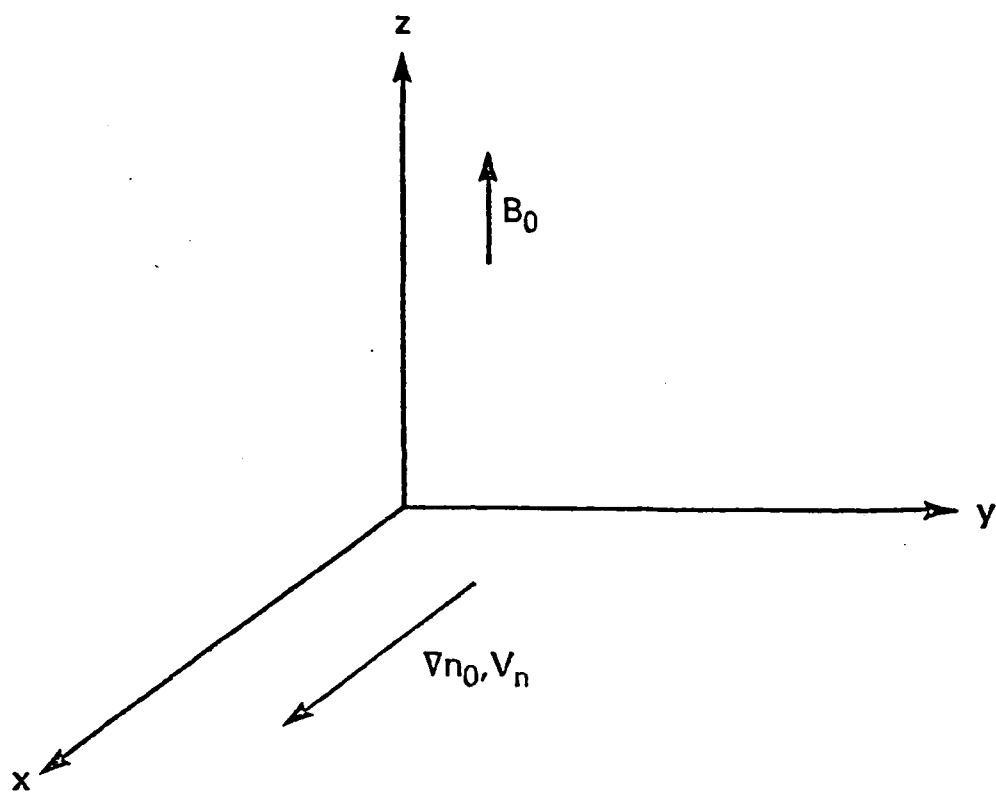
FIGURE CAPTIONS
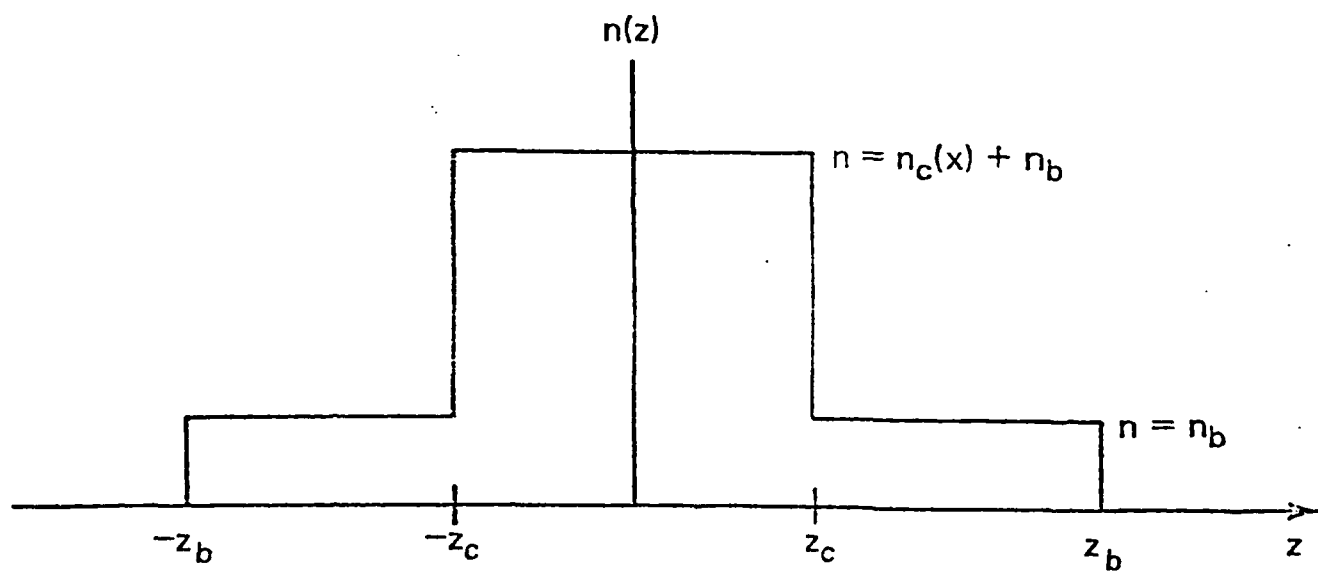
Fig. 1 Slab geometry and plasma model used in the analysis.

    (a) Geometry and plasma configuration.
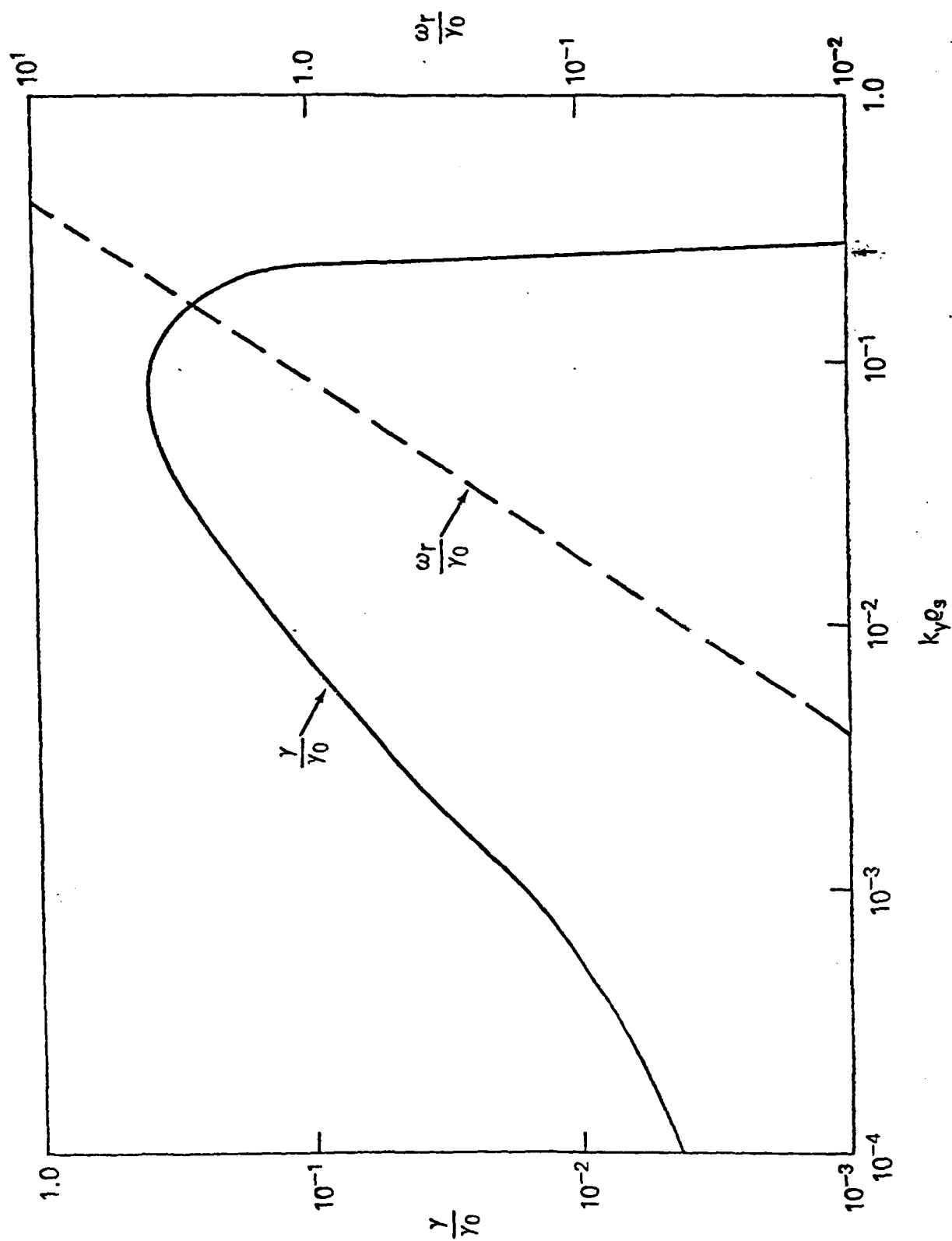
    (b) Cloud and background density profile.

Fig. 2 Plot of ω_r/ω_0 (dashed curve) and γ/γ_0 (solid curve) vs. $k_y\rho_s$ where $\omega = \omega_r + i\gamma$. Parameters used are described in text.

(a)

(b)

APPENDIX O

Finite Temperature Effects on the Evolution of

Ionospheric Barium Clouds in the Presence of a

Conducting Background Ionosphere

I. A High Altitude Incompressible Background Ionosphere

Finite Temperature Effects on the Evolution of Ionospheric Barium Clouds in the Presence of a Conducting Background Ionosphere

I. A High Altitude Incompressible Background Ionosphere

S. T. ZALESAK, P. K. CHATURVEDI,*
S. L. OSSAKOW, AND J. A. FEDDER

Geophysical and Plasma Dynamics Branch
Plasma Physics Division

*Science Applications, Inc.
McLean, VA 22102

July 24, 1984

NAVAL RESEARCH LABORATORY
Washington, D.C.

REPORT DOCUMENTATION PAGE

1a REPORT SECURITY CLASSIFICATION UNCLASSIFIED	1b RESTRICTIVE MARKINGS
2a SECURITY CLASSIFICATION AUTHORITY	3 DISTRIBUTION AVAILABILITY OF REPORT
2b DECLASSIFICATION DOWNGRADING SCHEDULE	Approved for public release; distribution unlimited.

4 PERFORMING ORGANIZATION REPORT NUMBER(S) NRL Memorandum Report 5346	5 MONITORING ORGANIZATION REPORT NUMBER(S)

6a NAME OF PERFORMING ORGANIZATION Naval Research Laboratory	6b OFFICE SYMBOL (If applicable) Code 4780	7a NAME OF MONITORING ORGANIZATION
6c ADDRESS (City, State and ZIP Code) Washington, DC 20375		7b ADDRESS (City, State and ZIP Code)

8a NAME OF FUNDING/SPONSORING ORGANIZATION Defense Nuclear Agency	8b OFFICE SYMBOL (If applicable)	9 PROCUREMENT INSTRUMENT IDENTIFICATION NUMBER

8c ADDRESS (City, State and ZIP Code) Washington, DC 20305	10 SOURCE OF FUNDING NOS			

10 SOURCE OF FUNDING NOS			
PROGRAM ELEMENT NO	PROJECT NO	TASK NO	WORK UNIT NO
62715H			DN580-072

11 TITLE (Include Security Classification)
(See page ii)

12 PERSONAL AUTHOR(S)
Zalesak, S.T., Chaturvedi, P.K.,* Ossakow, S.L.. and Fedder. J.A.

13a TYPE OF REPORT Interim	13b TIME COVERED FROM 10/83 TO 10/84	14 DATE OF REPORT (Yr., Mo., Day) July 24, 1984	15 PAGE COUNT 55

16 SUPPLEMENTARY NOTATION

*Science Applications Inc., McLean, VA 22102   (Continues)

17 COSATI CODES			18 SUBJECT TERMS (Continue on reverse if necessary and identify by block number)
FIELD	GROUP	SUB GR	Barium clouds Ionospheric barium clouds Striations Plasma clouds Bifurcation of barium clouds

19 ABSTRACT (Continue on reverse if necessary and identify by block number)

We show that under realistic ionospheric conditions, barium ion clouds hundreds of meters in diameter can be long-lived, quasi-stable, nonbifurcating structures. These structures may resemble "tadpoles," with a dense head, steep density gradients at the front, and a long, less dense tail. We assume that these structures are the final products of the recursive bifurcation of a considerably larger barium ion cloud, i.e., striations. The realistic ionospheric conditions to which we refer consist of a barium ion cloud with ion temperatures T_i of approximately $1000°$ K, coupled electrically to a background ionosphere of lower compressibility than itself, i.e., and F region. We show analytically that this combination of finite T_i and relatively incompressible background results in an effective diffusion of barium plasma, but more importantly, of total magnetic-field-line-integrated Pedersen conductivity Σ_p. The diffusion coefficient has a special form which allows the inner portions of the cloud to diffuse slowly, giving the cloud a long lifetime,

(Continues)

20 DISTRIBUTION AVAILABILITY OF ABSTRACT UNCLASSIFIED UNLIMITED X SAME AS RPT ☐ DTIC USERS ☐	21 ABSTRACT SECURITY CLASSIFICATION UNCLASSIFIED	
22a NAME OF RESPONSIBLE INDIVIDUAL S. T. Zalesak	22b TELEPHONE NUMBER (Include Area Code) (202) 767-3215	22c OFFICE SYMBOL Code 4780

DD FORM 1473, 83 APR   EDITION OF 1 JAN 73 IS OBSOLETE

11. TITLE (Include Security Classification)

Finite Temperature Effects on the Evolution of Ionospheric Barium Clouds in the Presence of a
Conducting Background Ionosphere
I. A High Altitude Incompressible Background Ionosphere

16. SUPPLEMENTARY NOTATION (Continued)

19. ABSTRACT (Continued)

and allows the outer, less dense portions of the cloud to diffuse rapidly, preventing cloud bifurcation.
Numerical simulations of the full nonlinear dynamics are then used to show that this diffusion does in
fact give rise to quasi-stable barium striations hundreds of meters in diameter. These findings are
consistent with the linear analysis of *Francis and Perkins* (1975).

CONTENTS

FINITE TEMPERATURE EFFECTS ON THE EVOLUTION OF IONOSPHERIC BARIUM CLOUDS IN THE PRESENCE OF A CONDUCTING BACKGROUND IONOSPHERE

I. A High Altitude Incompressible Background Ionosphere

1. Introduction

The nonlinear evolution of an artificial plasma cloud (e.g., a barium ion cloud) released in the earth's ionosphere is characterized by an overall bulk $\underline{E} \times \underline{B}$ motion, a one-sided steepening of plasma gradients, and by bifurcation [see Ossakow, 1979; Ossakow et al., 1982 and references therein] a process which we define here to mean the splitting of the cloud into two or more pieces. These pieces are sometimes referred to as "striations". All of the above motion and the resultant plasma structures are observed to be magnetic-field-aligned. That is, the plasma motion parallel to magnetic field lines consists primarily of diffusion and falling, while the perpendicular plasma motion is virtually identical for all plasma along a given field line. Hence one's best view of the structuring of the cloud is from a vantage point looking parallel to the magnetic field $\underline{B}$. This simplified description of barium cloud dynamics, seen along a line of sight parallel to $\underline{B}$, is depicted in Fig. 1. The sequence of drifting, steepening and bifurcating is, for sufficiently large striations, recursive: each striation becomes a new cloud which in turn forms its own striations. In the absence of some dissipative mechanism, it is believed that this process would continue indefinitely. In reality, the striation size becomes small enough to be comparable to the characteristic scale lengths of physical dissipation mechanisms, and further bifurcation ceases. A previous study by McDonald et al. [1981] attempted to quantify this concept within the context of a "one-level model", a mathematical model in which all conducting plasma was constrained to lie in a single two-dimensional plane perpendicular to the magnetic field. Implicit in

this model is the assignment of a single Pedersen mobility and hence compressibility to both the barium and background ionospheric plasma. In this model, the leading candidate for a dissipative mechanism is the ambipolar diffusion of electrons caused by electron-ion collisions. Using this mechanism, McDonald et al. [1981] calculated final unbifurcating striation sizes (from a so-called U shaped curve) for barium clouds of ~ 20 m (perpendicular to B). However, there is experimental evidence for the existence of long-lived "blobs" of plasma several hundred meters in diameter. The apparent stability of such large plasma structures has yet to find a satisfactory explanation within the one-level model. Ossakow et al. [1981] proposed including a zero temperature second level compressible background ionosphere below the cloud (see Scannapieco et al., 1976). This would allow image striations to build up and allow the conductivity in a striation to be amplified. This in turn would allow for larger conductivity ratios than if one had just a one level cloud. In turn, this could result in kilometer size unbifurcating striations by extrapolating the U shaped curve of McDonald et al. [1981] to higher conductivity ratios.

Here we postulate that the existence of a conducting background plasma with ion Pedersen mobility different from that of the barium plasma, combined with the finite temperature of the barium plasma, may allow the existence of stable striations with scale sizes of hundreds of meters. The essence of the mechanism is a phenomenon commonly referred to as "end shorting" first investigated in the context of barium clouds by Shiau and Simon [1974], who considered a completely incompressible background ionosphere, and showed that the normal electron ambipolar diffusion rates would be replaced by some fraction of the much higher ion diffusion rates caused by collisions of ions with neutrals. Francis and Perkins [1975] generalized the work of Shiau and Simon [1974] by

considering the cases of both incompressible and compressible background ionospheres. They concurred with Shiau and Simon [1974] that incompressible backgrounds exert a stabilizing influence, but noted that compressible backgrounds are destabilizing. In contrast, Vickrey and Kelley [1982] concluded that a background (compressible) E region should exert a stabilizing influence on high latitude irregularities. We shall address the question of the correctness of the above two analyses in a later paper. For the moment we note that: 1) Francis and Perkins [1975] performed a rigorous stability analysis of the problem; Vickrey and Kelley [1982] did not; 2) Francis and Perkins [1975] self-consistently included image formation (compressibility) in both the cloud and the background; Vickrey and Kelley [1982] did not (they took a passive load model); 3) Vickrey and Kelley [1982] included recombination chemistry; Francis and Perkins [1975] did not.

Our own conclusions are based on our view of barium cloud dynamics as consisting of a two-stage feed-back loop:

1) At any given time, the distribution of plasma density will, through the effect of these distributions on magnetic-field-line integrated Pedersen and Hall conductivities, bring about the creation of polarization electric fields whose purpose it is to maintain quasi-neutrality;

2) these electric fields, through Hall and Pedersen mobilities, affect the velocity of the plasma, which in turn affects the distribution of plasma density at the next instant of time.

We emphasize that it is only through its influence on magnetic-field-line integrated Pedersen and Hall conductivities that a change in plasma distribution [e.g., diffusion] will affect the polarization fields, which are the engine of plasma structure.

In the present study we have isolated the "enhanced" difusive effects (due to finite temperature effects and a two level model, where only ion-neutral collisions are included) on barium cloud striation evolution. A major conclusion derived from the nonlinear numerical simulation results presented here is that coupling to a nearly incompressible background ionosphere, i.e., an F region, can result in a cessation of striation bifurcation in F region ionospheric barium clouds.

In addition, a simplified analysis of the equation for the time evolution of the total field line integrated Pedersen conductivity shows that coupling to a compressible background ionosphere, i.e., E region, would result in destabilization of the striations (see Eq. (4-36) and the discussion following). Both of these results are consistent with the linear analysis of Francis and Perkins [1975].

In section 2 we describe the motion of ionospheric plasma and in section 3 the mathematical model is presented. Section 4 presents a simplified two level model. Section 5 describes the diffusion characteristics for a simplified two level model with a nearly incompressible background. Numerical simulation results using an incompressible background are presented in section 6. Section 7 presents the conclusions and thoughts on future work.

2. The Motion of Ionospheric Plasma

We shall be concerned here with the motion of plasma consisting of ions and electrons in the presence of a neutral gas and magnetic field $\underline{B}$, subject to an external force. We shall also be interested in the electric current $\underline{J}$ arising from the differential motion of the various species comprising the plasma. In the course of deriving the equations we make the following assumptions:

1) We assume the plasma can be adequately described by the fluid approximation. This assumes that the effective collision rate of each plasma species with itself is sufficiently high to maintain near Maxwellian distribution functions on time scales short compared to the times of interest, and is well satisfied for the plasmas we treat here.

2) We assume that the electric fields $\underline{E}$ are electrostatic (i.e., $\nabla \times \underline{E} = 0$) and hence can be described using a scalar potential ϕ such that $\underline{E} = -\nabla\phi$. Note that this implies $\partial\underline{B}/\partial t = 0$. The validity of this assumption can be related to the fact that the Alfven velocity is much larger than any other propagation speed of interest for the plasmas we treat here. The assumption is also checked a posteriori by verifying that the calculated currents and displacement currents produce negligible time variations in $\underline{B}$ which in turn produce negligible $\nabla \times \underline{E}$.

3) We assume plasma quasi-neutrality; that is,

$$\sum n_i q_i = n_e e \qquad (2.1)$$

where n is the number density, q is ion species charge, e is the electron charge, the subscripts i and e refer to ions and electrons respectively, and the sum is taken over all ion species. This assumption is a statement

that the Debye length is small compared to all length scales of interest, and again can be verified a posteriori by evaluating $\nabla \cdot \underline{E}$. Note that this assumption implies that $\nabla \cdot \underline{J} = 0$, where $\underline{J}$ is the electric current.

In addition to the above there are some other assumptions which, while they are not essential to the basic model, are nonetheless valid for many of the physical situations which we shall treat and impart a simplicity which we shall find convenient here.

4) We assume the electrostatic potential ϕ to be constant along magnetic field lines. As we shall see later, the electrical conductivity along magnetic field lines is much greater than that perpendicular to magnetic field lines, meaning that appreciable differences in potential along a field line will quickly be reduced by the resultant current. This assumption will break down for sufficiently small scale lengths perpendicular to the magnetic field, and for sufficiently large distances along the magnetic field.

5) We assume that the inertial terms in the plasma species momentum equations, i.e., the left hand side of Equation (2.3), are negligible with respect to the other terms in the equation. This assumption is justified whenever the time scales of interest are longer than the mean time between collisions for ions.

6) We neglect collisions between ions and electrons and between ions of different species. Later we shall also neglect collisions of electrons with neutrals. There are two reasons for this. First, the ion-neutral collision term ν_{in} can be shown to be the dominant term in the diffusion physics we consider here. (One must be careful, however, since these same assumptions will yield zero diffusion when the background conductivity is set to zero. To obtain the correct electron ambipolar rate in this limit,

the electron-ion and electron-neutral collision terms must be retained. We are not interested in this limit in this paper). Second, although exact closed form expressions for the ion and electron velocities in terms of the applied forces is possible when ion-electron collisions are retained [Fedder, 1980], the expressions are considerably more complex than those given below.

The continuity and momentum equations describing a single ion species and its associated electrons are:

$$\frac{\partial n_\alpha}{\partial t} + \nabla \cdot (n \underline{v}_\alpha) = 0 \tag{2.2}$$

$$(\frac{\partial}{\partial t} + \underline{v}_\alpha \cdot \nabla)\underline{v}_\alpha = \frac{q_\alpha}{m_\alpha} (\underline{E} + \frac{\underline{v}_\alpha \times \underline{B}}{c}) - \nu_{\alpha n}(\underline{v}_\alpha - \underline{U}_n)$$

$$- \frac{\nabla P_\alpha}{n_\alpha m_\alpha} + \underline{g} \tag{2.3}$$

where the subscript α takes on values i and e (denoting ions and electrons, respectively), n is the number density, $\underline{v}$ is the fluid velocity, P is pressure, $\underline{E}$ is the electric field, $\underline{g}$ is the gravitational acceleration, q is the charge, $\nu_{\alpha n}$ is the collision frequency with the neutral gas, $\underline{U}_n$ is the neutral wind velocity, c is the speed of light, and m is the particle mass. We can rewrite this equation as

$$\underline{F}_\alpha/m_\alpha + \frac{q_\alpha}{m_\alpha c} (\underline{v}_\alpha \times \underline{B}) - \nu_{\alpha n} \underline{v}_\alpha = 0 \tag{2.4}$$

where

$$\underline{F}_\alpha \equiv q_\alpha \underline{E} + m_\alpha g + \nu_{\alpha n} m_\alpha \underline{U}_n - \nabla P_\alpha / n_\alpha$$

$$- (\frac{\partial}{\partial t} + \underline{v}_\alpha \cdot \nabla) \underline{v}_\alpha m_\alpha \qquad (2.5)$$

If we place ourselves in a Cartesian coordinate system in which $\underline{B}$ is aligned along the z axis, and if we treat $\underline{F}_\alpha$ as a given quantity then a componentwise evaluation of Equation (2.4) yields a set of three equations in three unknowns, the three components of $\underline{v}_\alpha$. The formal solution is

$$\underline{v}_{\alpha\perp} = k_{1\alpha} \underline{F}_{\alpha\perp} + k_{2\alpha} \underline{F}_{\alpha\perp} \times \hat{\underline{z}} \qquad (2.6)$$

$$\underline{v}_{\alpha\parallel} = k_{0\alpha} \underline{F}_\parallel \qquad (2.7)$$

where

$$k_{1\alpha} = \frac{\nu_{\alpha n}}{\Omega_\alpha} \frac{c}{|q_\alpha B|} \left[1 - \frac{(\nu_{\alpha n}/\Omega_\alpha)^2}{1 + (\nu_{\alpha n}/\Omega_\alpha)^2} \right] \qquad (2.8)$$

$$k_{2\alpha} = \frac{c}{q_\alpha B} \left[1 - \frac{(\nu_{\alpha n}/\Omega_\alpha)^2}{1 + (\nu_{\alpha n}/\Omega_\alpha)^2} \right] \qquad (2.9)$$

$$k_{0\alpha} = (m_\alpha \nu_{\alpha n})^{-1} \qquad (2.10)$$

$$\hat{\underline{z}} \equiv \underline{B}/|B| \qquad (2.11)$$

$$\Omega_\alpha \equiv |\frac{q_\alpha B}{m_\alpha c}| \qquad (2.12)$$

The vector subscripts $\perp$ and $\parallel$ refer to the components of the vector which are perpendicular and parallel respectively to $\hat{\underline{z}}$. The quantities k_1, k_2,

and k_o above are referred to as the Pedersen, Hall, and direct mobilities respectively. It should be pointed out that Equations (2.6) and (2.7) are only truly closed form expressions when the inertial terms (the last term on the right hand side of Equation (2.5)) are neglected, an assumption we have made previously. Typical ranges for collision frequencies are: $\nu_{in} \sim 30$ sec^{-1}, $\nu_{en} \sim 800$ sec^{-1} at 150 km altitude; and $\nu_{in} \sim 10^{-1}$ sec^{-1}, $\nu_{en} \sim 1$ sec^{-1} at 500 km altitude.

As we will see later, we will use the concept of "layers" to distinguish the various ion species, so for the moment we consider only a single ion species, denoted by subscript i, and the associated electrons, denoted by subscript e. We also consider only singly charged ions so that $q_i = e$ and $q_e = -e$. Noting that $\nu_{en}/\Omega_e \approx 0$, we obtain

$$k_{1i} = \frac{\nu_{in}}{\Omega_i} R_i \frac{c}{e|B|} \qquad (2.13)$$

$$k_{1e} = 0 \qquad (2.14)$$

$$k_{2i} = R_i \frac{c}{eB} \qquad (2.15)$$

$$k_{2e} = -\frac{c}{eB} \qquad (2.16)$$

where

$$R_i \equiv (1 + \nu_{in}^2/\Omega_i^2)^{-1} \qquad (2.17)$$

We now define the perpendicular current

$$\underline{J}_\perp \equiv \sum_\alpha n_\alpha \, q_{\alpha} \underline{v}_{\alpha\perp} \tag{2.18}$$

Substituting Equations (2.13) through (2.16) and (2.6) into Equation (2.18), and using the quasi-neutrality approximation

$$n_1 \approx n_e \equiv n \tag{2.19}$$

we obtain

$$\underline{J}_\perp = \frac{\nu_{in}}{\Omega_i} R_i \frac{nc}{|B|} \underline{F}_{i1\perp}$$

$$+ \frac{nc}{B} (R_i \, \underline{F}_{i1\perp} + \underline{F}_{e\perp}) \times \hat{\underline{z}} \tag{2.20}$$

For the barium cloud problem we shall treat here, we shall only consider neutral winds, electric fields, gravity, and pressure gradients as external forces. Hence

$$\underline{F}_{i1\perp} = e \, \underline{E}_\perp + m_i \, \underline{g}_\perp + \nu_{in} \, m_i \, \underline{U}_{n\perp} - \nabla P_i / n \tag{2.21}$$

$$\underline{F}_{e\perp} = - e \, \underline{E}_\perp + m_e \, \underline{g}_\perp - \nabla P_e / n \tag{2.22}$$

Note that we have neglected the small term $\nu_{en} \, m_e \, \underline{U}_{n\perp}$ in Equation (2.22). We obtain

$$\underline{J}_\perp = \frac{\nu_{in}}{\Omega_i} R_i \frac{nc}{|B|} (e \, \underline{E}_\perp + m_i \, \underline{g}_\perp + \nu_{in} \, m_i \, \underline{U}_{n\perp} - \nabla P_i/n)$$

$$+ R_i \frac{nc}{B} \left[e\underline{E}_\perp (1 - R_i^{-1}) + (m_i + \frac{m_e}{R_i}) \, \underline{g}_\perp + \nu_{in} m_i \underline{U}_{n\perp} \right.$$

$$\left. - \nabla P_i/n - \nabla P_e R_i^{-1}/n \right] \times \underline{\hat{z}} \qquad (2.23)$$

Since $0.01 < R_i < 1.0$ we may neglect m_e/R_i with respect to m_i. Defining the Pedersen conductivity

$$\sigma_p \equiv R_i \frac{\nu_{in}}{\Omega_i} \frac{nce}{|B|} \qquad (2.24)$$

and noting that $1 - R_i^{-1} = - \nu_{in}^2/\Omega_i^2$ we obtain

$$\underline{J}_\perp = \sigma_p \left[\underline{E}_\perp + \frac{m_i}{e} \, \underline{g}_\perp + \nu_{in} \frac{m_i}{e} \underline{U}_{n\perp} - \frac{\nabla P_i}{ne} \right.$$

$$+ \frac{B}{|B|} \left(- \frac{\nu_{in}}{\Omega_i} \underline{E}_\perp + \frac{\Omega_i m_i}{\nu_{in} e} \, \underline{g}_\perp + \Omega_i \frac{m_i}{e} \underline{U}_{n\perp} \right.$$

$$\left. \left. - \frac{\Omega_i}{\nu_{in} ne} (\nabla P_i + R_i^{-1} \nabla P_e) \right) \times \underline{\hat{z}} \right] \qquad (2.25)$$

Our need for an expression for $\underline{J}_\perp$ stems from our need for its divergence to evaluate $\nabla \cdot \underline{J}$ ($= 0$ by quasi-neutrality), as we shall see in the next section.

3. Mathematical Model

We shall model our physical system using a simplified model as depicted in Figure 2. The magnetic field lines are assumed to be straight, to be aligned along the z axis of our cartesian coordinate system, and to terminate in insulators at $z = \pm\infty$. The plasma of interest is threaded by these magnetic field lines, and is divided into thin planes or "layers" of plasma perpendicular to the magnetic field. Since we have neglected collisions between different plasma species, we may use the device of layers to treat multiple ion species at a single point in space simply by allowing multiple layers to occupy the same plane in space, one for each ion species. In this way a "layer" consists only of a single ion species and its associated electrons.

Our quasi-neutrality assumption demands that

$$\nabla \cdot \underline{J} = \frac{\partial}{\partial x} J_x + \frac{\partial}{\partial y} J_y + \frac{\partial}{\partial z} J_z = 0 \qquad (3.1)$$

Integrating Equation (3.1) along z and noting from Figure 2 that J_z vanishes at $z = \pm\infty$ we obtain

$$\int_{-\infty}^{+\infty} \nabla_\perp \cdot \underline{J}_\perp \, dz = 0 \qquad (3.2)$$

where

$$\nabla_\perp \equiv \underline{\hat{x}} \frac{\partial}{\partial x} + \underline{\hat{y}} \frac{\partial}{\partial y} \qquad (3.3)$$

From our model as depicted in Figure 2 we may approximate the integral in
Equation (3.2) by a discrete sum

$$\sum_{k=1}^{K} \nabla_{\perp} \cdot \underline{J}_{\perp k} \, \Delta z_k = 0 \tag{3.4}$$

where the subscript k refers to the layer number, K is the total number of
layers in the system, and Δz_k is the thickness of layer k measured along
the magnetic field line. Within a layer, both the ion density n and the
ion-neutral collision frequency ν_{in} are assumed to be constant along a
magnetic field line. This enables us to introduce the three magnetic-
field-line integrated quantities:

$$N_k \equiv n_k \Delta z_k \tag{3.5}$$

$$\Sigma_{pk} \equiv \sigma_{pk} \Delta z_k = N_k \left(\frac{\nu_{in}}{\Omega_i} R_i \right)_k \frac{ce}{|B|} \tag{3.6}$$

$$\Sigma_{hk} \equiv \left(\frac{\nu_{in}}{\Omega_i} \right)_k \Sigma_{pk} \tag{3.7}$$

By our assumption of equipotential magnetic field lines and
electrostatic electric fields

$$\underline{E}_{\perp k}(x,y) = \underline{E}_o - \nabla_{\perp} \phi(x,y) \text{ for all } k \tag{3.8}$$

where $\underline{E}_o \equiv E_{ox} \hat{\underline{x}} + E_{oy} \hat{\underline{y}}$ is a constant, externally imposed electric field.
Then Equation (3.4) becomes

$$\nabla_\perp \cdot \left[\sum_{k=1}^{K} (\Sigma_{pk}) \nabla_\perp \phi \right] + \sum_{k=1}^{K} H_k = \sum_{k=1}^{K} \nabla_\perp \cdot \underline{J}_{\perp k}^{ext} \tag{3.9}$$

where

$$H_k \equiv - \frac{\partial}{\partial x} \left(\Sigma_{hk} \frac{\partial \phi}{\partial y} \right) + \frac{\partial}{\partial y} \left(\Sigma_{hk} \frac{\partial \phi}{\partial x} \right)$$

$$= - \frac{\partial \phi}{\partial y} \frac{\partial \Sigma_{hk}}{\partial x} + \frac{\partial \phi}{\partial x} \frac{\partial \Sigma_{hk}}{\partial y} \tag{3.10}$$

$$\underline{J}_{\perp k}^{ext} \equiv \Sigma_{pk} \left[\frac{m_i}{e} \underline{g}_\perp + \nu_{in} \frac{m_i}{e} \underline{U}_{n\perp} - \frac{\nabla P_i}{ne} + \underline{E}_o \right.$$

$$+ \frac{B}{|B|} \left\{ \frac{\Omega_i m_i}{\nu_{in} e} \underline{g}_\perp + \Omega_i \frac{m_i}{e} \underline{U}_\perp - \frac{\Omega_i}{ne \, \nu_{in}} \left(\nabla P_i + R_i^{-1} \nabla P_e \right) \right.$$

$$\left. \left. - \frac{\nu_{in}}{\Omega_i} \underline{E}_o \right) \times \hat{\underline{z}} \right]_k \tag{3.11}$$

and the subscript k denoting layer number on terms within parenthesis operates on all terms within those parentheses.

The system of equations we must solve consists of (3.9)-(3.11) and an equation of continuity for each layer:

$$\frac{\partial N_k}{\partial t} + \nabla \cdot (N_k \underline{v}_{ik}) = 0 \qquad k=1, \ldots, K \tag{3.12}$$

where $\underline{v}_i$ is given by Eq. (2.6)-(2.12).

4. Simplified Two-Level Model

    We make the following further simplifications in our model:

    a) We find that for ionospheric barium clouds the currents parallel to $\underline{B}$ are carried primarily by electrons, and the motion of ions parallel to $\underline{B}$ consists primarily of a slow diffusion plus a bulk falling of the cloud to lower altitudes (since $\underline{g} \cdot \underline{B} \neq 0$). It is therefore sufficient to represent the ions as an array of two-dimensional planes or layers of plasma perpendicular to $\underline{B}$, each moving with the bulk "falling" velocity along $\underline{B}$, and hence to treat numerically only the transport of ions perpendicular to $\underline{B}$ within each layer.

    b) We limit our discussion to a model consisting of only two layers or species of ions.

    c) We assume that the ion neutral collision frequency ν_{in} is constant within a layer.

    d) We assume that the only forces acting on the plasma are an external electric field $\underline{E}_o$ and pressure gradients.

With the above assumptions we have

$$\underline{J}^{ext}_{\perp k} = \Sigma_{pk}\left[(\underline{E}_o - \frac{\nabla P_i}{ne})_k\right.$$

$$\left. + \frac{B}{|B|}\left[-\frac{\nu_{in}\underline{E}_o}{\Omega_i} - \frac{\Omega_i}{ne\,\nu_{in}}(\nabla P_i + R_i^{-1}\nabla P_e)\right]_k \times \hat{\underline{z}}\right] \qquad (4.1)$$

If we assume $\underline{B}$ is along the positive z axis then $B/|B| = 1$ and we get

$$\nabla_{\perp} \cdot \underline{J}^{ext}_{\perp k} = \nabla_{\perp} \cdot \left(\Sigma_{pk}(\underline{E}_o - \frac{\nabla P_i}{ne})_k\right)$$

$$- \nabla_{\perp} \cdot \left(\Sigma_p \frac{\nu_{in}}{\Omega_i}\underline{E}_o \times \hat{\underline{z}}\right)_k + H_{pk} \qquad (4.2)$$

O-23

where

$$H_{pk} = - \nabla_\perp \cdot \left(\Sigma_p \frac{\Omega_i}{ne\, \nu_{in}} (\nabla P_i + R_i^{-1} \nabla P_e) \times \hat{\underline{z}} \right)_k \qquad (4.3)$$

Now

$$\left[\Sigma_p \frac{\Omega_i}{ne\, \nu_{in}} \right]_k = \left[R_i \frac{\nu_{in}}{\Omega_i} \frac{n\, c\, e}{|B|} \Delta z \frac{\Omega_i}{\nu_i ne} \right]_k$$

$$= \left[R_i \frac{c}{|B|} \Delta z \right]_k \qquad (4.4)$$

which is a constant within a layer if ν_{in} is constant within a layer (one of our assumptions). Then

$$H_{pk} = - \nabla_\perp \cdot \left(\text{constant } \nabla(P_i + R_i^{-1} P_e) \times \hat{\underline{z}} \right) = 0 \qquad (4.5)$$

(since $\nabla_\perp \cdot (\nabla C \times \hat{z}) = 0$ for any scalar field C).

Our final equations to be solved are then

$$\frac{\partial N_k}{\partial t} + \nabla_\perp \cdot (N_k \underline{v}_{k\perp}) = 0 \qquad k = 1,2 \qquad (4.6)$$

$$\nabla_\perp \cdot \left[(\Sigma_{p1} + \Sigma_{p2}) \nabla_\perp \phi \right] + H = \underline{E}_o \cdot \nabla_\perp (\Sigma_{p1} + \Sigma_{p2})$$

$$- \nabla_\perp \cdot \left(\Sigma_{p1} \frac{\nabla P_{i1}}{n_1 e} + \Sigma_{p2} \frac{\nabla P_{i2}}{n_2 e} \right) \qquad (4.7)$$

where

$$H \equiv -\frac{\partial}{\partial x}\left[(\Sigma_{h1} + \Sigma_{h2})(\frac{\partial \phi}{\partial y} - E_{oy})\right]$$
$$+ \frac{\partial}{\partial y}\left[(\Sigma_{h1} + \Sigma_{h2})(\frac{\partial \phi}{\partial x} - E_{ox})\right] \tag{4.8}$$

Looking at Eq. (4.7) we notice that ϕ may be separated into two parts:

$$\phi = \phi_E + \phi_P \tag{4.9}$$

$$\nabla_{\perp} \cdot \left[(\Sigma_{p1} + \Sigma_{p2})\nabla_{\perp}\phi_E\right] + H = \underline{E}_o \cdot \nabla_{\perp}(\Sigma_{p1} + \Sigma_{p2}) \tag{4.10}$$

$$\nabla_{\perp} \cdot \left[(\Sigma_{p1} + \Sigma_{p2})\nabla_{\perp}\phi_P\right] = -\nabla_{\perp}(\Sigma_{p1}\frac{\nabla P_{i1}}{n_1 e} + \Sigma_{p2}\frac{\nabla P_{i2}}{n_2 e}) \tag{4.11}$$

For reasons which shall become clear as we progress, we shall regard ϕ_E as that part of the potential field which tends to drive the cloud toward bifurcation. In fact, Eq. (4.10) coupled with (4.6) just form the basic inviscid two-level equations [Scannapieco et al., 1976]. We shall regard ϕ_P as that part of the potential field which tends to diffuse or anti-diffuse the edges of the cloud. First let us look at solutions to (4.11). If ∇P_{i1} and ∇P_{i2} vanish at our boundaries, the unique solution consistent with zero Neumann boundary conditions (vanishing of the normal derivative of ϕ_P at the boundary) gives:

$$-(\Sigma_{p1} + \Sigma_{p2})\nabla_{\perp}\phi_P = \Sigma_{p1}\frac{\nabla P_{i1}}{n_1 e} + \Sigma_{p2}\frac{\nabla P_{i2}}{n_2 e} \tag{4.12}$$

In general, the motion resulting from the forces proportional to $\nabla\phi_P$, ∇P_{i1} and ∇P_{i2} will be quite complex, not describable as the simple

superposition of a shear and a diffusion. However, in the special case of one of the layers being uniform, e.g., N_2 and T_{12} (T_i = ion temperature) hence Σ_{p2} and P_{12} uniform, then

$$\nabla \phi_P = \frac{-\Sigma_{p1}}{\Sigma_{p1} + \Sigma_{p2}} \frac{\nabla P_{i1}}{n_1 e} \tag{4.13}$$

We shall now treat this special case. One may conveniently think of level 1 as representing the barium cloud and level 2 the uniform background ionosphere.

We now use the equation of state

$$P_i = n \, T_i$$

where T_i is in energy units (T_i is the product of Boltzmann's constant and the temperature in degrees Kelvin), and assume thermal conductivities high enough such that T_i is constant and hence

$$\nabla P_i = T_i \nabla n \tag{4.14}$$

Then

$$\nabla \phi_P = \frac{-\Sigma_{p1}}{\Sigma_{p1} + \Sigma_{p2}} \frac{T_{i1} \nabla n_1}{n_1 e}$$

The velocity in level 1 resulting from the combined action of ∇P_1 and ϕ_P is

$$\underline{v}_{11P} = \left[\frac{\nu_{in}}{\Omega_1} R_1 \frac{c}{e|B|} \left(- e\nabla\phi_P - T_1 \frac{\nabla n}{n}\right)\right]_1$$

$$+ \left[R_1 \frac{c}{eB} \left(- e\nabla\phi_P - T_1 \frac{\nabla n}{n}\right)\right]_1 \times \hat{\underline{z}} \qquad (4.15)$$

Now

$$\left(- e\nabla\phi_P - T_1 \frac{\nabla n}{n}\right)_1$$

$$= T_{11} \frac{\nabla n_1}{n_1} \left(\frac{\Sigma_{p1}}{\Sigma_{p1} + \Sigma_{p2}} - 1\right)$$

$$= - T_{11} \frac{\nabla n_1}{n_1} \left(\frac{\Sigma_{p2}}{\Sigma_{p1} + \Sigma_{p2}}\right) \qquad (4.16)$$

Thus

$$\underline{v}_{11P} = \frac{-\Sigma_{p2}}{\Sigma_{p1} + \Sigma_{p2}} \left[\left(\frac{\nu_{in}}{\Omega_1} R_1 \frac{c}{e|B|} T_1 \frac{\nabla N}{N}\right)_1 \right.$$

$$+ \left. \left(R_1 \frac{c}{eB} T_1 \frac{\nabla N}{N}\right)_1 \times \hat{\underline{z}}\right] \qquad (4.17)$$

Note we have used $\frac{\nabla n}{n} = \frac{\nabla N}{N}$.

It is convenient to divide $\underline{v}_{11P}$ into two parts:

$$\underline{v}_{11P} = \underline{v}_{D1} + \underline{v}_{S1}$$

with the subscripts 1 and P suppressed but understood.

$$\underline{v}_{D1} = -\frac{\Sigma_{p2}}{\Sigma_{p1} + \Sigma_{p2}} \left(\frac{\nu_{in}}{\Omega_i} R_i \frac{c}{e|B|} T_i \frac{\nabla N}{N}\right)_1 \qquad (4.18)$$

$$\underline{v}_{S1} = -\frac{\Sigma_{p2}}{\Sigma_{p1} + \Sigma_{p2}} \left(R_i \frac{c}{eB} T_i \frac{\nabla N}{N}\right)_1 \times \hat{z} \qquad (4.19)$$

That $\underline{v}_{S1}$ represents shear flow at plasma gradients can be seen by noting that the velocity is always perpendicular to ∇N, and is largest where $\frac{\Sigma_{p2}}{\Sigma_{p1} + \Sigma_{p2}} \frac{\nabla N}{N}$ is a maximum, decaying in magnitude away from the region. The quantity $\underline{v}_S$ is of interest because it is a shear flow and hence may be stabilizing in certain cases (see Perkins and Doles [1975], Huba et al. [1982]). We do not consider the effects of $\underline{v}_S$ further in this paper except to note that for the special case of a uniform layer 2 being considered here, $\nabla \cdot \underline{v}_{S1} = 0$ and $\nabla N_1 \cdot \underline{v}_{S1} = 0$ which together imply $\nabla \cdot (N_1 \underline{v}_{S1}) = 0$, which is to say that $\underline{v}_{S1}$ has no effect on the time evolution of N_1. Since this breaks the feedback loop, it is difficult to see how a shear stabilization mechanism could be active in this case.

A consideration of $\underline{v}_D$ is really the heart of this paper. The quantity $\underline{v}_D$ is the source for ion diffusion in level 1. More importantly, it is the source for the diffusion of the total integrated Pedersen and Hall conductivities if level 2 is sufficiently incompressible (i.e., if ν_{in}/Ω_i in level 2 is sufficiently small), as we will show. Let us look at the effect of $\underline{v}_D$ on the ion continuity equation for level 1:

$$\frac{\partial N_1}{\partial t} = -\nabla \cdot (N_1 \underline{v}_{D1})$$

$$= +\nabla \cdot \left[\frac{\Sigma_{p2}}{\Sigma_{p1} + \Sigma_{p2}} \left(\frac{\nu_{in}}{\Omega_i} R_i \frac{c}{e|B|} T_i \nabla N\right)_1\right] \qquad (4.20)$$

This is just a diffusion equation for N_1 with diffusion coefficient

$$D_o = \frac{\Sigma_{p2}}{\Sigma_{p1} + \Sigma_{p2}} \left(\frac{\nu_{in}}{\Omega_i} R_i \frac{c}{e|B|} T_i \right)_1 \qquad (4.21)$$

(It should be noted that this diffusion coefficient is similar to that derived by <u>Goldman et al.</u>, 1976, and <u>Vickrey and Kelley</u>, 1982.)

For a barium cloud (level 1) at 180 km altitude we take $T_i \sim 1000^\circ$ K, $\frac{\nu_{in}}{\Omega_i} \sim 0.06$, $B = 0.5$ g, and get

$$D_o = \frac{\Sigma_{p2}}{\Sigma_{p1} + \Sigma_{p2}} (100 \text{ m}^2/\text{sec}) \qquad (4.22)$$

In the less dense regions of the barium cloud where Σ_{p1} is small compared to Σ_{p2}, the ion diffusion coefficient is quite large indeed. By contrast ambipolar diffusion rates induced by electron-ion and electron-neutral collisions yield diffusion coefficients on the order of 1 m²/sec. Thus our neglect of these collision terms seems justified. Unfortunately, N_1 is <u>not</u> the relevant quantity if one is interested in the effect of $\underline{v}_D$ on barium cloud dynamics. A look at Eq. (4.10) will convince the reader that if one wants to affect the time evolution of ϕ_E, the quantity which determines the bifurcation process, it is necessary to change the quantities $\Sigma_p \equiv \Sigma_{p1} + \Sigma_{p2}$ and $\Sigma_h \equiv \Sigma_{h1} + \Sigma_{h2}$, the <u>total</u> field line integrated Pedersen and Hall conductivities. Again we assume an initially uniform distribution of Σ_{p2} and N_2. We can only show the effects of $\underline{v}_D$ in the first instant of time here. Once images form in level 2, the problem yields only to numerical techniques. We need the velocity $\underline{v}_{D2}$ in level 2.

$$\underline{v}_{D2} = (\frac{\nu_{in}}{\Omega_i} R_i)_2 \frac{c}{e|B|} \frac{\Sigma_{p1}}{\Sigma_{p1} + \Sigma_{p2}} (T_{i1} \frac{\nabla N_1}{N_1}) \tag{4.23}$$

As a check, let us see the effect on $(N_1 + N_2)$

$$\frac{\partial N_2}{\partial t} = - \nabla \cdot (N_2 \underline{v}_{D2})$$

$$= - \nabla \cdot (\Sigma_{p2} e^{-2} \frac{\Sigma_{p1}}{\Sigma_{p1} + \Sigma_{p2}} (T_{i1} \frac{\nabla N_1}{N_1})) \tag{4.24}$$

$$\frac{\partial N_1}{\partial t} = - \nabla_1 (N_1 \underline{v}_{D1})$$

$$= + \nabla \cdot (\frac{\Sigma_{p2}}{\Sigma_{p1} + \Sigma_{p2}} \Sigma_{p1} e^{-2} T_{i1} \frac{\nabla N_1}{N_1})$$

$$= - \frac{\partial N_2}{\partial t} \tag{4.25}$$

So we see that

$$\frac{\partial (N_1 + N_2)}{\partial t} = 0 \tag{4.26}$$

which when combined with quasi-neutrality, is simply a statement that electrons can't diffuse. This is consistent with our neglect of electron-ion and electron-neutral collisions.

Now let us look at the effect of $\underline{v}_D$ on $\Sigma_p = \Sigma_{p1} + \Sigma_{p2}$. A similar analysis can be performed for Σ_h with similar results. However the bifurcation effects of Σ_h are small compared to those of Γ_p, and we shall not consider them here.

$$\frac{\partial \Sigma_{p1}}{\partial t} = \left(\frac{\nu_{in}}{\Omega_i} R_i\right)_1 \frac{ce}{|B|} \frac{\partial N_1}{\partial t} = \nabla \cdot (\underline{v}_{D1} \Sigma_{p1}) \qquad (4.27)$$

$$\frac{\partial \Sigma_{p2}}{\partial t} = \left(\frac{\nu_{in}}{\Omega_i} R_i\right)_2 \frac{ce}{|B|} \frac{\partial N_2}{\partial t} = \nabla \cdot (\underline{v}_{D2} \Sigma_{p2}) \qquad (4.28)$$

but

$$\frac{\partial N_1}{\partial t} = -\frac{\partial N_2}{\partial t} = -\frac{|B|}{ce} \left(\frac{\nu_{in}}{\Omega_i} R_i\right)_1^{-1} \frac{\partial \Sigma_{p2}}{\partial t} \qquad (4.29)$$

$$\frac{\partial \Sigma_{p1}}{\partial t} = -\frac{\left(\frac{\nu_{in}}{\Omega_i} R_i\right)_1}{\left(\frac{\nu_{in}}{\Omega_i} R_i\right)_2} \frac{\partial \Sigma_{p2}}{\partial t} \qquad (4.30)$$

$$\frac{\partial (\Sigma_{p1} + \Sigma_{p2})}{\partial t} = \frac{\partial \Sigma_{p1}}{\partial t} \left[1 - \left(\frac{\nu_{in}}{\Omega_i} R_i\right)_2 / \left(\frac{\nu_{in}}{\Omega_i} R_i\right)_1\right] \qquad (4.31)$$

Now

$$\frac{\partial \Sigma_{p1}}{\partial t} = -\nabla_\perp \cdot (\underline{v}_{D1} \Sigma_{p1}) \qquad (4.32)$$

We note that in Eq. (4.18) we may set $\nabla N_1/N_1 = \nabla \Sigma_{p1}/\Sigma_{p1}$ so that

$$\frac{\partial \Sigma_{p1}}{\partial t} = \nabla \cdot \left[\frac{\Sigma_{p2}}{\Sigma_{p1} + \Sigma_{p2}} \left(\frac{\nu_{in}}{\Omega_i} R_i \frac{c}{e|B|} T_i\right)_1 \nabla \Sigma_{p1}\right] \qquad (4.33)$$

Now since

$$\nabla \Sigma_{p2} = 0 \qquad (4.34)$$

we have

$$\nabla(\Sigma_{p1} + \Sigma_{p2}) = \nabla\Sigma_{p1} \tag{4.35}$$

and

$$\frac{\partial(\Sigma_{p1} + \Sigma_{p2})}{\partial t} = \nabla_\perp \cdot \left[\left(1 - (\nu_{in}R_1/\Omega_1)_2/(\nu_{in}R_1/\Omega_1)_1\right)\left(\frac{\Sigma_{p2}}{\Sigma_{p1} + \Sigma_{p2}}\right)\right.$$

$$\left.(\frac{\nu_{in}}{\Omega_1} R_1 \frac{c}{eB} T_1)_1 \nabla(\Sigma_{p1} + \Sigma_{p2})\right] \tag{4.36}$$

so we see that for Σ_p we again have a diffusion equation, but this time our nominal 100 m^2/sec diffusion coefficient is not only multiplied by $\Sigma_{p2}/(\Sigma_{p1} + \Sigma_{p2})$, reducing its effectiveness in the dense portions of the cloud, but it is further multiplied by the factor F where

$$F = 1 - \frac{(\nu_{in}R_1/\Omega_1)_2}{(\nu_{in}R_1/\Omega_1)_1} \tag{4.37}$$

Note that if $\nu_{in}R_1/\Omega_1$ is the same for both layers, the diffusion is reduced to zero. Furthermore, if $(\nu_{in}R_1/\Omega_1)_2 > (\nu_{in}R_1/\Omega_1)_1$ (a compressible background plasma, e.g., an E region) the diffusion coefficient is negative. That is, gradients in Σ_p will actually be steepened, rather than smoothed. For this reason we conclude that unless some rather fast recombination chemistry is taking place in the E region, the presence of a background E region is destabilizing, in accord with the findings of Francis and Perkins [1975].

The opposite extreme of $(\nu_{in}R_1/\Omega_1)_2 \ll (\nu_{in}R_1/\Omega_1)$ (background F region ionosphere) is more interesting since it closely approximates the conditions of most barium releases. It also yields the full nominal 100 m^2/sec diffusion coefficient, since $F = 1.0$, giving us some hope of

stopping the bifurcation process at scale sizes of hundreds of meters. Note that in this case the diffusion rate for Σ_p is the same as that for N_1. Also note that the case of $(\nu_{in}R_1/\Omega_1)_2$ small is the case where the Pedersen mobility and hence compressibility of the background is extremely low, meaning that only minimal images will be formed. It is a good approximation to take Σ_{p2} to be uniform for all time. One might well ask how this is possible given that the electrons can't diffuse, and that the barium ions are being allowed to diffuse in level 1. The answer is that there _are_ (small) images: the electrons lost to a field line in level 1 are "soaked up" on the same field line in level 2. But the number of electrons N_2 in level 2 is _extremely_ large. (N_2 must be large in order to contribute a significant Pedersen conductivity and yet have small $\nu_{in}R_1/\Omega_1$ (see Eq. 2.24)). Thus the electrons that are soaked up in level 2 induce only an extremely small percentage change in Σ_{p2}.

5. Diffusion Characteristics for a Simplified Two-level Model with a Nearly Incompressible Background Layer

In the last section we demonstrated that when the background ionosphere (layer 2) is nearly incompressible ($(\nu_{in}R_1/\Omega_1)_2$ is small) then the primary effect of a finite barium ion temperature is to introduce into the continuity equation for both N_1 and for Σ_p a diffusion term with diffusion coefficient D_0 given by Eq. (4.21). For parameters appropriate to a barium cloud at 180 km altitude we get Eq. (4.22):

$$D_o = \frac{\Sigma_{p2}}{\Sigma_{p1} + \Sigma_{p2}} \ (100 \ \text{m}^2/\text{sec}) \tag{4.22}$$

Since level 2 is nearly incompressible, we may regard Σ_{p2} as a constant.

Since it is proportional to N_1, the integrated barium cloud density, Σ_{p1} is larger in the center of the cloud and decays toward zero at the cloud edges. This means that the diffusion coefficient approaches 100 m^2/sec near the cloud edges, but may be considerably less than that value near the cloud center if $\Sigma_{p1} \gg \Sigma_{p2}$.

Previous attempts to explain the persistence of scale sizes of hundreds of meters for long periods of time after barium releases have inevitably encountered the following problems: 1) The diffusion coefficients required to stop the bifurcation of plasma clouds several hundred meters in diameter were higher than one could explain theoretically; 2) assuming the existence of such large (ordinary) diffusion coefficients, their effect would not only be to stop the bifurcation of the cloud, but also to diffuse the cloud away entirely in several minutes. The form of the diffusion coefficient given by Eq. (4.22) would seem to offer us some hope of overcoming both of these problems. Its success depends on the accuracy of the following qualitative picture of barium cloud bifurcation: We postulate a barium cloud such that $\Sigma_{p1} \gtrsim 5 \, \Sigma_{p2}$ so that the diffusion well inside the cloud is considerably reduced over that at its edges. We further postulate that bifurcation is a process which, in the absence of diffusion, starts at the edges of barium clouds and works its way inward. Our diffusion then satisfies the needed criteria perfectly: 1) It is very effective at the edges of the cloud, stopping bifurcation before it starts; 2) it is very ineffective at the central core of the cloud, giving it a long lifetime. Note that if this picture is correct then the barium clouds commonly known as large M clouds where

$$M \equiv \frac{\Sigma_{p1} + \Sigma_{p2}}{\Sigma_{p2}} \qquad\qquad (5.1)$$

will have extremely long lifetimes. In fact for $M \gtrsim 100$, the decay of the core is probably determined by ambipolar diffusion rates. The accuracy of this picture is best determined by numerical simulation techniques, to which we turn in the next section.

6. Numerical Simulations Using a Simplified Two-level Model with a Nearly Incompressible Background Layer

In this section we attempt to answer numerically the question posed in the last section: if we consider a barium cloud whose background conductivity is due primarily to high F region plasma (nearly incompressible plasma), is the diffusion coefficient given by Eq. (4.22) sufficient to stop the bifurcation of that cloud at a diameter of several hundred meters? In order to isolate the effects of this diffusion coefficient, we will make some further simplifications in our two-level model: 1) We assume that N_2 and hence Σ_{p2} remain uniform during all times of interest. This is completely consistent with our assumption of a nearly incompressible background plasma, as discussed at the end of Section 4; 2) We neglect the shear component $\underline{v}_S$ of the pressure-induced ion velocity as defined in Eq. (4.19). Again this is consistent with our assumption of a nearly incompressible background plasma which in turn implies a uniform Σ_{p2}, as shown in the discussion following Eq. (4.19); 3) We neglect the "Hall term" H in Eq. (4.4) and hence in Eq. (4.10). This is a good approximation as long as $v_{in}/\Omega_i < 0.1$; 4) We eglect Pedersen convection. That is, for all terms except those causing ion diffusion, we approximate the ion velocity with the electron velocity (see Eq. (6.4)

below). We know from our previous study [Zalesak et. al,, 1983] that the Pedersen mobility of the ions in response to $(\underline{E}_o - \nabla\phi_E)$ can have an effect on the "freezing" phenomenom, and it is our desire to isolate the effects of the pressure-induced diffusion. Hence we neglect ion Pedersen mobility except in the diffusion term.

The final equations to be solved numerically are then

$$\frac{\partial N_1}{\partial t} + \nabla_\perp \cdot (N_1 \underline{v}_1) = \nabla_\perp \cdot (D\nabla N_1) \tag{6.1}$$

$$\frac{\partial N_2}{\partial t} = 0 \tag{6.2}$$

$$\nabla_\perp((\Sigma_{p1} + \Sigma_{p2}) \nabla_\perp \phi_E) = \underline{E}_o \cdot \nabla_\perp (\Sigma_{p1} + \Sigma_{p2}) \tag{6.3}$$

$$\underline{v}_1 = \frac{c}{B^2} (\underline{E}_o - \nabla\phi_E) \times \underline{B} \tag{6.4}$$

$$D = \frac{\Sigma_{p2}}{\Sigma_{p1} + \Sigma_{p2}} D_{io} \tag{6.5}$$

$$\Sigma_{pk} \equiv N_k \left(\frac{\nu_{in}/\Omega_i}{1+(\nu_{in}/\Omega_i)^2}\right)_k \frac{ce}{|B|} \tag{6.6}$$

The initial conditions for the simulations were as follows

$$\Sigma_{p2} = 1.0 \tag{6.7}$$

$$\Sigma_{p1} = 4.0 \exp(-r^4/r_0^4) \tag{6.8}$$

$$r^2 = (x - x_o)^2 + (y - y_o)^2 \tag{6.9}$$

$$r_o = (250 \text{ m}) (1 + 0.001 \sin 8\theta) \tag{6.10}$$

$$\theta = \arctan \left((y-y_o)/(x - x_o) \right) \tag{6.11}$$

$$B = 0.5 \text{ gauss} \tag{6.12}$$

$$cE_o/B = 100 \text{ m/sec} \tag{6.13}$$

where x_o and y_o are the coordinates of the cloud center and the $\underline{E}_o \times \underline{B}$ velocity (cE_o/B) is in the negative y direction.

The above equations are solved numerically on a finite difference grid in an x-y cartesian geometry perpendicular to the magnetic field, which is assumed to be aligned along the z-axis. The 83 x 60 grid is stretched in all four directions, with the central 56 x 32 portion of the grid, which is centered on the steepening backside of the cloud, having a grid spacing of 10 m in both directions. The grid stretching allows the boundaries to be placed 4 km away from the edges of the central uniform mesh in all directions. The potential equation (6.3) is solved using a vectorized incomplete Cholesky conjugate gradient algorithm due to Hain (1980), which is an extension of the algorithm of Kershaw (1978). The continuity equation (6.1) is integrated forward in time using the fully multidimensional flux-corrected transport algorithms of Zalesak [1979].

In Figure 3 we show isodensity contours of Σ_{p1} for the initial conditions for all of the calculations we shall show. We have performed three calculations, varying the value of D_{io} from zero up to the physically realistic value of 100 m^2/sec. The purpose of this sequence is to show first that the diffusion does have an effect on the evolution of the cloud,

and second to show that this effect is much larger than that due to any numerical diffusion which may be present in the calculations. In Figure 4 we show the results for $D_{1o} = 0$. Note that even at the very early time of 14 seconds, bifurcation has already started. By 24 seconds, the main portion of the cloud has completely sheared in two. In Figure 5, we show the results for $D_{1o} = 25 \ m^2/sec$, one fourth of the physically realistic value. The development of the cloud has slowed considerably, showing that even at one fourth its physically realistic value, the physical diffusion is dominating the effects of whatever numerical diffusion may be present. At 14 seconds the cloud has not clearly begun to bifurcate. At 25 seconds, bifurcation has occurred, but is qualitatively and quantitatively different from that which took place when $D_{1o} = 0$. In Figure 6 we show the evolution of the cloud with the full, physically realistic value for D_{1o} of 100 m^2/sec. Bifurcation has now been halted. Rather, the cloud evolves into a streamlined "bullet" or "tadpole" shape in time, and then undergoes a slow diffusive decay. Even at the latest time calculated, 75 sec, there is no hint whatsoever of imminent bifurcation. Noting that for this cloud $M = (\Sigma_{p1} + \Sigma_{p2})/\Sigma_{p2}$ is 5 in the center of the cloud, which yields an effective diffusion coefficient of 20 m^2/sec there. This is still enough to result in substantial decay of the central core on time scales of minutes. Clouds with larger values of M in their centers would of course be longer-lived.

7. Conclusions and Future Work

The primary conclusion of this paper can be stated simply: Under realistic ionospheric conditions (where the plasma cloud couples to an incompressible background i.e., in F region), barium striations hundreds of meters in diameter can be long-lived, quasi-stable, non-bifurcating structures. These structures may resemble "tadpoles", with a dense head, steep density gradients at the front, and a long, less dense tail. If what one means by the term "freezing" is the above phenomenon, then we have shown that freezing does indeed exist.

The next obvious step is to test some of the approximations we have made in our preliminary numerical simulation model. Pedersen convection should be put back into the model, as well as the "Hall terms" in the potential equation. Finite images should be accounted for. Also we would like to test the combined effect of the presence of both a relatively incompressible F region background and a compressible E region on the dynamics of the cloud. Recombination chemistry must be included in this E region if it is to be modeled accurately (see Vickery and Kelley, 1982).

Another of our approximations which should be studied in detail is that the barium cloud and background ionosphere are being driven by an externally imposed electric field, or equivalently, by a neutral wind which doesn't vary in altitude. Were we to address an altitude-dependent neutral wind as a driver, some of our simple results would become less so. The most important factor would be that one could no longer argue that the bifurcation of the cloud depended only on Σ_{p1} and Σ_{p2}, since the potential equation (4.10) would then contain terms which depended explicitly on N_1 and N_2. Although this would not change the results for the incompressible background ionosphere considered here, it would appear to allow for the

END

FILMED

DTIC
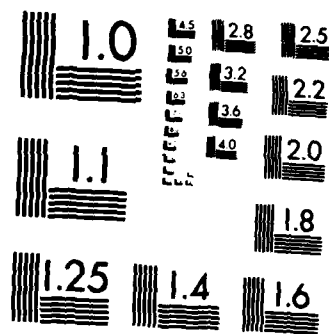
MICROCOPY RESOLUTION TEST CHART
NATIONAL BUREAU OF STANDARDS-1963-A

possibility of this end-shorting-induced diffusion being an effective bifurcation inhibiting mechanism even when the background ionosphere is compressible. We shall consider this case in our future work in this area.

It is also clear that we must address the validity of the perfect mapping of the electrostatic potential along $\underline{B}$. Given that we are now dealing with structures only a few hundred meters in diameter, with gradient scale lengths of a few tens of meters, it seems likely that we will have to deal with the question of how far the polarization field produced by the barium cloud maps along the magnetic field (Goldman et. al, 1976, Glassman and Sperling, 1983). One possible effect might be that the effective value of M would be increased, since the barium cloud could no longer "see" background plasma that was far from the cloud position along $\underline{B}$.
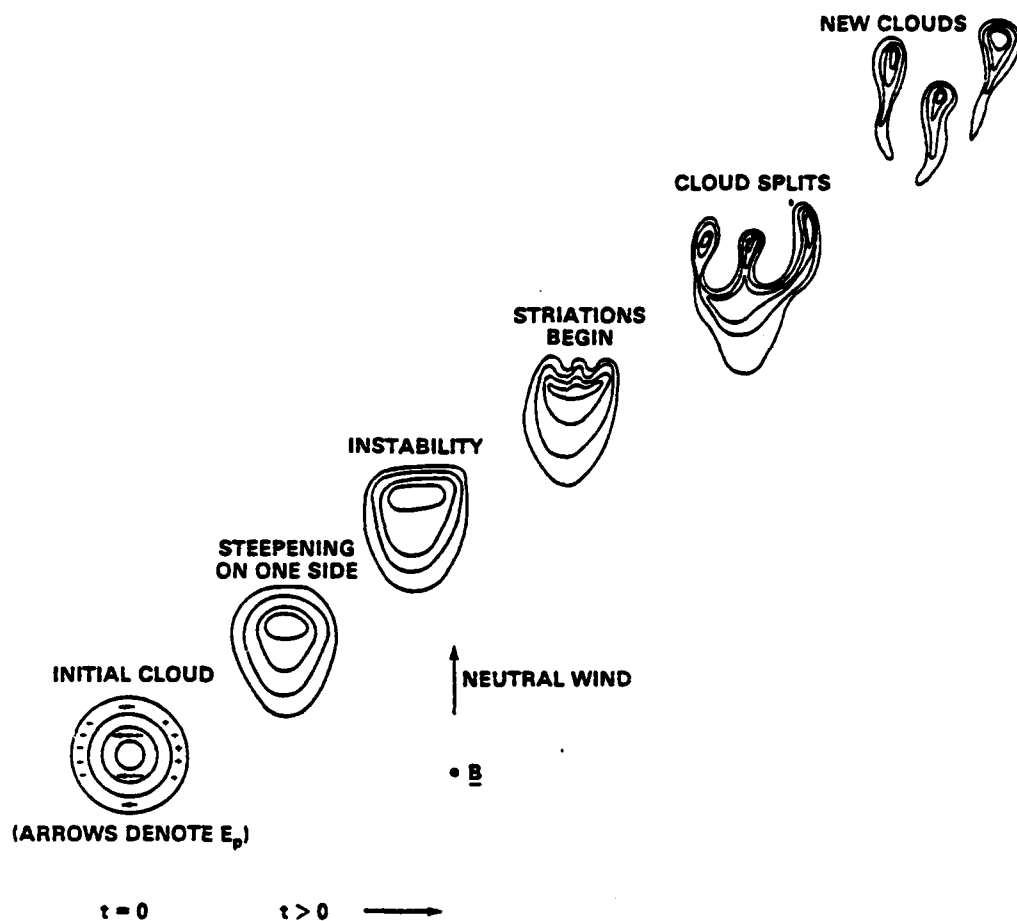
Figure 1. Sketch of the time evolution of a typical barium cloud in a plane perpendicular to the magnetic field, subject to an upward directed neutral wind or equivalently to a rightward directed external electric field. Lines demarking the cloud denote plasma density contours, with the highest plasma density in the center of cloud.
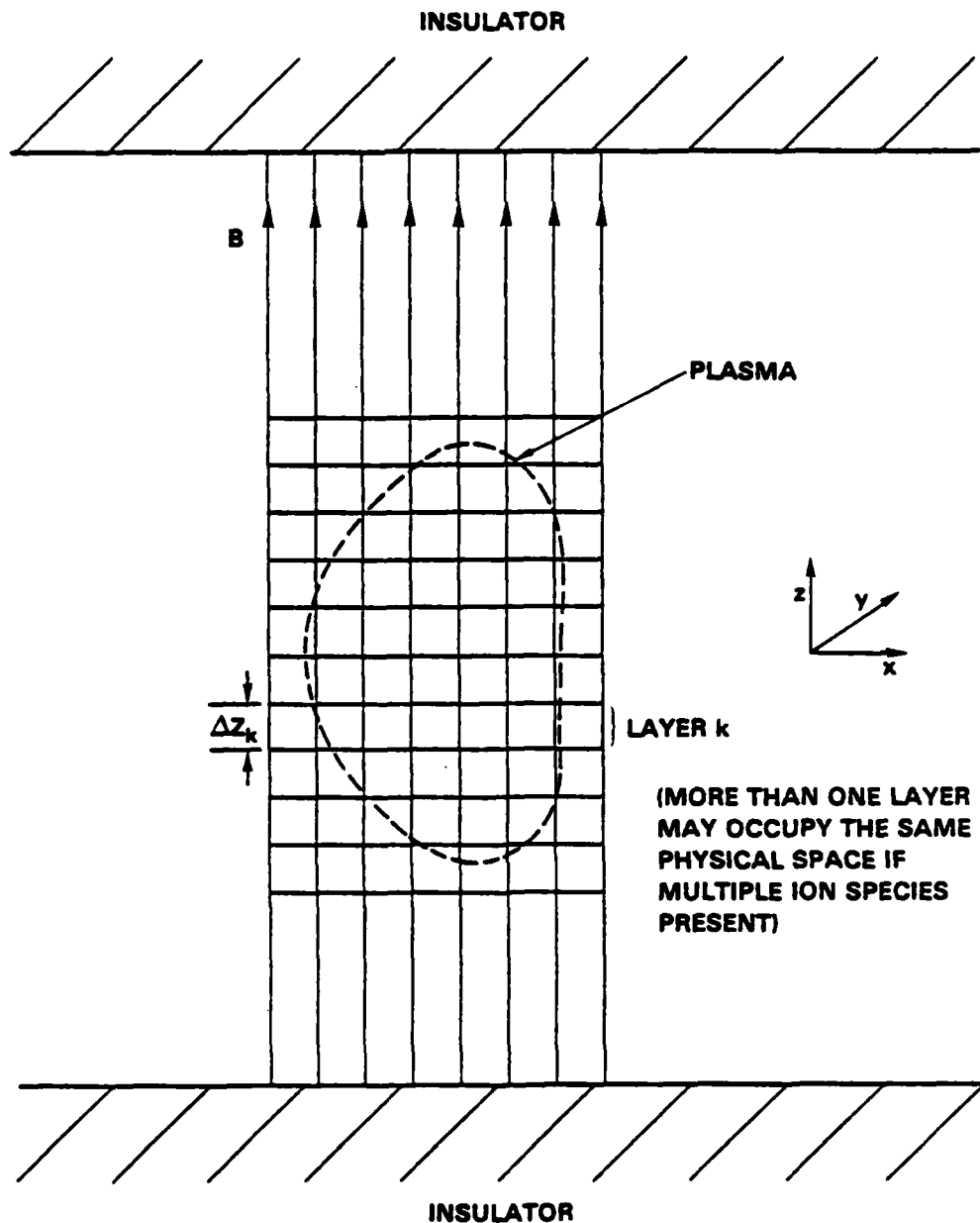
Figure 2. Model of plasma and magnetic field geometry used in this paper. Field lines terminate on insulators at $z = \pm \infty$. Plasma is divided into "layers" along z for mathematical and numerical treatment. Each layer consists of a single ion species and its associated electrons. Multiple collocated ion species are treated by having multiple collocated "layers".
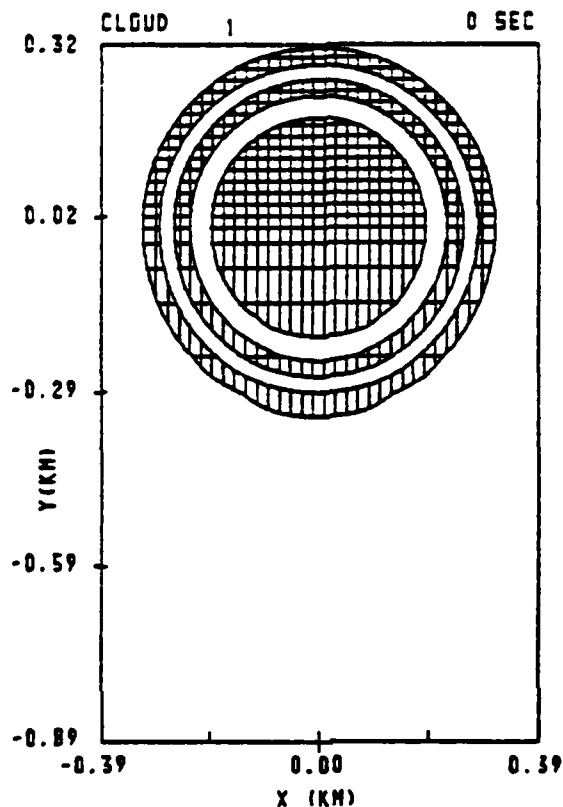
Figure 3. Isodensity contours, with areas between alternate contours shown cross-hatched, for the barium cloud used for the three numerical simulations shown in this paper. The center of the cloud is located at the point (0,0). The boundaries in x are located at $\pm$ 4.9 km. The boundaries in y are located at -4.0 km and +5.3 km respectively. The cross-hatching is done at every other grid line, so that one rectangle of cross hatching represents a 2 x 2 array of computational cells. Contours for this and all other plots in this paper are drawn at values for Σ_{p1} of 0.31, 0.71, 1.24, 1.92, and 2.82 (logarithmic spacing for total Pedersen conductivity).
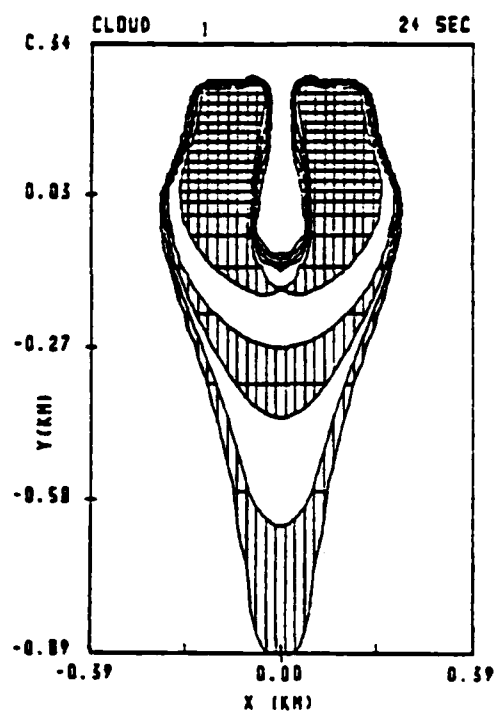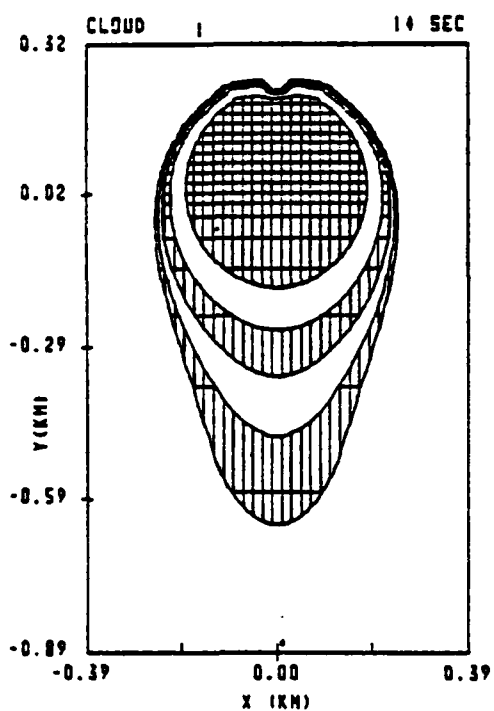
Figure 4. Time evolution of the cloud depicted in Figure 3 for the case $D_{1o} = 0$. Shown are isodensity contours at a) 14 sec, b) 24 sec. Contour values are as given in Figure 3.
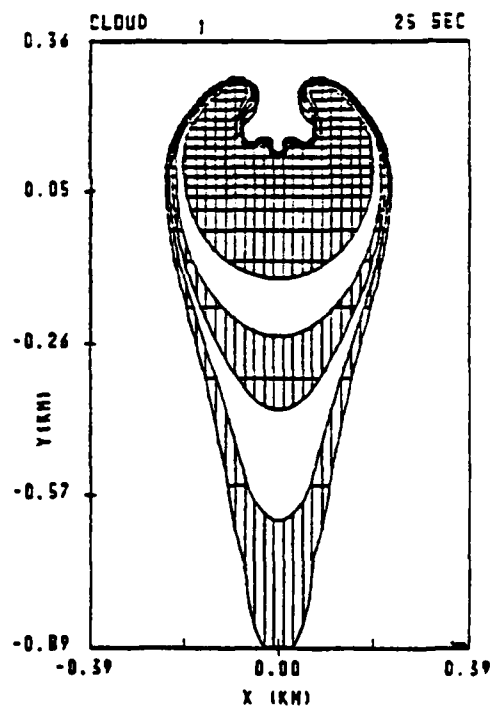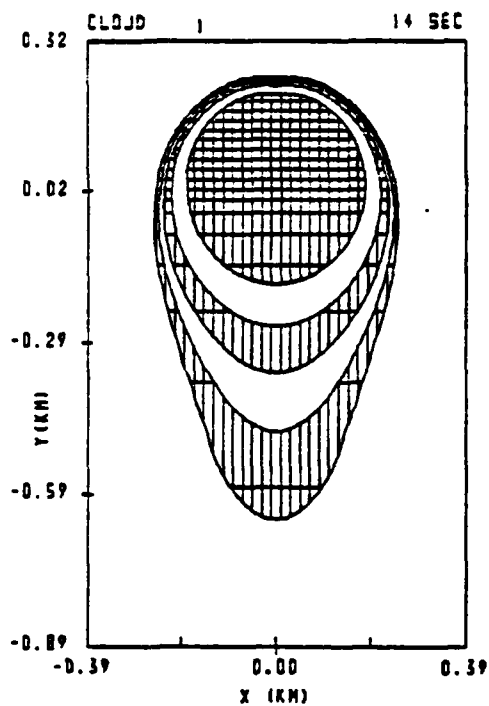
Figure 5. Time evolution of the cloud depicted in Figure 3 for the case $D_{io} = 25 \text{ m}^2/\text{sec}$. Shown are isodensity contours at a) 14 sec, b) 24 sec. Contour values are as given in Figure 3.
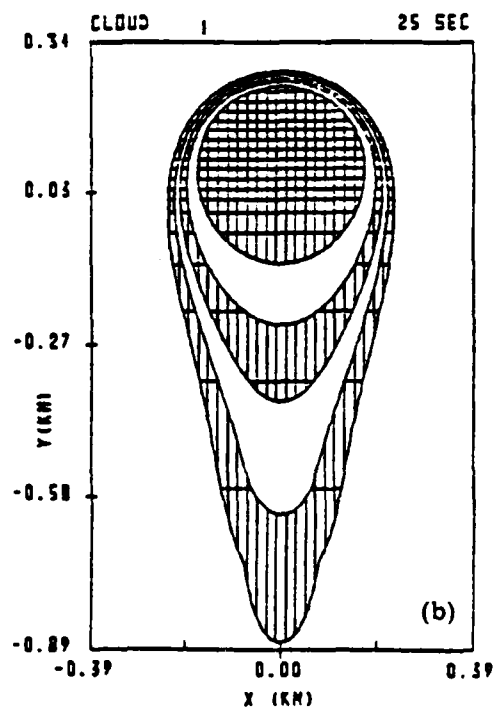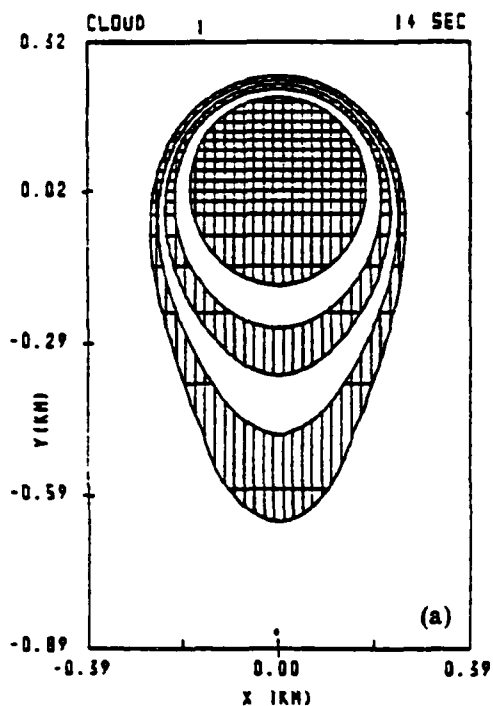
Figure 6. Time evolution of the cloud depicted in Figure 3 for the case $D_{lo} = 100$ m^2/sec (the physically realistic case). Shown are isodensity contours at a) 14 sec, b) 25 sec, c) 39 sec, d) 50 sec, e) 64 sec, f) 75 sec.
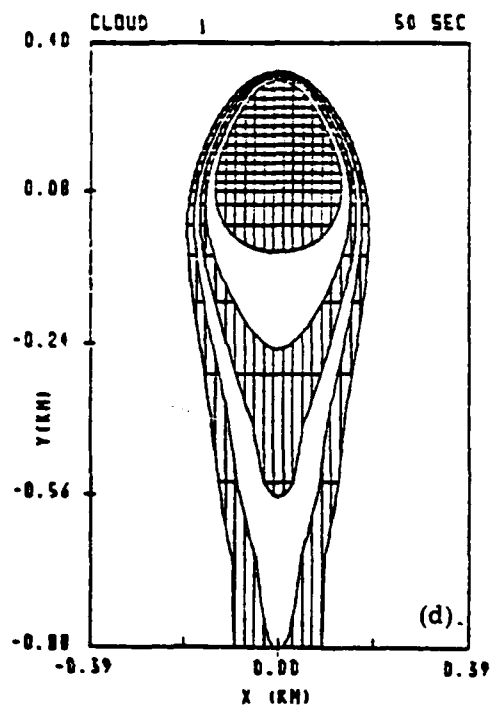
Figure 6, cont'd.   Time evolution of the cloud depicted in Figure 3 for

the   case D_{lo} = 100 m^2/sec (the   physically   realistic   case).

Shown are isodensity contours at a) 14 sec, b) 25 sec, c) 39
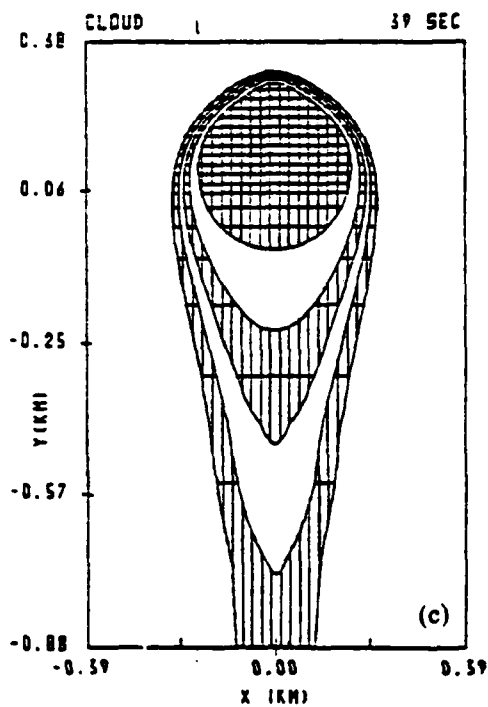
sec, d) 50 sec, e) 64 sec, f) 75 sec.

Figure 6, cont'd.   Time evolution of the cloud depicted in Figure 3 for the   case D_{io} = 100 m^2/sec (the   physically   realistic   case). Shown are isodensity contours at a) 14 sec, b) 25 sec, c) 39 sec, d) 50 sec, e) 64 sec, f) 75 sec.
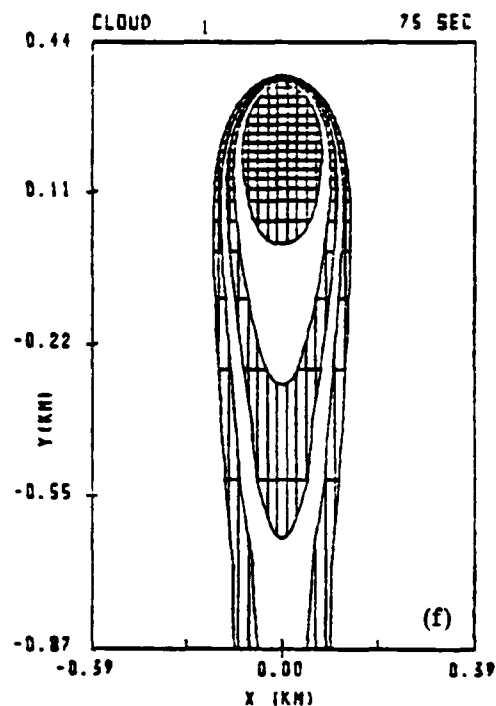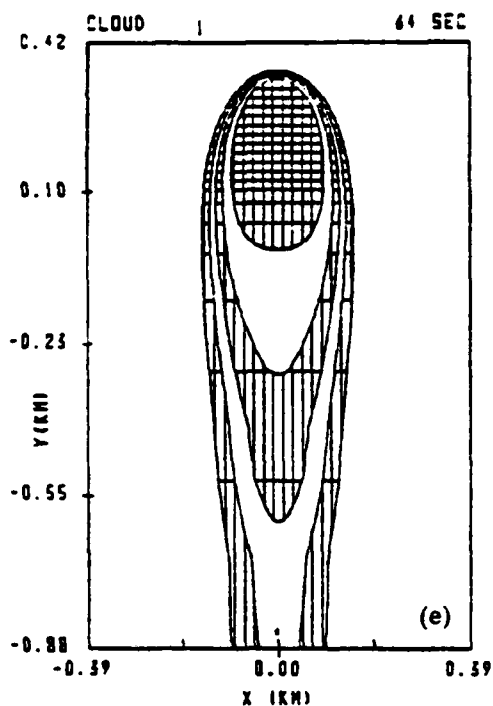
References

Fedder, J.A., Conductivity formulas for the disturbed ionosphere, Memo Report 4329, Naval Res. Lab., Washington, D.C., Sept., 1980. ADA089 374

Francis, S.H., and F.W. Perkins, Determination of striation scale sizes for plasma clouds in the ionosphere, J. Geophys. Res., 80, 3111, 1975.

Glassman, A.J. and J.L. Sperling, Electromagnetic theory of collisional interchange instabilities, J. Geophys. Res., 88, 10091, 1983.

Goldman, S.R., L. Baker, S.L. Ossakow, and A.J. Scannapieco, Striation formation associated with barium clouds in an inhomogeneous ionosphere, J. Geophys. Res., 81, 5097, 1976.

Hain, K., A non-recursive incomplete Cholesky decomposition method for the solution of linear equations with a sparse matrix, Memo Report 4264, Naval Res. Lab., Washington, D.C., June 1980. ADA087005

Huba, J.D., S.L. Ossakow, P. Satyanarayana, and P.N. Guzdar, Linear theory of the $\underline{E} \times \underline{B}$ instability with an inhomegeneous electric field, J. Geophys. Res., 88, 425, 1983.

Kershaw, D.S., The incomplete Cholesky-conjugate gradient method for the iterative solution of systems of linear equations, J. Comput. Phys. 26, 43, 1978.

McDonald, B.E., Ossakow, S.L., Zalesak, S.T., and Zubusky, N.J., "Scale sizes and lifetimes of F region plasma cloud striations as determined by the condition of marginal stability," J. Geophys. Res., 86, 5775, 1981.

Ossakow, S.L., Ionospheric irregularities, Rev. Geophys. Space Phys., 17, 521, 1979.

Ossakow, S.L., S.T. Zalesak, and M.J. Keskinen, A plausible hypothesis for striation freezing in ionospheric plasma clouds, Memo Report 4597, Naval Res. Lab., Washington, D.C., Aug. 1981.

Ossakow, S.L., M.J. Keskinen and S.T. Zalesak, Ionospheric irregularity physics modelling, AIAA Pap. 82-0147, 1982.

Perkins, F.W., and J.H. Doles III, Velocity shear and the $\underline{E}$ x $\underline{B}$ instability, J. Geophys Res., 80, 211, 1975.

Scannapieco, A.J., S.L. Ossakow, S.R. Goldman, and J.M. Pierre, Plasma cloud late time striation spectra, J. Geophys. Res., 81, 6037, 1976.

Shiau, J.N., and A. Simon, Barium cloud growth and striation in a conducting background, J. Geophys. Res., 79, 1895, 1974.

Vickrey, J.F., and M.C. Kelley, The effects of a conducting E layer on classical F region cross-field plasma diffusion, J. Geophys. Res., 87 4461, 1982.

Zalesak, S.T., Fully multidimensional flux-corrected transport algorithms for fluids, J. Comp. Phys., 31, 335, 1979.

Zalesak, S.T., J.A. Fedder, and S.L. Ossakow, Analysis and numerical simulation of the effect of ion Pedersen mobility on ionospheric barium clouds, J. Geophys. Res., 88, 8003, 1983.

APPENDIX P

A Three Dimensional Model of the Summer Monsoon

A THREE DIMENSIONAL MODEL OF THE SUMMER MONSOON

Keith D. Sashegyi
Science Applications Int. Corp.
Mclean, Va 22102

in collaboration with

Simon W. Chang
Naval Research Laboratory
Washington D.C.

INTRODUCTION

During the summer months, the southwest monsoon of Asia is
dominated by an intense low level jet, the "East African Jet",
which crosses the equator along the East African topography to
flow northward and turn eastward across the Arabian Sea to India.
A strong wind maximum is observed in the jet off the coastline of
Somalia over the western Arabian Sea. Various models have been
used to explain these features of the jet and its formation. These
models show that this low level jet is a cross-equatorial flow
forced by the summer monsoon and concentrated into a western
boundary jet by the north-south topographic barrier of the East
African highlands. In the one-layer reduced gravity barotropic
models (Anderson 1976; Hart, 1977; Bannon 1979a, 1979b, 1982) the
cross equatorial flow is forced by a prescribed sink in the
Northern Hemisphere and/or a source in the Southern Hemisphere in
the presence of a north-south barrier located to the west. These
models showed that the topographic barrier was necessary for the
formation of the low level jet. The wind maximum and the
curvature of the flow in the region were explained by
non-linearities (Anderson, 1976), realistic topographic forcing
(Krishnamurti et al., 1976) and by confluence of the Arabian
northerlies with the low level jet (Bannon, 1982). These
simulations, however, have not correctly placed the wind speed
maximum nor obtained the corect horizontal curvature of the flow
in the jet where it separates from the topography of east Africa.
Also, by their barotropic nature, they are unable to simulate the

P-5

vertical structure of the jet, allow for flow over the topographic barrier of East Africa, or include the effects of sensible heating contrasts as exist across the coastlines of Somalia and Saudi-Arabia.

The planetary boundary layer model of Krishnamurti et al. (1982), which is forced by a prescribed vertically varying pressure gradient, taken from observations, modelled the jet's vertical structure and more realistically simulated the curvature of the jet and the position of the wind speed maximum. No attempt was made however to separate the different possible causes for the curvature and the wind speed maximum. Sashegyi (1983) used a stratified linear model to investigate the steady response of prescribed monsoon heat sources including the latent heating caused by the monsoon convection and the sensible heating over the land areas of Somalia and Saudi-Arabia in an attempt to separate the possible mechanisms. The topographic barrier was modelled as a rigid meridional wall. With a monsoon latent heat source east of the western boundary wall, the low level jet separated abruptly from the western boundary, as is typical of the barotropic models, while the observations show a more gradual curvature of the jet from the topographic barrier. Surface sensible heating over Somalia and Saudi-Arabia was shown to shift the position at which the jet separated from the western boundary farther to the south, closer to that observed. A local wind maximum was also produced in the model along the coastline of Somalia and the curvature of

the jet was more gradual from the topographic barrier. The
results of this linear study indicate that sensible heating over
Somalia and Saudi-Arabia and the cold waters off the coast can
have important effects on the position of the wind maximum and the
curvature of the jet in the region (Sashegyi and Geisler, 1984).

OUR STUDY

In order to separate the various influences of topography and
the latent heating on the structure of the low level jet and to
investigate the effect of sensible heating contrasts between the
land and ocean areas, the three dimensional primitive equations
model of Chang and Madala (1980) was adapted to study the
structure and forcing of the monsoon circulation. The non-linear
model uses sigma coordinates, with five layers in the vertical.
The model with topography is integrated for six days from an
initial zonal average wind field for cases with and without a
prescribed convective heat source. The domain is 24 S to 48 N and
30 E to 110 E with a one degree resolution in longitude and two
degrees in latitude. The planetary boundary layer is modelled by
a single layer while a generalized similarity theory is used to
calculate the surface stress and heat flux (Chang, 1981). In
longitude cyclic boundary conditions are used, while the northern
and southern boundaries are open boundaries.

The horizontal structure of the heat source is the same as
the distribution of observed average July rainfall, which is shown
in Figure 1., while the vertical structure follows that for deep

cumulus convection in the tropics. Due to the short integration period the heating is taken as five times the July average. The initial zonal average wind and temperature field is forced during the integration by a nudging of the zonal average temperature (on the sigma surface) to its initial value with an e-folding time of two days. The initial zonal wind and mass field is initialized with nudging of the wind. After the initialization period, weak nudging is maintained (with an e-folding time of 5 days) and the model integrated for a further 3.5 days to a quasi-steady state.

INTERPOLATION AND INITIALIZATION

The initial zonally averaged wind and mass fields, taken from observations, are interpolated onto our model levels without topography (that is, at constant pressure levels). The mass and wind fields are balanced and then interpolated to the model sigma grid with topography. In our interpolation, the temperature is assumed to vary linearly in log pressure between the pressure levels. Even though the initial zonal wind and mass fields are balanced without the topography, the interpolation onto the sigma grid with topography leads to large errors in the pressure gradient term at the tropopause level over the Tibetan plateau. In fact a ficticious anticyclone with wind speeds reaching 5 to 10 m/s is produced by these errors over the plateau. Around the tropopause, our interpolation procedure fails to account for the tropopause inversion and so generates the above errors in the pressure gradient in sigma coordinates (Sundqvist, 1976). We use

a nudging of the wind field to initialize the initial zonal mass
and wind fields, and remove the errors caused by the steep and
high topography of the Tibetan plateau.

During an initial integration period of sixty hours, the mass
field is adjusted to the high topography dynamically through a
nudging of the wind field to its initial value, with a reducing
e-folding time from 0.1 day to 1 day.

RESULTS

Without the prescribed convective heat source, the response
is largely confined to the lower troposphere. We show the wind
field at the lowest model level in Figure 2. At the end of the
integration, the SE trades which reach 5 m/s are deflected across
the equator by the East African topography, as a low level jet.
The jet doesn't penetrate farther north than 8 N, curving
southward on its eastward path over the Arabian Sea and crossing
the extreme southern tip of India. A wind maximum of 7 m/s is
found over the northern tip of Madagascar and a further maximum of
5 m/s is centered on the equator along the topography.

With the monsoon heat source included, the low level cross
equatorial flow is stronger and broader. A monsoon trough is
located over the NW of India and a large high is found in the
upper troposphere with strong easterly winds of 21 m/s over
central India. In Figure 3, we show the wind field in this case
at the lowest model level. The low level SE trades are increased
in magnitude to 8 m/s due to subsidence forced by the monsoon

heating. The low level jet is also stronger and penetrates
farther north to 16 N in a broad stream of southwesterly flow
across the Arabian Sea. The jet is deeper over the Arabian Sea
and India, becoming more westerly with height. A low level wind
maximum of 9 m/s is found off the coastline of Somalia over the
western Arabian Sea in the region adjacent to where the Arabian
northerlies converge with the southwesterly flow.

The study this far indicates that the summer monsoon
circulation is primarily driven by the large scale convective
heating in the presence of topography. We can conclude also that
the low level wind maximum off the coast of Somalia is not a
result of the deflection of the SE trades into a jet crossing the
equator by the East African topography. But it is dynamically
related to the Northern Hemisphere cyclonic gyre forced by the
convective heating.

PRESENT STUDIES

The effect of the large surface sensible heat fluxes caused
by the high surface temperatures over Somalia and Saudi Arabia
during the summer are currently under investigation. The linear
results of Sashegyi (1983) indicate that such effects may be
important in the structure of the low level jet in the region.
Prescribed surface air temperatures, taken from observations over
land and equated to the sea surface temperature over water, are
used. The single boundary layer formulation using generalized
similarity theory (Chang, 1981) is used to calculate the heat

fluxes. Of interest is the origin of the low level wind maximum off the coast of Somalia.

A multi-layer planetary boundary layer has been developed which will be used to test the sensitivity of our results to increased vertical resolution in the boundary layer. It is expected that the fine structure of the jet along the topography of Eastern Africa will be improved, but that the above large scale features and the above conclusions will not change greatly. In the surface layer the fluxes are calculated as a function of the stability parameter z/L using the universal functions (Paulson 1970, Businger, 1973). In the mixed layer, the eddy diffusion coefficient is taken as a function of the shear and the stability.

FUTURE RESEARCH AND IMPROVEMENTS

The multi-layer planetary boundary layer version of the model can be used in the future to study the sea breeze effects on the low level jet caused by the large diurnal variation in the surface sensible heating over the land areas of Somalia and Saudi-Arabia. Rotunno (1983) in his linear study of the sea breeze circulation indicated a fundamental difference between the sea breeze response in low (between 30 S and 30 N) and high latitudes. The conventional sea breeze circulation of high latitudes was replaced at low latitudes with inertia-gravity waves which propogate away from the heating region. It is expected that interesting effects will be produced on the low level jet along the coastline of Eastern Africa in a fully non-linear simulation. Our model could

address these issues. The development of such a boundary layer
modelling capability will be useful also for other storm modelling
studies which require a detailed boundary layer formulation.

The high mountains in the present study created imbalances in
the mass and wind fields and the initial incident zonal flow
incident on the mountains required a careful initialization
procedure to adjust the wind and mass fields to the topography.
Nudging of the wind field was used with diabatic forcing to
initialize the wind and mass fields, while weaker nudging of the
thermal and wind field maintained the original zonal flow. Future
improvements could be made in the interpolation procedure by using
more levels at the tropopause level in order to better resolve the
inversion and interpolating directly onto the sigma grid from the
observed data to reduce the interpolation errors. The
initialization would then be carried out on the sigma surfaces.
Non-linear balance equation, normal mode initialization or the
bounded derivative technique, with diabatic forcing included,
would be more efficient than the nudging technique. The monsoon
circulation affords an excellent testing situation in the tropics
for initialization techniques.

REFERENCES

Anderson, D.L.T., 1976: The low level jet as a western boundary
current. Mon. Wea. Rev., 104, 907-921.

Bannon, P.R., 1979a: On the dynamics of the East African Jet. I.
Simulation of mean conditions for July. J. Atmos. Sci., 36,
2139-2152;

1979b: On the dynamics of the East African Jet. II.
Jet transients. J. Atmos. Sci., 36, 2153-2168;

1982: On the dynamics of the East African Jet.
III. Arabian Sea Branch. J. Atmos. Sci., 39,
2267-2278.

Businger, J.A., 1973: Turbulent transfer in the atmospheric
surface layer. Workshop on Micrometeorology. Duanne A.
Haugen, Editor., Amer. Meteor. Soc., Boston.

Chang, S.W., 1981: Test of a planetary boundary-layer
parameterization based on a generalized similarity theory in
tropical cyclone models. Mon. Wea. Rev., 109, 843-853.

Chang, S.W., and R.V. Madala, 1980: Numerical simulation of the
influence of sea surface temperatures on translating tropical
cyclones. J. Atmos. Sci., 37, 2617-2630.

Hart, J.E., 1977: On the theory of the East African low-level jet
stream. Pure. Appl. Geophys., 115, 1263-1282.

Krishnamurti, T.N., J. Molinari and H.-L. Pan, 1976: Numerical
Simulation of the Somali Jet. J. Atmos. Sci., 33, 2350-2362;

and V. Wong, H.-L. Pan, R. Pasch, J.Molinari, and P. Ardanuy, 1983: A three dimensional planetary boundary layer model for the Somali Jet. J. Atmos. Sci., 40, 894-908.

Paulson, C.A., 1970: The mathematical representation of wind speed and temperature profiles in the unstable atmospheric surface layer. J. Appl. Meteor., 9, 857-861.

Rotunno, R., 1983: On the linear theory of the land and sea breeze. J. Atmos. Sci., 40, 1999-2009.

Sashegyi, K.D., 1983: A linear dynamic model of the East African Jet in a stratified atmosphere. Ph.D. thesis, University of Miami, Miami, Florida;
and J.E. Geisler, 1984: A linear dynamic model of the East African Jet in a stratified atmosphere. Postprints, 15th Technical Conference on Hurricanes and Tropical Meteorology, 9-13 January, Miami, Amer. Meteor. Soc., 370-374.

Sundquist, H., 1976: On vertical interpolation and truncation in connection with use of sigma system models. Atmos., 14, 37-52.

FIGURE CAPTIONS

Figure 1. The average July rainfall rate in cms/day adapted from
the Jaeger climatology. The model topography is
contoured in thousands of meters.

Figure 2. The wind field at level 5, sigma = .975, for the case
of no convective heating. The maximum vector is 12
m/s. The model topography is contoured in thousands of
meters.

Figure 3. The wind field at level 5 for the case with the
convective heating. The wind vectors and topography as
in Fig. 2.

JULY   AVERAGE   RAINFALL RATE   CMS / DAY
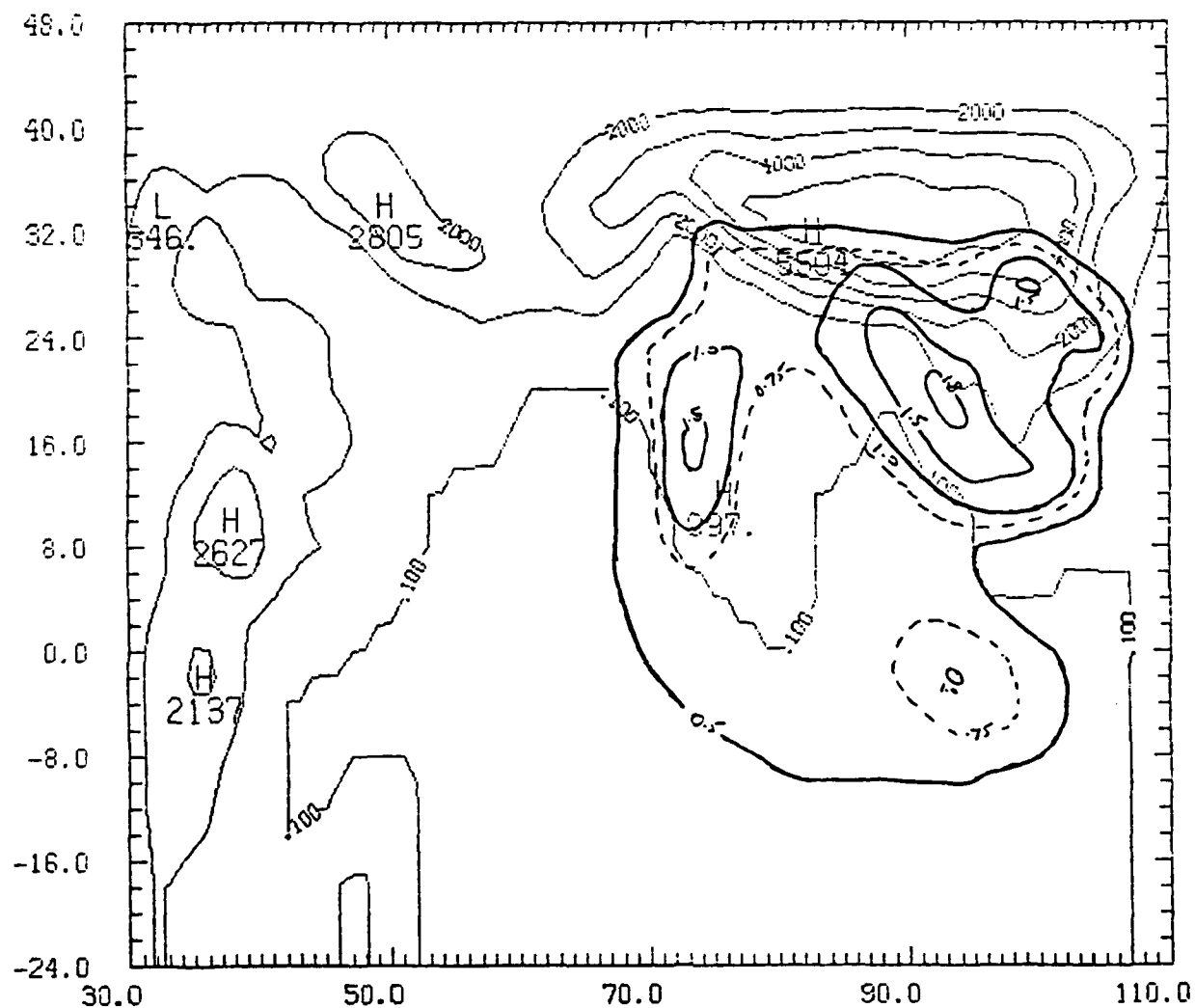
CONTOUR FROM 8980080   TO   208800   CONTOUR INTERVAL OF 0108000   PT(5,9)= 0108800E+00

Figure 1

TOPO(+MAR),BASE WIND(+SE TRADES 10M/S),2 DAY T-DAMP.,DELT=450
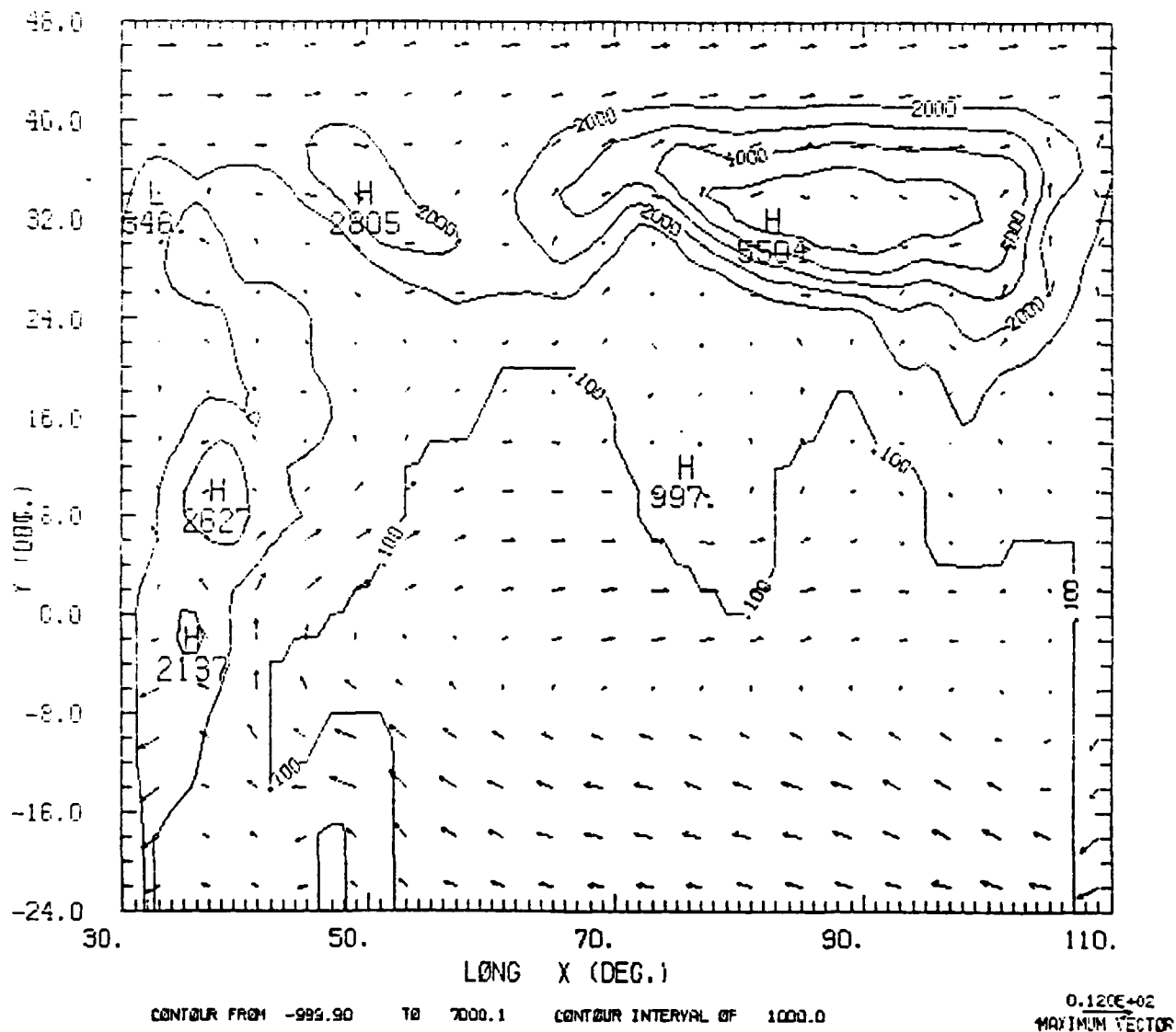
VELOCITY (M/S) AT LEVEL 5 AT T= 144 HR

LONG   X (DEG.)

CONTOUR FROM -999.90   TO   7000.1   CONTOUR INTERVAL OF   1000.0

0.120E+02
MAXIMUM VECTOR

Figure 2

TOPO(+MAR),3AVE U(+SE TRADES-10M/S),HEATING(YANAI)YE,T-DAMP30DY,DELT=450

VELOCIT (M/S) AT LEVEL 5 AT T= 144 HR

CONTOUR FROM -999.90   TO   7000.1   CONTOUR INTERVAL OF   1000.0

0.120E+02
MAXIMUM VECTOR
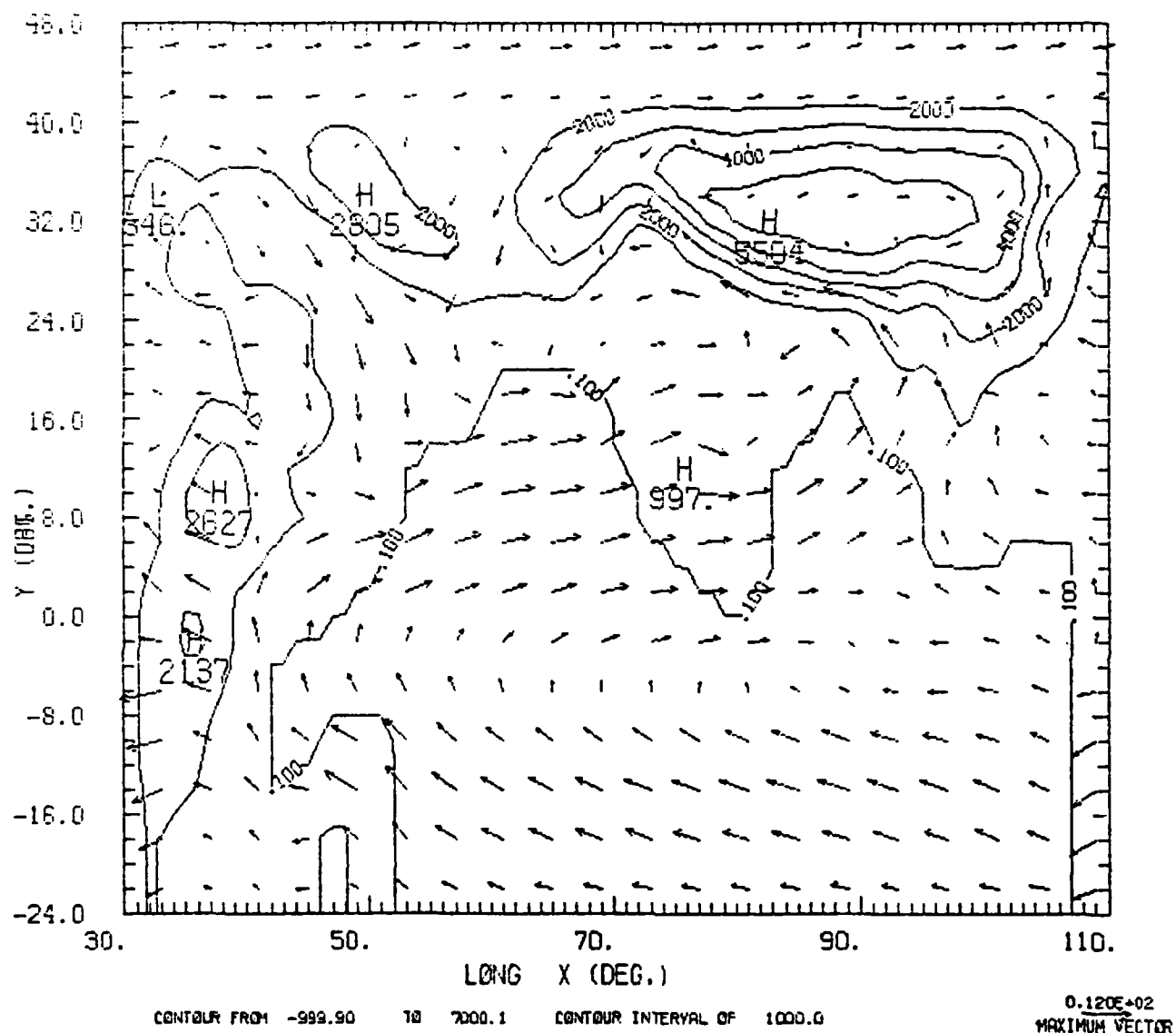
Figure 3

END

FILMED

5-85

DTIC